5-31-2013 12:00 AM

On The Development of a Dynamic Contrast-Enhanced Near-Infrared Technique to Measure Cerebral Blood Flow in the Neurocritical Care Unit

Jonathan T. Elliott
The University of Western Ontario

Supervisor
Keith St. Lawrence
The University of Western Ontario

Graduate Program in Medical Biophysics
A thesis submitted in partial fulfillment of the requirements for the degree in Doctor of Philosophy

ON THE DEVELOPMENT OF A DYNAMIC CONTRAST-ENHANCED NEAR-INFRARED TECHNIQUE TO MEASURE CEREBRAL BLOOD FLOW IN THE NEUROCRITICAL CARE UNIT

(Thesis format: Integrated Article)

by

Jonathan Thomas Elliott

Graduate Program in Medical Biophysics

A thesis submitted in partial fulfillment
of the requirements for the degree of
Doctor of Philosophy

The School of Graduate and Postdoctoral Studies
The University of Western Ontario
London, Ontario, Canada

Abstract

A dynamic contrast-enhanced (DCE) near-infrared (NIR) method to measure cerebral blood flow (CBF) in the neurocritical care unit (NCU) is described. A primary concern in managing patients with acquired brain injury (ABI) is onset of delayed ischemic injury (DII) caused by complications during the days to weeks following the initial insult, resulting in reduced CBF and impaired oxygen delivery.

The development of a safe, portable, and quantitative DCE-NIR method for measuring CBF in NCU patients is addressed by focusing on four main areas: designing a clinically compatible instrument, developing an appropriate analytical framework, creating a relevant ABI animal model, and validating the method against CT perfusion. In Chapter 2, depth-resolved continuous-wave NIR recovered values of CBF in a juvenile pig show strong correlation with CT perfusion CBF during mild ischemia and hyperemia (r=0.84, p<0.001). In particular, subject-specific light propagation modeling reduces the variability caused by extracerebral layer contamination. In Chapter 3, time-resolved (TR) NIR improves the signal sensitivity to brain tissue, and a relative CBF index is be both sensitive and specific to flow changes in the brain. In particular, when compared with the change in CBF measured with CT perfusion during hypocapnia, the deconvolution-based index has an error of 0.8%, compared to 21.8% with the time-to-peak method. To enable measurement of absolute CBF, a method for characterizing the AIF is described in Chapter 4, and the theoretical basis for an advanced analytical framework—the kinetic deconvolution optical reconstruction (KDOR)—is provided in Chapter 5. Finally, a multichannel TR-NIR system is combined with KDOR to quantify CBF in an adult pig model of ischemia (Chapter 6). In this final study, measurements of CBF obtained with the DCE-NIR technique show strong agreement with CT perfusion measurements of CBF in mild and moderate ischemia (r=0.86, p<0.001).

The principle conclusion of this thesis is that the DCE-NIR method, combining multidistance TR instrumentation with the KDOR analytical framework, can recover CBF values that are in strong agreement with CT perfusion values of CBF. Ultimately, bedside CBF measurements could improve clinical management of ABI by detecting delayed ischemia before permanent brain damage occurs.

Keywords

Near-infrared spectroscopy, cerebral blood flow, time-resolved, dynamic contrast-enhanced, delayed ischemic injury, acquired brain injury

Co-Authorship Statement

With the exception of Chapters 1 and 7, all chapters in this thesis are adapted from published journal articles, or manuscripts to be submitted in the near future. While the author of this thesis was the primary author in each of these publications, they have emerged from collaborative research involving a number of different scientists, technicians and clinicians.

Chapter 2 has been adapted from the paper entitled "Quantitative measurement of cerebral blood flow in a juvenile porcine model by depth-resolved near-infrared spectroscopy," published in the *Journal of Biomedical Optics* volume 15, issue 3 in 2010, which was written by Jonathan T. Elliott. Keith St. Lawrence assisted with the design of the study, provided supervision throughout the project, and reviewed the manuscript. Mamadou Diop designed the multichannel near-infrared system and provided technical insight. Kenneth Tichauer consulted on the analysis of the data, and reviewed the manuscript. Ting-Yim Lee supplied the nonparametric analytical program, supported the project through grant funding, and reviewed the manuscript. The author of this thesis was responsible for designing and executing the animal experiments, analyzing the data, and preparing the manuscript.

Chapter 3 has been adapted from the paper entitled "Variance of time-of-flight distributions is sensitive to cerebral blood flow as demonstrated by ICG bolus-tracking measurements in adult pigs," published in *Biomedical Optics Express* volume 4 in 2012, and written by Jonathan T. Elliott. Keith St. Lawrence and Adam Liebert assisted with the design of the study and provided supervision during experiments; additionally, they reviewed the manuscript. Daniel Milej and Anna Gerega consulted on the analysis of the data, specifically with respect to converting time-resolved measurements to statistical moments. Wojciech Weigl provided clinical insight and reviewed

the manuscript from this perspective. Mamadou Diop designed and engineered the time-resolved instrument, and consulted on the data collection. Laura B. Morrison provided support with the animal experimentation. The author of this thesis was responsible for designing and executing the animal experiments, collecting and analyzing the CT perfusion and near-infrared data, conducting the error analysis, and writing the manuscript.

Chapter 4 has been adapted from the paper entitled "Arterial input function of an optical tracer for dynamic contrast enhanced imaging can be determined from pulse oximetry oxygen saturation measurments," published in *Physics in Medicine and Biology* volume 57, issue 24 in 2013, and written by Jonathan T. Elliott. Keith St. Lawrence assisted with the design of the experiment and provided supervision and grant support. Kenneth Tichauer Ting-Yim Lee, and Brian Pogue all provided intellectual input and assisted with the review of the manuscript. Mamadou Diop provided technical support and Eric Wright assisted in the collection of the data and the instrument characterization. Laura Morrison assisted in the animal care and surgical procedures. The author of this thesis was responsible for designing and conducting the animal experiments, performing the error analysis, collecting and analyzing the data, and writing the manuscript.

Chapter 5 has been adapted from the article entitled "Model-independent dynamic constraint to improve the optical reconstruction of regional kinetic parameters," published in *Optics Letters* volume 37 in 2012, and written by Jonathan T. Elliott. Keith St. Lawrence supervised the project, made intellectual contributions, and reviewed the manuscript. Ting-Yim Lee assisted with the technical aspects of the nonparametric analysis, and reviewed the manuscript. Mamadou provided key intellectual contributions during fruitful discussions, and assisted with the editing of the manuscript. The author of this thesis conceived of the idea for combining

optical reconstruction and nonparametric analysis into a single step, wrote the computational code, conducted the numerical simulations, analyzed the data, and wrote the manuscript.

Chapter 6 has been adapted from the manuscript entitled "Measurement of cerebral hemodynamics in an adult pig model of ischemia using a quantitative dynamic contrast-enhanced optical method," which has been prepared for submission by Jonathan T. Elliott. Keith St. Lawrence provided supervisory support, assisted with the design of the experiment, consulted on the analysis of the data, and reviewed the manuscript. Mamadou Diop assisted with the optimization of the optical equipment, the analysis of the data, and the editing of the manuscript. Laura Morrison conducted the surgical procedures and animal preparations, and assisted with the CT acquisition. Christopher d'Esterre assisted with the analysis of the CT perfusion data, and the optimization of the ischemia procedure. Ting-Yim Lee provided support and input regarding the data analysis. The author of this thesis designed and conducted the animal experiments, designed and programmed the analysis software, collected and analyzed the data, performed the error analysis, and wrote the manuscript.

Appendix A has been adapted from "Single-step dual-tracer kinetic imaging approach to quantify molecular expression in fluorescent tomography," a manuscript prepared for submission by Jonathan T. Elliott. Keith St. Lawrence and Brian W. Pogue provided supervision, intellectual input and assistance with the design of the numerical simulations and revision of the manuscript. Kenneth Tichauer wrote a portion of the manuscript, specifically regarding the background of molecular imaging, and assisted with the design of the numerical simulations. Robert Holt provided support with NIRFAST and mesh-related programming, as well as with the tracer kinetics. The author of this thesis designed and programmed the simulations, collected and analyzed the results and wrote the manuscript.

Dedication

"Dixitque Deus fiat lux et facta est lux."

- Genesis 1:3

The steadfast love and devotion of my wife, Laura, continues to astound me each and every day. Thank you for believing in me, as a husband, a father, and a scientist. You encourage me daily, not just in my academic pursuits, but in all aspects of life, by your wonderful example of humility, hard-work, and patience.

To my son, Yianni, who is a little too young to read these words: I dedicate this thesis to you, in the hopes that you will find your own passion and thirst for knowledge, and express it in a way that is unique and personal to you.

I am indebted to my parents, in particular, for providing me so many opportunities to learn, explore, and travel during my formative years. To my father, you have taught me to value family, honesty, and integrity and continue to serve as an example for me in my own family life. To my late mother, from my earliest memories as a child, you truly appreciated and understood me for who I was. I miss you each and every day. To my sister, Jacobi, I have enjoyed so much our friendship over the years. I am excited to watch you find success in your own academic pursuits. Finally, I would also like to thank my parents-in-law, Jim and Brenda, and my brother- and sister-in-law, Ryan and Sarah, for supporting and encouraging me over these last few years.

S.D.G.

Acknowledgments

Without exception, every chapter of this thesis was brought together principally because of the dedication and support of many individuals, who past and present, form the warm and cultivating academic environment that I have enjoyed during my time in London.

I would first like to extend my thanks and gratitude to Dr. Keith St. Lawrence. I will no doubt remain indebted to Keith, my entire academic career, for providing me with the perfect balance of guidance and independence that resulted in such a positive experience as a graduate student. From Keith, I have learned one can be enthusiastic about science and at the same time, adopt a dispassionate, level-headed perspective. I desire to demonstrate this perfect balance of urgency and objectivity in my future research endeavors.

I have had the privilege of sharing an office with my colleague, Dr. Mamadou Diop, who is both a mentor and a friend. If the expression "*verba docent exempla trahunt"* holds true, then Mamadou exemplifies what it means to be hard-working and full of integrity, and I have found great encouragement in his mentorship and sense of perspective. I have enjoyed, in equal measure, discussing science and sharing stories about our kids.

I cannot give enough thanks to my friend and colleague Dr. Kenneth Tichauer, for taking me under his wing early on in my research career, while I was still an undergraduate. We have crossed paths in many different ways over these last few years, collaborating together in the world of tracer kinetics and optical imaging, meeting at conferences and touring the Upper Valley together with our families. Any success I might have in research began with the care and mentorship you extended to me in those early days at Lawson.

I would like to thank my advisory committee members, Dr. Ting-Yim Lee and Dr. Vladislav Toronov, for providing me with support and guidance these last few years. Also, a warm thanks to colleagues and students that have kept me excited about research.

My gratitude to the wonderful team of animal technicians led by Jennifer Hadway cannot be overstated. Jennifer, along with Laura Morrison and Lise Desjardins, provided continuous support with designing experiments, submitting protocols, running the PET/CT scanner, and of course, conducting the animal experiments. I am constantly amazed at the complicated tasks—*e.g.,* open heart surgery, brain surgery, and diagnostic imaging—they do day in and day out. A sincere thanks to all the support staff, from the administrative assistants that handle payroll and finances, to the prototyping lab, the hospital custodial staff, and countless others: their continual work ensures that everything runs smoothly.

Finally, the work presented in this thesis was supported by the public-at-large, through government grants and charitable foundations, including the Canadian Institutes of Health Research, the Heart and Stroke Foundation of Canada, and the Ontario Neurotrauma Foundation and an Ontario Graduate Scholarship. Health research, in particular, is relied upon by countless individuals and their families to solve important and often life-threatening problems. As such, I believe research is an expression of human compassion that we extend to one another. I am grateful for the opportunity to be a part of this noble pursuit.

Table of Contents

List of Tables

Lists of Figures

List of Appendices

List of Acronyms and Abbreviations

AATH	adiabatic approximation to the tissue homogeneity model
ABI	acquired brain injury
AIF	arterial input function
ANOVA	analysis of variance
ASL	arterial spin labeling
AUP	animal use protocol
BF	blood flow
BV	blood volume
CBF	cerebral blood flow
CBV	cerebral blood volume
CDC	Centers for Disease Control and Prevention
$CI_{0.95}$	95% confidence interval
CSF	cerebrospinal fluid
CPP	cerebral perfusion pressure
CPU	central processing unit
CT	computed tomography
CTP	computed tomography perfusion
$CTDI_w$	weighted computed tomography dose index

CW	continuous-wave
DA	diffusion approximation
DCE	dynamic contrast-enhanced
DII	delayed ischemic injury
DOT	diffuse optical tomography
DR	depth-resolved
DTOF	distribution of time-of-flight
ECL	extracerebral layer
EEG	electroencephalogram
EES	extracellular extravascular space
EGFR	epidermal growth factor receptor
EVS	extravascular space
FD	frequency domain
FEM	finite element method
FMT	fluorescence molecular tomography
GFLOPS	giga- floating-point operations per second
GPU	graphics processing unit
H_2O	water
Hb	deoxyhemoglobin

HbO_2	oxyhemoglobin
ICG	indocyanine green
ICP	intracranial pressure
IRF	impulse residue function
IVS	intravascular space
KDOR	kinetic deconvolution optical reconstruction
MC	Monte Carlo
MCML	Monte Carlo multi-layer
MCX	Monte Carlo eXtreme
MPP	mean partial pathlength
MRI	magnetic resonance imaging
MTT	mean transit time
NCU	neurocritical care unit
NIR	near-infrared
NIRS	near-infrared spectroscopy
NNLS	non-negative least squares
PDD	pulse dye densitometer
PET	positron emission tomography
PO	pulse oximeter

PRBC	packed red blood cells
ROI	region of interest
RTE	radiative transfer equation
SaO_2	arterial blood oxygen saturation
SAH	subarachnoid hemorrhage
SHARCNet	shared hierarchical academic research computing network
SNR	signal-to-noise ratio
SP	single-probe
SS	simple subtraction
TBI	traumatic brain injury
TCD	transcranial Doppler
TDF	thermal dilution flowmetry
TIF	tissue impulse function
TPSF	temporal point spread function
TR	time-resolved
TS	two-step
TSVD	truncated singular value decomposition
TTP	time-to-peak
XeCT	xenon-enhanced computed tomography

Chapter 1

INTRODUCTION

The objective of this introductory chapter is to provide the reader with an appreciation of why the topic of this doctoral thesis—the development and validation of near-infrared (NIR) methods to quantify cerebral blood flow (CBF) in the neurocritical care unit (NCU)—was studied. First, the rationale for this work will be provided within the context of the clinical problem: acquired brain injury (ABI). This will involve a description of the pathological mechanisms underlying some of the most common conditions treated in the NCU—traumatic brain injury (TBI) and nontraumatic subarachnoid hemorrhage (SAH). The importance of quantifying CBF for the management of these patients will be highlighted, and current methods for measuring CBF will be described. After establishing the motivation for this work, the theoretical basis of dynamic contrast-enhanced (DCE) NIR techniques, which encompasses the methods developed in this work, will be provided. In particular, the specific challenges of applying DCE-NIR methods to an adult head to measure CBF will be highlighted. This final point represents the main knowledge gap that this thesis will address.

1.1. Rationale

The neurocritical care unit (NCU) has emerged as a specialized intensive care unit responsible for the treatment of life-threatening neurological illnesses.

Often, patients admitted to the NCU are comatose or paralyzed and present with injuries to other parts of the body, making their management difficult. In a collaborative effort, neurointensivists, neurosurgeons, diagnosticians and nurses are responsible for the clinical management of NCU patients to ensure the best chance for survival (Diringer *et al* 2001). Acquired brain injuries—including TBI, diffuse acquired brain injury, stroke, and SAH from traumatic or aneurysmal origin—comprise the majority of cases for which patients are admitted to the NCU. For the purpose of this thesis, discussion will be limited entirely to ABI and principally those injuries caused by TBI and its sequelae, as well as SAH.

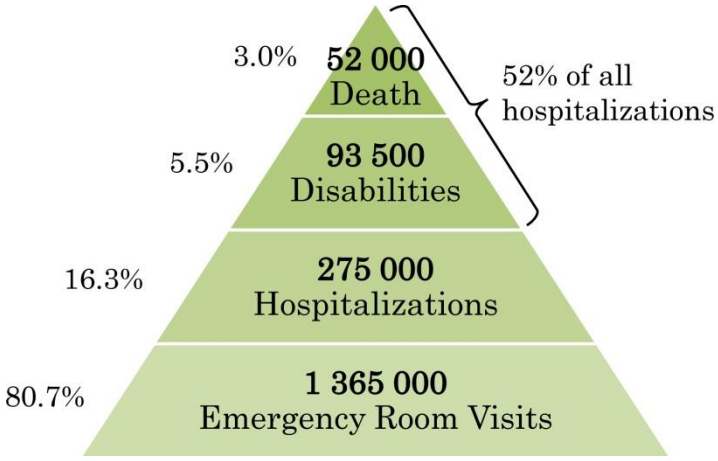

Figure 1.1: Prognosis of traumatic brain injury.

The approximate outcomes of 1.7 million TBIs that occurred annually in the United States during years 2002-2006. Of the 275,000 hospitalizations, 52% of individuals died or suffered permanent disability. (Figure adapted from Langois 2010 and Baron and Jallo 2007).

From an epidemiological standpoint, TBI is the single most common cause of death and disability among children and young adults (Langlois 2000). At least 1.7 million people sustain a TBI each year in the United States (figures from 2002-2006, when the US population was approximately 300 million); 275,000 of those individuals are subsequently hospitalized and about 52,000 of those injuries are ultimately fatal (CDC 2010). The term "traumatic brain injury" reflects an etiology (*i.e.*, a brain injury sustained in

trauma) rather than a specific pathology, which can be complex and multifaceted. Therefore, TBI is further stratified according to mechanism (blunt or closed injury versus penetrating or open injury), spatial pattern of disease (focal or diffuse), and severity of primary brain damage (Glasgow coma scale). Proper classification of TBI can help establish a prognosis, and provide insight into possible complications that are likely to follow. For example, a focal pattern of TBI is likely to result in cerebral contusions, hemorrhages, and hematomas (Baron and Jallo 2007).

In addition to TBI, the NCU supports patients with non-traumatic ABI such as ischemic stroke and subarachnoid hemorrhage. In particular, SAH accounts for about 5% of strokes, but remains among the most life-threatening neurological diseases and affects primarily adults under the age of 60. In fact, because SAH affects preferentially young individuals—with a mean age of 50 years (Nieuwkamp *et al* 2005)—the number of years of potential life lost by SAH accounts for about 25% of all stroke-related diseases (Johnson *et al* 1998; Hop *et al* 1997). Therefore, SAH has a societal impact comparable with ischemic stroke. Nontraumatic SAH—for which 85% of cases are secondary to the rupture of an aneurysm (Sehba *et al* 2012)—occurs when blood extravasates into the CSF-filled space between the arachnoid membrane and pia mater known as the subarachnoid space. The mortality rate of SAH is 40%, and includes approximately 10-20% of patients who die before receiving advanced medical care (Sehba *et al* 2012). Furthermore, SAH patients are susceptible to serious complications following the initial injury, which will be further discussed in the subsequent section (van Gijn J 2001).

1.2. Complications in acquired brain injury

1.2.1. Clinical presentation

Following the primary brain injury caused by either TBI or SAH, the principal concern of the NCU is to minimize complications during the acute recovery stage that compromise the outcome of the patient. Complications that develop secondary to the initial injury represent the single greatest threat to the outcome of the patient, as a significant portion of neurological damage develops during the days to weeks following hospitalization, rather than during the primary insult. Most often, these complications result from impaired blood flow which prevents adequate oxygen delivery to the brain tissue, resulting in permanent "secondary brain injury" or “delayed ischemic injury” (DII) (Wartenberg 2011; Coles 2004). Although DII is the manifestation of a pathological cascade beginning within hours of brain injury, it is a target for intervention since it tends to progress gradually while the patient is in the NCU. Therefore, a primary concern of the NCU is to detect and minimize these complications, which include intracranial hypertension, edema, vasospasm, and other bleeding disorders (Rincon and Mayer 2007), before permanent brain injury results.

Intracranial hypertension, in which intracranial pressure (ICP) becomes elevated, is among the most important complications that occur in brain injury patients. An increase in ICP usually results from a mass effect—either edematous or hemorrhagic in nature (Steiner and Andrews 2006). Since the skull acts as a closed container, ICP becomes elevated when the overall volume of three elements—brain parenchyma volume, blood volume, and cerebrospinal fluid (CSF)—increases. To some degree, slight variations in one element can be compensated by the other two according to the Monro-Kellie doctrine (Mokri 2001). Figure 1.2 shows a schematic of this compensatory mechanism.

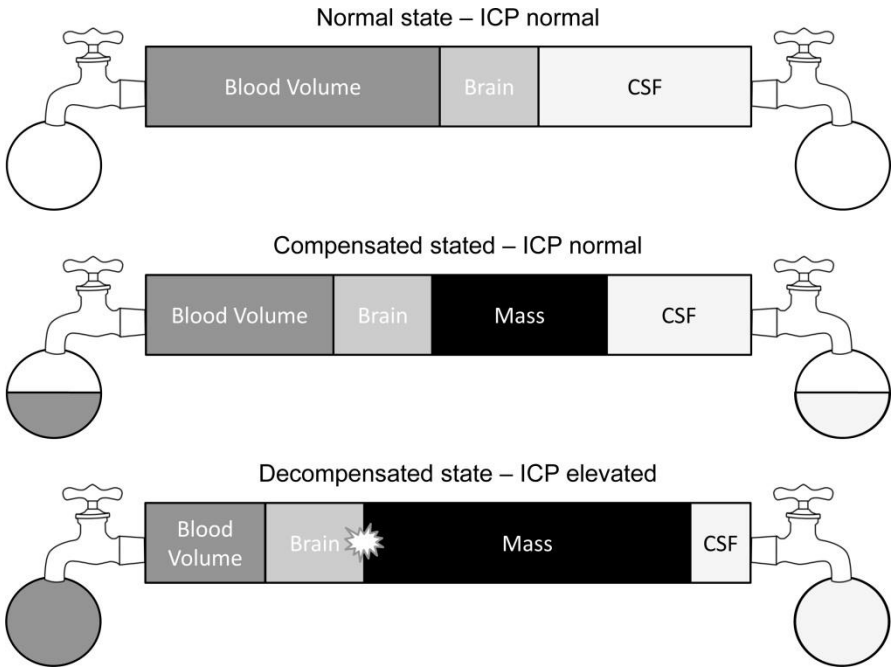

Figure 1.2: Compensatory mechanism

In a normal state, the intracranial pressure (ICP) is tightly regulated. When a mass effect occurs due to some underlying pathology, a small increase in volume can be accommodated by reductions in blood volume and cerebral spinal fluid (CSF). Larger increases overwhelm the compensatory mechanisms and brain tissue expansion causes elevated ICP leading to herniation and distortion.

Compensation occurs as either blood volume, or more often CSF, is reduced to accommodate the expanding lesion. In the latter case, CSF is reabsorbed and the production of new CSF is reduced in the presence of slightly elevated ICP (Cutler *et al* 1968). Continued expansion of the mass will result in progression through four stages of intracranial hypertension: total compensation, partial compensation, decompensation, and vasomotor paralysis (Barlow and Stewart 2007).

A principle cause of intracranial hypertension is brain edema, which increases the brain parenchymal volume. Defined as the swelling of brain tissue, brain edema can be vasogenic or cytotoxic in origin (Ropper 1984). In vasogenic edema, the blood-brain barrier is disrupted by the primary or secondary injury, allowing the extravasation of fluid and proteins across the

otherwise tightly regulated endothelium and into the interstitial space of the brain parenchyma. As a result, an osmotic gradient is created, drawing water into the interstitum. In cytotoxic edema, the primary insult causes a disruption in brain energy metabolism, resulting in a depletion of energy stores needed to maintain ion homeostasis (Liang *et al* 2007). The resulting increase in interstitial osmolality draws water across the blood-brain barrier and causes a subsequent increase in intracranial pressure. Edema of the brain can result in secondary brain injury if the increase in parenchyma volume overwhelms the compensatory mechanisms described in the previous paragraph.

An additional cause of intracranial hypertension is the development of a hematoma, a localized collection of blood outside of the vessels, which can pool between the dura mater and the skull (*i.e.*, epidural hematoma) or between the dura mater and the arachnoid mater (*i.e.*, subdural hematoma). Epidural and subdural hematomas are examples of extra-axial hemorrhage (Wilberger *et al* 1991)—bleeding that occurs outside of the brain tissue but within the skull. In addition to extra-axial hemorrhage, intra-axial or cerebral hemorrhage can also occur. When cerebral hemorrhage occurs secondary to brain injury, it is usually due to penetrating head trauma or acceleration-deceleration trauma (Udstuen and Claar 2001). In all of these examples, elevated ICP is a principle concern. In some circumstances, this can be mitigated by early evacuation of the hematoma (Wilberger *et al* 1991).

Delayed ischemic injury is also a primary concern in SAH, and develops in approximately one third of patients within the first two weeks. The main cause of DII in SAH patients is the development of vasospasms—spontaneous spasms in cerebral blood vessels leading to vasoconstriction—which have a high rate of mortality and must be treated aggressively (Crowley *et al* 2011). The risk of developing vasospasm following aneurysmal SAH appears to be related to blood clot burden, and is likely triggered by an

inflammatory response within the blood-vessel wall that manifests sometime between days 4 and 12 post-SAH. The fact that the amount of blood seen on the initial CT scan is the best predictor of the occurrence of vasospasm in aneurysmal SAH (Hijdra *et al* 1988) also suggests that vasospasm induction is blood-mediated. Cerebral vasospasm can also occur in TBI, and while the importance of vasospasm in aneurysmal SAH has been well-studied, considerable controversy surrounds the exact relationship between TBI and vasospasm (Werner and Engelhard 2007). Unlike in SAH, where vasospasm seems to be directly related to factors released by the blood clot, TBI-related vasospasms are frequently detected in patents without CT evidence of bleeding (Taneda *et al* 1996). This calls into question whether all vasospasms share the same pathophysiology, and underlines the challenge in managing patients for whom vasospasm-related complications may not be easily predicted based on CT imaging.

1.2.2. Clinical management

There is a growing body of evidence that suggests that the NCU has improved both survival and outcome in patients with ABI (English *et al* 2012; Varelas *et al* 2006). For example, a reduced mortality rate following intracerebral hemorrhage was observed in patients admitted to NCUs compared to general intensive care units (Diringer and Edwards 2001). Improvements in patient recovery has been principally due to the NCU's ability to manage the complications associated with secondary brain injury, which combine standard clinical practice of intensive care medicine with interventions that target specific complications such as elevated ICP, reduced CBF, and hemorrhage.

Osmotherapy is considered the first-line method for managing raised ICP and involves the rapid infusion of mannitol or hypertonic saline. Mannitol, a crystalline sugar alcohol, creates an osmolar gradient in the

brain, drawing water across the blood-brain barrier (Muizelaar *et al* 1984). A similar ICP-lowering effect is achieved by the infusion of hypertonic saline. When administered repeatedly, osmotherapy can be an effective means to manage raised ICP, notwithstanding the additional risks that require careful monitoring of electrolyte status and serum osmolarity. In addition to osmotherapy, decompressive craniectomy can be used to reduce ICP. Decompressive craniectomy involves removing part of the skull to allow the expansion of the brain parenchyma in the presence of uncontrollable elevated ICP. Despite being used for more than a century to manage brain swelling and ICP, its current use is controversial. Several previous studies (Hofmeijer *et al* 2009; Vahedi *et al* 2007; Jüttler *et al* 2007) reported neutral findings, and while a meta-analysis of these studies suggests a benefit to craniectomy in certain patient subgroups, further research is needed before routine decompression craniectomy can be recommended (Mitchell *et al* 2009).

While there is no general consensus on the treatment or prevention of DII following SAH, current treatment recommendations include prophylactic nimodipine (Barker *et al* 1996), along with the so-called "triple H" therapy (hypervolemia, hypertension, and hemodilution) (Weyer *et al* 2006). The motivation behind these treatments is to prevent contraction of cerebral arterial smooth muscle cells and/or to counter the effects of increased vascular resistance by increasing cerebral perfusion pressure and reducing blood viscosity. For instance, nimodipine, a dihydropyridine-type calcium channel blocker, inhibits the influx of extracellular calcium which acts on smooth muscle cells to effect vasoconstriction. As a standard-of-care, the only proven therapy for vasospasm is nimodipine (Weyer *et al* 2006); however, "triple-H" therapy may be indicated for individual patients on a case-by-case basis.

In addition to the management of DII, best evidence-based practices generally indicated for intensive care patients remain important for

neurotrauma patients. These include ensuring optimal oxygenation through proper ventilation, maintaining appropriate levels of glucose and nutrition, and monitoring temperature homeostasis. In particular, the injured brain is thought to have low tolerance to hypoglycemia, and is a concern unique to neurocritical care (Vespa *et al* 2006).

1.3. Assessing delayed ischemic injury

1.3.1. Current clinical methods

While many of the management options discussed in the previous section are effective in alleviating some of the deleterious complications that develop during recovery, a principle challenge is detecting the onset of DII in NCU patients. First, it is often difficult to differentiate between clinical features resulting from the primary injury and those symptoms that develop subsequently. Early signs of DII present as general neurological defects or reduced consciousness, which can also be attributed to other causes (*e.g.*, effect of sedatives, hypotension, heart failure). In addition, many NCU patients are comatose or heavily sedated, and clinical features are unreliable for these individuals (Vergouwen *et al* 2010).

Electroencephalography (EEG) is used to monitor cerebral electrical activity (*i.e.*, voltage fluctuations that result from neuronal activation in the cortex). Several studies have investigated the use of EEG to detect DII in SAH patients (Vespa *et al* 1997; Claassen *et al* 2004a) and TBI (Claasen *et al* 2004b), in part by identifying clinical features associated with energy failure. In particular, epileptic activity, which can be accurately detected using EEG, could exacerbate brain energy impairments and increase glutamate-mediated excitotoxicity (Vespa *et al* 1998). As well, a relationship between increased seizure activity and cerebral hyperglycolysis has been documented in several studies (Engel *et al* 1983; Evans *et al* 1984; Theodore *et al* 1983). Hyperglycolysis, which occurs acutely after severe TBI, is indicative of

impaired oxygen metabolism and can also occur during a major reduction in CBF (Bergsneider *et al* 1997). In general, SAH and TBI produce a wide variety of EEG abnormalities, some of which may be predictive of DII (Rivierez *et al* 1991; Claassen *et al* 2004). However, in all cases, large sets of EEG data must be interpreted by an expert, which is time consuming and subjective, making general clinical thresholds for directing patient therapy unlikely.

Intracranial pressure monitoring has become a mainstay of the NCU as a standard surrogate of CBF. Because these methods are invasive, their use is generally limited to poor-grade SAH (Wartenberg 2011) and severe TBI (Brain Trauma Foundation 2008). Being a surrogate of CBF, there is considerable controversy surrounding its use in directing patient therapy, since large variations in optimal thresholds are likely to exist due to differences in cerebral autoregulation (Jaeger *et al* 2007). Four randomized clinical trials reported no significant relationship between ICP monitoring and survival in TBI patients (Mauritz *et al* 2007; Mauritz *et al* 2008; Thompson *et al* 2008; Griesdale *et al* 2010), and two additional studies demonstrated conflicting results (Lane *et al* 2000; Shafi *et al* 2008). A sytematic review of these studies found that the benefit of routine ICP monitoring in severe TBI is not established and further research is needed (Mendelson *et al* 2012).

The gold standard in the diagnosis of vasospasm is cerebral angiography, despite having a specificity of only 50% (Uterberg *et al* 2001). In addition to angiography, vasospasm is monitored using transcranial Doppler (TCD), which can detect elevated blood flow velocities that occur with vessel narrowing (Sloan *et al* 1989). However, like in the case of ICP monitoring, vessel narrowing is only a surrogate of CBF, and not all patients with vasospasm develop DII (Vergouwen 2011). Furthermore, DII can occur in regions where large-vessel narrowing was not observed, but regional

hypoperfusion and oligemia were nevertheless present (Dhar *et al* 2012). Taken together, these studies suggest that vessel narrowing detected by angiography, or the resulting elevated blood flow velocity detected with TCD, are not reliable markers of DII, especially when neurological assessment is unavailable (Vajkoczy *et al* 2003).

Recently, thermal diffusion flowmetry (TDF) has been described as a potential method to measure absolute CBF and has been validated against XeCT in adult sheep. (Vajkoczy *et al* 2000). While the ability of TDF to measure CBF in absolute units is a positive step, the TDF technique is invasive, requiring microprobes to be inserted directly into the cortical parenchyma. The degree to which this might result in complications, such as intracerebral hemorrhage or infection, is not yet known. Another limitation of this technique is that it is only able to provide local CBF measurements from a very small region of tissue. As such, a single microprobe placed in the region of brain most susceptible to SAH-related vasospasm could miss up to 20% of cases (Vajkoczy *et al* 2003), likely requiring the placement of multiple microprobes with additional patient risk.

Finally, xenon-enhanced computed tomography (XeCT) has emerged as a promising method of measuring CBF in NCU patients (Yonas *et al* 1996), in part due to the advent of portable CT units that can be used at the patient bedside (Kim *et al* 2009). Like other CT perfusion methods, XeCT provides only a single snapshot of CBF and the use of ionizing radiation, as well as the expensive nature of inhaled xenon gas, precludes its use for frequent serial measurements.

1.3.2. Clinical value of measuring cerebral blood flow

In a normal, healthy adult, CBF is maintained by autoregulation at approximately 50 ml min^{-1} $100g^{-1}$. However, in pathological conditions, autoregulation is disrupted or overwhelmed and CBF can decrease to critical levels. When this occurs, depletion of high-energy phosphates—the brain's energy stores—occurs rapidly. If CBF falls below about 17 ml min^{-1} $100g^{-1}$, electrocortical activity is lost, as evinced by EEG, and increased anaerobic metabolism occurs (Sharbrough *et al* 1973). Further reduction of blood flow below 10 ml min^{-1} $100g^{-1}$ results in the loss of ion homeostasis (due to failed membrane integrity) and leads to an efflux of potassium from neurons. Cytotoxic edema and subsequent cell death follow quickly (Astrup *et al* 1981). In addition, the progression of tissue state from ischemia to infarction depends on the duration of the insult. For example, extremely low CBF (less than 5 ml min 100g) can result in an infarction within minutes. On the other hand, when CBF is held at around 18 ml min^{-1} $100g^{-1}$, permanent damage occurs only after several hours (Astrup *et al* 1981). This dependency of infarction on insult duration has been well established in the treatment of acute stroke, where tissue is salvaged by prompt recanalization.

As highlighted in the previous section, complications that occur following ABI—including elevated ICP from edema, hemorrhage or hematoma, and SAH-induced vasospasm—can severely reduce CBF and result in DII and poor patient outcome (Rincon and Mayer 2007). Current clinical methods to detect DII are limited, and involve monitoring surrogates of CBF (*e.g.*, ICP, CPP, blood velocity, etc.). A cursory review of literature supports two principle conclusions. First, each of these methods may be indicated for certain patients on a case-by-case basis; however, the systematic use of any of these techniques is not supported by current evidence. Second, emerging evidence supports the use of guideline-driven management of severe TBI patents (who present with heterogeneous features that are

unreliable for steering intervention) which has been shown to improve patient outcome (Griesdale *et al* 2012). Presumably, measurements of CBF, for which well-defined thresholds exist, have the potential of informing these clinical guidelines.

In an early study by Yonas and colleagues, CBF measurements by XeCT were acquired in fourteen SAH patients exhibiting symptoms of vasospasm (Yonas *et al* 1989). Regions of CBF above 18 ml min^{-1} $100g^{-1}$ did not progress to infarction, whereas areas with CBF lower than 12 ml min^{-1} $100g^{-1}$ resulted in conversion to infarction. For regions between 12 - 18 ml min^{-1} $100g^{-1}$, infarct conversion was variable. Although the sample size of the study was too small to accurately determine optimal thresholds for CBF predictive of infarct conversion, the determination of such a threshold could enable more individualized treatment to the patients with the most to gain (*i.e.*, with CBF values close to the threshold for which infarct conversion is variable).

Thermal-diffusion flowmetry was used to evaluate regional CBF in fourteen patients with high-grade SAH. In each patient, two TDF microprobes were inserted into the white matter of regions of the brain supplied by the artery that was affected by the aneurysm (which included the internal carotid artery, the anterior communicating artery, and the middle cerebral artery). Thermal-diffusion flowmetry values of CBF predicted symptomatic vasospasm in these patients with 85% sensitivity and 97% specificity when a threshold of 10 ml min^{-1} 100 g^{-1} was used. While the threshold used in this study was lower than loss of neuron function thresholds (*i.e.*, 18 ml min^{-1} $100g^{-1}$)—likely due to the lower blood flow in white matter where the probes were implanted—the reliability of TDF measurements was greater than TCD.

Most recently, CT perfusion was acquired in 85 SAH patients to determine a diagnostic threshold value with optimal sensitivity and specificity to DII (Dankbaar *et al* 2010). Values of CBF and mean transit time (MTT) were able to distinguish DII with greater than 70% accuracy. However, since imaging was only performed at a single time-point, more transient instances of vasospasm may have gone undetected.

The handful of studies investigating the ability of CBF measurements to predict subsequent development of DII in high-risk SAH patients suggests a CBF diagnostic threshold exists, and that a direct assessment of CBF can confirm vasospasm and enable aggressive treatment (Powers *et al* 1985; Soucy *et al* 1990). For this reason, the ability to directly measure CBF in patients with SAH has been highly sought by clinicians (Vajkoczy *et al* 2003). While the role of CBF measurements in TBI is less clear, it is well established that CBF less than 18 ml min^{-1} $100g^{-1}$ is present in about one third of TBI cases, and is correlated with poor outcome and early mortality (Bouma and Muizelaar 1995). Given the importance of proper stratification of patients in the randomized clinical trials of future therapies for ABI, CBF thresholds are likely to have an important role. The limitations of current methods highlight the need for a non-invasive bedside technique to measure CBF in NCU patients. Dynamic contrast-enhanced NIR techniques are well suited to this goal, and the remainder of this chapter will provide the necessary background on DCE methods in general, and in particular, on the DCE-NIR method that was developed for NCU applications.

1.4. Dynamic contrast-enhanced measurement of cerebral blood flow

1.4.1. History in humans

The pioneering work in the field of quantitative CBF measurement was accomplished largely by Kety and Schmidt, who in 1945 described a method

of measuring CBF based on the Fick principle (Kety and Schmidt 1945). This method utilized the highly diffusible gas nitrous oxide as a blood flow tracer. Cerebral blood flow was calculated by measuring the time-varying concentration of nitrous oxide in arterial blood and venous blood samples from the jugular bulb. A significant advancement in CBF measurements was achieved using radiolabeled ^{85}Kr instead of nitrous oxide, as this provided a means of assessing regional CBF by placing scintillation counting devices at various locations on the scalp (Lassen and Munck 1955). This approach was further improved by the use of radioactive ^{133}Xe, and through the work of Obrist who modified the Kety-Schmidt equation to account for three tissue compartments: extracerebral tissue, gray matter (which has a higher blood flow (BF)), and white matter (which has a lower BF) (Obrist *et al* 1967). Furthermore, the arterial input function (AIF) could be determined non-invasively from end-tidal ^{133}Xe measurements instead of requiring carotid artery catheterization, making the technique more desirable clinically. Diffusible tracer methods proved very popular in subsequent imaging approaches, including the first truly tomographic method of quantifying cerebral blood flow achieved using positron emission tomography (PET) and $H_2{}^{15}O$ (Frackowiak *et al* 1980).

Around the same time, Axel published the theoretical groundwork for DCE CT that implemented a sequence of scans following an intravenous bolus injection of contrast to determine CBF (Axel 1980). Unfortunately, the method required ultrafast acquisition times with little inter-scan delay times—something the CT scanners at the time were unable to accomplish. As well, the proposed method for analyzing the dynamic CT data relied on a number of assumptions and was prone to subject-dependent effects (such as the tissue hematocrit level) (Gobbel *et al* 1990). Nevertheless, the groundwork by Axel laid the foundation for CT perfusion, which would

receive considerable attention as CT technology and analytical methods improved over the next decade.

1.4.2. Current techniques

During the 1990s, CT scanners were developed with the capability of performing repeat scans with acquisition times of about 100 milliseconds and interscan delays of about 1-2 seconds, so that quantitative CBF measurements with dynamic CT imaging became feasible (Brix *et al* 1999). As a result, CT perfusion has emerged as a robust, reliable, and accurate tool to quantify CBF and is capable of providing parametric maps of CBF as well as cerebral blood volume (Cenic *et al* 2000), mean transit time (Eastwood *et al* 2002), and bolus arrival time (Eastwood *et al* 2002; Mayer *et al* 2000). Current CT perfusion techniques can be considered variations on the methodology outlined by Axel: CT slices are acquired at a high temporal resolution during the injection of a bolus injection of contrast agent. The analysis consists of reconstructing the time-series of images, defining the AIF and voxel or region-of-interest (ROI) specific tissue concentration curves, and performing kinetic analysis on these curves to recover kinetic parameter maps. Most techniques differ by the manner in which they perform the final step of kinetic analysis: mainly, whether they use a compartment-based approach (Miles 1991; Mullani and Gould 1983) or deconvolution approach (Cenic *et al* 2000; Eastwood *et al* 2002). The latter approach will be discussed in following section. In addition to CT perfusion, CBF measurements can be made using XeCT, DCE magnetic resonance imaging (MRI) (typically in conjunction with a gadolinium-based tracer) or with the MRI arterial spin labeling (ASL) technique (Wintermark *et al* 2005). In recent years, there has been a rekindled interest in XeCT due to the development of portable and intraoperative CT devices (Kim *et al* 2010). However, limitations of the device include the high costs of xenon gas and the use of ionizing radiation (120

mGy $CTDI_w$), which makes it unsuitable for bedside measurements of CBF on a continual basis.

1.4.3. Tracer kinetic modeling

The DCE NIR techniques presented in this thesis, in addition to CT perfusion, rely on a bolus injection of a contrast agent to provide hemodynamic information about a tissue region-of-interest (ROI). In this context, the contrast agent acts as a blood flow tracer, which by definition is a substance that behaves in the same manner as blood as it travels through the tissue of interest (Lassen and Perl 1979). The transport of the tracer through the microvasculature of the tissue can be described by constructing a kinetic model and applying it to time-dependent measurements of the tracer concentration. For example, the blood flow (F) to an organ can be determined using the Fick principle if the time-dependent concentration of tracer in the organ, $Q(t)$, in the arterial blood, $C_a(t)$, and the venous blood draining the organ, $C_v(t)$, are measured. In this case, the following expression describes the dynamic behaviour of the tracer:

$$\frac{dQ(t)}{dt} = FC_a(t) - FC_v(t). \qquad (1.1)$$

The most common type of model used in kinetic analysis is the Kety model, which describes the behaviour of a highly diffusible tracer in a single tissue compartment. Compartment models form the basis of the radioactive and stable Xenon CT techniques and the radioactive H_2O PET methods described in the previous section.

There is a fundamental problem with applying compartmental models to non-diffusible, intravascular tracers (*e.g.*, iodine-based CT contrast agents, and optical tracers such as indocyanine green (ICG) that bind to vascular proteins) because the intravascular space (IVS) dynamics are much faster

than the minimal extravascular space (EVS) component. Therefore, the tissue cannot be treated as a single, well-mixed compartment. Instead, it is more appropriate to consider the tissue vascular bed as a mesh of microvessels supplied by a single input and draining to a single output (Fig. 1.3), where each possible path from the artery to the vein has a specific transit time. In this case, the concentration of tracer in the tissue at a given time point is a function of its collective path through the capillary bed, as well as the AIF.

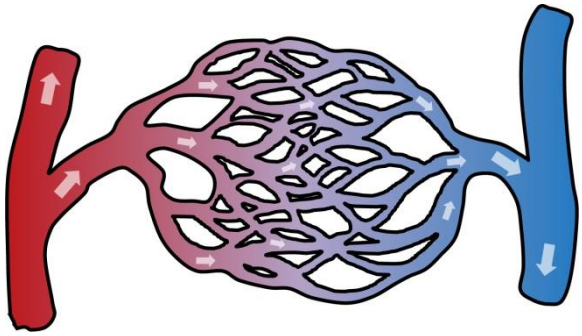

Figure 1.3: Blood flow through a capillary bed.

The convolution theory of kinetics treats the capillary bed as a black box, with an arterial input, a venous output, and a transfer function based on the distribution of transit times required by possible paths through the mesh.

The path that a particular tracer molecule takes is nondeterministic, but a distribution of transit times, $h(t)$, can be described for a bulk set of tracer molecules (Meier 1954). This distribution describes the effect of a time-invariant linear system on the input, $C_a(t)$, such that the venous output can be modeled as:

$$C_v(t) = \int_0^t C_a(u)h(t-u)du, \qquad (1.2)$$

where u is a dummy variable in the convolution. Equation 1.2 provides a definition for $C_v(t)$ that is not dependent on any modeling assumptions, such as instantaneous equilibrium, and by substitution, Eq. 1.1 becomes:

$$\frac{dQ(t)}{dt} = FC_a(t) - FC_a(t) * h(t). \tag{1.3}$$

where * represents the convolution operator. To simplify Eq. 1.3, a more convenient and closely related function, *R(t)*, called the impulse residue function is used to describe the dynamics of the system. *R(t)* is defined as the fraction of dye remaining in the system at time, t, following the injection of an idealized bolus (*i.e.*, a Dirac delta function), and is given by:

$$R(t) = 1 - \int_0^t h(u)du, \tag{1.4}$$

Substituting *R(t)* for *h(t)*, Eq. 1.3 becomes

$$Q(t) = C_a(t) * FR(t). \tag{1.5}$$

A deconvolution method (also called nonparametric analysis) is used to solve Eq. 1.5, and does not require any explicit assumptions regarding the underlying behaviour of the tracer beyond that required by the definition of a linear time-invariant system. In other words, knowledge of the number compartments and their distribution volumes are not necessary. However, deconvolution is a mathematically difficult problem from the perspective of real data analysis. In particular, even small amounts of noise in the measured functions $C_a(t)$ and $Q(t)$ are amplified during linear inversion due to the ill-conditioned nature of the inverse problem. Consider the matrix form of Eq. 1.5 following discretization:

$$\mathbf{Q} = F\mathbf{C_A}\mathbf{R} \tag{1.7}$$

where the arterial input function, $C_a(t)$, is now represented by the Toeplitz matrix:

$$\mathbf{C_A} = \begin{pmatrix} C_a(t=0) & 0 & \cdots & 0 \\ C_a(t=1) & C_a(t=0) & \cdots & 0 \\ \vdots & C_a(t=1) & \ddots & 0 \\ \vdots & \vdots & \vdots & \vdots \\ C_a(t=N_a-1) & C_a(t=N_a-2) & C_a(t=N_a-3) & C_a(t=N_a-N_t) \end{pmatrix} \quad (1.8)$$

The function *FR(t)* can be solved in a least squares sense by optimizing:

$$\arg\min_{F\mathbf{R}} \left\{ \left\| \mathbf{C_A} \cdot F\mathbf{R} - \mathbf{Q} \right\|^2 \right\} \quad (1.9)$$

where $\|.\|$ is the Euclidean norm. Because of the redundancy of information in $\mathbf{C_A}$, the problem is ill-conditioned, and minimization of Eq. 1.9 is highly susceptible to experimental noise. A complete discussion of rank-deficient and ill-posed problems is outside the scope of this thesis, but the reader is invited to refer to (Hansen 1987) for more information. To stabilize the minimization of Eq. 1.9, a number of options exist including truncated singular value decomposition, Tikhonov regularization, and mathematical constraints based on *a priori* knowledge (Dehghani *et al* 2007). All three methods have benefits and limitations depending on the information that is desired. Since this thesis is mainly concerned with the measurement of blood flow, it is assumed that the principle parameter of interest is *F*. As previously mentioned, the nonparametric method is useful when an explicit mathematical model of *R(t)* is unavailable. However, there are some basic assumptions about the shape of *R(t)* that can be inferred from an understanding of the basic physiology of microcirculation that are unlikely to be violated even under pathological conditions, and these form the basis for mathematical constraints that help stabilize the deconvolution (Lee 2005). These assumptions are:

(i) Tracer injected into a periphery vein will require a minimum amount of time to travel to the heart and be pumped to the tissue region-of-interrogation.

(ii) *R(t)* represents the residue function of a Dirac delta function; in this unique case, the entire bolus of dye would reach the tissue at a single instant in time.

(iii) In addition to *(ii)*, there would be a finite amount of time before the first molecule of dye left the region of interrogation.

(iv) The dye must enter the tissue via an artery and exit via a vein (*i.e.,* no retrograde flow will occur).

These assumptions, which are all derived from a basic understanding of physiology, will be satisfied under almost any clinically relevant condition; however, from a mathematical point-of-view, they can be used to construct rigid and powerful constraints that provide stability to the deconvolution. Assumption *(i)* defines a finite delay between the injection and appearance of dye, called the lag time, L, during which $Q = 0$. Assumptions *(ii)* and *(iii)* defines a plateau equal to unity that begins after L time, and lasts for a finite period of time called the minimum transit time, M. These provide the equality constraints for *R(t)*, mainly

$$\begin{aligned} R(t) &= 0 \qquad 0 \le t < L \\ R(t) &= 1 \qquad L \le t \le L + M \end{aligned} \tag{1.10}$$

Assumption *(iv)* essentially implies that *R(t)* must be monotonically decreasing, that is

$$\frac{dR(t)}{dt} \le 0 \qquad t > L + M \tag{1.11}$$

Finally, since there is no physical representation of negative tracer amount, *R(t)* must be non-negative for all t. This final constraint enables the use of the non-negative least-squares (NNLS) numerical method (Lawson and Hanson 1974). The nonparametric method described above has been

validated in CT perfusion using microspheres (Cenic *et al* 1999). For the studies in this thesis, MATLAB was used to minimize Eq. 1.9 subject to the inequality and equality constraints outlined above.

To a large degree, the use of DCE methods to measure CBF—and tracer kinetics in general—have been confined to more established medical imaging modalities such as CT, PET and MRI. However, in recent years, kinetic modeling has been increasingly used in optics in combination with light absorbing dyes. A major benefit of most optical techniques is that data can be collected at high temporal resolution and with a high signal-to-noise ratio (SNR). As a result, DCE methods are well suited to applications in optics, and recent studies have established biomedical optics as fertile ground for the advancement of new tracer kinetic methods and applications. In particular, the deconvolution method has been used to measure CBF in piglets (Brown *et al* 2002, Tichauer *et al* 2006, Diop *et al* 2010) and premature newborns (Arora *et al* 2013) and it provides a foundation for the analytical approaches used in Chapters 2-6 of this thesis.

1.5. Theoretical basis of near-infrared methods

1.5.1. Near-infrared scatter

Light scatter, (*i.e.* the deviation of light from a straight trajectory), is the dominant interaction with tissue in the near-infrared range between 700 - 1000 nm. The main causes of scatter in this range are Mie scatter and Fresnel reflection. A third type, Rayleigh scatter, represents interaction between light and very small particles, and is increasingly important at shorter wavelengths of light; therefore, it is outside the scope of this thesis. As light propagates through tissue, it interacts with cell membranes, tissue boundaries, and organelles; at each interface, light is reflected and refracted by these objects, and therefore experiences a deviation in trajectory. The majority of scattering in mammalian cells is thought to arise from structures

within the cell, *i.e.* organelles (Mourant *et al* 1998). Mie scatter characterizes the interaction of light with spherical particles of size similar to its wavelength, and is described by the Mie solution to Maxwell's equations (Mie 1908). Most organelles such as nuclei (3-10 μm) and mitochondria (1 μm) can be approximated as spheres or ellipsoids, and can therefore be described by Mie scatter.

A significant portion of scatter in brain tissue occurs by cell membranes, which are comprised of lipoproteins (Cope 1991). Since cells are significantly larger than the wavelength of NIR light, it is best to consider them as a set of randomly oriented flat, dielectric reflecting films (Cope 1991). The reflection and transmission of an incident plane wave of light as it moves between two media of differing refractive indices is described by the Fresnel equations. For a single, well defined interface, the amplitude and phase of the transmitted and reflected light can be readily determined if the angle of incidence and indices of refraction of the two media are known. However, it would be impossible to produce an analytical solution for the interaction of light between the roughly 1 x 10^8 cellular interfaces and organelles that typically exist within 1 mm^3 of tissue (estimated from Norazmi *et al* 1990 and Loud 1968). Instead, the scattering of light is described statistically using probability functions and empirically derived approximations.

The scatter of light in tissue is typically discussed in terms of the angle of scatter and the distance between scattering events. The scattering angle is most commonly described by the Heyney-Greenstein phase function, which was originally developed to describe the angular dependence of light scattering by small particles in interstellar dust clouds (Heyney and Greenstein 1941). The function describes the probability of a particular scattering elevation angle, θ, given the tissue's anisotropy factor, g:

$$p(\theta) = \frac{1}{4\pi} \frac{1 - g^2}{(1 + g^2 - 2g\cos\theta)^{3/2}}. \quad (1.12)$$

The anisotropy factor, g, is the mean cosine of the scattering angle, and in biological tissue, typically varies from 0 to 1. Such probability functions can be used to sample the bulk behaviour of light, and form the basis of modeling approaches collectively called Monte Carlo methods, which will be further discussed in subsection 1.5.4.

The average distance between scattering events is described in terms of the mean scattering length, l_s, of a medium, usually in units of mm. More commonly, the scattering property of tissue is defined by the scattering coefficient, μ_s, which is equal to 1 / l_s. For a medium with high scatter, such as tissue, after a sufficient number of scattering events, a photon has lost any knowledge of its incidence angle and can be considered effectively isotropic. In this case, the scatter of light can be approximated by a single parameter, the reduced scattering coefficient, μ_s', which is defined as:

$$\mu_s' = (1 - g)\mu_s \quad (1.13)$$

In addition, the wavelength dependence of μ_s' is well approximated by the so-called power law:

$$\mu_s'(\lambda) = A\lambda^{-b} \quad (1.14)$$

where A and b are constants either empirically determined or predicted by Mie theory, depending on the application (Wang 2000). A good understanding of the principles of light scatter is essential to any quantitative biomedical optical techniques. In particular, the probability function in Eq. 1.12 and the description of absorption in the next section form the basis for Monte Carlo methods.

1.5.2. Near-infrared absorption

As light propagates through a medium, energy from the incident field is transferred to particles in the medium, which are in turn excited to a higher energy state. While this excited state is short-lived, the resulting collisions that occur between these particles and neighbouring ones results in a transfers of energy—for example, by increasing the vibrational mode of the particle and therefore the kinetic energy of the system, or by re-emitting the light in a different color. This process is known as absorption, and causes a reduction in the intensity of a light beam as it travels through the medium. The first mathematical description of this process was given by Pierre Bouguer in 1729, and later extended by August Beer to include the dependency of light absorption not only on the pathlength through the medium, but also on the concentration of light absorbing molecules, or chromophores, in the medium. The resulting Beer-Lambert-Bouguer Law is a given by:

$$A = \ln \frac{I_0}{I} = \varepsilon \cdot C \cdot L, \tag{1.15}$$

where I_0 is the incident intensity, I is the transmitted intensity, (the log ratio of which is A, is the attenuation of light), C is the chromophore concentration, L is the pathlength of light through the medium, and ε is the specific extinction coefficient.

Within the NIR range of 700-1000 nm, there are three main endogenous absorbers of light: water, hemoglobin, and deoxyhemoglobin. Water is arguably the most important, since it is prevalent in biological tissue. Although the absorption of NIR light by water is relatively weak (about 50 times less than hemoglobin), because of its abundance in human tissue it has a significant effect. In particular, the specific absorption of water rapidly increases with wavelength after about 920 nm, effectively forming the

upper-limit on what is termed the "optical window" of NIR. The concentration of water in the adult brain is tightly regulated to a value of 80% by mass (Woodard and White 1986).

Since the pioneering work of Jobsis in the 1970s, hemoglobin and deoxyhemoglobin quantification has been a principle focus of many NIR techniques. This can be attributed to the unique spectral features of both of these chromophores in the NIR, and the clinical importance of hemoglobin in being the molecule responsible for the transport of oxygen from the lungs to the various tissues in the body. Structurally, hemoglobin is comprised of four subunits which are each able to bind a single O_2 molecule. Binding of oxygen occurs at the heme group—an iron ion held in a porphyrin ring (Caughey *et al* 1975) and induces a conformational change in its tertiary structure, resulting in a dramatic change in absorption characteristics. The effect of this change can be observed in the difference in specific absorption of deoxy- and oxy-hemoglobin depicted in Figure 1.4. In addition to marked differences in features at 760 nm and 900 nm, oxy- and deoxy-hemoglobin share an isobsetic point at 800 nm (*i.e.,* their specific extinction is equal at this wavelength). The difference in absorption spectra between the two hemoglobins forms the basis for the ability to determine oxygen saturation, for example, in pulse oximetry (Aoyagi 2003).

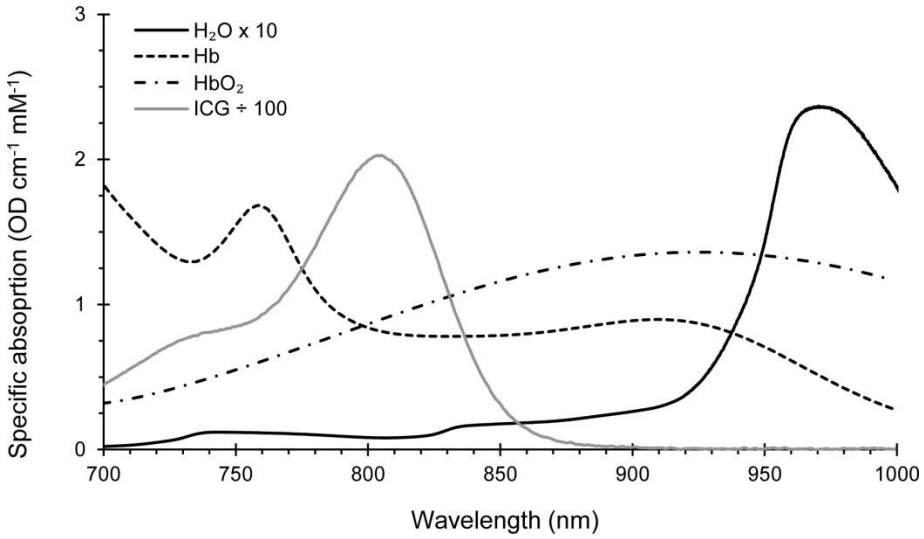

Figure 1.4: Specific absorption spectra of H_20, Hb, HbO_2 and ICG in the NIR range.

Values for H_2O and ICG are adjusted by a factor of 10^1 and 10^{-2}, respectively, for illustrative purposes. Spectra were obtained from (Oregon Medical Laser Clinic 2013).

1.5.3. Light propagation in tissue

Light transport, like any propagation of electromagnetic radiation, is governed by Maxwell's equations. In this paradigm, a beam of light interacts with an object resulting in elastic scattering (*i.e.*, the spreading of energy in all directions at the frequency of the incident beam), as well as absorption (*i.e.,* the conversion of incident energy to other forms such as heat). The resulting scattered field can undergo subsequent interactions with other objects. In a highly complex, multiple scattering regime, analytical solutions to Maxwell's equations become intractable (Wilson and Jacques 1990). Furthermore, to determine the superposition of multiple scattered fields, it is necessary to know the exact location of each scatterer. In tissue, due to Brownian motion, the scatterers exist in randomized positions. Therefore, it is more appropriate to consider light as comprised of individual photons that are absorbed or scattered by discrete random particles. This description of light is governed by the radiative transfer equation (RTE), which is given by:

$$\frac{1}{\upsilon}\frac{\partial}{\partial t}L(\mathbf{r},t,\hat{s})+\hat{s}\nabla L(\mathbf{r},t,\hat{s})=-(\mu_a+\mu_s)L(\mathbf{r},t,\hat{s})+\mu_s\int_{4\pi}L(\mathbf{r},t,\hat{s})P(\hat{s},\hat{s}')d\Omega'+S(\mathbf{r},t,\hat{s})$$

(1.16)

and describes the propagation of radiance $L(\mathbf{r},t,\hat{s})$ in the medium as a function of the position **r**, moving in direction $\hat{s}$, at time *t*. Other parameters include υ, the velocity of light in the medium, μ_a and μ_s, (the absorption and scattering coefficients, respectively), $P(\hat{s},\hat{s}')$, the scattering phase function, $S(\mathbf{r},t,\hat{s})$, the source term, and $d\Omega'$, the solid angle around $\hat{s}$.

To obtain analytical solutions specific to a particular problem, boundary conditions are applied to the RTE. The most common solution in the field of tissue optics is the diffusion approximation (DA). In the DA, it is assumed that the source of light is an isotropic point source, and that scattering within the medium is isotropic. This greatly simplifies Eq. 1.16, by eliminating the dependency on $\hat{s}$, and by reducing the phase function to a constant (*1/4π*). However, for short source-detector distances, and for complex arbitrary media, the diffusion approximation can be inaccurate. A statistical approach, rather than an analytical solution, can provide a powerful means of sampling the RTE while incorporating effects of anisotropy. These solutions are known as Monte Carlo methods.

1.5.4. Monte Carlo modeling

Monte Carlo simulations are a ubiquitous statistical approach used in a variety of applications—*e.g.* nuclear physics (Anderson 1986), computational biology (Huelsenbeck and Ronquist 2001), pricing financial derivatives (Glasserman 2003)—when a closed-form expression is unavailable or prohibitively difficult to formulate. Monte Carlo methods to model light-tissue interactions were introduced in 1983 by Wilson and Adam, and

modifications were made by various groups, before the publication of the Monte Carlo modeling of photon transport in multi-layered tissues (MCML) which forms the foundation of almost all modern Monte Carlo light propagation models (Wang *et al* 1995). Monte Carlo methods define probability functions that describe the expected values of parameters—*i.e.,* length between scattering events, direction of scatter and absorption—that describe the interaction of light with tissue. For a simulated photon of light, these probability functions are repeatedly sampled until the photon is either detected by a hypothetical photodetector, or absorbed by the medium. Then, the process is repeated for a large number of photons, typically 10^8, to describe the fluence and flux of light in terms of spatially and/or temporally dependent functions. To increase computational efficiency, some simplifications are made that are not believed to affect the overall outcome of the simulation. For example, photons are considered as "packets" which loose a portion of their energy with each scatter event, and following each scatter event, a photon continues, or is "killed"—with an increased likelihood of being killed as its energy diminishes. Another implicit assumption is that photons are independent of each other, and therefore, do not interact.

The MCML algorithm is divided into a series of decisions representing physical interactions. For example, a photon packet is launched from a source at a position and direction specified by the user. The first calculation determines the photons step size (*i.e.,* the distance from source to the first scattering event). To understand how this is done, recall the definition of the scattering coefficient from the previous section, which describes the expected number of scattering events per unit length. Since each unit length is expected to interact with a constant *fraction* of photons, a series of successive unit lengths will result in an exponentially decaying number of photons that have not been deviated from their trajectory. The probability of a photon having a step-size, s, is given by

$$p(s) = \mu_s e^{-\mu_s s} \tag{1.17}$$

This non-uniform probability function can be sampled with a computer-generated pseudorandom number using the following relationship (Wang and Wu 2007):

$$\int_0^x p(x)dx = \xi, \tag{1.18}$$

where ξ is a pseudorandom number in the interval 0 to 1. Substituting the probability function from Eq. 1.17 into Eq. 1.18, integrating, and replacing (1-ξ) with ξ on the basis that ξ is symmetrical about 0.5, yields

$$s = -\frac{\ln(\xi)}{\mu_s}. \tag{1.19}$$

This provides a sampling function for the step-size of a photon packet moving through a semi-infinite turbid medium (Wang *et al* 1995). In addition to the photon step size, the direction of scatter must be determined by sampling the azimuth angle, $\psi \in [0,2\pi]$, and the elevation angle $\theta \in [0,\pi]$. The manner in which Monte Carlo treats the directionality of scatter differentiates it from the DA and produces more accurate solutions in cases where the DA assumptions are invalid. The azimuth angle is sampled uniformly over the defined interval, but the elevation angle is determined by sampling the Henyey-Greenstein function that was introduced in subsection 1.5.1. Applying Eq. 1.18 to the phase function in Eq. 1.12,

$$\theta = \begin{cases} \cos^{-1}\left\{\frac{1}{2g}\left(1+g^2-\left[\frac{1-g^2}{1-g+2g\xi}\right]^2\right)\right\} & \text{for } g \neq 0 \\ \cos^{-1}(2\xi-1) & \text{for } g = 0 \end{cases} \tag{1.20}$$

Each successive scattering event causes a reduction in the weight, W, or energy of the photon packet, represented by a fraction of its initial weight. The reduction in weight, ΔW, is calculated by

$$\Delta W = \frac{\mu_a}{\mu_a + \mu_s} W \tag{1.21}$$

By sampling these three functions, Monte Carlo methods allow the user to provide the optical properties (μ_a, μ_s, and g) of the tissue, and calculate the fluence distribution (spatially or temporally) in the medium. In addition, the pathlength of light can be summed for each photon packet and the mean partial pathlength (MPP)—*i.e.,* the average pathlength of light in each region, or tissue type—can be recorded.

Small differences exist in between Monte Carlo methods in terms of how they handle reflection at boundaries (Fresnel reflection), layers or arbitrary geometries, detection of photons by a virtual photodetector, and parallelization or scalability. In Chapter 2, the Monte Carlo method used in the reported study was based upon the MCML code, and was written in house using the C++ programming language, so that it could be run on a high performance computing architecture called SHARCNet. In subsequent chapters, the Monte Carlo eXtreme (MCX) method by Fang is used. This algorithm is based on the earlier *tMCimg* algorithm by Boas and colleagues, which advanced the MCML algorithm to allow modeling of photon propagation in 3D segmented image volumes. The MCX method is essentially *tMCimg* written in such a way that enables the use of graphics processing units (GPUs) to run multiple instances of Monte Carlo in parallel. Because each simulated photon packet is treated as an independent event, the Monte Carlo problem is highly parallelizable; the first report of MCX demonstrated an acceleration of about 300 times on a GPU capable of 500 GFLOPS. The performance of GPUs has increased at a rate much greater than that of

central processing units, and at the time of the writing of this thesis, commercially available GPUs for personal computing use are capable of 2000-4000 GFLOPS. For a typical MCX simulation on an MRI human head atlas (Fang and Boas 2009), 10^8 photon packets could be simulated in 47.5 – 95 seconds.

1.6. Near-infrared measurements in adults

1.6.1. Extracerebral contamination

Near-infrared methods of measuring CBF have been successful, especially in neonatal applications (Arora *et al* 2013; Brown *et al* 2008; Edwards *et al* 1988; Tichauer *et al* 2009), where the scalp and skull is negligible and the head can be thought of as a homogenous region comprised mostly of brain tissue. However, when applied to adult subjects, these same methods measure signal that is comprised of multiple tissue layers including brain and scalp (Fig. 1.5). In some cases, the signal arising from the extra-cerebral layers (ECL) can account for more than half the overall signal.

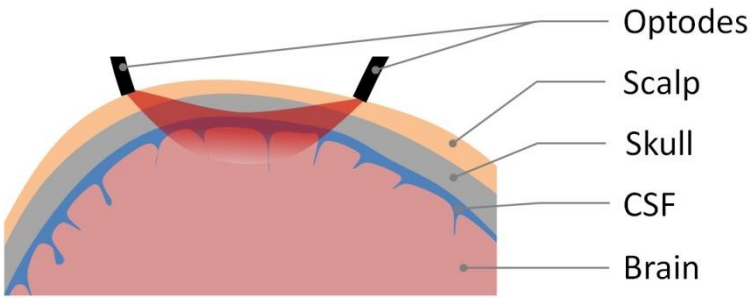

Figure 1.5: Interrogation of adult head with NIR light

Illustration of the underlying structure of the human head and the typical region of interrogation by a NIR optode pair spaced about 30 mm apart. Note the large contribution to light absorption by the extracerebral layer.

Both the scalp and skull are metabolically inactive and therefore poorly perfused tissues. For example, the blood flow in the scalp is about 1/10th that of the brain (approximately 5 ml min^{-1} $100g^{-1}$). As a result, single-probe NIR measurements acquired on the surface head, without accounting for

contamination from the ECL, produce CBF values that are significantly underestimated (Gora *et al* 2002). Figure 1.6 demonstrates the relationship between extracerebral thickness and brain signal percentage, determined using Monte Carlo simulations. To minimize the errors caused by ECL contamination, it is necessary to increase cerebral signal sensitivity and remove ECL signal contributions through some type of reconstruction method.

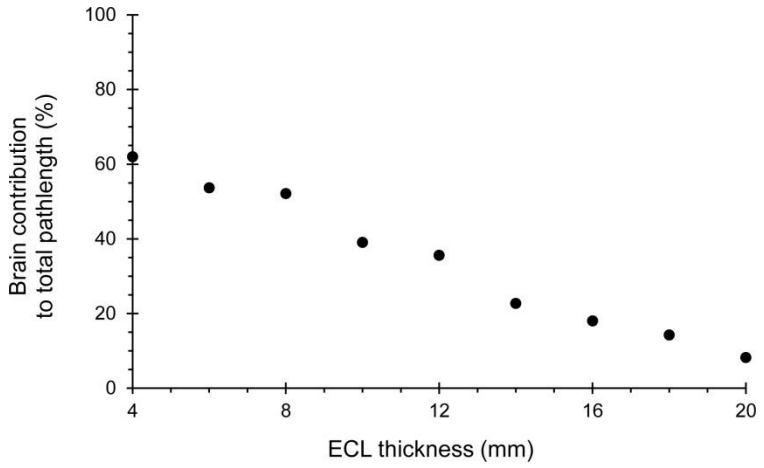

Figure 1.6: Effect of extracerebral layer thickness on brain sensitivity.

The effect of increasing ECL thickness on the percent contribution of brain tissue to the total differential pathlength for a 30 mm source-detector distance, as determined by two-layer Monte Carlo simulation. The ECL was assumed to comprise 60% scalp, 30% skull, and 10% CSF, and optical properties were taken from Strangman *et al* 2003.

1.6.2. Increasing cerebral sensitivity

Increasing the sensitivity to changes occurring in cerebral tissue reduces the amount of ECL contamination, thereby helping to differentiate signals from the ECL and the brain. This can be achieved through a combination of instrumentation improvements and more sophisticated analytical methods, which will both be discussed in this section. These advancements form the crux of this thesis, as detailed in the research objectives presented in Section 1.7.

Instrument-based solutions

The penetration depth of light increases as a function of source-detector distance; therefore, the easiest method of increasing sensitivity to the brain is by moving the detector optode further from the source. However, the flux of photons across the surface of the head rapidly decreases with source-detector distance representing an important trade-off that must be considered (Fig. 1.7)

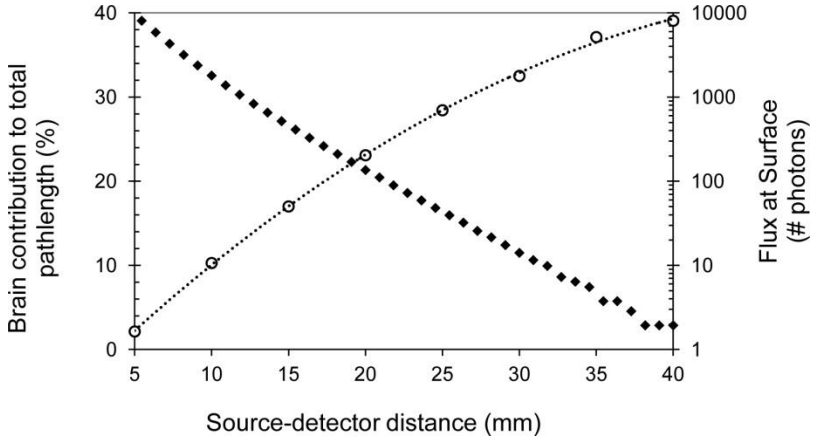

Figure 1.7: Effect of source-detector distance on brain sensitivity and photon count.

The effect of increasing source-detector distance on the percent contribution of brain tissue to the total differential pathlength assuming an ECL thickness of 10 mm. The flux of photons exiting the surface decreases almost 5 orders of magnitude over the range of source-detector distances.

Practically, a source-detector upper-limit of 40 mm is imposed by signal-to-noise considerations for most current systems that use emission and detection optodes comprised of fiber bundles with an active area on the order of 400 um in diameter. However, a recent study avoided the substantial loss of signal that occurs during fiber transmission by placing a photodetector directly on the surface of the head (Liebert *et al* 2011). In addition to minimizing fiber loss, this had the effect of increasing the active area diameter of the optode from 400 um to 8 mm, the diameter of the photocathode.

A logical extension to the single channel approaches that have been discussed is to deploy multiple optodes and collect data from these channels, simultaneously. This multi-distance, multichannel or depth-resolved approach allows the separation of information into superficial and deep components on the basis that light penetration increases with source-detector distance. It is important to note, however, that due to the diffuse nature of light, large source-detector distances only increase the proportion of signal from the brain and don't eliminate the ECL contribution all together. Nevertheless, by collecting information at multiple distances simultaneously, it is possible to separate out information in terms of tissue layers, using an optical reconstruction approach.

The development of time-resolved methods have greatly improved the amount of information that can be acquired with a small number of optodes and have opened up new avenues of exploration in terms of data analysis (Diop et al 2010; Diop and St. Lawrence 2012). Time-resolved NIR methods are photon counting techniques that use a laser light source to emit pulses of monochromatic light and fast detectors to measure the time-of-flight of each detected photon (*i.e.*, the time required for a photon to travel from the laser to the photomultiplier tube). This process is repeated, typically at a frequency of around 80 MHz until about 10^7 photons are measured, and a histogram called the distribution of times-of-flight (DTOF) is generated. Figure 1.8 shows a representative example of a DTOF collected on the surface of an adult pig head. A series of DTOFs, resolved to typically 1024 time-bins, can be collected continuously during the injection of a contrast agent at a rate of about 2.4 Hz across multiple detectors simultaneously, representing a staggering amount of information. Furthermore, because photons with longer times-of-flight are more likely to have visited deeper tissue than those with very short times-of-flight, selecting later time-bins has the effect of increasing brain sensitivity. Combining some or all of these technologies results in a rich

dataset full of information about the hemodynamics of the underlying brain tissue. However, only with well-developed analytical tools can this information be processed to yield accurate and quantitative measurements of CBF. The closely related concept of frequency-domain (FD) NIR provides analogous information to time-resolved NIR if measurements are collected across a range of modulation frequencies Mei *et al*, 2013). However, commercial FD systems typically use only a single modulation frequency.

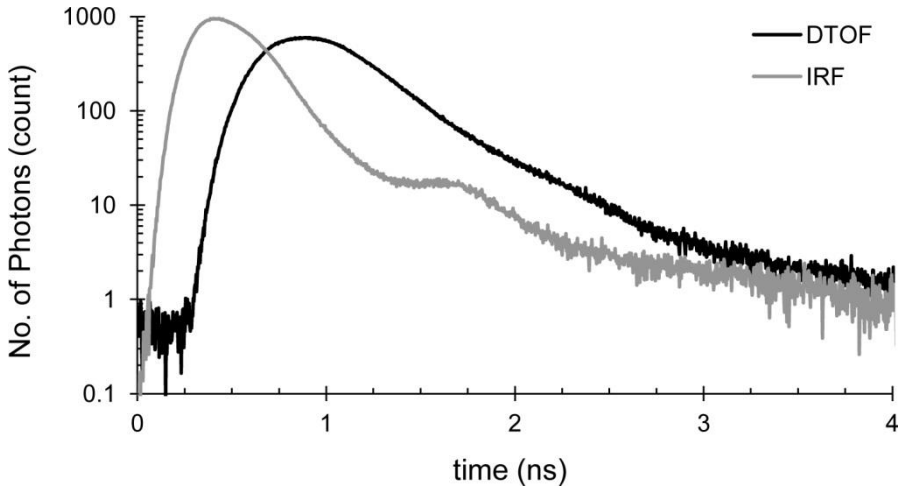

Figure 1.8: Distribution of time-of-flight and instrument response function.

The DTOF and IRF for measurements acquired with a 20 mm source-detector distance on an adult pig with an ECL thickness of 10.5 mm. Note the presence of an after-pulse in the IRF, defined as an increased probability of a photon being detected after an initial detection event, and is observed in almost all conventional PMTs.

Analytic-based solutions

Perhaps the simplest approach to incorporating multi-distance NIR information was proposed by Schytz and colleagues, in a technique that exploits the different amounts of ECL and brain signal contribution present in short (10 mm) and long (30 mm) source-detector distances (Schytz *et al* 2009). In this approach, the change in optical density in the brain was calculated by scaled subtraction of the short source-detector distance signal from the long source-detector distance signal. While the approach represents a good first step in trying to use multi-distance NIR measurements to isolate

the brain signal, the scaling factor was based on an assumed value and applied to the group as a whole. Therefore, the amount of intra-subject variability likely impacted the results of the study, which did not show sensitivity of NIR measurements to changes in CBF. A more robust approach is to properly model the light propagation in the head for each subject separately. This approach was used in the study highlighted in Chapter 2 of this thesis. While collection of CW NIR information at multiple distances can provide a limited ability to separate out the brain contribution to the signal, TR NIR offers an exquisite amount of information even in a single or few-channel approach. However, the main problem with TR NIR data is that the experimental DTOFs represent the convolution between the instrument response function (IRF) and the tissue impulse function (TIF). Although the IRF can be measured independently, the recovery of a TIF from the DTOF requires deconvolution of the signal; a challenging mathematical problem that has only recently been addressed successfully (Diop and St. Lawrence 2012). Therefore, the proper analysis of DTOFs to exploit the sensitivity of late-arriving time-bins has been challenging. An elegant approach was proposed by Liebert and colleagues, and involves determining the statistical moments of DTOFs—intensity, mean time-of-flight, and variance—effectively reducing the large dataset into three "principle components" (Liebert *et al* 2004). The kth order moment of the DTOF, $N(t)$, is defined as

$$m_k = \int_{t_1}^{t_2} t^k N(t) dt, \tag{1.23}$$

where t_1 and t_2 are temporal integration limits. In addition to reducing the size of the problem set, the influence of the IRF can be removed by using the change in the normalized moments:

$$A = \ln(m_0) \tag{1.24}$$

$$\langle t \rangle = \frac{m_1}{m_2} \tag{1.25}$$

$$V = \frac{m_1}{m_2} - \left(\frac{m_1}{m_0} \right)^2 \tag{1.26}$$

The change in attenuation, ΔA, change in mean time-of-flight, $\Delta\langle t \rangle$, and the change in variance, ΔV, are the principle moments used in moments-based TR NIR methods. Theoretically, there is no limit to the number of moments that can be used, however, noise increases significantly with order of moment. Conceptually, the relationship between moment order and brain sensitivity is not as straightforward as when considering the time bins of the DTOF. However, in general, the sensitivity of brain tissue is highest in higher order moments because changes in the tail of the TPSF have a more dramatic effect on the width and skewness of the distribution. Figure 1.9 shows the sensitivity of attenuation and variance to layers located at depths of 1, 5 and 9 mm. Note, the sharp increase in the sensitivity of variance to the 9 mm layer for source-detector distances greater than 30 mm.

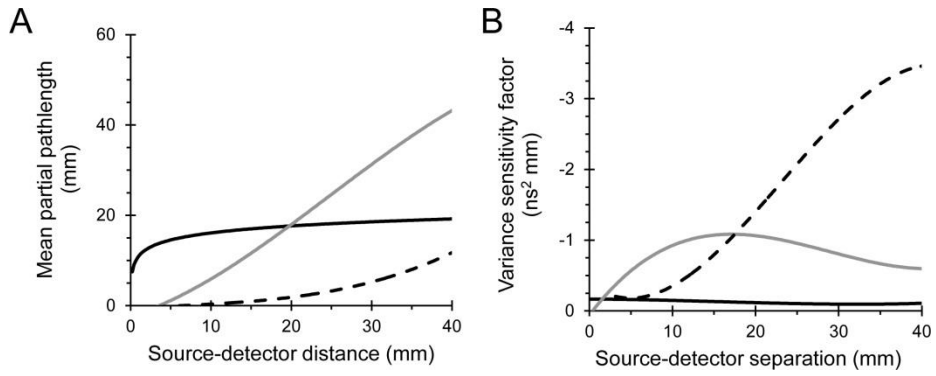

Figure 1.9: Moment sensitivity factors as a function of source-detector distance

(A) The relationship between source-detector distance and mean partial pathlength, the sensitivity factor for attenuation, and (B) the relationship between source-detector distance and variance sensitivity factor, corresponding to depths of 1 mm (solid black line), 5 mm (solid grey line) and 9 mm (dashed black line). Reproduced from Liebert *et al* 2004.

The sensitivity of a particular moment to a particular tissue region below the surface of the head is represented by its sensitivity factor. Sensitivity factors can be readily calculated using Monte Carlo simulations (Liebert *et al* 2004).

1.6.3. Multilayer reconstruction

The previous section described a variety of instrument-based and analytical approaches to increasing the sensitivity of the detected signal to brain tissue. However, proper isolation of the brain tissue signal requires the use of optical reconstruction: a general term that describes the recovery of local changes in tissue optical properties at a predefined region from a measured signal containing contributions from multiple regions. Optical reconstruction forms the basis for imaging methods including diffuse optical tomography (DOT) and fluorescence molecular tomography (FMT), and is analogous in some ways to CT and PET reconstruction. The optical reconstruction forward problem is given generally by

$$\partial S_\Omega = \sum_{J=1}^{N_J} A_J[\mu_J]\partial\mu_J, \tag{1.27}$$

where μ_J represents the collective optical properties defined for N_J spatial regions, and $\partial\mu_J$ is the local variations in optical properties responsible for the variation ∂S_Ω in the detected signal S_Ω associated with the background properties μ_J. The transformation between these two variations is given by A_J, also called the Jacobian. Optical reconstruction is performed by minimizing the difference between the experimental measurements of ∂S_Ω, and the predictions of the model based on the update equation (Eq. 1.27). Essentially, all optical reconstruction methods can be broken down into four considerations: (i) selection of linear or nonlinear solver, (ii) definition of the signal domain, (iii) calculation of the Jacobian, and (iv) availability of *a priori* knowledge or "priors".

Typically, DOT involving large variations in μ_a and μ_s must be solved with nonlinear iterative solvers. However, in the DCE-NIR methods described in this thesis, an assumption of linearity is made between the measured signal and the change in absorption caused by the introduction of tracer. This assumption is valid under the concentrations used in DCE methods, based on the fact that ICG has a negligible effect on scattering (Kuebler *et al* 1998) and its effect on the optical pathlength is negligible. The signal domain is defined primarily according to the spatial location of source and detector pairs used to construct the signal data. In DCE measurements acquired on the surface of the head, spatial information is typically simplified by using source-detector distance, ρ. The signal domain can be further divided into dimensions that are specific to the type of instrumentation used. For example, in broadband NIRS, signal can be defined according to wavelength, λ, as in DOT methods that employ spectral constraints (Corlu *et al* 2005). In the case of TR-NIR, the signal domain can be labeled according to time-of-flight, t, or when used in conjunction with a moments-based approach, moment order, k. Regardless of how the signal domain, Ω, is defined, the Jacobian must be defined accordingly, in addition to being defined for each region, J. In optical reconstruction, the Jacobian is essentially a matrix comprised of partial derivatives of fluence and flux taken with respect to μ_a and μ_s'. Therefore, to compute the Jacobian, light propagation models are needed. The two principle models—Monte Carlo and diffusion approximation, typically formulated as a finite element method (FEM) are used. The FEM approach has the benefit of being fast, flexible, and accurate under most conditions. As a result, it is the most widely used method for FMT reconstruction. Monte Carlo is computationally demanding, but more accurate, and calculation of TR DTOF functions is very straightforward. Furthermore, Monte Carlo methods for calculating the moments-based Jacobians are published (Liebert *et al* 2004).

The incorporation of priors into optical reconstruction is perhaps the most fertile ground for advances in quantitative DOT and FMT methods (Pogue *et al* 2011). The importance of priors can be understood from an algebraic perspective, in that optical reconstruction is an ill-posed and often underdetermined problem. Therefore, regularization (which is itself, fundamentally a prior in that it forces a solution with predetermined qualities—*i.e.* smoothness) and prior-based constraints are essential for converging to a unique solution. In recent years, a number of priors have been described and each has been implemented in a variety of different ways. For example, anatomical priors—information provided by an alternate imaging modality such as CT or MRI—can be implemented into the reconstruction process as a soft prior using Laplace regularization (Davis *et al* 2007). Another common approach is to use spectral priors to constrain the reconstruction of broadband data (Corlu *et al* 2005). Chapter 5, which is based on a paper published in Optics Letters, describes a previously unexploited prior based on temporal changes in absorption caused by the injection of tracer. This "kinetic prior" was incorporated directly into the optical reconstruction problem, in an approach referred to as kinetic deconvolution optical reconstruction (KDOR). The standard approach to extracting physiological measurements from DCE data is a two-step method of first performing image reconstruction and then recovering kinetic parameters with subsequent modeling. The use of KDOR mitigated much of the loss-of-information that occurs due to the ill-posed nature of unconstrained optical reconstruction (Elliott *et al* 2012). The KDOR approach is highlighted in Chapters 5 and 6, and Appendix A.

1.7. Research objectives

The goal of this doctoral work is to develop a reliable bedside optical technique capable of quantifying CBF in adult patients. It was hypothesized that CBF can be measured accurately by correcting for inter-subject

variability in tissue anatomy and optical properties. With this in mind, the following four objectives were addressed:

(i) Designing and optimizing a clinically-compatible instrument

(ii) Developing an analytical framework

(iii) Developing a clinically relevant ABI animal model

(iv) Validating the technique against CT perfusion

Each chapter in this thesis represents a progression toward the central goal, by advancing one or more of these objectives. A secondary goal of this thesis is to provide the reader with an appreciation for the way in which this research has unfolded, by which each study provided an important "piece to the puzzle".

1.8. Thesis outline

The reminder of the thesis is divided into five chapters outlining published or completed studies, and a final concluding chapter.

1.8.1. Measuring quantitative cerebral blood flow in a juvenile porcine model using multidistance continuous-wave near-infrared spectroscopy (Chapter 2)

Advancing CW-NIRS methods from neonatal applications to a juvenile pig model with a non-negligible ECL can be achieved by employing multi-distance measurements. This chapter summarizes the work presented in the paper “Quantification of CBF in a juvenile porcine model by depth-resolved near-infrared spectroscopy,” published in the *Journal of Biomedical Optics* in 2010 by Elliott JT, Diop M, Tichauer KM, Lee T-Y, and St. Lawrence K. The proposed depth-resolved approach, which uses an algebraic approach to separate signals by depth, is presented alongside with a comparison to a

simple-subtraction approach and the single-channel method used in neonatal studies. These optical methods are compared to CT perfusion measurements as a clinical gold standard.

1.8.2. Measuring cerebral blood flow changes in adult pigs with statistical moments of time-resolved near-infrared measurements (Chapter 3)

A single-channel time-resolved method to measure changes in blood flow using statistical moments of the time-of-flight distribution (DTOF) is presented. Previous DCE methods using moments have examined the time-to-peak of the dye concentration curve; a more robust method is presented that takes into account variations in the AIF. This method has the benefit of being relatively insensitive to uncertainties in optical properties and ECL thickness, but provides only a measure of the change in CBF. The work in this chapter is based on the paper entitled "Variance of time-of-flight distribution is sensitive to cerebral flow dynamics of indocyanine green as confirmed by comparing scalp and brain measurements in adult pigs" published in *Biomedical Optics Express* in 2013, by Elliott JT, Milej D, Gerega A, Weigl W, Diop M, Morrison LB, Lee T-Y, and St. Lawrence K. The work presents a series of animal experiments investigating the influence of extracerebral and cerebral blood flow on the proposed blood flow index, and represents a straightforward means of tracking CBF changes in a clinical setting.

1.8.3. Measuring the arterial input function with a standard pulse oximeter to facilitate the clinical implementation of DCE optical methods (Chapter 4)

All of the DCE methods described in this thesis require the measurement of the AIF—the time-dependent arterial concentration of dye. Currently, this can only be measured noninvasively by a pulse dye densitometer, which is a specialized device designed to measure arterial blood concentration of

indocyanine green. In this chapter, an alternative method is described which was first published in "Arterial input function of an optical tracer for dynamic contrast enhanced imaging can be determined from pulse oximetry oxygen saturation measurements" by Elliott JT, Wright EA, Tichauer KM, Diop M, Morrison LB, Pogue BW, Lee T-Y and St. Lawrence K, published in *Physics in Medicine and Biology* in 2012. The proposed method involves using a standard pulse oximeter device to measure the AIF, with the goal of overcoming practical obstacles to enable the use of DCE optical techniques in clinical settings.

1.8.4. Kinetic deconvolution optical reconstruction: theoretical basis and numerical simulations (Chapter 5)

To leverage the advances in instrumentation described in Chapter 3, a completely novel analytical approach was developed to combine the optical reconstruction of time-resolved multi-distance data with nonparametric kinetic analysis, or deconvolution, used in previous DCE NIR methods. The chapter is based largely on the published paper "Model-dependent constraint to improve the optical reconstruction of regional kinetic parameters" published in *Optics Letters* in 2012 by Elliott JT, Diop M, Lee T-Y, and St. Lawrence K. This paper presents the theoretical derivation of the KDOR concept, and demonstrates improved accuracy and precision in simulated blood flow measurements in the human head. The KDOR methodology is fully described in this chapter, and numerical simulations have been expanded for completeness.

1.8.5. Measuring cerebral hemodynamics in an adult pig model of ischemia with time-resolved near infrared and kinetic deconvolution optical reconstruction (Chapter 6).

The culmination of instrumentation and analytical advances is presented in this chapter, where the DCE TR-NIR method is used in combination with the KDOR approach to quantify CBF in adult pigs before and during cerebral ischemia. This work, which will be submitted to a peer-reviewed journal in the near future, establishes NIR as a potential tool to measure CBF in under ischemic conditions. In addition to multidistance time-resolved data collected before injection of ICG, segmented anatomical CT images are incorporated into an optimization framework to determine the subject-specific Jacobian used in KDOR.

1.8.6. Conclusions and future work (Chapter 7)

In the final chapter, the most significant findings from the previous five chapters are summarized within the context of the stated objectives in Section 1.7. In addition, areas of future work are discussed based on the findings and limitations determined in the studies. Finally, the principle conclusions of the thesis are presented.

1.9. References

Al-Tamimi YZ, Orsi NM, Quinn AC, Homer-Vanniasinkam S, Ross SA 2010 A review of delayed ischemic neurologic deficit following aneurysmal subarachnoid hemorrhage: historical overview, current treatment, and pathophysiology *World Neurosurg* 73(6) 654-667.

Anderson HL 1986 Metropolos, Monte Carlo and the MANIAC *Los Alamos Science* 14 96-108.

Aoyagi T 2003 Pulse oximetry: its invention, theory, and future *J Anesth* 17(4) 259-266.

Arora R, Ridha M, Lee D, Elliott JT, Diop M, Rosenberg H, Lee TY and St. Lawrence K 2013 Preservation of the metabolic rate of oxygen in preterm infants during indomethacin therapy for closure of the ductus arteriosus *Pediatr Res* doi:10.1038/pr.2013.53.

Astrup J, Siesjö BK, Symon, L 1981 Thresholds in cerebral ischemia-the ischemic penumbra *Stroke* 12(6) 723-725.

Axel L 1980 Cerebral blood flow determination by rapid-sequence computed tomography: theoretical analysis *Radiol* **137** 679-86.

Barker FG, Ogilvy CS 1996 Efficacy of prophylactic nimodipine for delayed ischemic deficit after subarachnoid hemorrhage: a metaanalysis *J Neurosurg* 84(3) 405-414.

Barlow A, Stewart W 2007 The pathology of raised intracranial pressure *Adv Clin Neuro Rehab* 7(5):25-27.

Baron EM, Jallo JI 2007 "TBI: pathology, pathophysiology, acute care and surgical management, critical care principles, and outcomes" in *Brain Injury Medicine* (Demos Medical Publishing: New York, NY).

Brain Trauma Foundation, American Association of Neurological Surgeons 2008 Guidlines for the management of severe traumatic brain injury VI Indications for intracranial pressure monitoring *J Neurotrauma* 25(3) 276-78.

Brix G, Bahner ML, Hoffmann U, Horvath A, Schreiber W 1999 Regional blood flow, capillary permeability, and compartmental volumes:

measurement with dynamic CT—initial experience *Radiology* 210(1) 269-276.

Brown DW, Picot PA, Naeini JG, Springett R, Delpy DT, Lee T-Y 2002 Quantitative near infrared spectroscopy measurement of cerebral hemodynamics in newborn piglets *Pediatr Res* 51(5) 564-570.

Bullock MR, Chesnut R, Ghajar J, Gordon D, Hartl R, Newell DW, Servadei F, Walters BC, Wilberger JE 2006 Guidelines for the Surgical Management of Traumatic Brain Injury Author Group *Neurosurgery* 58(3) S2-vi.

Caughey WS, Smyth GA, O'Keeffe DH, Maskasky JE, Smith MI 1975 Heme A of cytochrome c oxicase: structure and properties *J Biol Chem* 250(19) 7602-22.

CDC 2010 "Traumatic brain injury in the United States: emergency department visits, hospitalizations and deaths 2002-2006" National center for injury prevention and control (US Department of Health and Human Services: Atlanta, GA).

Cenic A, Nabavi DG, Craen RA, Gelb AW, Lee TY 2000 A CT method to measure hemodynamics in brain tumors: validation and application of cerebral blood flow maps *Am J Neuroradiol* 21:462–70.

Claassen J, Hirsch LJ, Kreiter KT, Du EY, Connolly ES, Emerson RG, Mayer SA 2004a Quantitative continuous EEG for detecting delayed cerebral ischemia in patients with poor-grade subarachnoid hemorrhage *Clin Neurophysiol* 2004;115(12):2699-2710.

Claassen J, Mayer SA, Kowalski RG, Emerson RG, Hirsch LJ 2004b Detection of electrographic seizures with continuous EEG monitoring in critically ill patients *Neurology* 62(10) 1743-1748.

Crowley RW, Medel R, Dumont AS, Ilodigwe D, Kassell NF, Mayer SA, Ruefenacht D, Schmiedek P, Weidauer S, Pasqualin A, Macdonald RL 2011 Angiographic vasospasm is strongly correlated with cerebral infarction after subarachnoid hemorrhage *Stroke* 42(4) 919-923.

Coles JP 2004 Regional ischemia after head injury *Curr Opin Crit Care* 10(2) 120-125.

Cope M 1991 The application of near infrared spectroscopy to non invasive monitoring of cerebral oxygenation in the newborn infant in *Ph.D. thesis* (University College London: London, UK).

Corlu A., Choe R, Durduran T, Lee K, Schweiger M, Arridge SR, Yodh AG 2005 Diffuse optical tomography with spectral constraints and wavelength optimization *Applied optics* 44(11) 2082-2093.

Cutler RWP, Page L, Galicich J, Watters GV 1968 Formation and absorption of cerebrospinal fluid in man *Brain* 91(4) 707-720.

Dehghani H, Srinivasan S, Pogue BW, Gibson A 2009 Numerical modelling and image reconstruction in diffuse optical tomography. *Phil Trans Royal Soc A: Math, Phys and Eng Sci* 367(1900) 3073-3093.

Dhar R, Scalfani MT, Blackburn S, Zazulia AR, Videen T, Diringer M 2012 Relationship between angiographic vasospasm and regional hypoperfusion in aneurysmal subarachnoid hemorrhage *Stroke* 43(7) 1788-1794.

Diop M, Lawrence KS 2012 Deconvolution method for recovering the photon time-of-flight distribution from time-resolved measurements *Opt Lett* 37(12) 2358-2360.

Diop M, Tichauer KM, Elliott JT, Migueis M, Lee T-Y, St. Lawrence K 2010 Time-resolved near-infrared technique for bedside monitoring of absolute cerebral blood flow *Proc of SPIE* 7555 75550Z.

Diringer MN, Edwards DF 2001 Admission to a neurologic/neurosurgical intensive care unit is associated with reduced mortality rate after intracerebral hemorrhage *Crit Care Med* 29(3) 635-640.

Eastwood, JD, Lev MH, Azhari T, Lee T-Y, Barboriak DP, Delong DM, Fitzek C, Herzau M, Wintermark M, Meuli R, Brazier D, Provenzale JM 2002 CT Perfusion Scanning with Deconvolution Analysis: Pilot Study in Patients with Acute Middle Cerebral Artery Stroke *Radiology* 222(1) 227-236.

Edwards AD, Richardson C, Cope M, Wyatt JS, Delpy DT, Reynolds, EOR 1988 Cotside measurement of cerebral blood flow in ill newborn infants by near infrared spectroscopy *Lancet* 332(8614) 770-771.

English SW, Turgeon AF, Owen E, Doucette S, Pagliarello G, McIntyre L. 2012 Protocol Management of Severe Traumatic Brain Injury in Intensive Care Units: A Systematic Review. *Neurocrit Care*

Evans RW 2006 Neurology and Trauma (Oxford University Press, Cambridge, UK).

Fang Q, Boas DA 2009 Monte Carlo simulation of photon migration in 3D turbid media accelerated by graphics processing units. *Opt Expr* 17(22) 20178-20190.

Gennarelli TA, Champion HR, Copes WS, Sacco WJ. Comparison of mortality, morbidity, and severity of 58,713 head injured patients with 144,447 patients with extracranial injuries. *J Trauma* 37(6); 1994.

Glasserman P 2010 Monte Carlo Methods in Financial Engineering (New York, NY: Springer Publishing) p 3.

Gobbel GT, Cann CE, Fike JR 1990 Measurement of regional cerebral blood flow using ultrafast computed tomography: theoretical aspects *Stroke* 22 768-71.

Gora F, Shinde S, Elwell CE, Goldstone JC, Cope M, Delpy DT, Smith M 2002 Noninvasive measurement of cerebral blood flow in adults using near-infrared spectroscopy and indocyanine green: a pilot study *J Neurosurg Anesthesiol* 14, 218-222.

Hansen PC 1987 Rank-deficient and discrete ill-posed problems: numerical aspects of linear inversion (SIAM: Philadelphia, PA).

Henyey LG, Greenstein JL 1941 Diffuse radiation in the galaxy *ApJ* 93, 70-83.

Hijdra A, van Gijn J, Nagelkerke NJ, Vermeulen M, van Crevel H 1988 Prediction of delayed cerebral ischemia, rebleeding, and outcome after aneurysmal subarachnoid hemorrhage *Stroke* 19:1250-6.

Hofmeijer J, Kappelle LJ, Algra A, Amelink GJ, van Gijn J, van der Worp HB 2009 Surgical decompression for space-occupying cerebral infarction (the Hemicraniectomy After Middle Cerebral Artery infarction with Life-threatening Edema Trial [HAMLET]): a multicentre, open, randomised trial *Lancet Neuro* 8(4) 326-333.

Huelsenbeck JP, Ronquist F 2001 MRBAYES: Bayesian inference of phylogenetic trees *Bioinformatics* 17(8) 754-755.

Jaeger M, Schuhmann MU, Soehle M, Nagel C, Meixensberger J 2007 Continuous monitoring of cerebrovascular autoregulation after

subarachnoid hemorrhage by brain tissue oxygen pressure reactivity and its relation to delayed cerebral infarction *Stroke* 38(3) 981-986.

Johnston SC, Selvin S, Gress DR 1998 The burden, trends, and demographics of mortality from subarachnoid hemorrhage *Neurology* 50 1413-18.

Jüttler E, Schwab S, Schmiedek P, Unterberg A, Hennerici M, Woitzik J, Hacke W 2007 Decompressive Surgery for the Treatment of Malignant Infarction of the Middle Cerebral Artery (DESTINY) A Randomized, Controlled Trial *Stroke* 38(9) 2518-2525.

Kety SS, Schmidt CF 1945 The determination of cerebral blood flow in man by the use of nitrous oxide in low concentrations *Am J Physiol* 143 53-66.

Kuebler WM, Sckell A, Habler O, Kleen M, Kuhnle GE, Welte M, Goetz AE 1998 Noninvasive measurement of regional cerebral blood flow by near-infrared spectroscopy and indocyanine green *J Cereb Blood Flow Met* 18(4) 445-456.

Kim MN, Durduran T, Frangos S, Edlow BL, Buckley EM, Moss HE, Kofke WA 2010 Noninvasive measurement of cerebral blood flow and blood oxygenation using near-infrared and diffuse correlation spectroscopies in critically brain-injured adults *Neurocritical care* 12(2) 173-180.

Langlois J 2000 "Traumatic Brain Injury in the United States: Assessing Outcomes in Children" *National Center for Injury Prevention and Control of the Centers for Disease Control and Prevention* (US Department of Health and Human Services: Atlanta, GA).

Lassen NA, Munck O 1955 The cerebral blood flow in man determined by the use of radioactive krypton *Acta Physiologica Scandinavica* 33(1) 30-49.

Lawson CL, Hanson RJ 1974 Solving least squares problems (SIAM: Philadelphia, PA).

Lee TY 2005 Method and apparatus for calculating blood flow parameters. *US Patent No. 6,898,453.*

Liang D, Bhatta S, Gerzanich V, Simard JM 2007 Cytotoxic edema: mechanisms of pathological cell swelling *Neurosurg focus* 22(5) E2.

Liebert A, Wabnitz H, Steinbrink J, Obrig H, Moller H, Macdonald R, Villringer A, Rinneberg H 2004 Time-resolved multidistance near-infrared spectroscopy of the adult head: intracerebral and extracerebral absorption changes from moments of distribution of times of flight of photons *Appl Opt* **43** 3037-3047.

Liebert A, Sawosz P, Milej D, Kacprzak, M, Weigl W, Botwicz M, Mączewska J, Fronczewska K, Mayzner-zawadzka E, Królicki L, Maniewski R 2011 Assessment of inflow and washout of indocyanine green in the adult human brain by monitoring of diffuse reflectance at large source-detector separation *J Biomed Opt* 16(4) 046011.

Loud, AV 1968 A quantitative stereological description of the ultrastructure of normal rat liver parenchymal cells *J Cell Bio* 37(1) 27-46.

Maas AIR, Stocchetti N, Bullock R. Moderate and severe traumatic brain injury in adults. The Lancet 7(8):728-741; 2008.

Marmarou A, Anderson R, Ward JD, *et al* 1989 "The Traumatic Coma Data Bank: monitoring of ICP" *Intracranial Pressure VII* (Springer-Verlag, Berlin, Germany) 549–551

Mayer TE, Hamann GF, Baranczyk J, Rosengarten B, Klotz E, Wiesmann M, Brueckmann HJ 2000 Dynamic CT perfusion imaging of acute stroke. *Am J Neurorad* 21(8) 1441-1449.

Mie G 1908 Contributions to the optics of turbid media, particularly of colloidal metal solutions (translated from German) *Ann Phys* 25(3) 377-445.

Miles KA 1991 Measurement of tissue perfusion by dynamic computed tomography *Brit J Radiol* 64(761) 409-412.

Mokri B 2001 The Monro–Kellie hypothesis Applications in CSF volume depletion *Neurology* 56(12) 1746-1748.

Mourant JR, Freyer JP, Hielscher AH, Eick AA, Shen D, Johnson TM 1998 Mechanisms of light scattering from biological cells relevant to noninvasive optical-tissue diagnostics *Appl Opt* 37(16) 3586-3593.

Muizelaar JP, Lutz HA, Becker DP 1984 Effect of mannitol on ICP and CBF and correlation with pressure autoregulation in severely head-injured patients *J Neurosurg* 61(4) 700-706.

Muizelaar JP, Marmarou A, Ward JD, Kontos HA, Choi SC, Becker DP, Young HF 1991 Adverse effects of prolonged hyperventilation in patients with severe head injury: a randomized clinical trial *J Neurosurg* 75(5) 731-739.

Norazmi MN, Hohmann AW, Skinner JM, Jarvis LR, Bradley J 1990 Density and phenotype of tumour-associated mononuclear cells in colonic

carcinomas determined by computer-assisted video image analysis *Immunology* 69(2) 282.

Obrist WD, Thompson HK, King H, Wang HS 1967 Determination of regional cerebral blood flow by inhalation of 133-Xenon *Circ Res* 20(1) 124-135.

Oregon Medical Laser Clinic 2012 Optical Properties Spectra *http://omlc.ogi.edu/spectra/* Accessed Jan 18, 2013.

Pogue BW, Davis SC, Leblond F, Mastanduno MA, Dehghani H, Paulsen KD 2011 Implicit and explicit prior information in near-infrared spectral imaging: accuracy, quantification and diagnostic value *Phil Trans Royal Soc A: Math, Phys and Eng Sci* 369(1955) 4531-4557.

Powers WJ, Grubb RL Jr, Baker RP, Mintun MA, Raichle ME 1985 Regional cerebral blood flow and metabolism in reversible ischemia due to vasospasm: determination by positron emission tomography *J Neurosurg* 62:539–546.

Rabinstein AA, Friedman JA, Weigand SD, McClelland RL, Fulgham JR, Manno EM, Atkinson JL, Wijdicks EF 2004 Predictors of cerebral infarction in aneurysmal subarachnoid hemorrhage *Stroke* 35(8) 1862-1866.

Rincon F, Mayer SA 2007 Neurocritical care: a distinct discipline? *Curr Opin Crit Care* 13(2) 115-121.

Ropper AH 1984 Brain edema after stroke: clinical syndrome and intracranial pressure *Arch Neurol* 41(1) 26-29.

Sehba FA, Hou J, Pluta RM, Zhang JH 2012 The importance of early brain injury after subarachnoid hemorrhage *Prog Neurobiol* 97(1) 14-37.

Seelig JM, Becker DP, Miller JD, Greenberg RP, Ward JD, Choi SC 1981 Traumatic acute subdural hematoma: major mortality reduction in comatose patients treated within four hours *New Engl J Med* 304(25) 1511.

Schabel MC 2012 A unified impulse response model for DCE-MRI *Mag Reson Med* 68(5):1632-46.

Schytz HW, Wienecke T, Jensen LT, Selb J, Boas DA, Ashina M 2009 Changes in cerebral blood flow after acetazolamide: an experimental study comparing near-infrared spectroscopy and SPECT *Eur J Neurol* 16(4) 461-467.

Sharbrough FW, Messick JM, Sundt TM 1973 Correlation of continuous electroencephalograms with cerebral blood flow measurements during carotid endarterectomy *Stroke* 4 674-83.

Sloan MA, Haley EC, Kassell NF, Henry ML, Stewart SR, Beskin RR, Tomer JC 1989 Sensitivity and specificity of transcranial Doppler ultrasonography in the diagnosis of vasospasm following subarachnoid hemorrhage *Neurology* 39(11) 1514-1514.

Soucy JP, McNamara D, Mohr G, Lamoureux F, Danais S 1990 Evaluation of vasospasm secondary to subarachnoid hemorrhage with technetium-99mhexamethyl-propyleneamine oxime (HM-PAO) tomoscintigraphy *J Nucl Med* 31(6) 972–977.

Steiner LA, Andrews PJD 2006 Monitoring the injured brain: ICP and CBF. *Brit J Anaesth* 97(1) 26-38.

Strangman G, Franceschini MA, Boas DA 2003 Factors affecting the accuracy of near-infrared spectroscopy concentration calculations for focal changes in oxygenation parameters *Neuroimage* 18(4) 865–879.

St Lawrence K, Verdecchia K, Elliott J, Tichauer K, Diop M, Hoffman L, Lee T-Y 2013 Kinetic model optimization for characterizing tumour physiology by dynamic contrast-enhanced near-infrared spectroscopy *Phys Med Biol* 58(5) 1591.

Suarez JI, Tarr RW, Selman WR 2006 Aneurysmal subarachnoid hemorrhage *N Engl J Med* 354(4) 387-96.

Taneda M, Kataoka K, Akai F, Asai T, Sakata I 1996 Traumatic subarachnoid hemorrhage as a predictable indicator of delayed ischemic symptoms *J Neurosurg* 84(5) 762-768.

Thurman DF, Alverson CM, Dunn KA, Guerrero JM, Sniezek JE 1999 Traumatic Brain Injury in the United States: A Public Health Perspective. *J Head Trau Rehab* 14(6) 602-615.

Tichauer KM, Brown DW, Hadway J, Lee T-Y., St. Lawrence KS 2006 Near-infrared spectroscopy measurements of cerebral blood flow and oxygen consumption following hypoxia-ischemia in newborn piglets *J App Physiol* 100(3) 850-857.

Udstuen GJ, Claar, JM 2001 Imaging of acute head injury in the adult *Seminars in Ultrasound, CT and MRI* 22(2) 135-147

Unterberg AW, Sakowitz OW, Sarrafzadeh AS, Benndorf G, Lanksch WR 2001 Role of bedside microdialysis in the diagnosis of cerebral vasospasm following aneurysmal subarachnoid hemorrhage *J Neurosurg* 94(5) 740-749.

Vahedi K, Vicaut E, Mateo J, Kurtz A, Orabi M, Guichard JP, Bousser MG 2007 Sequential-design, multicenter, randomized, controlled trial of early decompressive craniectomy in malignant middle cerebral artery infarction (DECIMAL Trial) *Stroke* 38(9) 2506-2517.

Vajkoczy P, Roth H, Horn P, Lucke T, Thomé C, Hubner U, Schmiedek P 2000 Continuous monitoring of regional cerebral blood flow: experimental and clinical validation of a novel thermal diffusion microprobe *J Neurosurg* 93(2) 265-274.

Vajkoczy P, Horn P, Thome C, Munch E, Schmiedek P 2003 Regional cerebral blood flow monitoring in the diagnosis of delayed ischemia following aneurysmal subarachnoid hemorrhage. J Neurosurg, 98(6) 1227-1234.

van Gijn J, Rinkel GJ 2001 Subarachnoid haemorrhage: diagnosis, causes and management *Brain* 124:249-78; 2001.

Varelas PN, Eastwood D, Yun HJ, Spanaki MV, Hacein Bey L, Kessaris C, Gennarelli TA. Impact of a neurointensivist on outcomes in patients with head trauma treated in a neurosciences intensive care unit. J Neurosurg 2006;104(5):713-719.

Vergouwen MD, Vermeulen M, van Gijn J, Rinkel GJ, Wijdicks EF, Muizelaar JP, Mendelow AD, Juvela S, Yonas H, Terbrugge KG, Macdonald RL, Diringer MN, Broderick JP, Dreier JP, Roos YB. Definition of delayed cerebral ischemia after aneurysmal subarachnoid hemorrhage as an outcome event in clinical trials and observational studies: proposal of a multidisciplinary research group. Stroke 2010;41(10):2391-2395.

Vergouwen MD 2011 Vasospasm versus delayed cerebral ischemia as an outcome event in clinical trials and observational studies *Neurocrit Care* 15(2):308-311.

Vespa P, Boonyaputthikul R, McArthur DL, Miller C, Etchepare M, Bergsneider M, Glenn T, Marin N, Hovda D 2006 Intensive insulin

therapy reduces microdialysis glucose values without altering glucose utilization or improving the lactate/pyruvate ratio after traumatic brain injury *Crit Care Med* 34 850–56.

Vespa PM, Nuwer MR, Juhasz C, Alexander M, Nenov V, Martin N, Becker DP 1997 Early detection of vasospasm after acute subarachnoid hemorrhage using continuous EEG ICU monitoring *Electroencephalogr Clin Neurophysiol* 103(6):607-615.

Wang L, Jaques SL, Zheng L 1995 MCML - Monte Carlo modeling of light transport in multi-layered tissues *Comp Meth Prog Biomed* 47:131-46.

Wartenberg KE 2011 Critical care of poor-grade subarachnoid hemorrhage *Curr Opin Crit Care* 17(2) 85-93.

Wang L, Jacques SL, Zheng L 1995 MCML—Monte Carlo modeling of light transport in multi-layered tissues. *Comp Met Prog Biomed* 47(2), 131-146.

Wang LV, Wu H 2007 Biomedical optics: principles and imaging (Wiley-Interscience: Hoboken, NJ).

Wang RK 2000 Modelling optical properties of soft tissue by fractal distribution of scatterers *J Mod Opt* 47(1), 103-120.

Werner C, Engelhard K 2007 Pathophysiology of traumatic brain injury *Brit J Anaesth* 99(1) 4-9.

Weyer GW, Nolan CP, Macdonald RL 2006 Evidence-based cerebral vasospasm management *Neurosurg Focus* 21(3) 1-10.

WHO 1996 "Investing in Health Research and Development." Ad Hoc Committee on Health Research Relating to Future Intervention Options (World Health Organization: Geneva, CH).

Wilberger JE, Harris M, Diamond DL 1991 Acute subdural hematoma: morbidity, mortality, and operative timing *J Neurosurg* 74(2) 212-218.

Wintermark M, Sesay M, Barbier E, Borbély K, Dillon WP, Eastwood JD, Glenn TC, Grandin CB, Pedraza S, Soustiel JF, Nariai T, Zaharchuk G, Caillé JM, Dousset V, Yonas H 2005 Comparative overview of brain perfusion imaging techniques. *J Neurorad* 32(5) 294-314.

Woodard HQ, White DR 1986 The composition of body tissues *Br J Radiol* 59 1209-1218.

Yonas H, Sekhar L, Johnson DW, Gur D 1989 Determination of irreversible ischemia by xenon-enhanced computed tomographic monitoring of cerebral blood flow in patients with symptomatic vasospasm. *Neurosurg* 24(3) 368.

Yonas H, Pindzola RP, Johnson DW 1996 Xenon/computed tomography cerebral blood flow and its use in clinical management *Neurosurg Clin N Amer* 7(4) 605.

Chapter 2

MEASURING QUANTITATIVE CEREBRAL BLOOD FLOW IN A JUVENILE PORCINE MODEL USING MULTIDISTANCE CONTINUOUS-WAVE NEAR-INFRARED SPECTROSCOPY

This chapter is adapted from the work entitled "Quantitative measurement of cerebral blood flow in a juvenile porcine model by depth-resolved near-infrared spectroscopy" by Elliott JT, Diop M, Tichauer KM, Lee T-Y, and St. Lawrence K, published in the *Journal of Biomedical Optics* in 2010. The focus of this paper is to extend the quantitative continuous-wave (CW) near-infrared spectroscopy (NIRS) methods of measuring blood flow to a scenario where the extracerebral layer (ECL) is non-negligible: the juvenile pig model. The original journal article from which this chapter was adapted can be found at *http://biomedicaloptics.spiedigitallibrary.org/article.aspx?articleid=1103440.*

2.1. Introduction

The rationale for measuring cerebral blood flow (CBF) at the intensive care bedside was explained in Chapter 1. In particular, the ideal monitoring tool should be noninvasive, portable, quantitative, and fully compatible with the clinical environment. Although dynamic contrast-enhanced (DCE) near-

infrared (NIR) methods require the injection of indocyanine green (ICG), this procedure is considered minimally invasive since intravenous access is ubiquitous in the context of intensive care. Furthermore, the dye is extremely safe as reflected in the low incidence of adverse reaction (approximately 1 in 250 000 (Garski *et al* 1978)). The portability of NIR is attractive, since current methods of quantifying blood flow (*e.g.*, CT, MRI, PET) are of limited use in intensive care since patients are often unstable and not easily transported to imaging suites. In fact, it is estimated that adverse effects occur in up to 70% of transfers involving critically-ill patients (Waydhas 1999).

Continuous-wave, broadband, NIRS is a particularly robust technique that is compatible with the intensive care environment as it is relatively insensitive to ambient light. Dynamic contrast-enhanced NIRS capable of measuring CBF employs either a change in arterial oxygenation or a bolus injection of the light absorbing ICG. Both methods have been shown to provide accurate CBF measurements in animal models and neonates (Themelis *et al* 2007; Tachtsidis *et al* 2009; Brown *et al* 2002; Tichauer *et al* 2006; Springett *et al* 2001; Patel *et al* 1998). However, when applied to juvenile or adult subjects, measuring CBF accurately has proven difficult. The main reason for the reduced accuracy is the non-negligible effects on the near-infrared signal of the ECL, as discussed in the previous chapter. Because of the ECL, CBF is substantially underestimated (Owen-Reece *et al* 1996; Gora *et al* 2002; Rothoerl *et al* 2003). As such, NIRS has yet to develop into a clinically feasible method for patients older than a few weeks of age, and intensivists continue to rely on invasive subdural CBF techniques or intracranial pressure (ICP) probes to infer changes in cerebral hemodynamics. Not only do these techniques carry a risk of infection and bleeding, evidence suggests that adhering to a set ICP threshold does not

always ensure adequate oxygen delivery owing to differences in intracranial compliance between patients (Wright 2007; Stiefel *et al* 2006).

This chapter describes a multidistance continuous-wave NIRS method enabling depth-resolved measurements to quantify CBF in the presence of significant ECL signal contamination. The approach is partly based on a previous method for measuring CBF in neonates (Brown *et al* 2002), but depth sensitivity is improved by collecting NIR signal from two detection probes placed at different distances from the source. The relationship between the depth of light penetration and source-detector distance forms the basis for the separation of intra- and extra-cerebral signals (Hongo *et al* 1995). Monte Carlo simulations of a two-layer medium were performed using subject-specific optical properties and ECL thickness parameters optimized from CT anatomical priors and second-derivative spectroscopy measurements of water, which was assumed to have a concentration of 80% in the brain. Monte Carlo simulation results were then used to determine the mean partial pathlengths (MPPs) for each layer and source-detector pair, which were used to reconstruct the time-dependent concentration of ICG in brain. The brain tissue concentration curve, in addition to the arterial input function, was used to recover CBF using a nonparametric model (Cenic *et al* 1999).

The set of experiments highlighted in this chapter validates the multidistance CW NIRS technique by collecting measurements of CBF with NIRS and CT perfusion (Cenic *et al* 1999) over a range of hemodynamic states in juvenile pigs. These results are compared with two other analytical approaches: the single-probe method identical to that used in the previous neonatal studies (Brown *et al* 2002), and a simple-subtraction method whereby MPP values are assumed for the entire group (Schytz *et al* 2009).

2.2. Materials and methods

2.2.1. Animal experiment

The study was approved by the Animal Use Subcommittee of the Canadian Council on Animal Care at the University of Western Ontario (AUP #2007-050-06). Eight juvenile Duroc x Landrace crossbred pigs were delivered from a local supplier on the morning of the experiment. The pigs were tracheotomized and mechanically ventilated while anaesthetized by 3% isoflurane. Cannulae were inserted into each ear for injection of the NIRS and CT contrast agents. An additional cannula was inserted into a femoral artery for continuous monitoring of arterial blood pressure and to allow blood samples to be collected for gas and glucose analysis. Following the surgical procedure, isoflurane was reduced to 1.75% and the animals were allowed to stabilize for 1 hour before measurements were collected.

Near-infrared spectroscopy and CT measurements of CBF were collected concomitantly over a range of blood flow values. The range was achieved by adjusting the respiratory rate in each animal to produce distinct levels of arterial blood CO_2 tension ($PaCO_2$): hypocapnia ($PaCO_2$ < 28 mm Hg), normocapnia ($PaCO_2$ ≈ 40 mm Hg) and hypercapnia ($PaCO_2$ > 50 mm Hg).

2.2.2. Instrumentation

An in-house developed continuous-wave spectrometer was used to collect broadband, near-infrared intensity data (Diop *et al* 2009). The main components of the system included an illumination unit, a multiplexer, and a spectrometer consisting of a holographic grating and a cooled charge-coupled device. The illumination unit was a 50-W quartz halogen light bulb that was bandpass filtered to remove light outside the 600 to 1000 nm range. The filtered light was coupled to a 2-m fiber-optic bundle (emission optode) with a

numerical aperture of 0.55 and a 3.5-mm diameter active area. The opposite end of the emission optode was placed on the scalp of the animal and held in position by a specially designed probe holder. Two optical fiber bundles (detection optodes) with the same specifications as the emission optode were positioned at 10 and 30 mm distances from the emitter to collect light having traveled through the multi-layered tissue. Light collected by the detection probes was sequentially recorded at intervals of 200 ms using a multiplexer as described in detail elsewhere (Diop *et al* 2009).

2.2.3 Near-infrared spectroscopic measurements of cerebral blood flow

Cerebral blood flow was measured using a bolus-tracking method that requires an intravenous bolus injection of ICG (0.1 mg/kg in 1 ml of sterile water), followed by continuous measurements of the time-varying concentrations of ICG in arterial blood and brain tissue (Brown *et al* 2002). The arterial concentration, $C_a(t)$, was measured by a pulse dye densitometer (PDD) (DDG-2001 A/K, Nihon Kohden, Tokyo, Japan) and the tissue concentration, $C(t)$, was measured by NIRS. Recall from Chapter 1 that the two concentration curves are related by the following equation:

$$C(t) = C_a(t) * FR(t) \tag{2.1}$$

where $FR(t)$ is the flow-scaled impulse residue function and * represents the convolution operator. A necessary assumption is that blood flow remains constant during the bolus-tracking experiment, which typically lasts about 70 seconds. An in-house developed deconvolution routine was used to calculate $FR(t)$ from the measured arterial and tissue concentration curves (Cenic *et al* 1999).

2.2.4. Single-probe near-infrared spectroscopy

If it is assumed that the head is a homogeneous medium—*i.e.*, the contribution from the ECL is negligible—then the modified Beer-Lambert Law can be used to determine time-dependent changes in the concentrations of chromophores in brain from the change in light attenuation, $\Delta A(\lambda,t)$, measured from a detector:

$$\Delta A(\lambda,t) = \sum_n \varepsilon_n(\lambda) \cdot \Delta C_n(t) \cdot DPL \qquad (2.2)$$

In this equation, λ represents wavelength, $\varepsilon_n(\lambda)$ is the wavelength-dependent extinction coefficient of each chromophore (corrected for the wavelength dependence of the pathlength (Cope *et al* 1991)), $\Delta C_n(t)$ is the concentration change in the ith chromophore, and DPL is the total differential pathlength in the medium, averaged across the fitting range 800–880 nm. Without attempting to remove ECL signal contamination, the absolute change in the tissue concentration of ICG, $C(t)$, following an injection of the dye can be determined from $\Delta A(\lambda,t)$ data acquired at a source-detection distance of 30 mm. By collecting broadband NIRS spectra, the DPL can be determined by second differential analysis using the spectral features of water absorption, which are distinct at 740 nm and 830 nm, and assuming a water concentration in the brain of 80% (Matcher *et al* 1994). This single-probe homogenous approach is referred to as single-probe (SP) NIRS.

2.2.5. Depth-resolved near-infrared spectroscopy

If the ECL is non-negligible, brain signal can potentially be resolved with NIRS by modeling the head as a two-layered medium and simultaneously collecting ICG tissue concentration curves from two detection optodes placed at different source-detector distances. The modified Beer-Lambert Law can be generalized for this collection geometry as follows (Hiraoka *et al* 1993):

$$\Delta A(\lambda,t)=\sum_{n}\sum_{j}\varepsilon_{n}(\lambda)\cdot\Delta C_{n,j}(t)\cdot MPP_{n} \tag{2.3}$$

where $\Delta A(\lambda,t)$ is the wavelength-dependant change in attenuation measured by the detector at time t, $\Delta C_{n,j}$ is the concentration of the nth chromophore in the jth layer, MPP_n is the mean partial pathlength of light in the jth layer. Depth-resolved measurements can be obtained by collecting signal at multiple source-detector distances. Assuming that all other chromophore concentrations remain constant during the time that the bolus is measured, the concentration of ICG in the jth layer, $C_j(t)$ is related to the change in attenuation measured at the ith source-detector distance by:

$$\Delta A_{i}(\lambda,t)=\sum_{j}\varepsilon_{icg}(\lambda)\cdot C_{j}(t)\cdot MPP_{i,j} \tag{2.4}$$

Note that this expression is a specialized version of the optical reconstruction forward problem (Eq. 1.27). Recovering the layer-specific ICG concentration, $C_j(t)$, is achieved by optimizing the following expression:

$$\arg\min_{C_j}\left\|\Delta A_{i}(\lambda)-\varepsilon_{icg}(\lambda)\cdot C_{j}\cdot MPP_{i,j}\right\|^{2} \quad \text{subject to} \quad C_{j}\geq 0. \tag{2.5}$$

To solve Eq. 2.5, MPPs were estimated from a look-up table generated from Monte Carlo simulations for various ECL thicknesses and various ECL component (skull, scalp, and CSF) ratios (see subsection 2.2.7). First, the thickness of the ECL was measured from a CT anatomical image of the subject's head. Second, a set of potential MPPs were selected from the library from simulations that employed ECL thicknesses within 20% of the measured value. Third, for each potential set of MPPs, second derivative spectroscopy was applied to baseline attenuation data (*i.e.*, attenuation data acquired prior to ICG injection) to calculate the concentration of water in the brain, $C_{H2O,brain}$. Finally, the set of MPP values that resulted in a water

concentration closest to the assumed value of 80% was selected. Equation 2.5 was solved using these MPP values to recover $C_f(t)$. The brain concentration curve, $C_2(t)$, along with the arterial input function, $C_a(t)$, were deconvolved to recover FR(t) from Eq. 2.1. The deconvolution procedure used in this study is explained in depth in subsection 1.4.3. This multistep procedure is referred to as depth-resolved (DR) NIRS.

2.2.6. Simple-subtraction technique

If anatomical priors are unavailable, it has been proposed that ECL contamination can be reduced by calculating a weighted difference in attenuation measurements from the two optodes (Schytz *et al* 2009). In a two-distance approach, if the light collected by an optode placed at 10 mm is assumed to have interrogated only the ECL and the mean partial pathlength of light through the ECL is assumed to be the same for light collected at both distances, Eq. 2.4 can be simplified to

$$C_{brain}(t) = \frac{\Delta A_2(\lambda, t) - \Delta A_1(\lambda, t)}{\varepsilon_{icg}(\lambda) \cdot r \cdot DPL} \tag{2.6}$$

where ΔA_1 and ΔA_1 are change in attenuation measured at 10 mm and 30 mm source-detector distances. Values for *DPL* and *r* were estimated from the literature (Owen-Reece *et al* 1996); a pathlength factor of 5.9 was chosen (van der Zee *et al* 1992) (corresponding to a *DPL* of 177 mm for a source-detector distance of 30 mm) and the fraction of the *DPL* through the brain, *r*, was assumed to be 0.35. This value represents the group average determined from the Monte Carlo simulations presented in the following section. The same values of *DPL* and *r* were used to analyze all data sets, irrespective of the animal's ECL thickness. This simple subtraction technique is referred to as simple subtraction (SS) NIRS.

Table 2.1: Optical properties used in the Monte Carlo simulations

Medium	μ_s' (mm^{-1})		μ_a (mm^{-1})	
	760 nm	830 nm	760 nm	830 nm
Scalp	0.73	0.66	0.0177	0.0191
Skull	0.93	0.86	0.0125	0.0136
CSF	0.01	0.01	0.0021	0.0026
Brain	1.18	1.11	0.0195	0.0106

Values are taken from literature (Strangman *et al* 2003).

2.2.7. Monte Carlo Library Generation

Monte Carlo simulations have been extensively used to model light propagation in multi-layered media (Hiraoka *et al* 1993). To generate the MPPs required for equations 2.3-2.5, a Monte Carlo code in C++ was programed based on the code first published by Wang and colleagues (1995), using the optical properties listed in Table 2.1. A library of MPP values was generated for combinations of different ECL thickness (5 to 20 mm in steps of 1 mm) and relative scalp-to-bone ratios (3:7, 4:6, 5:5, 6:4, and 7:3; effectively varying the bulk optical properties of the ECL) at two wavelengths (760 and 830 nm).

The use of only two wavelengths to characterize MPP over the fitting range was necessary because central processing unit (CPU)-based Monte Carlo simulations are time consuming—*n.b.,* graphics processing unit (GPU)-based solutions (Fang and Boas 2009) were not published at the time this study was conducted. These particular wavelengths were used because their optical properties for the various extra- and intra-cerebral tissues are well documented, and they are also close to a distinct water feature at 740 nm and enclose the peak absorption of ICG at 805 nm. Small discrepancies between wavelengths was accounted for by correcting $\varepsilon(\lambda)$ for the wavelength dependency of pathlength (Cope 1991).

Simulations were performed in parallel on the Shared Hierarchical Academic Research Computing Network (SHARCNet) system, a high performance computer cluster, and required 4-6 CPU hours per simulation on average for 10^8 photons on a 2.2 GHz CPU core.

2.2.8. Computed tomography perfusion imaging

Computed tomography images of CBF were acquired using a LightSpeed QXi multislice CT scanner (GE Healthcare, Milwaukee, WI). Eight 5 mm-thick coronal slice scans (80 kVp, 190 mA) were collected at 1 s intervals for 40 s upon injection of 1.0 ml/kg of the iodinated contrast agent iohexol (300 mg/ml; Omnipaque™, GE Healthcare); the injection rate was 1 ml/s.

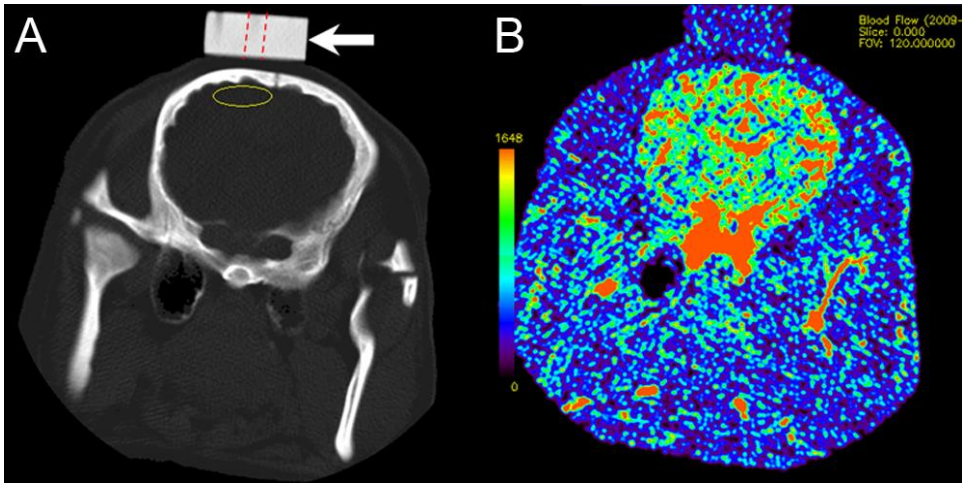

Figure 2.1: CT anatomical and perfusion images

(A) CT anatomical image showing the region of interest (yellow outline) directly below the optical probe holder (white arrow). Red dashed lines on probe holder indicate position of the optode. (B) Corresponding cerebral blood flow map determined by CT perfusion.

Parametric maps of CBF were generated from the cine images using CT Perfusion 3 software (GE Healthcare). Regions of interest were defined on the CBF images that corresponded to the brain volume interrogated by the NIRS probes (Figure 2.1A). The thickness of the ECL was measured using anatomical CT images acquired at the start of the experiment. Since the

probe-holder was visible on the CT image, ECL thickness could be measured directly below the location of the optodes (Figure 2.1B).

2.2.9. Statistical Analysis

All data are presented as mean ± SE unless otherwise stated. SPSS 16.0 (SPSS, Chicago, IL) was used for all statistical analyses and statistical significance was defined as $p < 0.05$. Physiological parameters were analyzed using one-way ANOVAs and a Tukey's test for post-hoc analyses. Correlations between CT and NIRS CBF were analyzed using parametric linear regression. Non-parametric analysis was used to analyze the relationship between the errors in the NIRS CBF measurements and ECL thickness.

2.3. Results

Cerebral blood flow measurements were acquired in eight juvenile pigs. All pigs were between one and two months of age with a mean weight of 16.2 ± 0.5 kg. The thickness of the ECL, as determined from anatomical CT images, ranged from 7.5 to 14.5 mm, with a mean value of 10.4 ± 0.6 mm. In total, 25 ICG runs were completed; however, four NIRS measurements could not be analyzed. In three cases the concentration of ICG injected was below the threshold required for accurate PDD analysis and in one case the CT contrast agent concentration was too low.

The results of the physiological parameters for the eight pigs at the three different conditions are summarized in Table 2.2. As expected, average $PaCO_2$ and pH values were significantly different between hypo-, normo- and hyper- capnia groups ($p < 0.05$). No statistically significant differences were observed for any of the other physiological parameters.

Table 2.2: Physiological parameters during the three conditions.

	Hypocapnia (n_x=6)††	Normocapnia (n_x=13)	Hypercapnia (n_x=6)
Heart Rate, beats/min	122 ± 5	132 ± 5	159 ± 15*
Mean arterial pressure, mmHg	54.5 ± 2.0	57.8 ± 1.9	63.2 ± 1.9*
Arterial PCO_2, torr	22.6 ± 1.3	38.9 ± 1.2*	57.4 ± 4.4*†
Arterial PO_2, torr	238.7 ± 21.0	227.1 ± 15.8	212.9 ± 22.1
Arterial pH	7.58 ± 0.02	7.43 ± 0.01*	7.30 ± 0.03*†

Values are mean ± SE. *p < 0.05 compared with hypocapnia. †p < 0.05 compared with normocapnia. ††n_x refers to the number of ICG runs acquired at each capnic level.

To determine the error caused by ignoring the ECL, the SP-NIRS approach was applied to ICG tissue concentration curves acquired with a source-detection distance of 30 mm and the resulting CBF estimates were compared with CBF measured by CT perfusion. Figure 2.2A depicts an example of the time-dependent change in optical density measured at both optode distances following ICG injection.

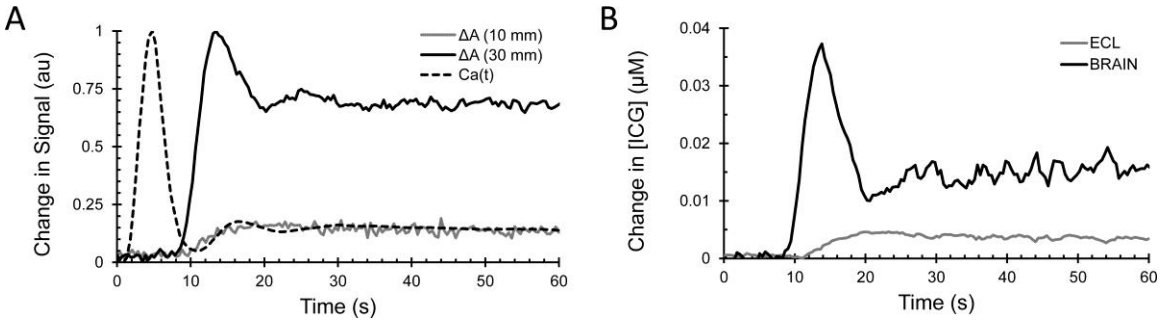

Figure 2.2: Measured optical signals and recovered tissue dye concentration curves.

(A) The change in optical density following ICG injection at 1 cm and 3 cm detector probes measured at 800 nm, and (B) the corresponding change in ICG concentration in the ECL and brain following data processing by the DR-NIRS method. Data are from the same ICG run in an animal with an ECL thickness of 14 mm.

Figure 2.3 shows the SP-NIRS CBF measurements plotted as a function of the corresponding CBF measurements acquired with CT perfusion. The SP-NIRS technique consistently underestimated CBF and no significant correlation was observed between CBF measurements from the two techniques. The mean CBF determined by SP-NIRS was 18.17 ± 3.26 ml min^{-1} $100g^{-1}$, which was significantly different from the mean CBF value determined by CT perfusion (69.91 ± 3.25 ml min^{-1} $100g^{-1}$, $p < 0.001$).

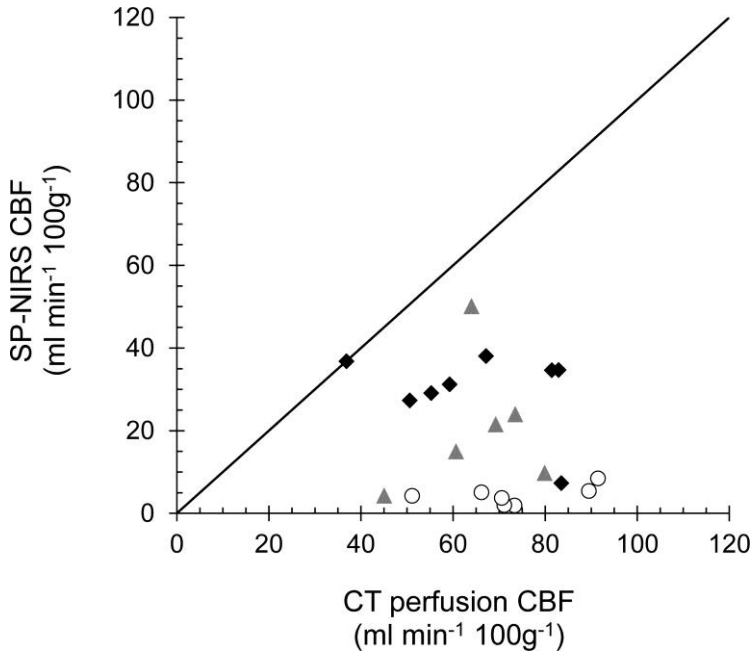

Figure 2.3: Comparison of SP-NIRS CBF and CT perfusion CBF

Correlation plot comparing CBF measurements acquired by CT perfusion and single-probe NIRS. Symbols represent the data grouped according to ECL thickness: less than or equal to 8 mm (solid diamonds), between 8 and 12 mm (shaded triangles), and greater than or equal to 12 mm (open circles). No significant correlation between CBF measurements from the two techniques was detected. The line of unity (dashed line) is shown for comparison.

Figure 2.4 shows CBF values derived from the SS-NIRS technique plotted as a function of the corresponding CBF values determined from CT perfusion. Similar to the SP-NIRS results, no significant correlation was observed between CBF measurements from the two techniques. The mean CBF calculated by SS-NIRS (42.80 ± 7.58 ml min^{-1} $100g^{-1}$) was greater than that determined using SP-NIRS, but still underestimated the mean CBF calculated from the CT perfusion data set.

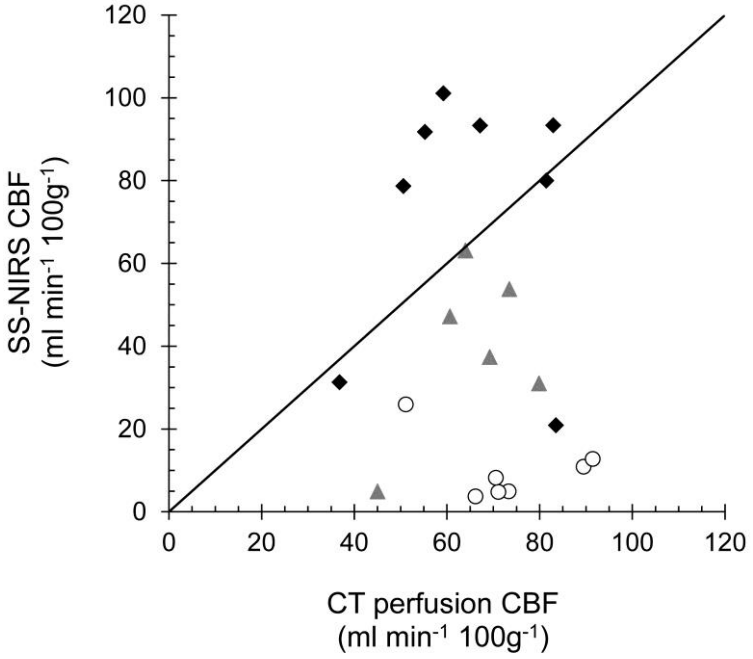

Figure 2.4: Comparison of SS-NIRS CBF and CT perfusion CBF

Correlation plot comparing CT and SS-NIRS measurements of CBF. Symbols represent three ECL groups described in figure 2.3. No significant correlation between the two measurements was detected. The dashed line indicates the line of unity.

The correlation between CBF measurements from DR-NIRS and CT perfusion is shown in Figure 2.5. In this case, a strong, statistically significant correlation was revealed ($r^2 = 0.714$, *slope* = 0.92, $p < 0.001$). The mean CBF measured using the DR-NIRS approach was 64.93 ± 3.47 ml min^{-1} $100g^{-1}$, which was not significantly different from that measured by CT perfusion.

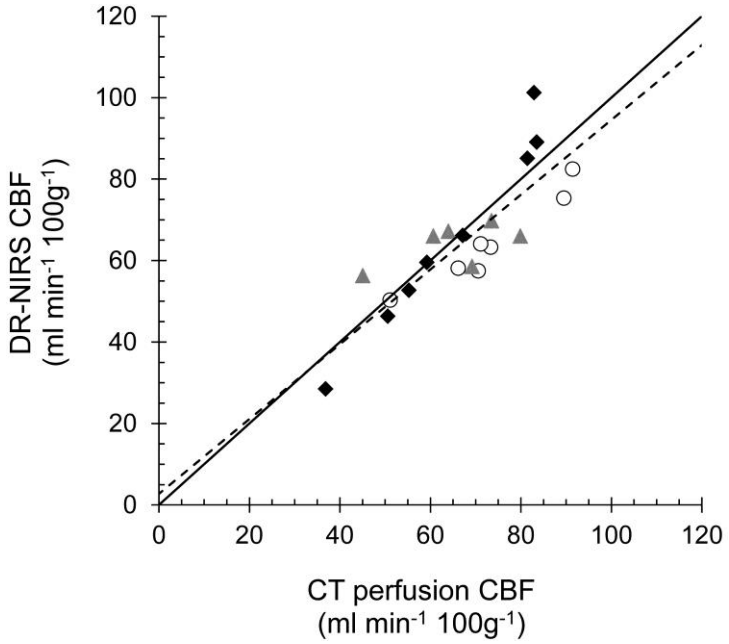

Figure 2.5: Comparison of DR-NIRS CBF and CT perfusion CBF

Correlation plot comparing the CT and DR-NIRS measurements of CBF. Symbols represent three ECL groups described in figure 4. The solid line represents the line of regression (r^2 = 0.714, slope = 0.92, intercept = 2.7, $p < 0.001$), and the line of unity (dashed line) is shown for comparison.

A Bland-Altman plot was used to investigate the existence of any bias in the CBF measurements and to determine the variability in the measurements (Figure 2.6). The mean difference between the two techniques was −2.83 ml min^{-1} $100g^{-1}$. The limits of agreement, *i.e.*, the region in which 95% of the differences lay, were −19.63 ml min^{-1} $100g^{-1}$ and 14.00 ml min^{-1} $100g^{-1}$. No discernible CBF-dependent errors were observed.

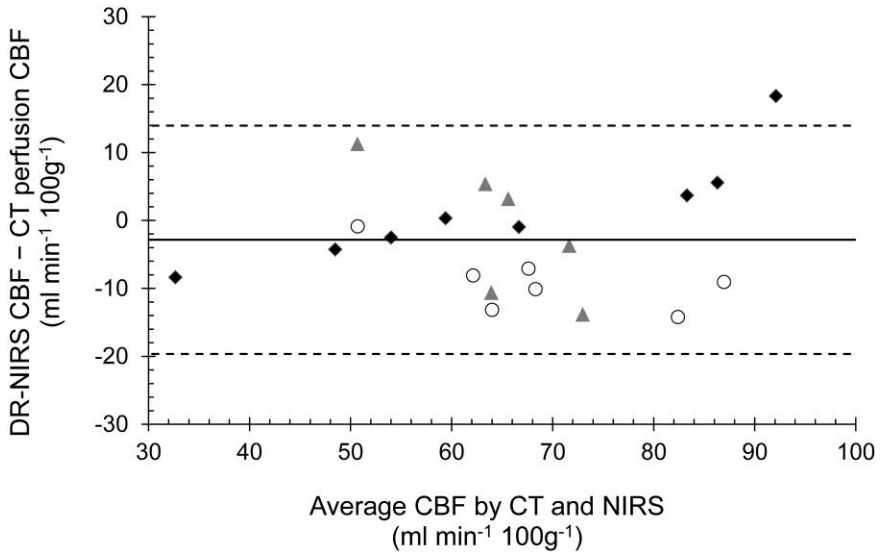

Figure 2.6: Bland-Altman plot of DR-NIRS and CT perfusion CBF

Bland-Altman plot comparing CT and DR-NIRS measurements of CBF. Symbols represent three ECL groups, as described in figure 4. The mean difference between the two measurements (solid line) is −2.83 ml min^{-1} $100g^{-1}$. The limits of agreement (dashed lines), within which 95% of the differences reside, are 13.97 and −19.63 ml min^{-1} $100g^{-1}$.

Non-parametric regression analysis was performed to further investigate the relationship between ECL thickness and the percent difference between CT perfusion and CBF values obtained with each of the NIRS techniques. Significant correlations were observed for both SP-NIRS (ρ = -0.884, $p < 0.001$) and SS-NIRS (ρ = -0.861, $p < 0.001$). In contrast, there was no correlation between ECL thickness and percent difference in CBF values for DR-NIRS.

2.4. Discussion

An integral part of critical care management of ABI patients is the maintenance of adequate CBF to avoid secondary brain injury. Near-infrared spectroscopy has long been recognized for its potential as a non-invasive bedside cerebral monitor due to its portability and sensitivity to cerebral hemodynamics (McCormick *et al* 1991). However, its application to adult patients has been challenged by the significant signal contamination from the

scalp and skull. Previous studies have reported that CBF collected using traditional NIRS approaches can be underestimated by more than a factor of 3, due primarily to the increase in optical pathlength through extra-cerebral tissue (Owen-Reece *et al* 1996). Moreover, not only does ECL contamination affect the accuracy of the CBF measurements, studies using ICG bolus tracking methods have found that NIRS is also insensitive to changes in CBF, which questions if NIRS can even be used to monitor relative CBF (Schytz *et al* 2009; McCormick *et al* 1991). To overcome this major hurtle, a multidistance NIRS approach was developed to resolve depth-specific information. Monte Carlo simulations were used in conjunction with the two-layer modified Beer-Lambert law to extract the cerebral ICG concentration curve from multi-distance NIRS data. The use of subject-individualized Monte Carlo simulations to model depth-resolved NIRS has been proposed previously in neural activation studies (Boas et al 2002; Custo *et al* 2010; Yamada *et al* 2009). Selection of the appropriate simulation parameters for each animal was based on its specific ECL geometry (*i.e.*, thickness and relative scalp-to-skull ratio) determined from anatomical CT images. A fixed cerebral water concentration provided an additional constraint in the selection process. The main finding of this paper was that CBF measurements obtained with our Monte-Carlo driven, depth-resolved NIRS technique correlated well with CT perfusion data (a clinically validated and widely used technique for measuring CBF in humans (Konstas *et al* 2009a, 2009b)). As a corollary, we found that the more simplistic SP-NIRS and SS-NIRS techniques did not provide reliable measurements of CBF.

It was expected from previous studies (Owen-Reece *et al* 1996; Gora *et al* 2002) that the SP-NIRS technique would be inadequate for measuring CBF in the intact adult head since the cerebral NIR signal comprises only about 30% of the total signal at a source-detector distance of 30 mm (see subsection 1.6.1). Qualitatively, this effect can be seen in the attenuation signal shown

in Figure 1.2A. Signal collected by the 30 mm detector probe demonstrates a relatively slow washout, typical of ECL tissue and attributable to its lower blood flow. The effect of the significant ECL MPP was evident by the large underestimations of CBF, calculated from the long-distance NIRS data compared to the measurements acquired with CT perfusion. Furthermore, no correlation between the two techniques was observed over a range of CBF from 35 to 90 ml min^{-1} $100g^{-1}$. These results agree with previous studies conducted in humans (Gora *et al* 2002; Rothoerl *et al* 2003) and clearly demonstrate that SP-NIRS is unsuitable for measuring CBF in adults.

Marginal improvements were observed for SS-NIRS, which relied upon an assumed value of the mean partial pathlength in brain, over the SP-NIRS approach; however, it also performed poorly relative to DR-NIRS. It might be anticipated that even if SS-NIRS cannot accurately measure absolute CBF, a correlation with CT perfusion could be expected, but this was not observed. The most likely explanation for this discrepancy is that the relative contributions of brain and ECL varied substantially from experiment to experiment, as suggested by the dependency of SS-NIRS error on the ECL thickness revealed by non-parametric analysis. Further analysis of the data revealed that assuming the ECL MPPs are the same for both distances introduced an error. The difference in the actual ratio compared to the assumed ratio of unity was correlated with the error in SS-NIRS measured CBF ($r = -0.76$, $p < 0.01$), suggesting that the large variability in the SS-NIRS data has its source in the error of MPP values used in this approach. Since the calculation of CBF is heavily dependent on the height of the ICG curve, which in turn is dependent on the chosen value of brain MPP, any discrepancy between the assumed MPP and the true value will lead to considerable variance in the CBF estimate. These findings suggest that in order to measure CBF precisely, a case-by-case method of calculating the MPP values is prerequisite. These results also provide a plausible reason for

the failure of SS-NIRS to detect changes in CBF in healthy human subjects, as reported in a recent study (Schytz *et al* 2009), and may help to explain some of the contamination issues observed in studies measuring cerebral blood saturation by spatially resolved NIRS (Muehlschlegel and Lobato 2006).

The approach presented in the current study is based on a previously validated technique using broadband continuous-wave NIRS to measure CBF in neonates (Brown *et al* 2002). In contrast to the simpler techniques presented above, the DR-NIRS technique attempted to correct for the primary sources of inter-subject variability. By using independent Monte Carlo simulations, with *a priori* information of the ECL thickness, MPP values can be defined on a subject-by-subject basis. Furthermore, by using a continuous-wave broadband NIRS system, second derivative spectroscopy can assist with selecting the appropriate MPP values. By virtue of the fact that the water concentration in brain is known (80%) and relatively stable (Matcher *et al* 1994), the MPP selection process was constrained to only those choices that met this criterion. Finally, our system uses a shutter multiplexing system that allows for rapid collection of NIR signals from multiple probes with high fidelity (Diop *et al* 2009). It is likely that these characteristics contributed to the strong correlation that was observed between CBF measurements from CT perfusion and DR-NIRS (Figure 2.5) and also resulted in the small bias revealed by the Bland-Altman method (Figure 2.6). When compared with the previous validation study published by our group for the neonatal pig model which also used CT perfusion (Brown *et al* 2002), the 95% confidence intervals shown in the Bland-Altman plot were only slightly larger (±16.8 ml min^{-1} $100g^{-1}$ compared to ±12.7 ml min^{-1} $100g^{-1}$ in the previous study). Given the sources of uncertainty introduced by the depth-resolved approach, as well as the decreased signal-to-contrast ratio, it is encouraging to note that the difference in precision was only marginal.

There are a few significant limitations in this study which should be addressed. The first concern pertains to the reliance on *a priori* knowledge of the ECL geometry from anatomical imaging. Certainly, a completely independent technique would be more attractive and may potentially emerge in the future. However, given that standard procedure for head trauma neurological assessment upon admittance includes CT or MRI scanning, the requirement of this additional information for subsequent NIRS measurements does not represent a significant burden. A second concern is the possibility that the two-layer Beer-Lambert model used to characterize light propagation through the pig head may not adequately represent the human head. Similarly, this approach relied on assumed optical properties for the ECL. While the selected brain MPP value was constrained by the known water concentration—a benefit of using broadband NIRS—uncertainties in the assumed scattering and absorption coefficients for the different extra-cerebral layers (scalp, skull and CSF) are likely to affect the accuracy of the CBF measurements. More complex instrumentation, such as frequency-domain and time-resolved NIRS have the ability to calculate the optical properties directly from reflection measurements either by employing an analytical model (Kienle and Patterson 1997) or fitting to Monte Carlo simulations (Elliott *et al* 2011). In particular, multi-distance time-resolved NIR methods have the benefit of also being more sensitive to deeper tissue structures, and for this reason, the work presented in subsequent chapters will explore this instrumentation.

A final limitation with this study pertains to the animal model that was used. First, the mean thickness of the ECL in these animals was 10 mm and, consequently, was more representative of a juvenile patient group than an adult one. Second, the thick temporalis muscles originating in the temperoparietal region have evolved in the pig to allow powerful mastication are more metabolically demanding than the human scalp (Ström *et al* 1986).

As a result, the blood flow values are significantly higher than what is expected in the human (on the order of 3-4 times higher). Furthermore, hypo- and hyper-capnia conditions are likely to elicit a global vascular response. These factors combined result in an animal model that is likely more favourable than the clinical scenario in terms of measuring CBF accurately. All of these issues will be addressed in subsequent chapters, and ultimately culminate with the validation of the kinetic deconvolution optical reconstruction (KDOR) method of analyzing multidistance time-resolved DCE NIR measurements (Chapter 6).

2.5. Conclusion

The salient finding of the present study is that, in contrast to the SP- and SS-NIRS methods, the DR-NIRS technique demonstrated for the first time that accurate measurements of CBF can be acquired with NIRS despite the presence of a significant ECL. These results highlight the promise of using NIRS for acquiring bedside measurements of CBF in neurological intensive care patients, demonstrating the potential of NIRS to greatly improve clinical management of these individuals.

2.6. References

Brown DW, Picot PA, Naeini JG, Springett R, Delpy DT, Lee T-Y 2002 Quantitative near infrared spectroscopy measurement of cerebral hemodynamics in newborn piglets *Pediatr Res* 51(5) 564-570.

Boas DA, Franceschini MA, Dunn AK, Strangman G 2002 Non-invasive imaging of cerebral activation with diffuse optical tomography in *Optical Imaging of Brain Function* (CRC Press: Boca Raton, FL).

Cenic A, Nabavi DG, Craen RA, Gelb AW, Lee TY 1999 Dynamic CT measurement of cerebral blood flow: a validation study *AJNR Am J Neuroradiol* 20(1) 63-73.

Cenic A, Nabavi DG, Craen RA, Gelb AW, Lee TY 2000 A CT method to measure hemodynamics in brain tumors: validation and application of cerebral blood flow maps *Am J Neuroradiol* 21 462–70.

Cope M 1991 The application of near infrared spectroscopy to non invasive monitoring of cerebral oxygenation in the newborn infant in *Ph.D. thesis* (University College London: London, UK).

Diop M, Elliott JT, Tichauer KM, Lee T-Y, St Lawrence K 2009 A broadband continuous-wave multichannel near-infrared system for measuring regional cerebral blood flow and oxygen consumption in newborn piglets *Rev Sci Instrum* 80(5) 054302.

Elliott JT, Tichauer KM, Diop M, Lawrence KS 2011 Fast Monte Carlo fitting of two-layered tissue structures for short source–detector distances. *Proc of SPIE* 7896 789611.

Fabbri F, Sassaroli A, Henry ME, Fantini S 2004 Optical measurements of absorption changes in two-layered diffusive media *Phys Med Biol* 49(7) 1183-1201.

Fang Q, Boas DA 2009 Monte Carlo simulation of photon migration in 3D turbid media accelerated by graphics processing units. *Opt Expr* 17(22) 20178-20190.

Garski TR, Staller BJ, Hepner G, Banka VS, Finney RA, Jr 1978 Adverse reactions after administration of indocyanine green *JAMA* 240(7) 635.

Gora F, Shinde S, Elwell CE, Goldstone JC, Cope M, Delpy DT, Smith M 2002 Noninvasive measurement of cerebral blood flow in adults using near-infrared spectroscopy and indocyanine green: a pilot study *J Neurosurg Anesthesiol* 14(3) 218-222.

Hiraoka M, Firbank M, Essenpreis M, Cope M, Arridge SR, van der Zee P, Delpy DT 1993 A Monte Carlo investigation of optical pathlength in inhomogeneous tissue and its application to near-infrared spectroscopy *Phys Med Biol* 38(12) 1859-1876.

Hongo K, Kobayashi S, Okudera H, Hokama M, Nakagawa F 1995 Noninvasive cerebral optical spectroscopy: depth-resolved measurements of cerebral haemodynamics using indocyanine green *Neurol Res* 17(2) 89-93.

Kienle A, Patterson MS 1997 Improved solutions of the steady-state and the time-resolved diffusion equations for reflectance from a semi-infinite turbid medium *J Opt Soc Am A Opt Image Sci Vis* 14(1) 246-254.

Kohl-Bareis M, Obrig H, Steinbrink J, Malak J, Uludag K, Villringer A 2002 Noninvasive monitoring of cerebral blood flow by a dye bolus method: separation of brain from skin and skull signals *J Biomed Opt* 7(3) 464-470.

Kohno S, Miyai I, Seiyama A, Oda I, Ishikawa A, Tsuneishi S, Amita T, Shimizu K 2007 Removal of the skin blood flow artifact in functional near-infrared spectroscopic imaging data through independent component analysis *J Biomed Opt* 12(6) 062111.

Konstas AA, Goldmakher GV, Lee T-Y, Lev MH 2009 Theoretic basis and technical implementations of CT perfusion in acute ischemic stroke, part 1: Theoretic basis *AJNR Am J Neuroradiol* 30(4) 662-668.

Konstas AA, Goldmakher GV, Lee T-Y, Lev MH 2009 Theoretic basis and technical implementations of CT perfusion in acute ischemic stroke, part 2: technical implementations *AJNR Am J Neuroradiol* 30(5) 885-892.

Leung TS, Tachtsidis I, Tisdall M, Smith M, Delpy DT, Elwell CE 2007 Theoretical investigation of measuring cerebral blood flow in the adult human head using bolus Indocyanine Green injection and near-infrared spectroscopy *Appl Opt* 46(10) 1604-1614.

Liebert A, Wabnitz H, Obrig H, Erdmann R, Moller M, Macdonald R, Rinneberg H, Villringer A, Steinbrink J 2006 Non-invasive detection of fluorescence from exogenous chromophores in the adult human brain *Neuroimage* 31(2) 600-608.

Liebert A, Wabnitz H, Steinbrink J, Moller M, Macdonald R, Rinneberg H, Villringer A, Obrig H 2005 Bed-side assessment of cerebral perfusion in stroke patients based on optical monitoring of a dye bolus by time-resolved diffuse reflectance *Neuroimage* 24(2) 426-435.

Liebert A, Wabnitz H, Steinbrink J, Obrig H, Moller M, Macdonald R, Villringer A, Rinneberg H 2004 Time-resolved multidistance near-infrared spectroscopy of the adult head: intracerebral and extracerebral absorption changes from moments of distribution of times of flight of photons *Appl Opt* 43(15) 3037-3047.

Matcher SJ, Cope M, Delpy DT 1994 Use of the water absorption spectrum to quantify tissue chromophore concentration changes in near-infrared spectroscopy *Phys Med Biol* 39(1) 177-196.

McCormick PW, Stewart M, Goetting MG, Dujovny M, Lewis G, Ausman JI 1991 Noninvasive cerebral optical spectroscopy for monitoring

cerebral oxygen delivery and hemodynamics *Crit Care Med* 19(1) 89-97.

Muehlschlegel S, Lobato EB 2006 Con: all cardiac surgical patients should not have intraoperative cerebral oxygenation monitoring *J Cardiothorac Vasc Anesth* 20(4) 613-615.

Owen-Reece H, Elwell CE, Harkness W, Goldstone J, Delpy DT, Wyatt JS, Smith M 1996 Use of near infrared spectroscopy to estimate cerebral blood flow in conscious and anaesthetized adult subjects *Br J Anaesth* 76(1) 43-48.

Patel J, Marks K, Roberts I, Azzopardi D, Edwards AD 1998 Measurement of cerebral blood flow in newborn infants using near infrared spectroscopy with indocyanine green *Pediatr Res* 43(1) 34-39.

Rothoerl RD, Schebesch KM, Faltermeier R, Woertgen C, Brawanski A 2003 Lack of correlation between Xenon133 and near infrared spectroscopy/indocyanine green rCBF measurements *Neurol Res* 25(5) 528-532.

Saager RB, Berger AJ 2005 Direct characterization and removal of interfering absorption trends in two-layer turbid media *J Opt Soc Am A Opt Image Sci Vis* 22(9) 1874-1882.

Schytz HW, Wienecke T, Jensen LT, Selb J, Boas DA, Ashina M 2009 Changes in cerebral blood flow after acetazolamide: an experimental study comparing near-infrared spectroscopy and SPECT *Eur J Neurol* 16(4) 461-467.

Stiefel MF, Udoetuk JD, Spiotta AM, Gracias VH, Goldberg A, Maloney-Wilensky E, Bloom S, Le Roux PD 2006 Conventional neurocritical

care and cerebral oxygenation after traumatic brain injury *J Neurosurg* 105(4) 568-575.

Steinbrink J, Wabnitz H, Obrig H, Villringer A, Rinneberg H 2001 Determining changes in NIR absorption using a layered model of the human head *Phys Med Biol* 46(3) 879-896.

Strangman G, Franceschini MA, Boas DA 2003 Factors affecting the accuracy of near-infrared spectroscopy concentration calculations for focal changes in oxygenation parameters *Neuroimage* 18(4) 865–879.

Ström D, Holm S, Clemensson E, Haraldson T, Carlsson GE 1986 Gross anatomy of the mandibular joint and masticatory muscles in the domestic pig Sus scrofa *Arch Oral Bio* 31(11) 763-768.

Springett R, Sakata Y, Delpy DT 2001 Precise measurement of cerebral blood flow in newborn piglets from the bolus passage of indocyanine green *Phys Med Biol* 46(8) 2209-2225.

Tachtsidis I, Tisdall MM, Leung TS, Pritchard C, Cooper CE, Smith M, Elwell CE 2009 Relationship between brain tissue haemodynamics, oxygenation and metabolism in the healthy human adult brain during hyperoxia and hypercapnea *Adv Exp Med Biol* 645 315-320.

Themelis G, D'Arceuil H, Diamond SG, Thaker S, Huppert TJ, Boas DA, Franceschini MA 2007 Near-infrared spectroscopy measurement of the pulsatile component of cerebral blood flow and volume from arterial oscillations *J Biomed Opt* 12(1) 014033.

Tichauer KM, Hadway JA, Lee T-Y, St Lawrence K 2006 Measurement of cerebral oxidative metabolism with near-infrared spectroscopy: a validation study *J Cereb Blood Flow Metab* 26(5) 722-730.

van der Zee P, Cope M, Arridge SR, Essenpreis M, Potter LA, Edwards AD, Wyatt JS, McCormick DC, Roth SC, Reynolds EO, Delpy DT 1992 Experimentally measured optical pathlengths for the adult head, calf and forearm and the head of the newborn infant as a function of inter optode spacing *Adv Exp Med Biol* 316 143-153.

Wang L, Jacques SL, Zheng L 1995 MCML--Monte Carlo modeling of light transport in multi-layered tissues *Comput Methods Programs Biomed* 47(2) 131-146.

Waydhas C 1999 Intrahospital transport of critically ill patients *Crit Care* 3(5) R83-9.

Wright WL 2007 Multimodal monitoring in the ICU: when could it be useful? *J Neurol Sci* 261(1-2) 10-15.

Yamada T, Umeyama S, Matsuda K 2009 Multidistance probe arrangement to eliminate artifacts in functional near-infrared spectroscopy *J Biomed Opt* 14(6) 064034.

Zhang Q, Strangman GE, Ganis G 2009 Adaptive filtering to reduce global interference in non-invasive NIRS measures of brain activation: how well and when does it work? *Neuroimage* 45(3) 788-794.

Chapter 3

MEASURING CEREBRAL BLOOD FLOW CHANGES IN ADULT PIGS WITH STATISTICAL MOMENTS OF TIME-RESOLVED NEAR-INFRARED MEASUREMENTS

This chapter is adapted from the work entitled "Variance of time-of-flight distribution is sensitive to cerebral blood flow as demonstrated by ICG bolus-tracking measurements in adult pigs" by Elliott JT, Milej D, Gerega A, Weigl W, Diop M, Morrison LB, Lee T-Y, Liebert A and St. Lawrence K, published in *Biomedical Optics Express* in 2013. The focus of this paper is two-fold: to investigate the specificity of time-resolved measurements to cerebral blood flow (CBF) effects by sequential acquisition on the intact and ischemic scalp, the skull, and directly on the dura matter; and, to determine the sensitivity of time-resolved measurements acquired on the surface of the head to hypocapnic decrease in CBF. Furthermore, this chapter describes a method using more advanced instrumentation than in the previous continuous-wave (CW) near-infrared spectroscopy (NIRS) study, as well as a more accurate animal model of the adult neurotrauma patient, but highlights an analytical approach that is only able to determine *relative changes* in CBF. The original journal article from which this chapter was adapted can be found at *http://www.opticsinfobase.org/boe/abstract.cfm?uri=boe-4-2-206*

3.1. Introduction

In the previous chapter, a broadband CW-NIRS method of quantifying CBF was presented. The salient finding of this study was that reconstruction of brain-specific optical changes is possible using a multi-distance reconstruction technique stabilized with anatomical (*i.e.*, CT or MRI imaging data) and physiological/spectral (*i.e.*, assumed water concentration of 80%) priors. However, this approach was applied to smaller animals whose anatomy more closely approximates the juvenile patient. Furthermore, it is likely that the higher blood flow observed in the scalp of pigs compared with humans limits the conclusions that can be drawn regarding the performance of the method in adult subjects. To this end, the work presented in Chapter 3 describes the application of the more sensitive time-resolved (TR) NIR instrumentation to investigate the influence of extracerebral hemodynamics and optical properties (by systematically removing the scalp and skull) on the measured signal. In addition, measurements acquired directly on the brain were compared with contralateral measurements acquired on the head surface during normo- and hypo-capnia. In this way, both the sensitivity—*i.e.*, the ability to reliably detect changes in CBF or hemoglobin concentrations—as well as the specificity—*i.e.*, the confidence that a change in signal reflects only the brain and not the extracerebral tissue—were investigated.

Dynamic contrast-enhanced (DCE) methods based on analysis of the statistical moments of measured distributions of times-of-flight of photons (DTOF) have been proposed as a way to increase the sensitivity to signal changes occurring in the brain over conventional CW NIRS methods (Liebert *et al* 2004). Following an injection of the vascular tracer indocyanine (ICG), it is possible to record the concentration-dependent changes in three statistical moments of DTOFs: total number of photons, N, mean time-of-flight, $\langle t \rangle$, and variance, V. To date, the moments-based technique has been applied to

healthy volunteers (Liebert *et al* 2004, Jelzow *et al* 2012), stroke patients (Steinkellner *et al* 2010; Liebert *et al* 2005), and other neurotrauma patients (Liebert *et al* 2012), and qualitative analysis strongly suggests that the time-dependent change in variance of the DTOF shows good sensitivity to absorption changes occurring in the brain. However, these previous studies employed qualitative methods, or attempted to quantify changes in CBF using the time-to-peak (TTP) method, a relatively straightfoward but indirect method of measuring change in CBF (Steinkellner *et al* 2010; Kuebler *et al* 1998; Terborg *et al* 2003), that is also dependent on cerebral blood volume (CBV) and variations in the arterial input function (AIF).

To further investigate the potential pitfalls associated with the TTP method limitation, an error analysis was conducted. In particular, the dependency of TTP accuracy on the CBV and the TTP of the arterial input function is highlighted. As an alternative to this method, a nonparametric deconvolution-based method is introduced (Cenic *et al* 1999; Brown *et al* 2002; Elliott *et al* 2012) that enables the recovery of a relative blood flow index, *dBF*. While this method differs from the quantitative deconvolution method used in the previous chapter (since only a relative blood flow index is recovered), the advantage of this approach compared to TTP measurements is that confounding effects due to the AIF and CBV are removed.

In this study, an adult pig model is used to conduct a within-subject comparison of moments collected on the surface of the scalp and moments collected directly on the brain. In Part A (subsection 3.4.1), the experiments involved manipulating the extracerebral layer to cause perturbations in both scalp blood flow and the extracerebral optical properties (by surgically altering the ECL composition). In Part B (subsection 3.4.2), DCE-NIR measurements are acquired directly on the brain and contralaterally on the scalp during normocapnia and hypocapnia—the latter causes CBF to

decrease. Concomitant measurements were acquired by CT perfusion (CTP) for comparison.

3.2. Theory

3.2.1. Statistical moments of distributions of times-of-flight

Time-resolved NIR techniques measure the times-of-flight of individual photons at each detector over a few hundred milliseconds, building a histogram that approximates a distribution function. It has been demonstrated theoretically (Zaccanti *et al* 1995) and experimentally (Steinbrink *et al* 2001) that later time-bins correspond to a group of photons are statistically more likely to have interrogated deeper tissue structures. Therefore, changes in absorption of light in brain tissue, for example following the injection of dye, will differentially affect certain time bins in the DTOF. A transformation can be written as follows:

$$\Delta N_i = \sum_j A_{i,j} \cdot \Delta \mu_{a,j}, \tag{3.1}$$

where ΔN_i is the change in the number of photons occurring in the i^{th} time-bin of the DTOF, $\Delta \mu_{a,j}$ is the change in absorption coefficient in the j^{th} layer, and $A_{i,j}$ is the sensitivity matrix describing the transformation between these two functions. Since the experimentally measured DTOF is in reality a convolution between ΔN_i and the instrument response function (IRF), direct analysis of the DTOF is challenging (Diop *et al* 2012). A simpler approach is to use statistical moments, m_k, of the DTOF:

$$m_k(t) = \int_{t_1}^{t_2} t^k N(t) dt, \tag{3.2}$$

where k is the order of the moment, and t_1 and t_2 are temporal integration limits. This approach reduces the dimension of the problem in Eq. 3.1, and

the change in normalized moments is independent of the IRF (Liebert *et al* 2004). Furthermore, it has been demonstrated previously that higher-order moments are more sensitive to changes occurring in deeper tissues (Liebert *et al* 2004). A similar transformation to Eq. 3.1 can be written:

$$\Delta m_k = \sum_j A_{k,j} \cdot \Delta \mu_{a,j}, \tag{3.3}$$

where $A_{k,j}$ is the sensitivity matrix describing transformation between a change in the k^{th} moment and the change in absorption coefficient occurring in the j^{th} layer. The changes in three moments are used to describe the time-dependent changes that occur in the head following a bolus injection of dye: attenuation, A, which is related to the zeroth moment, mean time of flight, $\langle t \rangle$, and variance of the DTOF, V. The mathematical definitions of these moments and the sensitivity factors corresponding to the change in these moments are given in Table 3.1. Sensitivity factors can be determined with analytical (Kacprzak *et al* 2007) or Monte Carlo based methods (Steinbrink *et al* 2001; Liebert *et al* 2003); the latter was used for this study.

Table 3.1: Definitions of statistical moments

Name	Related moment	Formula	Sensitivity factor
Attenuation	zeroth moment (area under the curve)	$A = \ln(m_0)$	MPP
Mean time of flight	first normalized moment	$\langle t \rangle = m_1/m_0$	MTSF
Variance	second centralized moment	$V = m_2/m_0 - (m_1/m_0)^2$	VSF

The three moments used in DTOF analysis, along with their formulae and the abbreviations for their sensitivity factors. *MPP, mean partial pathlength; MTSF, mean time-of-flight sensitivity factor; VSF, variance sensitivity factor.*

3.2.2. Indicator dilution theory

The previous section provides the mathematical basis for understanding how a change in the absorption coefficient of underlying tissues will produce a change in the measured moments. With dynamic contrast-enhanced techniques, this change in absorption is caused by the injection of an exogenous dye. If all other chromophores are assumed constant for the period of time required to collect a measurement, then the change in absorption coefficient in a tissue of interest as a function of time, T, is related to the tissue dye concentration, C, by

$$\Delta\mu_a(T) = C(T) \cdot \varepsilon \cdot \ln(10), \tag{3.4}$$

where ε is the wavelength-dependent extinction coefficient of the dye. Following a bolus injection into a peripheral vein, the dye is delivered first to the heart, where it is subsequently pumped though the arterial circulatory system to all tissues of the body. According to the convolution theorem (Meier and Zierler 1954), the time-dependent tissue dye concentration is given by:

$$C(T) = F \cdot \int_0^T C_a(u) \cdot R(T-u)du, \tag{3.5}$$

where F is blood flow, $C_a(T)$ is the time-dependent arterial concentration of dye (*i.e.*, the AIF), and $R(T)$ is referred to as the impulse residue function. $R(t)$ represents the fraction of dye remaining in the tissue at time, T, following an idealized bolus injection. The convolution theorem can be derived from the Fick Principle and a previous publication provides additional details of this derivation (Elliott *et al* 2011). The function $C_a(T)$ is common to all tissue regions in the body, while in contrast, $R(T)$ and F are specific to each tissue region. Therefore, if $C(T)$ is characterized from signal containing information from multiple regions of tissue, F and $R(T)$ are in reality a weighted average of the tissue-specific functions represented in the

probed region. In the case that the region-of-interrogation contains multiple layers of tissue, a more rigorous expression is found by combining Eqs. 3.3 and 3.4 with the convolution in Eq. 3.5, yielding the moment-specific solution:

$$\Delta m_k(T) = \sum_j F_j \cdot \varepsilon \cdot \ln(10) \cdot A_{k,j} \int_0^T C_a(u) \cdot R_j(T-u)du. \qquad (3.6)$$

This convolution describes the fundamental relationship between the behavior of contrast agent in the tissue and the measured change in DTOF moments.

3.2.3. Quantification of blood flow changes

In this paper, we investigated two different approaches of measuring change in CBF: the time-to-peak method and the relative deconvolution method. The time-to-peak of the tissue function, TTP_C, is defined as the time elapsed between the first appearance of dye, T_0, and the peak concentration of dye, T_{max} (Fig. 3.1).

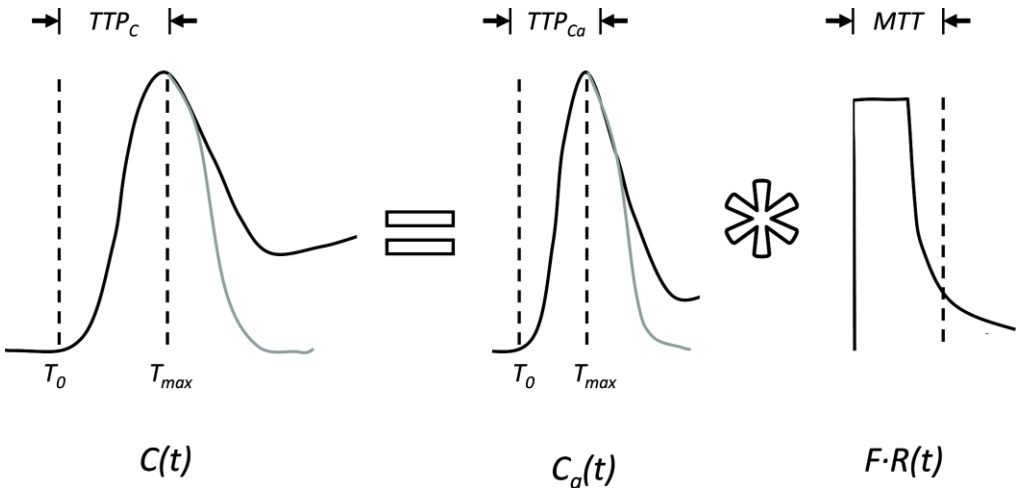

Figure 3.1: Time-to-peak analysis

A depiction of the time-to-peak (TTP) method. Hypothetical tissue and arterial concentration curves including the effects of dye recirculation are shown by the solid black lines, along with their corresponding TTP values (TTP_C and TTP_{Ca}, respectively). The solid grey lines represent the first moments of the concentration curves without the effects of recirculation.

The time-to-peak can be related to CBF using the first moments of the tissue and arterial concentration curves. A property of a convolution is that the first moments are additive (Jaynes 2003) and, therefore, Eq. 3.5 can be written as:

$$\langle t \rangle_C = \langle t \rangle_{Ca} + MTT. \tag{3.7}$$

The mean transit time (MTT), which is the first moment of the flow-scaled *R(t)*, is equal to *CBF/CBV* by the central volume principle (Meier and Zierler 1954). Typically, tissue and arterial functions can be approximated by gamma variate functions (Thompson *et al* 1964). However, over the interval $T_0 < t \leq T_{max}$, these functions can be approximated by a symmetrical function, such as a Gaussian. In this case, the first moment equals the time-to-peak: $\langle t \rangle_C = TTP_C$ and $\langle t \rangle_{Ca} = TTP_{Ca}$. Eq. 3.7 can be rewritten as:

$$TTP_C = TTP_{Ca} + \frac{CBV}{CBF}. \tag{3.8}$$

Note that TTP_C not only depends on CBF, but also on CBV and TTP_{Ca}. Therefore, the influence of initial values of these two parameters must be considered when interpreting the relative change in TTP_C.

An alternative approach to characterizing the DCE curves is to perform a deconvolution to recover a relative blood flow index, *dBF*, representing the scalar quantity defined by the summation in Eq. 3.6. Generally, *dBF* for the k^{th} moment is

$$dBF_k = \sum_j F_j \cdot \varepsilon \cdot \ln(10) \cdot A_{k,j}. \tag{3.9}$$

It has been suggested that the variance of measurements acquired on the scalp has greater sensitivity to brain tissue and the influence of the extra-

cerebral layers is relatively small (Liebert *et al* 2004). If this is the case, the variance sensitivity factors for the extracerebral layers are approximately zero and the summation in Eq. 3.9 collapses to:

$$dBF_{\Delta V} \approx CBF \cdot \varepsilon \cdot \ln(10) \cdot VSF, \tag{3.10}$$

where VSF is the sensitivity factor for the brain layer. If VSF remains constant between measurements, the change in dBF equals the true change in CBF (ΔCBF). To recover dBF, an algorithm incorporating physiologically derived constraints was used to stabilize the deconvolution, which is an inherently unstable process. This algorithm has been described and validated previously, both for CT perfusion (Cenic *et al* 1999), and near-infrared techniques in neonatal models (Brown *et al* 2002; Diop *et al* 2010b) as well as in more complex multi-regional scenarios (Elliott *et al* 2010; Elliott *et al* 2012).

3.2.4. Influence of CBV and AIF on time-to-peak measurements

A series of numerical simulations were performed to determine the effect of CBV and AIF on the relationship between ΔTTP_C and ΔCBF. To investigate the effect of CBV, cerebral blood volume was related to cerebral blood flow according to the Grubb relationship (Grubb *et al* 1974):

$$CBV = g \cdot CBF^{\gamma}. \tag{3.11}$$

where g and γ are empirically derived parameters. Values for g and γ are described in the rhesus monkey as 0.8 and 0.38 (Grubb *et al* 1974), and similar CBV values have been measured in humans (Grubb *et al* 1977). For the simulations, g was set to 0.8 and γ varied between 0.2 and 0.6 to investigate how the relationship between ΔTTP_C and ΔCBF (Eq. 3.8) was affected by changes in CBV. In these simulations, TTP_{Ca} was set to zero, which represents the ideal case where the arterial input function is a Dirac

delta function. The results are summarized in Fig. 3.2A. Similarly, the effect of TTP_{Ca} on Eq. 3.8 was performed by setting $\gamma = 0.38$ and varying TTP_{Ca} from 0 to 6 seconds. These results are summarized in Fig. 3.2B.

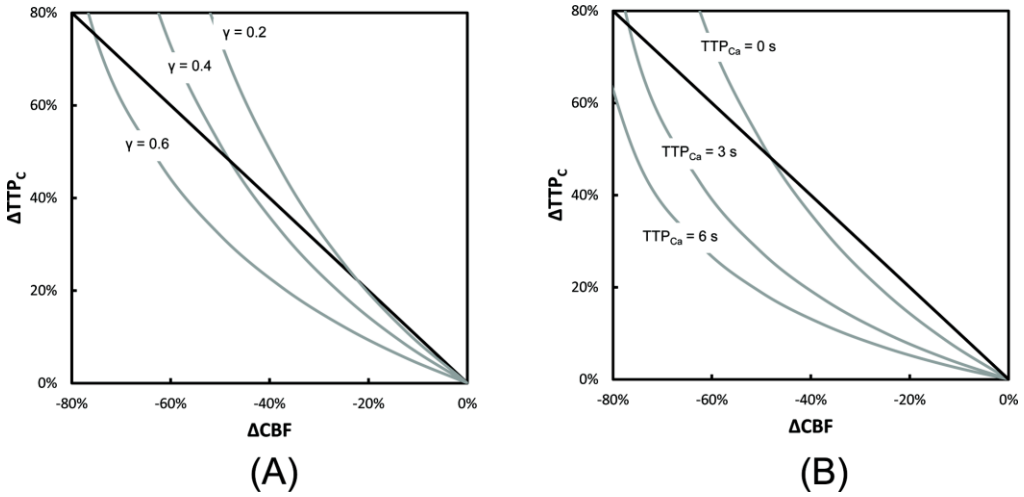

Figure 3.2: Effect of CBV and AIF on TTP analysis.

The relationship between changes in tissue-curve TTP (ΔTTP_C) and changes in CBF (ΔCBF) (grey lines). (A) The effect of varying the relationship between CBV and CBF, which was performed using the Grubb relationship for γ = 0.2, 0.4 and 0.6, and setting TTP_{Ca} = 0. (B) The effect of varying the arterial TTP (TTP_{Ca}) from 0 to 6 s with γ set to 0.38. The solid lines show the negative unity slope for comparison.

The results of the simulations illustrated in Fig. 3.2 predict that the relationship between ΔTTP_C and ΔCBF can be strongly influenced by how CBV and CBF are related, and by the finite width of the AIF (*i.e.*, TTP_{Ca}).

3.3. Materials and methods

3.3.1. Instrumentation

A time-resolved near-infrared system, assembled in-house, was used for all optical measurements. A detailed description of this system and its characterization can be found in (Diop *et al* 2010b). Briefly, a picosecond diode laser light source (LDH-P-C-810, PicoQuant, Germany) emitting at 802 nm, close to the peak absorption wavelength of ICG, was used. The laser output was attenuated by a neutral density filter to below ANSI safety limits

for skin exposure (52.2 mW/cm^2 measured at fiber output compared to limit of 317 mW/cm^2 for 800 nm), and a pulse repetition rate of 80 MHz was used. The beam was coupled into a 1.5-m long multimode fiber (core = 400 µm and N.A. = 0.22; Fiberoptics Technology, Pomfret, CT) and directed onto the scalp. Photons exiting the tissue were collected by a fibre bundle 1.5 m long. The proximal end of the bundle was placed on scalp to provide measurements at a source-detector distance of 30 mm. The source and detector light-guides were held in place using a probe holder, constructed from black polychloroprene rubber. The distal end of the collection optode was secured in front of an electromechanical shutter (SM05, Thorlabs, Newton, NJ). Light transmitted through the shutter was passed through a bandpass filter (FEB800-10, Thorlabs) to remove fluorescence emission, before being collected by a Peltier-cooled photomultiplier tube (PMT). A photon count rate corresponding to roughly 1% of the laser repetition rate was used.

3.3.2. Animal experiments

All animal experiments were conducted following the guidelines of the Canadian Council on Animal Care and approved by the Animal Use Subcommittee at the University of Western Ontario (AUP #2007-050-06). Duroc x Landrace crossbred pigs (n = 4) were acquired from a local supplier on the morning of the experiment. Animals were anesthetized with 1.75-3% isofluorane, tracheotomized and mechanically ventilated on an oxygen/medical air mixture. A femoral artery was catheterized to monitor heart rate and blood pressure and to collect blood gas samples. Body temperature was maintained between 37.5 and 38.5°C throughout the experiment.

Following a 1-h stabilization period, the rubber probe holder was placed on the head and fixed in place with tissue glue (Vetbond™ 1469SB, 3M Health Care, St. Paul, MN). The respiration rate, anesthetic levels and

glucose levels were closely monitored and adjusted to ensure that physiological parameters remained stable throughout the experiment.

All four animals were included in Part A (*i.e.*, the manipulation of the extracerebral layers) and two animals were included in Part B (*i.e.*, the manipulation of CBF). In Part A, two sets of time-resolved measurements during inflow and washout of ICG (0.1 mg/kg, Cardiogreen, Sigma-Aldrich, St. Louis, MO) were acquired on the surface of the head. All measurements were separated by a delay of 20 min to allow sufficient time for clearance of the dye. After these scalp measurements, three incisions were made around the probe holder to reduce scalp blood flow. The tissue medial to the probe holder was left intact and the three incisions were cauterized to stop bleeding. Two sets of measurements were acquired under this ischemic scalp condition. After the exact position of the probe holder was marked, the underlying scalp was removed using the probe holder as a guide. Two measurements were acquired directly on the skull of the animals at approximately the same location as the previous measurements. Following the skull measurements, holes were carefully drilled through the skull in the same locations. Probes were inserted into the holes until they rested directly on the dura matter. In this way, two sets of time-resolved measurements were acquired on the brain.

In Part B, time-resolved measurements were acquired directly on the brain and then concomitantly on the contralateral scalp during normocapnia and hypocapnia. Hypocapnia was achieved by adjusting the respiration rate on the mechanical ventilator until blood CO_2 concentration reached 25 mmHg. Computed tomography perfusion measurements were acquired using a CT scanner (LightSpeed QXi, GE Healthcare, Milwakee, WI) during normocapnia and hypocapnia. Each cine scan (80 kVp, 190 mA) was acquired for 40 s following injection of the contrast agent (1.0 ml/kg of 300 mg/ml 300-Isovue, Bracco Diagnostics Inc., Princeton, NJ) at an injection rate of 1 ml/s.

Eight coronal slices (5 mm thick, temporal resolution of 1 s) were used to generate CBF maps using CT Perfusion 4 software (GE Healthcare). Region-of-interests were drawn encompassing the cortical tissue of each hemisphere which approximate the region interrogated by the NIR light.

3.3.3. Data processing

Data processing was performed in the MATLAB programming environment (MathWorks, Natick, MA). Prior to the analysis, the DTOFs of diffusely reflected photons were denoised using a three-step method which uses an Anscombe transformation, followed by wavelet denoising and then subsequent inverse Anscombe transformation, as described previously (Diop *et al* 2012). Denoising was done to reduce the susceptibility of higher moments to noise-related artifacts. Statistical moments were calculated from the denoised datasets using a previously described approach (Liebert *et al* 2003). For calculating the moments, the upper integration limit was defined on the level of 5% of the maximum of the DTOF in order to reduce the influence of any remaining noise. Following subtraction of IRF contribution, moments were smoothed using the Savitzky-Golay algorithm (11.6 second window span, 6^{th} order polynomial) to remove high-frequency components not related to dye kinetics.

Attenuation and variance of the DTOFs were analyzed using the time-to-peak method and the kinetic deconvolution method. When presenting the percent change in TTP, values were multiplied by −1 to facilitate comparison with the other indices. These four values were obtained for all time-resolved measurements. For Part A, analysis of differences between groups was performed using SPSS 17.0 (IBM, Armonk, NY). Statistical significance was considered to be $p < 0.05$.

3.4. Results

3.4.1. Part A: Extracerebral manipulations

During these experiments, the extracerebral environment was manipulated in several ways to demonstrate the sensitivity of the measured parameters to perfusion changes in the different layers. Blood flow indices were determined under four conditions: (i) baseline, (ii) following partial scalp ischemia, (iii) probes placed on the skull, and (iv) probes placed directly on the brain (17 datasets were collected from 4 animals). The shape of the tissue concentration curves acquired on the scalp showed large differences between the different moments of DTOFs (A, $<t>$ and V). Furthermore, the higher order moments showed less variability when the extracerebral layer was manipulated compared to attenuation. Figure 3.3 shows the attenuation ICG curves and the variance ICG curves for one animal under the four conditions. This representative example was typical of all animals. Figure 3.3C shows the similarity between the ICG curves derived from the scalp variance measurements and the brain attenuation measurements.

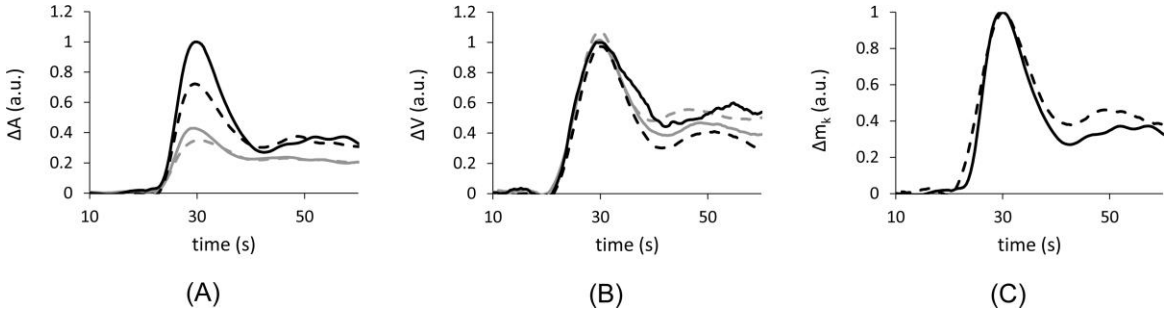

Figure 3.3: Dynamic contrast-enhanced curves during ECL manipulation

Representative curves from one animal (pig #2) under the four conditions. In this case, the thickness of the extracerebral layer was 10.2 mm. (A) Change in attenuation (ΔA) for measurements made on intact scalp (solid grey), ischemic scalp (dashed grey), skull (dashed black) and brain (solid black). (B) Change in variance (ΔV) for the same conditions. (C) ΔA measured on the brain (solid black) compared with ΔV measured on the scalp (dashed black). Curves are normalized to brain curve.

In terms of the qualitative blood flow indices (*TTP* and *dBF*) calculated from changes in attenuation (ΔA) and variance (ΔV) of the DTOF, Figure 3.4 summarizes the percent difference between the measurements under the three extracerebral manipulations and the measurement directly on the brain. From the ΔA measurements, the average difference was −47.9 ± 7.8% for *dBF* and −8.0 ± 6.31% for TTP. From the ΔV measurements, the average difference was −0.2 ± 2.43% for dBF and by −3.5 ± 2.22% for *TTP*. The values for ΔV *TTP*, ΔV *dBF*, and ΔA *TTP* were not significantly different, but ΔA *dBF* was significantly lower than the other three parameters ($p < 0.001$).

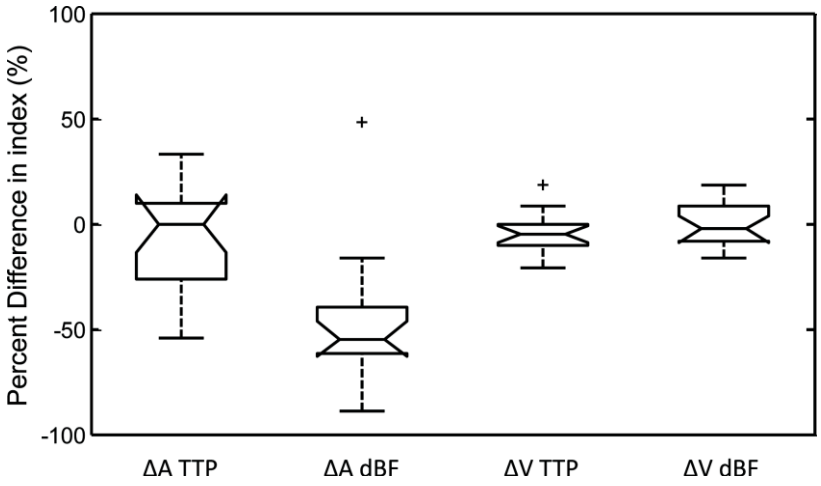

Figure 3.4: Variations in blood flow indices during ECL manipulation.

Box-and-whisker plot of the difference in measured blood flow indices during the extracerebral manipulations compared to measurements acquired on the brain. Each parameter was evaluated from seventeen measurements acquired in four pigs. Boxes are bound by 1st and 3rd quartiles, with the center line indicating the median. Error bars represent the range of the data, and crosses signify outliers. Only ΔA *dBF* was significantly different from the expected change of zero ($p < 0.001$). Additionally, none of ΔA *TTP*, ΔV *TTP*, or ΔV *dBF* differed significantly from each another, as measured by a paired t-test.

3.4.2. Part B: Hypocapnic challenge

To augment the results of Part A, we further analyzed the sensitivity of the attenuation and variance *TTP* and *dBF* measurements to reductions in CBF caused by hypocapnia. Sequential bilateral measurements were made in two animals during normocapnia and hypocapnia. On the ipsilateral side,

measurements were made directly on the brain and on the contralaterial side, measurements were made on the scalp. A reduction in CBF was observed during hypocapnia as depicted by the CBF maps generated by CT perfusion (Fig. 3.5).

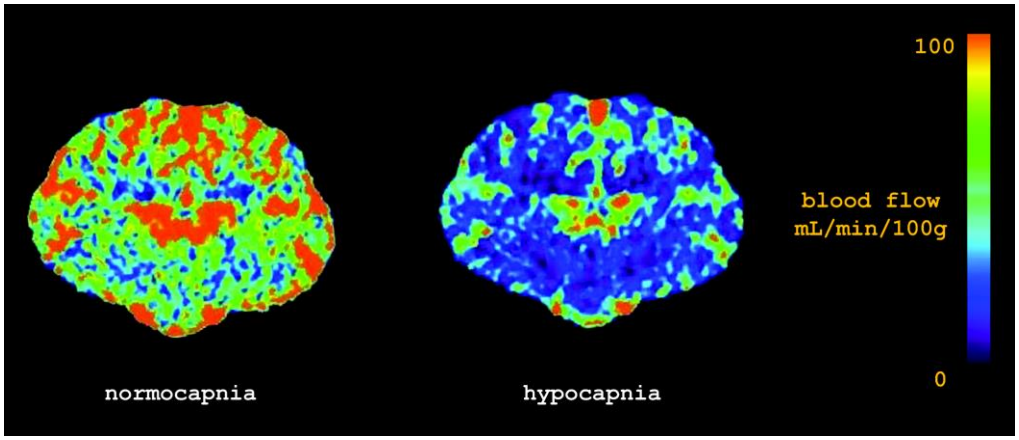

Figure 3.5: CT perfusion maps during normocapnia and hypocapnia

CT perfusion images of the brain from one animal during normocapnia and hypocapnia. The mean reduction in global CBF during hypocapnia was 43% in this case.

Qualitatively, a large reduction of amplitude was also observed in ΔV from the DTOFs measured on the contralateral site that reflected ΔA measured directly on the brain. There was also a decrease in ΔA measured on the scalp; however, it was less marked. Figure 3.6 provides a representative example of the ΔA and ΔV ICG curves during normo- and hypo- capnia.

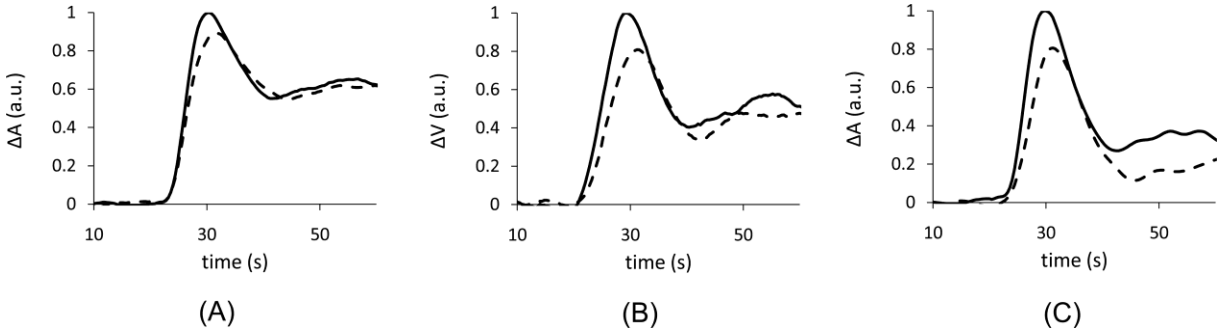

Fig. 3.6: Dynamic contrast-enhanced curves during hypocapnia

Representative curves from one animal under normocapnia (solid lines) and hypocapnia (dashed lines). (A) The change in attenuation (ΔA) made on intact scalp for the two

conditions. (B) The change in variance (ΔV) made on intact scalp for the two conditions. (C) ΔA measured directly on the brain for the two conditions. Note: curves have been normalized to the maximum of the normocapnia curve.

Table 3.2 summarizes the hypocapnic changes CBF and scalp blood flow measured by CT perfusion and the corresponding quantitative NIRS blood flow indices from the two animals. As a reference, the values obtained with the NIRS indices were compared to CBF values obtained by CT perfusion—the current clinical standard-of-care.

Table 3.2: Comparison of TTP and dBF changes during hypocapnia

	Animal #1		*Animal #2*	
	Percent Change	Error	Percent Change	Error
		Ipsilateral (brain)		
CTP brain	−32.0%	-	−44.4%	-
CTP scalp	-	-	-	-
ΔA TTP	−16.7%	15.3%	10.5%	54.9%
ΔV TTP	−21.1%	10.9%	4.5%	48.9%
ΔA dBF	−28.0%	3.9%	−45.5%	−1.1%
ΔV dBF	−31.6%	0.4%	−42.3%	2.1%
		Contralateral (scalp)		
CTP brain	−31.7%	-	−42.2%	-
CTP scalp	−19.1%	-	−29.3%	-
ΔA TTP	−16.7%	15.1%	−22.2%	20.0%
ΔV TTP	−20.0%	11.7%	−26.3%	15.9%
ΔA dBF	−20.9%	10.9%	−27.4%	14.8%
ΔV dBF	−31.6%	0.1%	−42.7%	−0.5%

Percent change in the blood flow indices (*TTP* and *dBF*) obtained by analysis of attenuation (ΔA) and variance (ΔV) of DTOF during hypocapnia. Measurements were obtained directly on the brain and on the contralateral scalp. The error values are relative to the CBF change measured by CT perfusion (CTP). The thickness of the extracerebral layer was 10.2 mm and 11.2 mm for animal 1 and 2, respectively.

3.5. Discussion

A number of recent studies have suggested that the DTOF variance signal collected on the scalp is sensitive to decreased CBF in neurological disorders such as stroke (Steinkellner *et al* 2010; Liebert *et al* 2005). The principle objective of this study was to verify these findings in an adult pig model in which scalp and cerebral blood flow could be manipulated. The results of Part A indicated that the ΔV signal was less sensitive to the extracerebral layer than the corresponding ΔA signal, as demonstrated by the greater variability in the shape of the ΔA ICG concentration curves over the different manipulations of the extracerebral layers. In general, the dynamics of the ΔA ICG curves reflected flow contributions from both scalp and brain. The curves shown in Fig. 3.3 illustrate that the ΔA signal acquired under the ischemic scalp condition resulted in the slowest kinetics, whereas the ΔA signal acquired directly on the brain have the fastest. The ΔA signals collected on the skull and the intact scalp demonstrated intermediate kinetics. The former was the most similar to the brain ICG curve since the thickness of the skull in this animal was only about 5 mm. Interestingly, the shape of the ΔA ICG curve acquired on the intact scalp was more similar to the ΔA signal collected on the skull rather than the signal acquired from ischemic scalp, despite the fact that the thickness of the extracerebral layer approximately doubled.

The influence of the extracerebral layer on the shape of the ΔA ICG curve is also reflected in the *TTP* and *dBF* measurements shown in Figure 3.4. In both cases, the increased variability was not due to increased measurement error, but rather, it was attributed to the different flow contributions under the four conditions. The *dBF* measurements determined from the ΔA ICG curves that included an extracerebral layer were also consistently lower than the value determined from the brain ICG curve. This is because ΔA *dBF* represents a weighted average of the blood flow in each

layer scaled by its mean partial pathlength. Therefore, the addition of each extracerebral layer resulted in a reduction in average blood flow within the region of interrogation

The faster ICG dynamics for the ΔA signal collected on the intact scalp would appear to be at odds with previous studies involving human subjects, in which a large difference in the shape of the ΔA and ΔV ICG curves was reported (Liebert *et al* 2004; Steinkellner *et al* 2010; Liebert *et al* 2006). This apparent discrepancy can be attributed to differences in head anatomy between pigs and humans. We found that the pig's scalp was highly vascularized and well perfused, likely to supply the thick temporalis muscles that originate at the temporoparietal region of the head. This observation was confirmed by CT perfusion, which revealed an average scalp blood flow of approximately 25 ml min^{-1} $100g^{-1}$. In contrast, scalp blood flow in the human head, as determined by a radioactive xenon clearance technique, was only about 5 ml min^{-1} $100g^{-1}$ (Friberg *et al* 1986). Given this difference, the ischemic scalp condition in Part A more closely reflects the intact human scalp.

In contrast to the ΔA signals, the ΔV ICG curves shown in Fig. 3.3B exhibited less sensitivity to the extracerebral tissue. In this case, there was a noticeable improvement in the similarity of the ICG curves acquired under the two extremes—*i.e.*, on the brain and on the ischemic scalp—compared to the ICG curves obtained from the ΔA signal. This insensitivity to the top layers was also reflected in the lower variability observed in the ΔV *TTP* and *dBF* values across the four conditions, as shown in Fig. 3.4. As well, the underestimation of CBF by ΔA *dBF* was not observed when *dBF* was determined from the ΔV signals.

A secondary objective of this study was to compare two analytical methods of tracking change in CBF from the measured DTOF moments. The

metric of choice in these studies has been time-to-peak, since it is relatively easy to calculate, and can be applied to normalized signals of variance of the DTOF. The ability to use the normalized signal makes *TTP* a robust longitudinal tool because it will be relatively insensitive to small changes in the signal amplitude, for example, from light coupling issues. This is a major benefit when using time-resolved equipment that is sensitive to light coupling and noise; however, time-to-peak also has some drawbacks that may not always be appreciated. In particular, a limitation of the TTP method is the implicit assumption that the AIF is consistent from measurement to measurement. In a clinical environment, it may be difficult to achieve an AIF of reproducible shape, since bolus injections are operator dependent, and the AIF depends on the cardiac output of the patient. For example, in the ipsilateral measurements acquired from animal #2 (Table 3.2), *TTP* measurements did not correctly identify the large decrease in CBF. Further investigation revealed that the arterial *TTP* changed in the opposite direction by 30%, obscuring the expected change in tissue *TTP* caused by hypocapnia. After adjusting the tissue *TTP* value to account for the unexpected change in arterial *TTP*, the change in ΔV *TTP* was −13.6% instead of 4.5%. In certain applications, such as inter-hemisphere comparisons in stroke patients, the absolute change in *TTP* (as opposed to the percent change in *TTP*) is independent of the arterial input function (Steinkellner *et al* 2010). However, when percent change in *TTP* is used as a surrogate of percent change in CBF across serial injections of ICG, any variability in the arterial input function, including systemic physiological changes, will have a dramatic effect on the accuracy of the measurement.

Another important consideration with using the time-to-peak method as a surrogate CBF is that it also depends on CBV and the time-to-peak of the AIF (Eq. 3.8). Therefore, it exhibits a non-linear relationship with CBF. The numerical simulations depicted in Fig. 3.2 demonstrate how the

relationship between ΔCBF and ΔTTP can be altered by both the relationship between CBV and CBF (the Grubb relationship) and the finite width of the AIF. In these simulations, both effects cause the measured ΔTTP to be underestimated relative to the true change in CBF. Interestingly, when CBF decreases by about 80%, which would be similar to the expected perfusion reduction during clinical ischemia, this error is not as severe.

An alternative method to analyzing DCE data is derived from the convolution theory of tracer kinetics. If the AIF is measured, a deconvolution method can be used to recover the blood flow index, *dBF*, which is equal to the average blood flow in the region of interrogation weighted by the layer-specific sensitivity factor (Eq. 3.9). In addition to accounting for variability in the AIF, the deconvolution method also decouples the effects of blood flow, blood volume and mean transit time. When ΔA is measured in the intact head, the acquired signal is highly sensitive to extracerebral tissue, and the average blood flow recovered by deconvolution will represent a weighted average of scalp and cerebral blood flow as shown in Fig. 3.4. In contrast, the region of interrogation represented in the ΔV signal has greater sensitivity to brain tissue and, therefore, the change in *dBF* better reflects the true change in CBF. Note that this relative approach is in contrast to previous methods that recover absolute CBF from time-resolved measurements acquired directly from the brain, or in a scenario where the scalp contribution is negligible. In these special cases, deconvolution of the ΔA signal permits recovery of absolute CBF in units of ml $min^{-1}100g^{-1}$, since the differential pathlength can be measured directly from the time-resolved data (Diop *et al* 2010a).

In Part B, concomitant measurements were acquired on the ipsilateral brain and the contralateral scalp during normocapnia and hypocapnia in two animals. In addition, CT perfusion measurements were acquired under the two conditions to measure scalp and cerebral blood flow. Table 3.2

summarizes the percent change in *TTP* and *dBF* caused by hypocapnia for both animals. Despite a small sample size, three observations can be made about these results. First, all four ΔV *dBF* values and the two ΔA *dBF* values derived from ispilateral measurements exhibited good agreement with the CBF values from CT perfusion. Second, contralateral ΔA *dBF* measurements were almost identical to the scalp blood flow values from CT perfusion. When considered along with the results of Part A, this suggests that ΔA is mainly interrogating the extracerebral layer, while ΔV is sensitive to the brain. Finally, all eight TTP measurements (when the corrected TTP measurement for animal #2 as described above is substituted), showed a consistent underestimation of the CBF change measured by CT perfusion. This underestimation occurred whether the measurements were acquired on the scalp or directly on the brain. The numerical simulations presented in subsection 3.2.4 provide insight into this underestimation: the average arterial TTP in the animal experiments was about 4 seconds and the Grubb exponent, γ, was about 0.4 (determined from the CT perfusion data). For this combination, a 40% decrease in CBF is predicted to result in a roughly 20% change in TTP.

3.6. Conclusions

The salient finding of this study was that the variance of the DTOF was relatively insensitive to changes in extracerebral blood flow and optical properties caused by physically manipulating the extracerebral layers in the pig. A corollary finding was that the variance signal measured on the scalp was sensitive to changes in CBF. Finally, while both *TTP* and *dBF* obtained from the variance signal showed similar robustness in the presence of extracerebral variability, *dBF* had better sensitivity to hypocapnic CBF changes when compared to CT perfusion. This improvement suggests a benefit to measuring the AIF during acquisition of DCE time-resolved data. Despite differences in scalp blood flow in this animal model compared to

humans, the methods presented in this study for measuring CBF changes are translatable to the human adult.

3.7. References

Brown DW, Picot PA, Naeini JG, Springett R, Delpy DT, Lee T-Y 2002 Quantitative near infrared spectroscopy measurement of cerebral hemodynamics in newborn piglets *Pediatr Res* 51 564-570.

Cenic A, Nabavi DG, Craen RA, Gelb AW, Lee TY 2000 A CT method to measure hemodynamics in brain tumors: validation and application of cerebral blood flow maps *Am J Neuroradiol* 21 462–70.

Cenic A, Nabavi DG, Craen RA, Gelb AW, Lee T-Y 1999 Dynamic CT measurement of cerebral blood flow: a validation study *Am J Neuroradiol* 20 63-73.

Cope M 1991 The application of near infrared spectroscopy to non invasive monitoring of cerebral oxygenation in the newborn infant *Ph.D. thesis* (University College London, London, U.K.) p 290.

Diop M, Lawrence KS 2012 Deconvolution method for recovering the photon time-of-flight distribution from time-resolved measurements *Opt Lett* 37 2358-2360.

Diop M, Tichauer KM, Elliott JT, Migueis M, Lee T-Y, St Lawrence K 2010a Comparison of time-resolved and continuous-wave near-infrared techniques for measuring cerebral blood flow in piglets *J Biomed Opt* 15 057004.

Diop M, Tichauer KM, Elliott JT, Migueis M, Lee T-Y, St. Lawrence K 2010b Time-resolved near-infrared technique for bedside monitoring of absolute cerebral blood flow *Proc. of SPIE* 7555 75550Z.

Diop M, Elliott JT, Tichauer KM, Lee T-Y, St Lawrence K 2009 A broadband continuous-wave multichannel near-infrared system for measuring regional cerebral blood flow and oxygen consumption in newborn piglets," *Rev Sci Instrum* 80(5) 054302.

Elliott JT, Diop M, Lee T-Y, Lawrence KS 2012 Model-independent dynamic constraint to improve the optical reconstruction of regional kinetic parameters *Opt Lett* 37 2571-2573.

Elliott JT, Diop M, Tichauer KM, Lee T-Y, St. Lawrence K 2011 Monte Carlo based modeling of indocyanine green bolus tracking in the adult human head *Proc. of SPIE* 7896 78960E.

Elliott JT, Diop M, Tichauer KM, Lee T-Y, St Lawrence K 2010 Quantitative measurement of cerebral blood flow in a juvenile porcine model by depth-resolved near-infrared spectroscopy *J Biomed Opt* 15 037014.

Fabbri F, Sassaroli A, Henry ME, Fantini S 2004 Optical measurements of absorption changes in two-layered diffusive media *Phys Med Biol* 49(7) 1183-1201.

Friberg L, Kastrup J, Hansen M, Bulow J 1986 Cerebral effects of scalp cooling and extracerebral contribution to calculated blood flow values using the intravenous 133Xe technique *Scand J Clin Lab Invest* 46, 375-379.

Garski TR, Staller BJ, Hepner G, Banka VS, Finney RA, Jr. 1978 Adverse reactions after administration of indocyanine green *JAMA* 240(7) 635

Gora F, Shinde S, Elwell CE, Goldstone JC, Cope M, Delpy DT, M. Smith M 2002 Noninvasive measurement of cerebral blood flow in adults using near-infrared spectroscopy and indocyanine green: a pilot study *J Neurosurg Anesthesiol* 14 218-222.

Grubb RL, Raichle ME, Eichling JO, Ter-Pogossian MM 1974 The effects of changes in PaCO2 on cerebral blood volume, blood flow, and vascular mean transit time *Stroke* 5 630-639.

Grubb RL, Raichle ME, Eichling JO, Gado MH 1977 Effects of subarachnoid hemorrhage on cerebral blood volume, blood flow, and oxygen utilization in humans *J Neurosurg* 46 446-453.

Hiraoka M, Firbank M, Essenpreis M, Cope M, Arridge SR, van der Zee P, Delpy DT 1993 A Monte Carlo investigation of optical pathlength in inhomogeneous tissue and its application to near-infrared spectroscopy *Phys Med Biol* 38(12) 1859-1876.

Hongo K, Kobayashi S, Okudera H, Hokama M, Nakagawa F 1995 Noninvasive cerebral optical spectroscopy: depth-resolved measurements of cerebral haemodynamics using indocyanine green *Neurol Res* 17(2) 89-93.

Jaynes ET 2003 Probability Theory: The Logic of Science (Cambridge University Press, Cambridge, UK).

Jelzow A, Wabnitz H, Obrig H, Macdonald R, Steinbrink J 2012 Separation of indocyanine green boluses in the human brain and scalp based on time-resolved in-vivo fluorescence measurements *J Biomed Opt* 17 057003.

Kacprzak M, Liebert A, Sawosz P, Zolek N, Maniewski R 2007 Time-resolved optical imager for assessment of cerebral oxygenation *J Biomed Opt* 12 034019.

Kohl-Bareis M, Obrig H, Steinbrink J, Malak J, Uludag K, Villringer A 2002 Noninvasive monitoring of cerebral blood flow by a dye bolus method:

separation of brain from skin and skull signals *J Biomed Opt* 7(3) 464-470.

Kohno S, Miyai I, Seiyama A, Oda I, Ishikawa A, Tsuneishi S, Amita T, Shimizu K 2007 Removal of the skin blood flow artifact in functional near-infrared spectroscopic imaging data through independent component analysis *J Biomed Opt* 12(6) 062111.

Konstas AA, Goldmakher GV, Lee T-Y, Lev MH 2009 Theoretic basis and technical implementations of CT perfusion in acute ischemic stroke, part 2: technical implementations *AJNR Am J Neuroradiol* 30(5) 885-892.

Kuebler WM, Sckell A, Habler O, Kleen M, Kuhnle GE, Welte M, Messmer K, Goetz AE 1998 Noninvasive measurement of regional cerebral blood flow by near-infrared spectroscopy and indocyanine green *J Cereb Blood Flow Metab* 18 445-456.

Landsman ML, Kwant G, Mook GA, Zijlstra WG 1976 Light-absorbing properties, stability, and spectral stabilization of indocyanine green *J Appl Physiol* 40 575-583.

Leung TS, Tachtsidis I, Tisdall M, Smith M, Delpy DT, Elwell CE 2007 Theoretical investigation of measuring cerebral blood flow in the adult human head using bolus Indocyanine Green injection and near-infrared spectroscopy *Appl Opt* 46(10) 1604-1614.

Liebert A, Milej D, Wojciech W, Gerega A, Kacprzak M, Mayzner-Zawadzka E, Maniewski R 2012 Assessment of brain perfusion disorders by ICG bolus tracking with time-resolved fluorescence monitoring *Optical Society of America Technical Digest* BTu3A.20.

Liebert A, Wabnitz H, Obrig H, Erdmann R, Moller M, Macdonald R, Rinneberg H, Villringer A, Steinbrink J 2006 Non-invasive detection of fluorescence from exogenous chromophores in the adult human brain *Neuroimage* 31 600-608.

Liebert A, Wabnitz H, Steinbrink J, Moller M, Macdonald R, Rinneberg H, Villringer A, Obrig H 2005 Bed-side assessment of cerebral perfusion in stroke patients based on optical monitoring of a dye bolus by time-resolved diffuse reflectance *Neuroimage* 24 426-435.

Liebert A, Wabnitz H, Steinbrink J, Obrig H, Moller M, Macdonald R, Villringer A, Rinneberg H 2004 Time-resolved multidistance near-infrared spectroscopy of the adult head: intracerebral and extracerebral absorption changes from moments of distribution of times of flight of photons *Appl Opt* 43 3037-3047.

Liebert A, Wabnitz H, Grosenick D, Moller M, Macdonald R, Rinneberg H 2003 Evaluation of optical properties of highly scattering media by moments of distributions of times of flight of photons *Appl Opt* 42 5785-5792.

Matcher SJ, Cope M, Delpy DT 1994 Use of the water absorption spectrum to quantify tissue chromophore concentration changes in near-infrared spectroscopy *Phys Med Biol* 39(1) 177-196.

McCormick PW, Stewart M, Goetting MG, Dujovny M, G. Lewis G, Ausman, JI 1991 Noninvasive cerebral optical spectroscopy for monitoring cerebral oxygen delivery and hemodynamics *Crit Care Med* 19(1) 89-97.

Meier P, Zierler KL 1954 On the theory of the indicator-dilution method for measurement of blood flow and volume *J Appl Physiol* 6 731-744.

Muehlschlegel S, Lobato EB 2006 Con: all cardiac surgical patients should not have intraoperative cerebral oxygenation monitoring *J Cardiothorac Vasc Anesth* 20(4) 613-615.

Owen-Reece H, Elwell CE, Harkness W, Goldstone J, Delpy DT, Wyatt JS, Smith M 1996 Use of near infrared spectroscopy to estimate cerebral blood flow in conscious and anaesthetized adult subjects *Br J Anaesth* 76(1) 43-48.

Patel J, Marks K, Roberts I, Azzopardi D, Edwards AD 1998 Measurement of cerebral blood flow in newborn infants using near infrared spectroscopy with indocyanine green *Pediatr Res* 43(1) 34-39.

Rothoerl RD, Schebesch KM, Faltermeier R, Woertgen C, Brawanski A 2003 Lack of correlation between Xenon133 and near infrared spectroscopy/indocyanine green rCBF measurements *Neurol Res* 25(5) 528-532.

Saager RB, Berger AJ 2005 Direct characterization and removal of interfering absorption trends in two-layer turbid media *J Opt Soc Am A Opt Image Sci Vis* 22(9) 1874-1882.

Schytz HW, Wienecke T, Jensen LT, Selb J, Boas DA, Ashina M 2009 Changes in cerebral blood flow after acetazolamide: an experimental study comparing near-infrared spectroscopy and SPECT *Eur J Neurol* 16(4) 461-467.

Springett R, Sakata Y, Delpy DT 2001 Precise measurement of cerebral blood flow in newborn piglets from the bolus passage of indocyanine green *Phys Med Biol* 46(8) 2209-2225.

Steinbrink J, Wabnitz H, Obrig H, Villringer A, Rinneberg H 2001 Determining changes in NIR absorption using a layered model of the human head *Phys Med Biol* 46 879-896.

Steinkellner O, Gruber C, Wabnitz H, Jelzow A, Steinbrink J, Fiebach JB, Macdonald R, Obrig H 2010 Optical bedside monitoring of cerebral perfusion: technological and methodological advances applied in a study on acute ischemic stroke *J Biomed Opt* 15 061708.

Strangman G, Franceschini MA, Boas DA 2003 Factors affecting the accuracy of near-infrared spectroscopy concentration calculations for focal changes in oxygenation parameters *Neuroimage* 18(4) 865–879.

Stiefel MF, Udoetuk JD, Spiotta AM, Gracias VH, Goldberg A, Maloney-Wilensky E, Bloom S, Le Roux PD 2006 Conventional neurocritical care and cerebral oxygenation after traumatic brain injury *J Neurosurg* 105(4) 568-575.

Tachtsidis I, Tisdall MM, Leung TS, Pritchard C, Cooper CE, Smith M, Elwell CE 2009 Relationship between brain tissue haemodynamics, oxygenation and metabolism in the healthy human adult brain during hyperoxia and hypercapnea *Adv Exp Med Biol* 645 315-320.

Terborg C, Birkner T, Schack B, Weiller C, Rother J 2003 Noninvasive monitoring of cerebral oxygenation during vasomotor reactivity tests by a new near-infrared spectroscopy device *Cerebrovasc Dis* 16 36-41.

Themelis G, D'Arceuil H, Diamond SG, Thaker S, Huppert TJ, Boas DA, Franceschini MA 2007 Near-infrared spectroscopy measurement of the pulsatile component of cerebral blood flow and volume from arterial oscillations *J Biomed Opt* 12(1) 014033.

Thompson HK, Starmer CF, Whalen RE, McIntosh HD 1964 Indicator Transit Time Considered As A Gamma Variate *Circ Res* 14 502-515.

Tichauer KM, Hadway JA, Lee T-Y, St Lawrence K 2006 Measurement of cerebral oxidative metabolism with near-infrared spectroscopy: a validation study *J Cereb Blood Flow Metab* 26(5) 722-730.

United States Food and Drug Administration 2012 Approved Drug Products with Therapeutic Equivalence Evaluations (FDA: Silver Spring, MD).

van der Zee P, Cope M, Arridge SR, Essenpreis M, Potter LA, Edwards AD, Wyatt JS, McCormick DC, Roth SC, Reynolds EOR, Delpy DT 1992 Experimentally measured optical pathlengths for the adult head, calf and forearm and the head of the newborn infant as a function of inter optode spacing *Adv Exp Med Biol* 316 143-153.

Wang L, Jacques SL, Zheng L 1995 MCML–Monte Carlo modeling of light transport in multi-layered tissues *Comput Methods Programs Biomed* 47(2) 131-146.

Waydhas C 1999 Intrahospital transport of critically ill patients *Crit Care* 3(5) R83-9.

Wright WL 2007 Multimodal monitoring in the ICU: when could it be useful? J Neurol Sci 261(1-2) 10-15.

Yamada T, Umeyama S, Matsuda K 2009 Multidistance probe arrangement to eliminate artifacts in functional near-infrared spectroscopy *J Biomed Opt* 14(6) 064034.

Zaccanti G, Contini D, Gurioli M, Ismaelli A, Liszka L, Sassaroli A 1995 Detectability of inhomogeneities within highly diffusing media *Proc. SPIE* 2389 755.

Zhang Q, Strangman GE, Ganis G 2009 Adaptive filtering to reduce global interference in non-invasive NIRS measures of brain activation: how well and when does it work? *Neuroimage* 45(3) 788-794.

Chapter 4

MEASURING THE ARTERIAL INPUT FUNCTION WITH A STANDARD PULSE OXIMETER TO FACILITATE THE CLINICAL IMPLEMENTATION OF DCE OPTICAL METHODS

The contents of this chapter have been adapted from the journal article published in 2012, entitled "Arterial input function of an optical tracer for dynamic contrast enhanced imaging can be determined from pulse oximetry oxygen saturation measurements" by Elliott JT, Wright EA, Tichauer KM, Diop M, Morrison LB, Pogue BW, Lee T-Y, and St. Lawrence K in *Physics in Medicine and Biology*. All of the dynamic contrast enhanced (DCE) near infrared (NIR) methods presented in this thesis (including the DCE fluorescence molecular tomography (FMT) and diffuse optical tomography (DOT) methods in Appendix A) require the proper characterization of the arterial input function (AIF). This chapter presents a practical solution to characterizing the AIF using a standard pulse oximeter (PO), offering an alternative to the current pulse dye densitometer (PDD) devices that are specialized and not typically compatible with small animal imaging. The original journal article from which this chapter is adapted can be found at *http://iopscience.iop.org/0031-9155/57/24/8285*

4.1. Introduction

In Chapters 2 and 3, nonparametric kinetic analysis was used to quantify CBF and to provide a meaningful relative blood flow index, respectively. Both these methods, (and additionally, the method highlighted in the next two chapters) require that the AIF—the time-dependent change in arterial dye concentration—be characterized. This is a common requirement not just in DCE optical methods, but in medical imaging in general where tracer kinetic modeling is commonly used to characterize physiological processes (Sourbron and Buckley 2012). Extracting quantitative measurements from kinetic data requires that the AIF be measured, because it describes the delivery of tracer to the tissue. Therefore, proper characterization of the AIF is an important goal in many modalities, including optical imaging. In this thesis, as well as in many other optical applications, the tracer indocyanine green (ICG) is used. Indocyanine green acts as an intravascular tracer in most tissues due to its binding with plasma proteins (*e.g.*, albumin). Since ICG is FDA approved (United States Food and Drug Administration 2012), it has been used in clinical settings to assess neurological function (Steinkellner *et al* 2010; Liebert *et al* 2005) and to characterize breast tumours (Schneider *et al* 2011), in addition to measuring cerebral blood flow (CBF) in Chapter 2 and elsewhere (Brown *et al* 2002; Diop *et al* 2010; Springett *et al* 2001). The principles of tracer kinetic modeling can also be applied to targeted optical contrast agents that are conjugated with ligands to study receptor binding potential and drug delivery mechanisms (Becker *et al* 2001).

To properly measure the AIF of an optical dye, a device known as a PDD is usually needed (Iijima *et al* 1997). However, these units are specialized pieces of equipment that are not commonly found and are only optimized for determining the AIF of ICG. Furthermore, in preclinical small animal studies, no PDD is available that functions at the high heart rates of these animals. Because of these obstacles, more simplistic kinetic models are

used that do not correct for AIF-dependent effects. For example, dynamic contrast-enhanced MRI techniques will perform kinetic analysis on tissue measurements with the assumption that the AIF is constant across measurements or patients, but these assumptions can be problematic and lead to errors in the recovered parameters (Parker *et al* 2006). The wider application of kinetic modeling to quantify important parameters such as blood flow, vascular leakage and receptor binding potential requires a more accessible method of measuring the AIF.

The methodology presented in this chapter enables the conversion of an off-the-shelf pulse oximeter (PO) into a PDD. This is accomplished by deriving a mathematical relationship between the arterial concentration of dye and the negative change in apparent SaO_2 measured by the pulse oximeter, which occurs because the increase in absorption due to the dye is interpreted as an increase in deoxyhemoglobin. While this interference has been previously observed (Sidi *et al* 1987), this study is the first time it has been used to actually quantify the AIF. Validation experiments were conducted in rabbits using a small animal oximetry device (MouseOx, STARR Life Sciences, Oakmont, PA), but the approach is translatable to the clinic, capitalizing on the ubiquity of pulse oximeters.

4.2. Theory

4.2.1. Pulse oximetry

Pulse oximeters record oscillations in light attenuation (ΔA_1 and ΔA_2) at two wavelengths (λ_1 and λ_2) that results from oscillations in arterial blood vessel diameter, ΔD, in response to the beating heart (Aoyagi 2003). Oxyhemoglobin and deoxyhemoglobin are the dominant light-absorbing molecules in the blood for the wavelengths selected by pulse oximeters. In this case, the changes in attenuation can be approximated using the Beer-Lambert Law:

$$\Delta A_1 = \left(\varepsilon_{a,1} \cdot C_a + \varepsilon_{b,1} \cdot C_b\right) \cdot \Delta D \tag{4.1a}$$

$$\Delta A_2 = \left(\varepsilon_{a,2} \cdot C_a + \varepsilon_{b,2} \cdot C_b\right) \cdot \Delta D, \tag{4.1b}$$

where C_a and C_b are the concentrations of oxyhemoglobin and deoxyhemoglobin, respectively, and $\varepsilon_{a,i}$ and $\varepsilon_{b,i}$ are their corresponding extinction coefficients defined for $i = (\lambda_1, \lambda_2)$. In pulse oximetry, equations 4.1a and 4.1b are rearranged to determine SaO_2 as follows:

$$\Delta A_1 = \left(\varepsilon_{a,1} \cdot SaO_2 \cdot tHb + \varepsilon_{b,1} \cdot (1 - SaO_2) \cdot tHb\right) \cdot \Delta D \tag{4.2a}$$

$$\Delta A_2 = \left(\varepsilon_{a,2} \cdot SaO_2 \cdot tHb + \varepsilon_{b,2} \cdot (1 - SaO_2) \cdot tHb\right) \cdot \Delta D, \tag{4.2b}$$

where SaO_2 is the oxygen saturation ratio, defined as C_{HbO2} / tHb, and tHb, the total hemoglobin concentration, equals C_a + C_b. In practice, scattering and partial volume errors arising from the expansion of non-blood media create systematic errors in the measured signal. To overcome many of the subject-dependent errors, the channel-dependent information is converted to a ratio:

$$\Phi = \frac{\Delta A_1}{\Delta A_2} = \frac{\varepsilon_{a,1} \cdot SaO_2 + \varepsilon_{b,1} \cdot (1 - SaO_2)}{\varepsilon_{a,2} \cdot SaO_2 + \varepsilon_{b,2} \cdot (1 - SaO_2)}. \tag{4.3}$$

Small errors that still remain in this expression are generally calibrated by adjusting the intensity and gains of the electronics until the actual SaO_2 measured by hemoximetery matches the SaO_2 recovered by solving Eq. 4.3. Alternatively, a calibration curve can be used to generate a linear approximation:

$$\Phi = M_s \cdot SaO_2 + b_s, \tag{4.4}$$

where M_s and b_s are the calibration factors determined by the manufacture, typically obtained from healthy subjects (Mendelson 1992), to convert the measured change in light absorption SaO_2.

The addition of another chromophore (such as an intravenously injected optical dye) will not appreciably alter the calibration process described above if it does not cause an appreciable change in the scattering properties of the tissue and does not substantially accumulate in the non-blood media within the region of interrogation. The relationship between the apparent SaO_2 ($aSaO_2$) reported by the pulse oximeter and the concentration of injected dye can be given by

$$\frac{\varepsilon_{a,1} \cdot aSaO_2 + \varepsilon_{b,1} \cdot (1 - aSaO_2)}{\varepsilon_{a,2} \cdot aSaO_2 + \varepsilon_{b,2} \cdot (1 - aSaO_2)} = \frac{\varepsilon^*_{a,1} \cdot SaO_2 + \varepsilon^*_{b,1} \cdot (1 - SaO_2) + \varepsilon^*_{i,1} \cdot \frac{C_i}{tHb}}{\varepsilon^*_{a,2} \cdot SaO_2 + \varepsilon^*_{b,2} \cdot (1 - SaO_2) + \varepsilon^*_{i,2} \cdot \frac{C_i}{tHb}} \tag{4.5}$$

where C_i represents the concentration of the additional chromophore and $\varepsilon_{i,j}$ represents the extinction coefficient of the i^{th} chromophore at the j^{th} wavelength that is normally used by the system. Extinction coefficents, $\varepsilon_{i,j}^*$, represent the extinction coefficient of the i^{th} chromophore at the j^{th} wavelength that is actually used to acquire the measurement. If the native probes are used to acquire the signal, then $\varepsilon_{i,j}^*$ is equal to $\varepsilon_{i,j}$. However, if a customized probe is used to modify the emission wavelength of the probe, $\varepsilon_{i,j}^*$ must be adjusted for the difference in absorption at the new wavelength. This additional parameter allows the use of a different wavelength of light in order to increase the sensitivity of the system to the desired optical dye, as was done in the validation experiments. The variable $aSaO_2$ represents the apparent SaO_2 that is reported by the instrument, whereas the variable SaO_2 represents the actual SaO_2. The latter can be measured before the injection and assumed to be constant during the period that the AIF is measured.

Finally, the total haemoglobin concentration, *tHb*, is determined from a venous blood sample. To obtain C_i, Eq. 4.5 is solved using the *fminsearch* function in MATLAB (The MathWorks, Natick, MA).

4.2.2. Tracer kinetic modeling

In tracer kinetic modeling, the time-dependent concentration of contrast agent in tissue, $C_t(t)$, is related to the AIF by the convolution in Eq. 1.5 (Meier and Zierler 1954). The specific definition of the impulse residue function, $R(t)$, will change depending on the behaviour of the contrast agent in the tissue region of interest. For the purpose of this validation paper, the adiabatic approximation to the tissue homogeneity model (AATH), which characterizes blood flow and tracer leakage into the surrounding tissue, was used to simulate tissue concentration curves (St Lawrence and Lee 1998). The impulse residue function, $R(t)$, derived from the AATH model is given by:

$$R(t) = \left(1 - \Theta(t - T_c)\right) + Ee^{-\frac{EF}{V_e}(t - T_c)}\Theta(t - T_c) \qquad (4.6)$$

where $\Theta(t)$ is the Heaviside step function, T_c is the transit time through the capillary, E is the extraction fraction of the dye from the IVS to the EVS, V_e is the distribution of tracer in the EVS and F is blood flow. The tracer kinetic portion of the error analysis in the next section was conducted for an untargeted tracer using the input summarized in Table 4.1.

Table 4.1: Input parameters

Parameter	Units	Input value
Blood flow, F	ml min^{-1} 100g^{-1}	15.0
Capillary transit time, T_c	s	6.5
EVS distribution volume, V_e	ml 100g^{-1}	75.0
Permeability-surface area product, PS	ml min^{-1} 100g^{-1}	10.4

Input parameters for the AATH forward model (Eq. 4.6) used in the validation experiment.

4.3. Methods

4.3.1. Validation of arterial input functions measured by pulse oximetry

An error analysis based on simulated data was conducted to better understand the effect of certain variables on the ability to recover the AIF accurately. First, the measurement resolution of the recovered dye concentration was characterized since it depends on the resolution of the pulse oximeter SaO_2 channel, the absorption properties of the dye, and *tHb*. For this analysis, *tHb* was fixed at 12 g/dl, the true SaO_2 was set to 95%, and the apparent SaO_2 was decreased from 95% to 75% in steps of 0.1%, which is the resolution of the SaO_2 data stored by the MouseOx system. The concentration of dye at each SaO_2 level was recovered from Eq. 4.5 using the extinction coefficients of indocyanine green. This was repeated for different "red channel" wavelengths from 600 to 900 nm to determine the relationship between the selected wavelength and the resolution of the measured dye concentration. Next, the effect of total haemoglobin concentration on the measurement resolution of the recovered dye concentration was investigated. The "red channel" wavelength was fixed at 760 nm, the true SaO_2 was set to 95%, and the apparent SaO_2 was decreased from 95% to 75% in steps of 0.1%. The concentration of dye at each SaO_2 level was recovered, and this process was repeated for *tHb* values from 5 to 25 g/dl.

In the second part of the experiment, the relationship between the PDD measured dye concentration and the dye curves extracted with the PO method were investigated in a rabbit model (see subsection 4.3.3). Regression plots were generated for each set of ICG curves, and a meta-analysis was performed to determine the mean and 95% confidence interval of the regression slopes. Theoretical tissue curves were generated by the AATH model using the measured AIF from the pulse oximeter and from the PDD to further understand how differences between the two AIFs would affect the

accuracy of the derived model parameters. The 'true' *Ct(t)* was generated using the PDD-measured AIF and the values of the model parameters given in Table 4.1. The AIF derived from pulse oximetry was then used to recover best-fit estimates of the model parameters from the theoretical *Ct(t)* curve by the *fminsearch* minimization function. The percent difference between the recovered and input *F* and *PS* values were determined.

4.3.2. Instrumentation

For the validation experiments, a small animal pulse oximeter (MouseOx, STARR Life Sciences, Oakmont, PA) was used. This unit is sensitive to fast heart rates, making it suitable for mouse and rat experiments, in addition to animals with slower heart rates such as rabbits. Custom-made probes with a "red channel" wavelength of 753 nm were used to improve the sensitivity of the pulse oximeter to ICG (see Fig. 4.1). The extinction coefficients for the left side of Eq. 4.5 were provided by the engineering team at STARR Life Sciences, whereas the modified extinction coefficients for the right side of Eq. 4.5 were determined in two steps: first, the light source spectrum was characterized with an off-the-shelf broadband spectrometer (QEE65000, Ocean Optics, Dunedin, FL). Second, this reference spectrum was used as a probability density function to sample from the extinction spectra of the three chromophores, which have been previously measured (Landsman *et al* 1976). Finally, a pulse-dye densitometer (DDM2000, Nihon Koden, Japan) capable of measuring the AIF in rabbits, which have a normal heart rate range of 190-310 bpm (Murphy *et al* 2011), was used to validate the AIF obtained from pulse oximetry. This instrument has been previously validated by comparison to serial blood sampling (Iijima *et al* 1998).

4.3.3. Animal experiments

All animal experiments were approved by the animal use committee at Western University (AUP #2009-087). Measurements using the PO and PDD were acquired in four New Zealand white rabbits (*Oryctolagus cuniculus*), approximately 6 months old (weight = 2.8 ± 0.3 kg). Animals were induced and maintained with isofluorane gas anaesthesia at 4% and 2.5% concentration, respectively. A mixture of 2:1 oxygen and medical air was maintained for the duration of the experiment, and blood gases, glucose, and rectal temperature were monitored frequently. The pulse oximeter and PDD probes were placed on separate hind limbs, and adequate signal strength was verified in both instruments before proceeding with tracer injection. Animals were allowed to rest for 30 minutes to stabilize before the experiment was started.

For each animal experiment, a solution of ICG (Cardiogreen, Sigma-Aldrich, St. Louis, MO; 0.3 mg kg^{-1} ml^{-1} dissolved in 0.5 ml of sterile water) was prepared. A total of two bolus injections were administered by intravenously with approximately 40 min between injections to allow the ICG to clear the system. Boli were rapidly injected, resulting in a first-pass full width half maximum of approximately 5 seconds. During each injection, data were acquired by the PO and PDD simultaneously, and downloaded to a laptop for subsequent analysis. The sampling rate of the pulse oximeter was 15 Hz; the PPD records each measurement at systole (equivalent to approximately 5 Hz in these animals) to a maximum of approximately 6 Hz. Heart rate, arterial oxygen saturation, and total haemoglobin were also measured and recorded, with the latter being measured by hemoximetry (ABL 80 FLEX CO-OX, Radiometer, Copenhagen, Denmark).

4.4. Results and discussion

4.4.1. Error analysis

Measurement resolution is defined as the minimum change in dye concentration that produces a detectable instrument response. The recorded SaO_2 channel used to calculate the dye concentration has a measurement resolution of 0.1%. Additionally, the degree to which a change in dye concentration causes a response in the SaO_2 channel depends on the absorption properties of that dye. These two factors ultimately determine the AIF measurement resolution. For error analysis, simulations were performed by varying the "red channel" of the dye from 600 to 900 nm (step size: 5 nm), while fixing SaO_2 at 95% and *tHb* at 12 g/dL. Fig 4.1 depicts the measurement resolution as a function of the wavelength of the "red" channel, which is the numerator in Eq. 4.5, when ICG is used as the optical dye. The absorption spectrum of ICG is shown for comparison. Note that the resolution function is not a perfect mirror of the ICG spectrum due to the additional influence of the other chromophores.

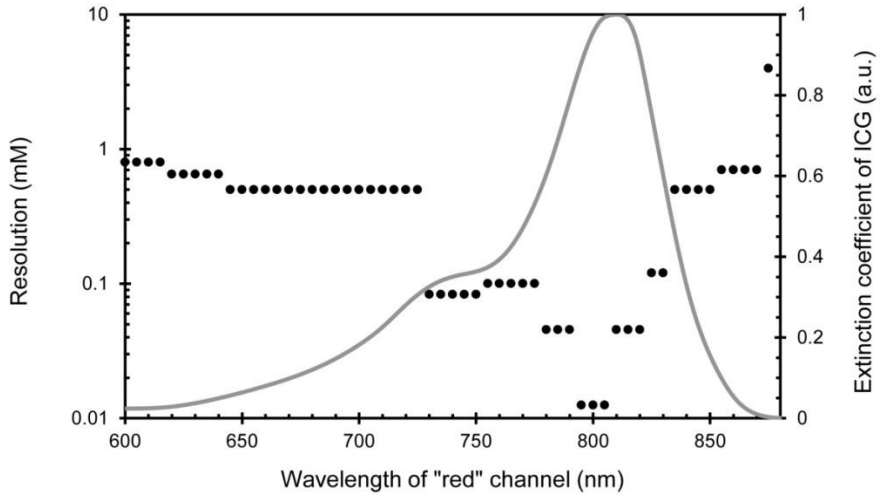

Figure 4.1: Influence of "red" channel wavelength on measurement resolution

The measurement resolution of the dye concentration extracted from the pulse oximeter SaO2 channel plotted on a log scale (black line), and the corresponding ICG absorption spectrum in plasma (gray line) plotted on an arbitrary linear scale.

As expected, the highest measurement resolution is achieved when a "red channel" wavelength is used that corresponds to the absorption peak of the dye (802 nm for ICG in plasma). If a light source is used that corresponds to the absorption peak of ICG, then a pulse oximeter that has a measurement resolution of 0.1% is capable of resolving 0.01 mM changes in dye concentration. A standard pulse oximeter, which employs a light source of around 650 nm would be able to resolve submilimolar (~0.5 mM) concentrations.

The amount of endogenous light absorption depends on the total haemoglobin concentration, *tHb*. Therefore, the relative effect of the dye on the overall signal change will depend on this parameter, which ultimately will affect the measurement resolution. An error analysis was performed by varying *tHb* from 5 to 25 g/dL (step size: 0.25 g/dL). A "red channel" wavelength of 760 nm was used, and SaO2 was set to 95%.

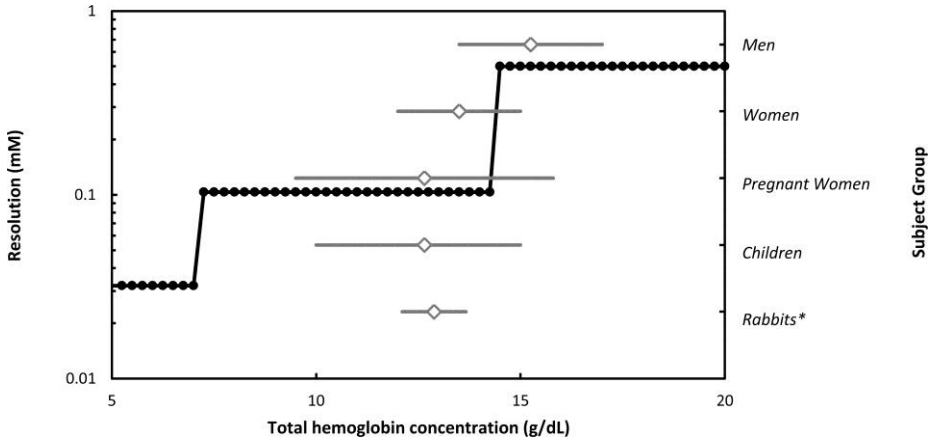

Figure 4.2: Influence of hemoglobin concentration variations on measurement resolution

The measurement resolution of the dye concentration extracted from the pulse oximeter SaO_2 channel plotted on a log scale (black line) versus the total haemoglobin (*tHb*). A forest plot of *tHb* reference ranges are shown to provide context (London Laboratory Services Group 2012; Abbassi-Ghanavati *et al* 2009). *Values obtained from animals used in this experiment.

Figure 4.2 summarizes the relationship between tHb and dye measurement resolution, and normal haemoglobin ranges are highlighted for several patient groups by a forest plot. The error analysis suggests two distinct resolution levels within the range of normal human haemoglobin concentration, which may reduce the performance of the technique in a certain subjects such as healthy adult men, by a factor of approximately 5. It is important to note that the abrupt changes in measurement resolution are not artificial, but represent an amplification of the rounding error resulting from the SaO2 channel measurement resolution of 0.1%.

4.4.2. Validation experiment

A representative example of the AIF acquired with the PDD plotted alongside the AIF calculated from pulse oximetry is depicted in Fig. 4.3. In this case, the slope and y-intercept of the regression between the two curves was 0.915 and 0.1 mM, respectively. There was a −3.3% difference in the peak concentration, and a −10.2% and 5.5% percent difference in F and PS when the pulse oximeter AIF was used to extract the kinetic parameters from Ct(t) generated from the PDD-measured AIF.

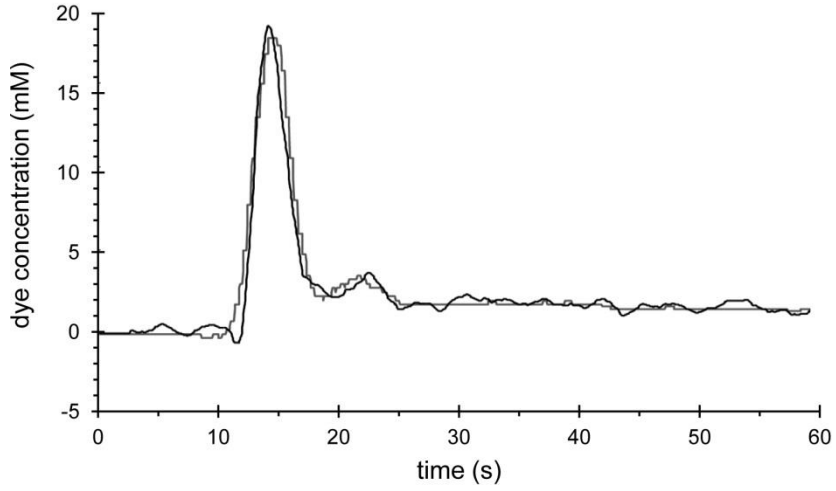

Figure 4.3: Arterial input functions measured by the two instruments

The AIF recovered with the PO method (gray line) using the method presented in this Chapter, and the AIF directly recovered using the PDD (black line).

This analysis was performed for all measurements across the four rabbits used in the study, and group means were determined as well as the 95% confidence intervals for each parameter. Figure 4.4 summarizes the regression results for the group analysis. The mean slope was 0.92, bound by a 95% confidence interval of 0.787 - 1.063. The mean y-intercept was 0.2 mM with a 95% confidence interval of –0.3 - 0.6 mM.

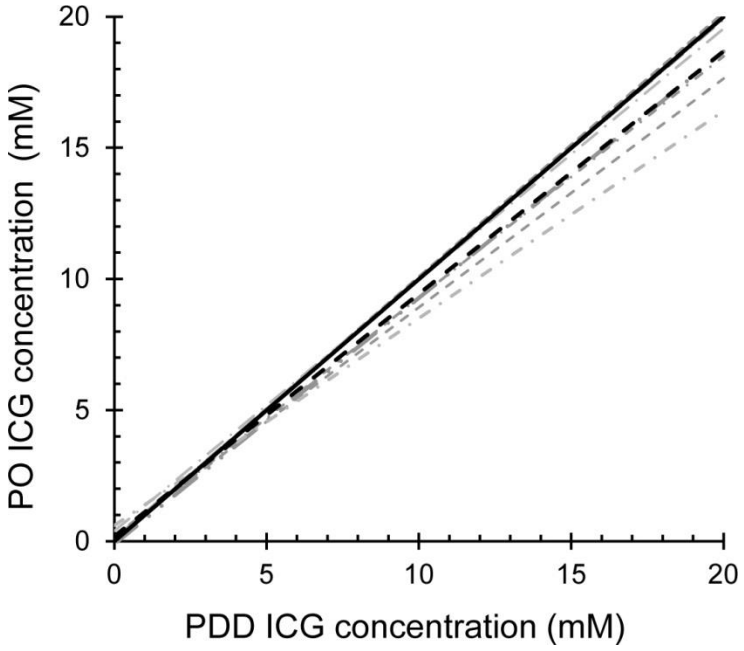

Figure 4.4: Relationship between PO and PDD measured ICG concentration

The regression plot comparing ICG concentration values obtained with the PO and the PDD simultaneously. The individual regression lines-of-best fit (n=8) were determine separately for the two ICG boli given to each of the four animals. The average line of best fit is indicated by the dashed line (*slope* = 0.92 ± 0.03, *y-intercept* = 0.18 ± 0.09 mM)

Figure 4.5 shows the Bland-Altman plot comparing the ICG concentration values obtained with the PDD and PO techniques. Linear regression analysis revealed a significant relationship between difference and mean concentration ($p < 0.05$) suggesting a proportional bias. The bias was defined by the line with a slope = −0.052 and a y-intercept = 0.19 mM. The

95% confidence intervals for the slope and y-intercept were −0.13 - 0.2 and −0.28 - 0.66, respectively.

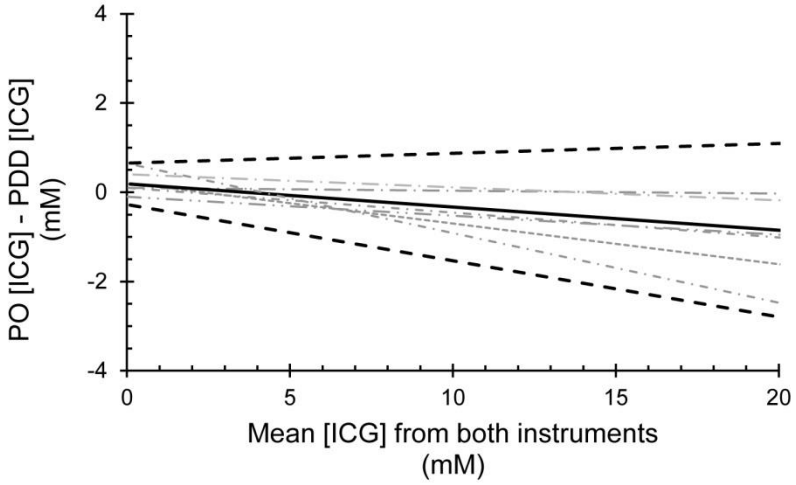

Figure 4.5: ICG concentration Bland-Altman plot

The Bland –Altman plot comparing the ICG concentration measurements obtained with the PDD and calculated from PO measurements of SaO2. As in Fig. 4.3, data are represented by lines-of-best fit of each ICG bolus (n=8). The mean difference between the two techniques is indicated by the solid line, and the 95% confidence interval is indicated by the dashed line.

As suggested by the proportional bias in the Bland-Altman analysis, the pulse oximeter tended to underestimate the concentration of ICG at high concentrations. This could be in part due to the dynamic range of the detectors used by this specific oximeter, which may not be as sensitive to SaO*2* below 60%.

Table 4.2 summarizes the group mean and confidence intervals for the percent differences in peak concentration, F, PS, and T_c extracted from the theoretical ICG tissue concentration data using the AIF from the pulse oximeter AIF rather than the true AIF from PDD. In addition, the p values from a paired t-test comparisons of values obtained using the two AIFs are shown. While there was no significant difference in the parameters obtained with the two AIFs, blood flow measurements were most affected by the underestimation in high ICG concentrations previously mentioned.

Table 4.2: Percent difference in recovered parameters

Parameter	Mean	95% Confidence Interval	*p* value
Peak concentration	−7.4%	−27.6 - 12.8%	0.23
Blood flow, F	−8.5%	−23.3 - 6.3%	0.06
Permeability-surface area product, PS	1.7%	−7.4 - 10.9%	0.45
Capillary transit time, T_c	1.5%	−6.5 – 9.5%	0.40

Percent difference in parameters recovered using the pulse oximeter AIF from the forward data generated using the DDG AIF. Results of the paired *t-test* between input and recovered values are shown in the fourth column.

The results of this study suggest that the commonly used pulse oximeter can be readily converted to a PDD fairly easily, which provides an accessible means of acquiring an AIF for use in tracer kinetic studies. Advancements in dynamic contrast-enhanced optical techniques have resulted in the ability to assess cerebral hemodynamics in neonates (Arora *et al* 2012), stroke patients (Steinkellner *et al* 2010) and traumatic brain injury patients (Keller *et al* 2001), and to localize and assess tumors in breast cancer patients (Schneider *et al* 2011). In addition, dynamic contrast-enhanced techniques have been described for a wide of range of applications including diagnosis of peripheral artery disease (Kang *et al* 2010) and monitoring muscle oxygenation (Boushel and Piantadosi 2000), and have been theoretically described for pre-clinical imaging methods such as fluorescence molecular tomography (Elliott *et al* 2012). In all cases, the ability to measure the AIF would enable the use of more sophisticated and more accurate kinetic models that would account for the between-subject variability in AIFs (Schneider *et al* 2011). For example, recent work by Schneider and colleagues demonstrated the ability of NIRx to detect breast cancer in a group of patients undergoing biopsy (Schneider *et al* 2011). In that study, relative metrics such as time-to-peak and relative peak concentration were used to discriminate between benign and malignant

tissues. The acquisition of the AIF would allow blood flow and vascular leakage of the regions of interest to be characterized, possibly providing additional sensitivity and specificity, and would also reduce intra-subject variability since measuring the AIF implicitly accounts for differences in blood circulation. Despite the benefit of characterizing the AIF, only a limited number of groups regularly employ a PDD because they are expensive and few units have been approved for patient use. The methodology described in this note enables clinicians and researchers to instead capitalize on pulse oximeters, which exist in virtually every advanced trauma center or intensive care unit around the world, and can be combined with current dynamic contrast-enhanced optical techniques at little additional cost.

In small animal imaging, an additional challenge to measuring the AIF is that no PDD device has been developed that is compatible with the high heart rates of rodents. There are, however, several pulse oximeter devices, including the MouseOx device used in this study, which are suitable for heart rates up to 900 bpm and can therefore be used to measure the AIF. Doing so would enable more sophisticated tracer kinetic models that could determine key parameters in the study of cancer development and treatment. For example, plasma input two-tissue compartment models (Mintun *et al* 1984) could be used to quantify molecularly targeted optical probe binding.

While the method described in this paper will be useful for a variety of applications, there are several limitations that will ultimately determine whether the use of a pulse dye densitometer is more appropriate. First, the accuracy of the recovered dye concentration will be affected by any errors in the extinction coefficients in Eq. 4.5, as well as the accuracy of the measured *tHb* concentration. The former can be minimized if the peak wavelength of the two channels can be obtained either from the manufacturer of the device, or by spectrometric measurement by the user. Careful consideration of Eq. 4.5 reveals that an error in *tHb* concentration will result in an equal error in

recovered dye concentration. This could be important, for example, in the critical care setting, where trauma patients presenting lower initial haemoglobin concentration may receive a packed red blood cell (PRBC) transfusion to improve the oxygen carrying capacity of the blood. In this case, a PRBC-corrected value of *tHb* may be helpful, where *tHb* is incremented by 1 g for every one unit of infused PRBC (Christy *et al* 2011). More significantly, the limited measurement resolution of this approach in certain circumstances may hinder its applications. As demonstrated in the error analysis, measurement resolution issues are addressed by using higher dye concentrations, constructing custom probes that use a "red channel" wavelength at the peak absorption of the dye-of-interest, and being aware of the potential *tHb*-related pitfall. In some cases, however, the measurement resolution may still be limited. For example, when performing a tracer kinetic binding study, only a limited concentration of dye can be injected to avoid receptor saturation. However, given that demand often drives technological advances, the adoption of this technique as a means of measuring the AIF may result in the development of pulse oximeters capable of 0.01% or better SaO_2 measurement resolution.

4.5. Conclusions

The results of this study demonstrate that with a basic understanding of pulse oximetry, it is possible to convert an off-the-shelf pulse oximeter into a dye densitometer that can be used to approximate the arterial input function in dynamic contrast-enhanced studies. This finding has immediate applications in both clinical and preclinical contexts.

4.6. References

Abbassi-Ghanavati M, Greer L G and Cunningham F G 2009 Pregnancy and laboratory studies: a reference table for clinicians *Obstet Gynecol* 114 1326-31

Aoyagi T 2003 Pulse oximetry: its invention, theory, and future *J Anesth* 17 259-66

Arora R, Ridha M, Lee D, Elliott JT, Diop M, Rosenberg H, Lee TY and St. Lawrence K 2013 Preservation of the metabolic rate of oxygen in preterm infants during indomethacin therapy for closure of the ductus arteriosus *Pediatr Res* doi:10.1038/pr.2013.53.

Becker A, Hessenius C, Licha K, Ebert B, Sukowski U, Semmler W, Wiedenmann B and Grotzinger C 2001 Receptor-targeted optical imaging of tumors with near-infrared fluorescent ligands *Nat Biotechnol* 19 327-31

Boushel R and Piantadosi C A 2000 Near-infrared spectroscopy for monitoring muscle oxygenation *Acta Physiol Scand* 168 615-22

Brown D W, Picot P A, Naeini J G, Springett R, Delpy D T and Lee T Y 2002 Quantitative near infrared spectroscopy measurement of cerebral hemodynamics in newborn piglets *Pediatr Res* 51 564-70

Christy J M, Stawicki S P, Jarvis A M, Evans D C, Gerlach A T, Lindsey D E, Rhoades P, Whitmill M L, Steinberg S M, Phieffer L S and Cook C H 2011 The impact of antiplatelet therapy on pelvic fracture outcomes *J Emerg Trauma Shock* 4 64-9

Diop M, Tichauer K M, Elliott J T, Migueis M, Lee T Y and St Lawrence K 2010 Comparison of time-resolved and continuous-wave near-infrared techniques for measuring cerebral blood flow in piglets *J Biomed Opt* 15 057004

Elliott J T, Diop M, Lee T Y and Lawrence K S 2012 Model-independent dynamic constraint to improve the optical reconstruction of regional kinetic parameters *Opt Lett* 37 2571-3

Elliott J T, Diop M, Tichauer K M, Lee T Y and St Lawrence K 2010 Quantitative measurement of cerebral blood flow in a juvenile porcine model by depth-resolved near-infrared spectroscopy *J Biomed Opt* 15 037014

Iijima T, Aoyagi T, Iwao Y, Masuda J, Fuse M, Kobayashi N and Sankawa H 1997 Cardiac output and circulating blood volume analysis by pulse dye-densitometry *J Clin Monit* 13 81-9

Iijima T, Iwao Y and Sankawa H 1998 Circulating blood volume measured by pulse dye-densitometry: comparison with (131)I-HSA analysis *Anesthesiology* 89 1329-35

Kang Y, Lee J, Kwon K and Choi C 2010 Dynamic fluorescence imaging of indocyanine green for reliable and sensitive diagnosis of peripheral vascular insufficiency *Microvasc Res* 80 552-5

Keller E, Wolf M, Martin M and Yonekawa Y 2001 Estimation of cerebral oxygenation and hemodynamics in cerebral vasospasm using indocyaningreen dye dilution and near infrared spectroscopy: a case report *J Neurosurg Anesthesiol* 13 43-8

Landsman M L, Kwant G, Mook G A and Zijlstra W G 1976 Light-absorbing properties, stability, and spectral stabilization of indocyanine green J *Appl Physiol* 40 575-83

Liebert A, Wabnitz H, Steinbrink J, Moller M, Macdonald R, Rinneberg H, Villringer A and Obrig H 2005 Bed-side assessment of cerebral perfusion in stroke patients based on optical monitoring of a dye bolus by time-resolved diffuse reflectance *Neuroimage* 24 426-35

London Laboratory Services Group 2012 Laboratory Test Information Guide: Complete Blood Count. Ed L Gopaul

Meier P and Zierler K L 1954 On the theory of the indicator-dilution method for measurement of blood flow and volume *J Appl Physiol* 6 731-44

Mendelson Y 1992 Pulse oximetry: theory and applications for noninvasive monitoring *Clin Chem* 38 1601-7

Mintun M A, Raichle M E, Kilbourn M R, Wooten G F and Welch M J 1984 A quantitative model for the in vivo assessment of drug binding sites with positron emission tomography *Ann Neurol* 15 217-27

Murphy M J, Tichauer K M, Sun L, Chen X and Lee T Y 2011 Mean transit time as an index of cerebral perfusion pressure in experimental systemic hypotension *Physiol Meas* 32 395-405

Parker G J, Roberts C, Macdonald A, Buonaccorsi G A, Cheung S, Buckley D L, Jackson A, Watson Y, Davies K and Jayson G C 2006 Experimentally-derived functional form for a population-averaged high-temporal-resolution arterial input function for dynamic contrast-enhanced MRI *Magn Reson Med* 56 993-1000

Schneider P, Piper S, Schmitz C H, Schreiter N F, Volkwein N, Ludemann L, Malzahn U and Poellinger A 2011 Fast 3D Near-infrared breast imaging using indocyanine green for detection and characterization of breast lesions *Rofo* 183 956-63

Sidi A, Paulus D A, Rush W, Gravenstein N and Davis R F 1987 Methylene blue and indocyanine green artifactually lower pulse oximetry readings of oxygen saturation. Studies in dogs *J Clin Monit* 3 249-56

Sourbron S P and Buckley D L 2012 Tracer kinetic modelling in MRI: estimating perfusion and capillary permeability Phys Med Biol 57 R1-33

Springett R, Sakata Y and Delpy D T 2001 Precise measurement of cerebral blood flow in newborn piglets from the bolus passage of indocyanine green *Phys Med Biol* 46 2209-25

St Lawrence K S and Lee T Y 1998 An adiabatic approximation to the tissue homogeneity model for water exchange in the brain: I. Theoretical derivation *J Cereb Blood Flow Metab* 18 1365-77

Steinkellner O, Gruber C, Wabnitz H, Jelzow A, Steinbrink J, Fiebach J B, Macdonald R and Obrig H 2010 Optical bedside monitoring of cerebral perfusion: technological and methodological advances applied in a study on acute ischemic stroke *J Biomed Opt* 15 061708

United States Food and Drug Administration 2012 Approved Drug Products with Therapeutic Equivalence Evaluations. (Silver Spring, MD)

Chapter 5

KINETIC DECONVOLUTION OPTICAL RECONSTRUCTION: THEORETICAL BASIS AND NUMERICAL SIMULATIONS

This chapter highlights the kinetic deconvolution optical reconstruction (KDOR) methodology, which can be applied to a variety of dynamic contrast enhanced (DCE) biomedical optics problems. The theoretical basis for KDOR was published in "Model-independent dynamic constraint to improve the optical reconstruction of regional kinetic parameters" by Elliott JT, Diop M, Lee T-Y, and St. Lawrence K, in *Optics Letters* in 2012. This chapter is an expanded version of the Letter, providing additional details on the theory and numerical results. The original Letter from which this chapter is adapted can be found at *http://www.opticsinfobase.org/ol/abstract.cfm?uri=ol-37-13-2571*

5.1. Introduction

Chapters 2 and 3 highlighted the use of DCE near-infrared (NIR) methods to measure tissue hemodynamic parameters: blood flow (BF), blood volume (BV) and mean transit time (MTT). Analogous to DCE methods in computed tomography (CT) and magnetic resonance imaging (MRI), the methodology requires the injection of a bolus of contrast agent, the recording of the time-dependent signal change, and then the reconstruction of time-dependent contrast concentration for each pixel or region-of-interest. As in CT and MRI,

the conventional approach is a two-step (TS) process that first involves reconstructing a time-series of DCE images or datapoints, followed by performing kinetic analysis on the data from individual regions or image pixels to recover the parameters of interest (Cenic *et al* 2000). For example, in Chapter 2, continuous-wave (CW) NIR measurements were collected at two source-detector distances, and separation of brain and extracerebral layer (ECL) information was achieved using subject-specific anatomical and spectral priors to estimate mean partial pathlength (MPP) values. In Chapter 3, the variance of the time-resolved signal was used to increase sensitivity to cerebral blood flow (CBF), and was deconvolved with the arterial input function (AIF) to estimate change in CBF. These steps represent first steps towards the goal of a robust bedside tool to measure CBF in the neurocritical care unit. However, the first study used an animal model that was an imperfect representation of the clinical reality, and was likely a "best-case scenario." The second study achieved partial separation of brain and ECL signal enabling the quantification of *changes* in CBF, but would require calibration with another imaging modality in order to provide absolute CBF.

The principle challenge to addressing the limitations in the previous studies is that complete separation of DCE signal arising from different tissue regions is non-trivial. First, the volume of interrogation is optically heterogeneous, with each region exhibiting different scattering and absorption properties. The adult head is comprised of scalp, skull, cerebrospinal fluid (CSF) and brain (which can be further divided into grey and white matter), each of which interacts with light differently. Therefore, the sensitivity function (or Jacobian) in the reconstruction forward problem is likely to contain model errors since the exact optical properties of each region are not known. Furthermore, even if the exact optical environment is sufficiently characterized, the scattering nature of light means that information measured across multiple source-detector pairs is highly similar.

This degree of interrelatedness reflected in the Jacobian results in an ill-posed system (Bonfert-Taylor *et al* 2012), which is a common theme in almost all biomedical optical reconstruction problems.

Subsequent kinetic analysis further complicates matters since nonparametric kinetic analysis (*i.e.*, deconvolution) is an unstable mathematical problem, often requiring modeling constraints to achieve acceptable precision (Lee 2005; Wirestam *et al* 2000). An implicit assumption is that the image region-of-interest or region-specific tissue concentration curve contains information from only one homogeneous tissue region. Because of the problems with spatial reconstruction, this assumption is invalid in many optical applications where the medium is heterogeneous and, as a result, quantitative kinetic analysis has been elusive.

Combining spatial reconstruction and kinetic deconvolution into a single mathematical system improves both problems and enables the reconstruction of kinetic parameters from multiple regions. In this chapter, the theoretical basis for this "kinetic deconvolution optical reconstruction" (KDOR) approach will be provided and, as a proof-of-principle, numerical simulations of time-resolved NIR measurements on the adult head are described. The accuracy and precision of KDOR recovered parameters will also be compared with values calculated using the traditional TS approach.

5.2. Theory

The KDOR approach combines the traditionally distinct steps of image reconstruction and tracer kinetic modeling in order to improve accuracy and precision of the recovered kinetic parameters (BF, BV, and MTT). Recall that optical reconstruction is governed by the forward problem, which in matrix form is given by

$$\mathbf{S} = \mathbf{AC}. \tag{5.1}$$

In this case, $\mathbf{S}$ is the optical signal data vector (usually defined for a finite set of spatial coordinates or source-detector distances), $\mathbf{C}$ is the concentration of tracer in tissue (defined on the spatial set of nodes, voxels, or regions representing the imaging domain, Ω), and $\mathbf{A}$ is the transformation between these two vectors (conventionally referred to as the "Jacobian"). The Jacobian is defined for the domains of $\mathbf{S}$ and $\mathbf{C}$, and includes scaling factors such as ε, the extinction coefficient of the tracer. The exact domains of $\mathbf{S}$ and $\mathbf{C}$ will vary for different applications. For example, in reflectance measurements on the head, $\mathbf{C}$ is typically defined for two regions (ECL and brain) and $\mathbf{S}$ is collected at various source-detector distances. Other ways of encoding $\mathbf{S}$ include: source-detector pair, i; moment order, k; and time-of-flight, t. Notwithstanding differences in the encoding of $\mathbf{S}$, optical reconstruction involves solving

$$\arg\min_{C} \left\{ \| AC - S \|^2 \right\}, \tag{5.2}$$

either in the least-squares sense, or using an iterative solver such as the Levenberg-Marquardt algorithm (Dehghani *et al* 2008). The recovered $\mathbf{C}$ vector is equivalent to a concentration map when spatially oriented according to the coordinates of Ω.

When $\mathbf{S}$ is characterized temporally with a resolution on the order of seconds to minutes, tracer kinetic theory can be used to describe the behavior of $\mathbf{C}$ as a function of time. The time-dependent change in dye concentration at any location in the medium is given by the convolution between a global AIF, $C_a(t)$ (since the same circulatory system feeds all tissue regions) and a flow-scaled impulse residue function $FR(t)$ (Eq. 1.5). The KDOR algorithm is formulated by substituting this definition for $\mathbf{C}$ into Eq. 5.1, yielding:

$$\mathbf{S} = \mathbf{B}\mathbf{R}_\mathbf{F}, \tag{5.3}$$

where $\mathbf{B}$ is the Kronecker product, $\mathbf{A}\otimes\mathbf{C_A}$, $\mathbf{R_F}$ is the vector constructed by stacking all node-specific *FR(t)* functions, and $\mathbf{S}$ is the vector constructed by stacking all time-specific data vectors. Quantification of blood flow, *F*, along with other kinetic parameters is achieved by the recovery of $\mathbf{R_F}$ through

$$\arg\min\left\{\left\|BR_F - S\right\|^2\right\} \quad \text{subject to} \quad \mathbf{GR_F} \le \mathbf{0} \text{ and } \mathbf{HR_F} = \mathbf{0} \tag{5.4}$$

Equality and inequality constraints $\mathbf{G}$ and $\mathbf{H}$ are block matrices with identical-sized partitions equal to the number of regions, constructed based on the physiological assumptions outlined in subsection 1.4.3 for a single kinetic region. For example, in the case where $\mathbf{R_F}$ represents the hemodynamic functions of three regions, the constraints in Eq. 5.4 would be represented by:

$$\mathbf{G} = \begin{bmatrix} \mathbf{g}_1 & \mathbf{0} & \mathbf{0} \\ \mathbf{0} & \mathbf{g}_2 & \mathbf{0} \\ \mathbf{0} & \mathbf{0} & \mathbf{g}_3 \end{bmatrix}, \quad \mathbf{H} = \begin{bmatrix} \mathbf{h}_1 & \mathbf{0} & \mathbf{0} \\ \mathbf{0} & \mathbf{h}_2 & \mathbf{0} \\ \mathbf{0} & \mathbf{0} & \mathbf{h}_3 \end{bmatrix}, \tag{5.5}$$

where $\mathbf{g_j}$ and $\mathbf{h_j}$ are the inequality and equality constraint vectors for the j^{th} region. Recall from Eqs. 1.10 and 1.11 in the first chapter, that constraints are defined for time-intervals given by the lag time, L_j, which is equal to the time between the injection and first appearance of dye, and the minimum transit time, M_j, which is the shortest time that an idealized bolus (*i.e.*, a Dirac-delta function) can travel across the capillary bed within the region of interrogation, specific to the j^{th} region. In this case, the compartment $\mathbf{h_j}$ in the equality constraint presented in Eq. 5.5 is represented as:

$$\mathbf{h_j} = \begin{array}{c} \\ L_j \\ \\ \\ \\ M_j - 1 \\ \\ \end{array} \overbrace{\begin{bmatrix} 1 & 0 & \cdots & 0 \\ 0 & 1 & \cdots & 0 \\ \vdots & \vdots & \cdots & \vdots \\ 0 & 0 & \cdots & 1 \\ 0 & 0 & \cdots & 0 \\ 0 & 0 & \cdots & 0 \\ \vdots & \vdots & \cdots & \vdots \\ 0 & 0 & \cdots & 0 \end{bmatrix}}^{L_j} \overbrace{\begin{bmatrix} 0 & 0 & 0 & \cdots & 0 & 0 \\ 0 & 0 & 0 & \cdots & 0 & 0 \\ \vdots & \vdots & \vdots & \cdots & \vdots & \vdots \\ 0 & 0 & 0 & \cdots & 0 & 0 \\ 1 & -1 & 0 & \cdots & 0 & 0 \\ 0 & 1 & -1 & \cdots & 0 & 0 \\ \vdots & \vdots & \vdots & \cdots & \vdots & \vdots \\ 0 & 0 & 0 & \cdots & 1 & -1 \end{bmatrix}}^{M_j} \overbrace{\begin{bmatrix} 0 & \cdots & \cdots & 0 \\ 0 & \cdots & \cdots & 0 \\ \vdots & \cdots & \cdots & \vdots \\ 0 & \cdots & \cdots & 0 \\ 0 & \cdots & \cdots & 0 \\ 0 & \cdots & \cdots & 0 \\ \vdots & \cdots & \cdots & \vdots \\ 0 & \cdots & \cdots & 0 \end{bmatrix}}^{N_T - L_j - M_j}, \tag{5.6}$$

where N_T is the number of columns in $\mathbf{C_A}$. Similarly, the compartment $\mathbf{g_j}$ in the inequality constraint in Eq. 5.5 is represented as:

$$\mathbf{g_j} = \begin{array}{c} \\ \\ \\ \\ \\ N_T \\ \\ \\ \\ \\ \\ \\ N_T - 1 \\ \\ \end{array} \overbrace{\left[\begin{array}{ccccccc} 1 & 0 & 0 & \cdots & \cdots & \cdots & \\ 0 & 1 & 0 & \cdots & \cdots & \cdots & \\ 0 & 0 & 1 & \cdots & \cdots & \cdots & \\ \vdots & \vdots & \vdots & \ddots & \cdots & \cdots & \\ \vdots & \vdots & \vdots & \cdots & \ddots & \cdots & \\ \vdots & \vdots & \vdots & \cdots & \cdots & \ddots & \\ \vdots & \vdots & \vdots & \cdots & \cdots & \cdots & \\ \vdots & \vdots & \vdots & \cdots & \cdots & \cdots & \\ \vdots & \vdots & \vdots & \cdots & \cdots & \cdots & \\ 0 & 0 & 0 & \cdots & \cdots & \cdots & \\ 0 & 0 & 0 & \cdots & \cdots & \cdots & \\ 0 & 0 & 0 & \cdots & \cdots & \cdots & \\ \hline 0 & 0 & 0 & \cdots & 0 & 0 & \\ 0 & 0 & 0 & \cdots & 0 & 0 & \\ \vdots & \vdots & \vdots & \cdots & \vdots & \vdots & \\ 0 & 0 & 0 & \cdots & 0 & 0 & \end{array}\right.}^{M_j + L_j - 1} \overbrace{\left.\begin{array}{ccc} \cdots & \cdots & \cdots \\ \cdots & \cdots & \cdots \\ \cdots & \cdots & \cdots \\ \cdots & \cdots & \cdots \\ \cdots & \cdots & \cdots \\ \cdots & \cdots & \cdots \\ \cdots & \cdots & \cdots \\ \cdots & \cdots & \cdots \\ \cdots & \cdots & \cdots \\ 0 & 0 & 0 \\ 0 & 0 & 0 \\ 0 & 0 & 0 \\ \hline 1 & -1 & 0 \\ 0 & 1 & -1 \\ \vdots & \vdots & \vdots \\ 0 & 0 & 0 \end{array}\right]}^{N_T - M_j - L_j + 1}. \tag{5.7}$$

It is therefore necessary to determine L and M for all tissue regions before the minimization of Eq. 5.4. This is done iteratively by solving Eq. 5.4 for different L_j and M_j values, and then comparing the reconstructed signal, S, to the experimentally measured signal. To speed up the process, only the first

30 seconds of the signal was used in the optimization. Figure 5.1 shows a representative example of this fitting procedure, which is analogous to the procedure used in the single-region deconvolution except that an iterative search was used instead of an exhaustive search (Lee 2005).

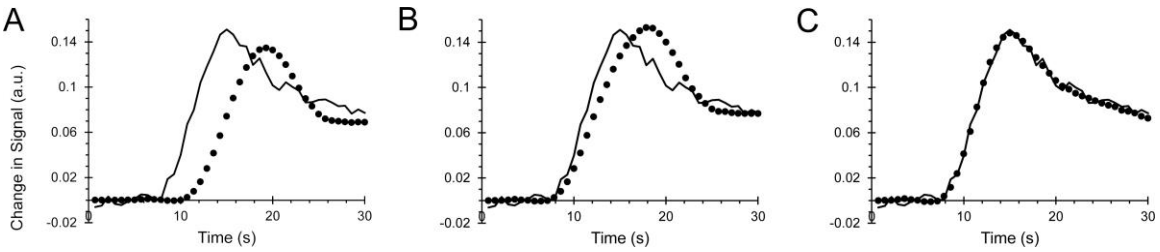

Figure 5.1: Iterative search of lag and minimum transit time.

The implementation of equality and inequality constraints in the deconvolution method require that the lag time, L and minimum transit time, M, be defined. This was done iteratively: the initial guesses for L and M shown in (A) were adjusted so that (B) shows the optimized value for L and (C) shows the convergence of both L and M.

Once the values of L and M are optimized, Eq. 5.4 is minimized for all time points to recover $\mathbf{R_F}$. Finally, hemodynamic parameters are recovered from the region-specific $FR(t)$ functions: BF is recovered by determining the maximum of $FR(t)$, since $R(t)$ is a normalized function with a maximum of unity (Meier and Zierler 1954); BV is given by the area under $FR(t)$, and MTT can be calculated by the central volume principle (Zierler 1965) where $MTT = BV / BF$.

5.3. Methods

5.3.1. Forward model of the adult head

A segmented finite element mesh of an adult human head was obtained online from the mesh-based Monte Carlo (MMC) repository (http://mcx.sf.net/mmc/). The MMC program and related files were developed by Qianqian Fang and are available free to use (Fang 2010). The adult head model was segmented from an MRI into four tissue regions: scalp, skull, CSF,

and brain. For the purpose of the forward model, these were assigned the optical properties summarized in Table 5.1.

Table 5.1: Optical properties used in the Monte Carlo simulations

Medium	μ_s' (mm^{-1})	μ_a (mm^{-1})	g
Scalp	0.70	0.018	0.9
Skull	0.80	0.013	0.9
CSF	0.01	0.002	0.9
Brain	1.10	0.015	0.9

Continuous-wave signals were simulated for source-detector distances of 10, 20, 30 and 40 mm. First, MMC was used to simulate photon propagation in the adult head mesh, and photons "detected" at the four source-detector distances were recorded. Then, the mean partial pathlengths were determined from the photon history files using a previously described method (Boas *et al* 2002). In this way, the Jacobian, **A**, was constructed to relate the change in absorption occurring in the brain and in the ECL (representing the scalp, skull, and CSF) to the change in signal for the four distances. Time-dependent absorption changes in the two regions were generated by first convolving a simulated $C_a(t)$ with layer-specific $FR(t)$ functions defined by a gamma variate model (Thompson *et al* 1964) to obtain region-specific $C(t)$ curves. These curves were then converted to change in absorption coefficient using the ICG specific absorption at 800 nm. An example is shown in Fig. 5.2.

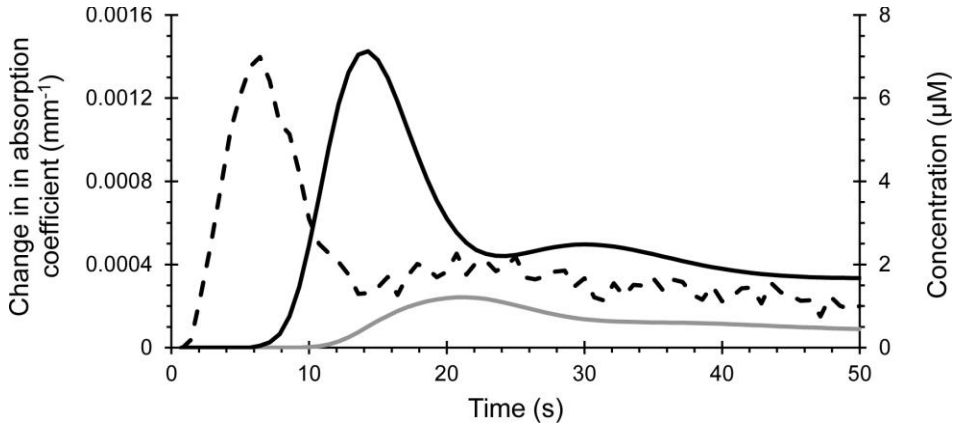

Figure 5.2: Change in tissue absorption coefficient

The dye-induced change in tissue absorption coefficient in the scalp (gray line) and brain (black line) used in the forward model. Absorption curves are plotted along with the $C_a(t)$ function (dashed line, secondary y-axis) used in the simulations.

Gaussian noise of 10% was added to both the arterial input function and the signal data vector. Noise was generated independently for each simulation using a unique pseudorandom number seed.

5.3.2. Data reconstruction

The KDOR reconstruction method was performed by numerical optimization of Eq. 5.4 using the MATLAB function *lsqlin*. The TS method, on the other hand, involves first performing spatial reconstruction to recover the brain and ECL specific $C(t)$ curves, and then deconvolving these curves with the $C_a(t)$ function using the single-region method described in subsection 1.4.3. Spatial reconstruction was regularized with the truncated singular-value decomposition (TSVD) method which has been proposed elsewhere for this application (Liebert *et al* 2004) and is an example of a common regularization method to stabilize optical reconstruction.

A reconstruction Jacobian, A_{rec}, was used in both KDOR and TS reconstructions, which differed from the Jacobian used to generate the forward data to avoid committing an "inverse crime". The reconstruction Jacobian was essentially a noisy version of the forward Jacobian to simulate

uncertainty in the sensitivity factors that occurs during experimental conditions. Two aspects of uncertainty were added to the reconstruction Jacobian: the total sensitivity factor for each channel was randomly varied between ± 10% of the original value, and the *ratios* between region-specific sensitivity factors and the total sensitivity factor for that channel were varied between ± 10%. These randomizations represent uncertainties that would be introduced if the bulk scattering coefficient was inaccurate, or if there were inaccuracies in the ECL thickness, respectively. For each iteration, A_{rec} was uniquely randomized with a new pseudorandom number seed.

5.3.3. Numerical experiments

Numerical experiments were conducted to compare the accuracy and precision of the KDOR and TS methods. Hemodynamic input parameters used to generate the forward data were held constant for all iterations. For the ECL, BF = 5 ml min^{-1} $100g^{-1}$, BV = 1 ml $100g^{-1}$, and MTT = 12 s and for the brain, BF = 50 ml min^{-1} $100g^{-1}$, BV = 4 ml $100g^{-1}$ and MTT = 5 s. Reconstruction was repeated 100 times on the forward data to compare the precision of the KDOR and TS methods.

5.4. Results and discussion

Brain-specific absorption curves obtained from the TS and KDOR approaches are shown in Fig. 5.3. Note that the TS absorption curve is recovered in the first step of the procedure, and then subsequently analyzed to recover the hemodynamic function. The KDOR absorption curve is generated by convolving the recovered *FR(t)* function with the original arterial input function. Two important differences are observed when comparing these curves. First, the TS curve shows a bias in the peak absorption compared to the input curve, of about -10%, whereas, the KDOR curve shows no discernible bias. In addition, the variability in the TS curve was two times

greater than the KDOR curve around the absorption peak, and this variability increased to five times at all other time points.

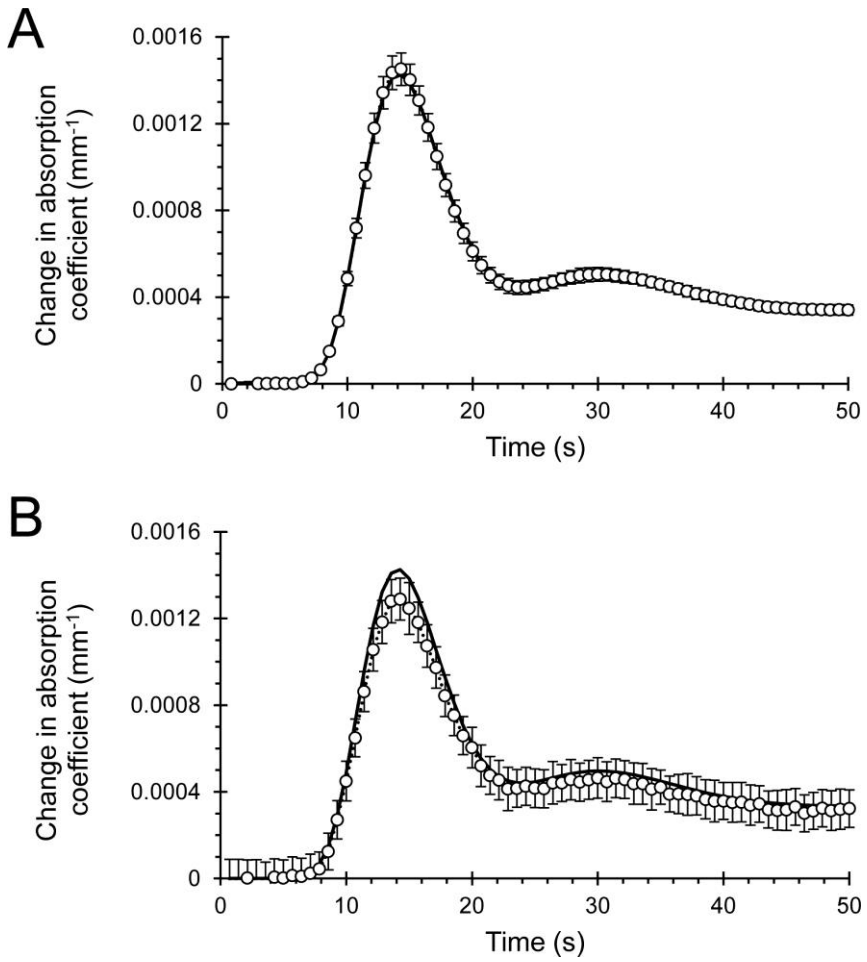

Figure 5.3: Brain tissue change in absorption coefficient recovered with KDOR and TS

(A) The brain change in absorption coefficient recovered with the KDOR method (open circles), and (B) the change in absorption coefficient recovered with the TS method (open circles). Both are compared with the true input curves (black solid line). Data points are the mean of 100 iterations, and error bars are the standard deviation.

Next, the average *FR(t)* curves recovered with the two approaches, which are shown in Fig. 5.4, were compared. Interestingly, the ECL curves are recovered well by both methods, suggesting that there is sufficient information present in the measured signal pertaining to this region to allow direct reconstruction with minimal regularization.

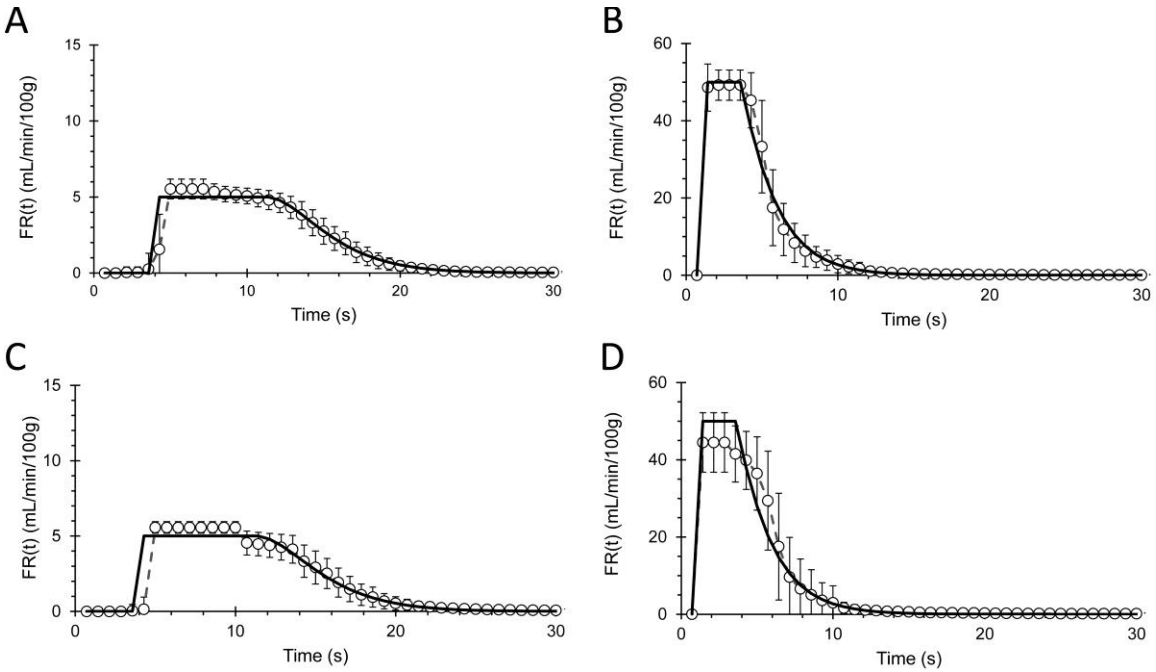

Figure 5.4: Impulse residue functions recovered with KDOR and TS

(A) and (B) show the true (solid black line) and recovered (open circles) FR(t) curves for the ECL and brain tissue, respectively, calculated with the KDOR algorithm. (C) and (D) show the true and recovered curves for the ECL and brain tissue, respectively, obtained using the TS method. Data points are the mean of 100 iterations, and error bars are standard deviation.

However, the reconstructed brain *FR(t)* curves show marked differences between the two methods, similar to the differences seen in the absorption curves. In particular, the TS approach seemed to do a poor job of capturing the shape of the top of the curve. Since the plateau is used to calculate BF, this resulted in an underestimation of BF by 11%. The precision of the recovered curves was higher for the scalp region, and higher when using KDOR compared to TS. Taken together, these results suggest that errors in the TS during spatial reconstruction propagate into the kinetic analysis, resulting in increased variability and an underestimation bias.

The three hemodynamic parameters of interest (BF, BV and MTT) were calculated for the two tissue regions from the recovered *FR(t)* curves. Box-and-whisker plots shown in Fig. 5.5 summarize the results of the kinetic analysis.

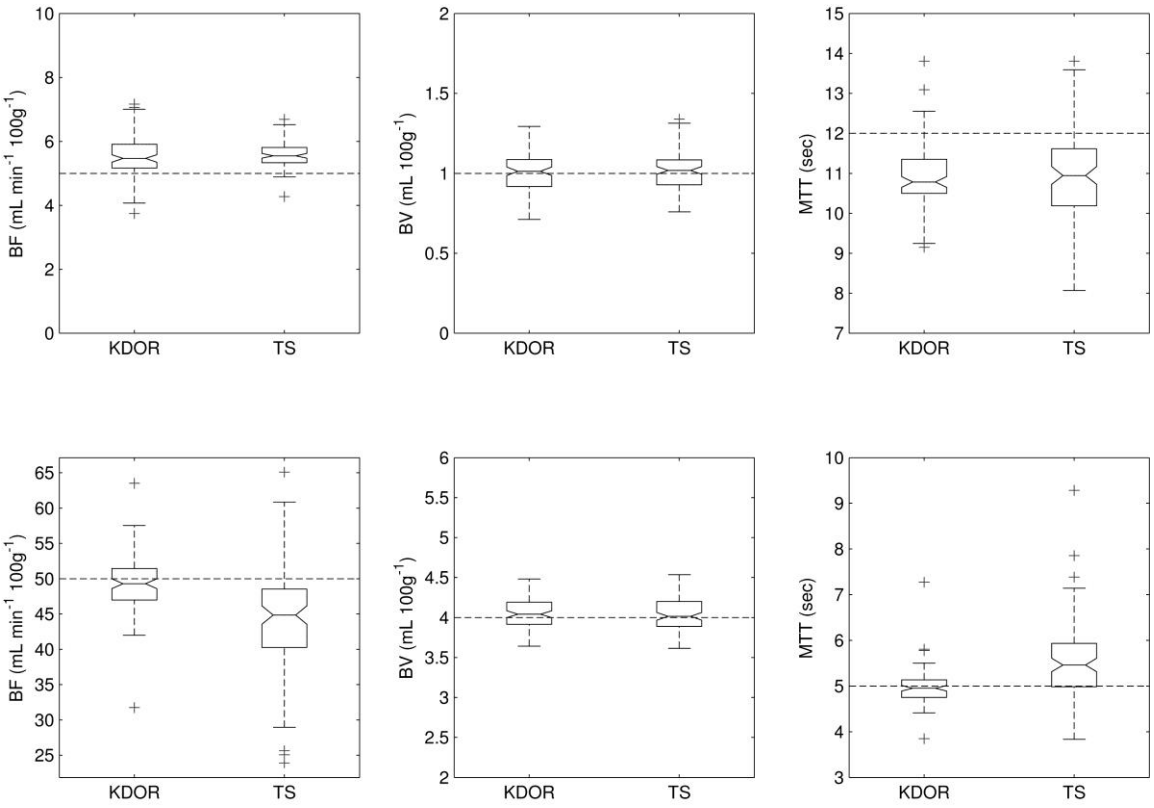

Figure 5.5: Hemodynamic parameters recovered with the two methods

Box-and-whisker plots of the blood flow (BF), blood volume (BV) and mean transit time (MTT) recovered with the KDOR and TS methods for scalp (top row) and brain (bottom row) regions. Boxes are bound by the 1st and 3rd quartiles, and the median is given by the centre line. Error bars are min and max, with outliers shown as crosses. Dashed lines show the true value of the parameter.

In general, the KDOR method does a better job of recovering the hemodynamic parameters than the TS method. In particular, the mean error in recovered CBF was −1.4% using the KDOR approach, compared with −11.0% using the TS approach. Additionally, the precision of the CBF estimate derived from the KDOR method was about two times greater.

The improvements that were observed by using the KDOR are most likely a result of the reduced loss-of-information when solving the inverse problem in Eq. 5.3. In particular, when compared to the spatial reconstruction problem in Eq. 5.1, the linear operator in Eq. 5.3 (*i.e.*, the Kronecker product of $\mathbf{A}$ and $\mathbf{C_A}$) is of higher rank since its rank is equal to the

sum of the ranks of $\mathbf{A}$ and $\mathbf{C_A}$ (Laub 2005). In signal processing, the numerical rank (also called the effective rank or pseudorank) is often more instructive than the algebraic rank, and is defined as the number of columns in the matrix that, with respect to some error tolerance, are practically linearly independent (Hansen 1998). Since measurement and modeling errors do not depend on the analytical method, the resulting effective rank is also higher in the KDOR inversion than in the TS inversions. Furthermore, the ability to constrain the KDOR inversion temporally, using rigid physiologically derived equality and inequality constrains is likely to add further stability to the inverse problem. The exact degree to which these constraints improve reconstruction will depend on how different the *FR(t)* functions are for the different regions. For example, if two regions of very similar *FR(t)* functions are interrogated, there is likely to be crosstalk between the two regions as the amount of interrelated information in $\mathbf{B}$ is increased. However, in this case, since the regions are so similar to begin with, any crosstalk will have a negligible effect on overall accuracy. An additional benefit to using the KDOR approach is that it can be applied to data that is encoded across any number of different dimensions (*e.g.*, spectral, spatial, as well as temporal in the case of time-resolved data). Because it is compatible with the use of other constraints (*e.g.*, spectral and anatomical priors) it has the potential to improve optical—and potentially photoacoustic or optoacoustic—reconstruction across a wide range of applications.

5.5. Conclusions

Taken together, these numerical simulations suggest that KDOR enables the accurate and precise characterization of hemodynamics for a wide range of conditions. Based on these encouraging results, the next chapter will validate multi-distance, time-resolved NIR measurements of cerebral hemodynamics recovered using the KDOR method in an animal model of cerebral ischemia. This represents a final step in the development of instrumentation and

analytical methods presented in this thesis to monitor adult patients in the neurocritical care unit.

5.6. References

Boas D, Culver J, Stott J, Dunn A 2002 Three dimensional Monte Carlo code for photon migration through complex heterogeneous media including the adult human head *Optics express* 10(3) 159-170.

Bonfert-Taylor P, Leblond F, Holt RW, Tichauer K, Pogue BW, Taylor EC 2012 Information loss and reconstruction in diffuse fluorescence tomography *JOSA A* 29(3) 321-330.

Cenic A, Nabavi DG, Craen RA, Gelb AW, Lee TY 2000 A CT method to measure hemodynamics in brain tumors: validation and application of cerebral blood flow maps *Am J Neuroradiol* 21:462–70.

Dehghani H, Eames ME, Yalavarthy PK, Davis SC, Srinivasan S, Carpenter CM, Pogue BW, Paulsen KD 2008 Near infrared optical tomography using NIRFAST: Algorithm for numerical model and image reconstruction *Commun Numer Methods* 25(6) 711-32.

Elliott JT, Diop M, Lee T-Y, St. Lawerence K 2012a Model-independent dynamic constraint to improve the optical reconstruction of regional kinetic parameters *Opt Lett* 37 2571-73.

Elliott JT, Wright EA, Tichauer KM, Diop M, Morrison LB, Pogue BW, Lee T-Y, St. Lawrence K 2012b Arterial input function of an optical tracer for dynamic contrast enhanced imaging can be determined from pulse oximetry oxygen saturation measurements *Phys Med Biol* 57(24) 8285.

Fang Q 2010 Mesh-based Monte Carlo method using fast ray-tracing in Plücker coordinates *Biomed Opt Exp* 1(1) 165-175.

Hansen PC 1998 *Rank-deficient and discrete ill-posed problems: Numerical aspects of linear inversion* (SIAM: Philadelphia, PA) p 46.

Laub AJ 2005 *Matrix Analysis for Scientists and Engineers* (SIAM: Philadelphia, PA) p 141.

Lee TY 2005 Method and apparatus for calculating blood flow parameters. *US Patent No. 6,898,453.*

Liebert A, Wabnitz H, Steinbrink J, Obrig H, Moller M, Macdonald R, Villringer A, Rinneberg H 2004 Time-resolved multidistance near-infrared spectroscopy of the adult head: intracerebral and extracerebral absorption changes from moments of distribution of times of flight of photons *Appl Opt* 43(15) 3037-3047.

Meier P, Zierler KL 1954 On the theory of the indicator-dilution method for measurement of blood flow and volume *J Appl Physiol* 6(12) 731-44.

Thompson HK, Starmer CF, Whalen RE, McIntosh HD 1964 Indicator transit time considered as a gamma variate *Circ Res* 14 502-515.

Wirestam R, Andersson L, Ostergaard L, Bolling M, Aunola JP, Lindgren A, Geijer B, Holtås S, Ståhlberg F 2000 Assessment of regional cerebral blood flow by dynamic susceptibility contrast MRI using different deconvolution techniques *Magn Res Med* 43(5) 691-700.

Zierler KL 1965 Equations for measuring blood flow by external modeling of radioisotopes *Circ Res* 16 309-21.

Chapter 6

MEASURING CEREBRAL HEMODYNAMICS IN AN ADULT PIG MODEL OF ISCHEMIA WITH TIME-RESOLVED NEAR INFRARED AND KINETIC DECONVOLUTION OPTICAL RECONSTRUCTION

This chapter presents the validation of cerebral hemodynamic parameters measured by time-resolved (TR) near-infrared (NIR) in combination with the kinetic deconvolution optical reconstruction (KDOR) analytical method in an adult pig model of ischemia. As such, this work extends the theoretical derivations presented in the previous chapter, establishing the outlined methodology as a robust technique capable of accurately quantifying cerebral blood flow (CBF), cerebral blood volume (CBV) and mean transit time (MTT). This chapter is based on a manuscript entitled "Measurement of cerebral hemodynamics in an adult pig model of ischemia using a quantitative dynamic contrast-enhanced optical method" by Elliott JT, Diop M, Morrison LB, d'Esterre CD, Lee T-Y, and St. Lawrence K, which will be submitted to a peer-reviewed journal in the near future.

6.1. Introduction

In the previous chapter, the kinetic deconvolution optical reconstruction (KDOR) analytical method was introduced and, based on numerical

simulations, it was suggested that KDOR could be used to recover cerebral hemodynamics from multi-distance dynamic contrast-enhanced (DCE) NIR measurements, even in the presence of large extracerebral layer (ECL) signal contamination. By employing the KDOR approach, while at the same time leveraging improvements in optical instrumentation presented in Chapter 3 (*i.e.*, time-resolved NIR), it is hypothesized that resulting CBF measurements acquired in an adult pig during baseline, hypocapnia and ischemia will show strong agreement with CT perfusion measurements, similar to the continuous-wave, two-step approach in Chapter 2 demonstrated on a juvenile pig model with less ECL contamination. Furthermore, by validating this approach in a clinically relevant model, using anatomical and dynamic priors that are also available clinically, this study represents a final staging ground before deploying DCE-NIR in clinical trials.

With this goal in mind, this chapter will address three main objectives. First, the KDOR method will be used in combination with time-resolved NIR measurements acquired at four source-detector distances to evaluate the CBF and CBV in an adult pig under three physiological states: baseline, hypocapnia, and ischemia. Concomitant measurements will be acquired using CT perfusion, in similar fashion to the juvenile pig study presented in Chapter 2, and regression and Bland-Altman analysis will be used to determine the difference between the two techniques. Second, to induce ischemia in the adult pig, intracortical injections of endothelin-1 will be administered. The reproducibility of this method will be determined, and the resulting lesion will be described in terms of three abnormal tissue states: infarct core (defined as CBF < 10 ml min^{-1} $100g^{-1}$), penumbra (defined as CBF between 10 ml min^{-1} $100g^{-1}$ and 20 ml min^{-1} $100g^{-1}$), benign oligemia (defined as CBF between 20 and 40 ml min^{-1} $100g^{-1}$) and normal tissue state (defined as CBF > 40 ml min^{-1} $100g^{-1}$). In particular, for the purpose of this experiment, it is important to understand how each tissue state is

contributing to the region interrogated by the NIR light. Finally, an error analysis will be conducted to investigate the effect of probe positioning errors (*i.e.*, corregistration with CT or MRI anatomical information) and model dependent errors caused by inaccuracy in the ECL reduced scattering coefficient input value, which has a stronger influence on the sensitivity factors (*e.g.*, mean partial pathlength) than absorption coefficient. In particular, the dependency of the method on correctly estimating the optical properties of the ECL provides insight into whether or not TR NIR instrumentation (which is more complex and expensive than CW instrumentation, but provides greater sensitivity) is needed in clinical applications.

6.2. Materials and methods

6.2.1. Animal protocol

Animal experiments were conducted according to the guidelines of the Canadian Council on Animal Care and approved by the Animal Use Committee at Western University (AUP #2007-050-06). Eight Duroc x Landrace crossbred pigs (*Sus scrofa domesticus,* weight = 15.4 ± 0.74 kg, 6 females) were obtained from a local supplier on the day of the experiment. Following anesthetic induction with 1.75-3% isoflurane, the animals were tracheotomized and mechanically ventilated on a mixture of oxygen and medical air. A polychloroprene probe holder was constructed in-house and fixed on the head of the animal with tissue glue (Vetbond® (*n*-butyl cyanoacrylate), 3M, St. Paul, MN). The adult pig has thick temporalis muscles that originate at the temperoparietal region of the head are highly vascularized, resulting in a scalp blood flow of about 25 ml min^{-1} $100g^{-1}$ (Elliott *et al* 2013b)—much higher than is typical in the adult scalp, estimated to be 5-8 ml min^{-1} $100g^{-1}$ (Friberg *et al* 1986). To improve the relevance of the animal model, three surgical incisions were made (caudial,

rostral, and lateral to the probe holder) to reduce the blood flow to about 10 ml min^{-1} $100g^{-1}$, measured with CT perfusion. Following the preparation and surgical procedures, the animals were moved to the CT imaging suite and allowed to stabilize for 1-hr before the experiment was continued.

6.2.2. Study design

The study consisted of collecting CT and DCE-NIR measurements at three different levels of CBF. Following stabilization, physiological parameters were recorded and a DCE-NIR measurement was acquired over a period of about 5 minutes. The optical probes were removed from the probe holder and a CT perfusion scan was performed. Following the CT scan, the probes were replaced in the probe holder, and a second DCE-NIR measurement was acquired. A period of at least 15 minutes was given between DCE-NIR measurements to allow for clearance of the dye. This process was repeated for the hypocapnia and ischemia conditions, resulting in a total of six optical datasets and three CT perfusion datasets for each animal. A total of five animals were subjected to all three conditions and a total of three animals were subjected to only baseline and hypocapnia conditions; for two animals, the experiments were conducted before a protocol modification was submitted to allow the ischemia procedure, and for one animal, endothelin-1 was unavailable.

6.2.3. Modification of cerebral blood flow

Hypocapnia was achieved by adjusting the ventilation rate on the mechanical ventilator to achieve a PCO_2 of 25 mmHg. Blood gas levels were confirmed using a hemoximeter (ABL 80 FLEX CO-OX, Radiometer, Copenhagen, Denmark). Once the appropriate PCO_2 level was achieved, the physiological parameters were allowed to stabilize before proceeding with the experiment. Ischemia was achieved by intracortical injection of endothelin-1 (Sigma-Aldrich, St. Louis, MO), a potent vasoconstrictor. A burr hole was drilled

through the scalp and skull just lateral to the probe holder, half way between the source optode and the 40 mm detector optode. A 30-Ga needle was carefully inserted into the cortical tissue, angled towards midline, and a low-dose CT scan was performed to confirm the location of the needle tip. The needle was connected to a catheter, which in turn was connected to a syringe containing approximately 1 μg/kg of endothelin-1 in 0.1 ml of sterile water. Using a syringe pump, the contents of the syringe were delivered to the cortical tissue over 10 minutes. Data collection proceeded 10 minutes after the endothelin-1 injection was finished.

The reproducibility of endothelin-induced blood flow change was reported as the standard deviation of mean CBF across the DCE NIR region of interrogation (determined from light propagation modeling). The reproducibility of infarct-size was determined tracing the infarct perimeter free-hand, and computing the corresponding area using image analysis software (ImageJ 1.46, National Institutes of Health, Bathsheba, MD). The area was determined on the eight blood flow maps, and the volume was calculated by multiplying the sum of the areas from each stack by the slice thickness (5 mm).

6.2.4. Physiological measurements

In addition to CT and DCE-NIR measurements, physiological parameters were monitored throughout the experiment, including: arterial oxygen saturation, heart rate, respiration rate, end-tidal CO_2, mean arterial pressure, and rectal temperature. In addition, a hemoximeter was used to measure arterial blood pH, PCO_2, PO_2, and glucose. The main purpose of collecting these measurements was to ensure physiological stability at each of the three conditions, which was achieved by adjusting the respiration rate on the mechanical ventilator, and by maintaining temperature and glucose homeostasis via a heated blanket and dextrose administration, respectively.

6.2.5. Instrumentation

Optical measurements were collected using a time-resolved NIR system that has been described previously (Diop *et al* 2010), and is depicted in Fig. 6.1. The system comprised of a picosecond diode laser light source that was used to emit 802 nm light pulses with a repetition rate of 80 MHz. A 1.5-m long multimode fiber was used to guide the light from the source to the surface of the animal head at a single position. Photons exciting the scalp were collected by four optodes configured linearly at distances of 6, 20, 30, and 40 mm from the source, which was guided through bandpass filters (FEB800-10, Thorlabs, NJ; to exclude fluorescence) to four photomultiplier tubes (PMC-100, Becker & Hickl Gmbh, Berlin, Germany). To perform DCE-NIR measurements, time-of-flight histograms were collected every 0.4 seconds for a total of 320 seconds during the passage of indocyanine green (ICG), the optical dye used as a contrast agent. Baseline data of 12.8 s were collected before the bolus injection. Distributions of time-of-flight (DTOF) were measured at all four channels simultaneously. In addition, the arterial input function (AIF) was acquired using a pulse dye densitometer (DDM2000, Nihon-Koden, Japan).

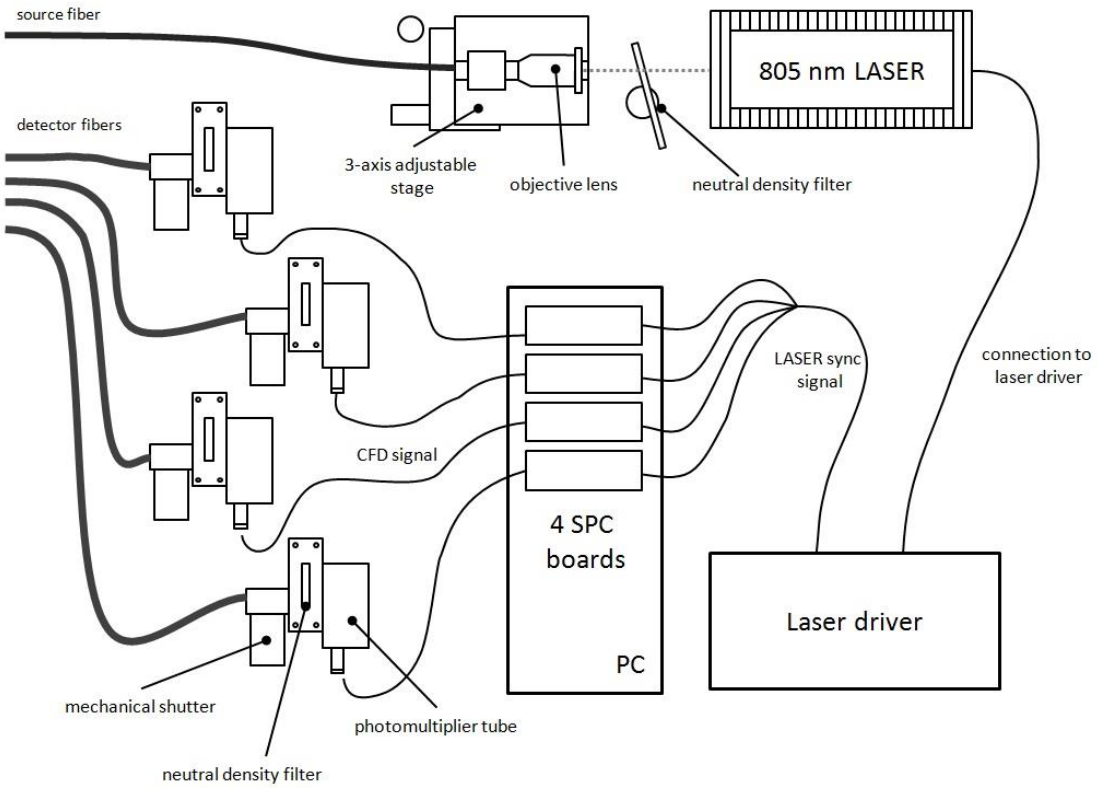

Figure 6.1: Layout of the time-resolved NIR system

The source fiber guides the pulsed light towards the sample, where it is collected by four fibers, and detected using four photomultiplier tubes (PMTs). The PMTs send constant fraction descriminator (CFD) signal to the four single-photon counting (SPC) boards located in the PC where the data is stored and displayed. The PMT data is synchronized to the laser driver via a sync cable.

Computed tomography anatomical images and CT perfusion maps were acquired using the LightSpeed QXi scanner (GE Healthcare, Waukesha, WI). Dynamic CT data was acquired during the bolus injection of an iodine-based contrast agent (1.0 mL/kg of iopamidol [300-Isovue®], Bracco S.p.A., Milan, Italy) at a rate of 1 ml/s. CT data was used as anatomical information in the light propagation modeling, as previously described (Elliott *et al* 2013a) Region-of-interest analysis was performed on CT perfusion parameteric maps to determine the mean value of CBF, CBV, and MTT within the volume of tissue interrogated by the DCE-NIR light. The region-of-interrogation was estimated from Monte Carlo generated sensitivity maps (Fang and Boas 2009). In addition to DCE-NIR validation, CT perfusion maps

were also used to confirm the magnitude and volume of the ischemic lesion following endothelin-1 injection.

6.2.6. Data analysis

The DTOFs measured at the four source-detector distances were converted to the three statistical moments of attenuation, mean time-of-flight and variance (Liebert *et al* 2004), which were smoothed using a Savitzky-Golay filter (using a window size of 12 seconds and a 7th order polynomial) prior to being analyzed (Savitzky and Golay 1964). The KDOR method, which was developed in-house and has been described in detail previously (Elliott *et al* 2013a; Elliott *et al* 2012b) was used to analyze the DCE-NIR moments. Briefly, CT anatomical images were segmented manually into scalp, skull, and brain, and Monte Carlo eXtreme (Fang and Boas 2009) was used to model light propagation at the source-detector positions used in the experiment. The transformation between the detected signal and the change in dye concentration in the tissue regions, known as the Jacobian, A, was calculated from the Monte Carlo results (Liebert *et al* 2004) using optical properties determined by fitting the baseline (pre-ICG) time-resolved data (Diop *et al* 2010) and anatomical information from the CT image. The Jacobian function, the DCE-NIR data and the AIF are input into the KDOR algorithm, which was used to recover BF, BV, and MTT for the ECL and brain regions. Specifically, these three parameters were calculated from region-specific impulse residue functions, based on the previously described method (Meier and Zierler 1954). A schematic of this process is provided in Fig. 6.2.

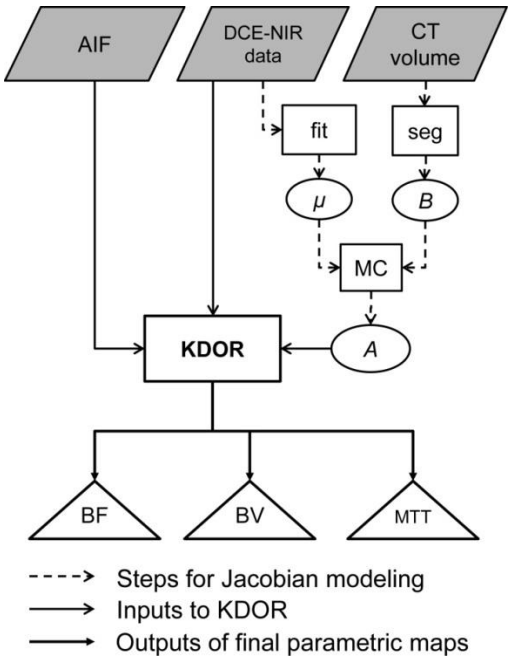

Figure 6.2: KDOR workflow

Flow chart outlining the steps involved in recovering the hemodynamic parameters. The parallelograms indicate the measured data from the three devices. Rectangles represent the analytical processes used: *fit*, diffusion approximation (DA) fitting routine; *seg*, manual or automatic segmentation; and *MC*, Monte Carlo modeling of the Jacobian. Intermediary parameters are represented by ovals: μ, region-specific bulk optical properties, *B,* binary segmented CT volume; and *A*, Jacobian. Finally, the recovered hemodynamic parameters (BF, blood flow; BV, blood volume; and MTT, mean transit time) are indicated by triangles.

The ECL fitting step (*fit*) involved optimizing the difference norm of time-resolved data collected at the 6 mm source-detector distance and the time-resolved function generated with the reflectance model of the diffusion approximation (Kienle and Patterson 1997). This procedure is described in detail elsewhere (Diop *et al* 2010). Segmentation (seg) was performed manually, slice-by-slice, on CT anatomical data that was acquired with a slice thickness of 5 mm.

6.2.7. Error analysis

An error analysis was conducted to investigate the influence of errors in the anatomical information used in the KDOR procedure that might occur during the clinical implementation of this technique. If it is assumed that the CT

images can be accurately segmented from clinical-resolution scans, then a potential source of error when inputting the anatomical information into the KDOR algorithm is co-registration of the optical probe positions using either feducial markers or a landmarking system (such as SLM10-20; Custo *et al* 2010). Errors in probe positioning could result in differences between the modeled and actual ECL geometry. This error was investigated by generating DCE-NIR forward data on a two-layer slab (ECL and brain) according to a previously described method (Elliott *et al* 2012). Following the addition of 5% Gaussian noise to the NIR and AIF signals, CBF was recovered with KDOR using a Jacobain modeled with four-layer slabs of varying thicknesses. The thickness of the ECL was varied between 14 and 17 mm, representing the variation in thickness measured from T2-weighted MRI images of 5 healthy subjects for positional changes of approximately 15 mm (data not published).

6.2.8. Statistical analysis

All data are presented as mean ± SEM unless otherwise indicated. An analysis of variance (ANOVA) was used to uncover any physiological condition effects on the physiological parameters, which were further investigated with Tukey's post hoc test when appropriate.

Linear regression analysis was performed on each hemodynamic parameter (CBF, CBV, and MTT) to examine correlations between the values obtained using the two techniques (DCE-NIR and CT perfusion). Since datasets included multiple measurements from the same animal, independence could not be assumed and therefore a variation of the generalized estimating equation was utilized (Zeger *et al* 1988). First, a linear fit was applied to the data from each animal separately. A t-test was used to compare the slope and intercept values obtained from each animal to a null hypothesis (*i.e.*, a slope of zero). Upon rejection of the null hypothesis,

the distribution of slopes was compared with a slope of unity to determine if the mean regression line was significantly different from the line of identity.

For the CBF regression plot (Fig. 6.6), the 95% confidence bounds on the regression line-of-best fit (*i.e.*, the region containing the 95% of the distribution of lines-of-best fit assuming a Gaussian random effect) were calculated. Finally, the degree of similarity between CBF measurements acquired with the two techniques was evaluated using a Bland-Altman plot (Bland and Altman, 1986). Differences with $p < 0.05$ were considered significant.

6.3. Results

6.3.1. Physiological parameters

Table 1 summarizes the physiological parameters of the eight pigs averaged for each condition. Respiration rate, which was artificially increased by adjusting the mechanical ventilator setting, was significantly higher during hypocapnia and ischemia conditions. This resulted in the intended decrease in pCO_2 measured from arterial samples, which was significantly different during hypocapnia and ischemia compared with baseline. A significant decrease was also observed in end-tidal CO_2 measurements. No significant differences were observed in SaO_2, HR, MAP, pO_2, glucose and temperature. The mean ECL thickness in these animals was 12.0 ± 0.6 mm (ranging from 10.5 to 14 mm), measured from CT images.

Table 6.1: Physiological parameters at each condition

	SaO_2 (%)	HR (min^{-1})	RR (min^{-1})	MAP (mmHg)	pCO_2 (torr)	pO_2 (torr)	glucose (mM)	temp (°C)
Baseline	100 ± 0	108 ± 2	29 ± 1*	49± 2	37.3 ± 0.7	168.6 ± 29.4	5.3 ± 1.0	37.3
Hypocapnia	99 ± 1	109 ± 4	46 ± 1*	46 ± 2	24.2 ± 1.2*	149.4 ± 10	5.4 ± 1.2	37.4
Ischemia	99 ± 0	124 ± 17	41 ± 2[b]	47 ± 4	26.0 ± 2.4*	138.4 ± 15.2	5.2 ± 0.8	37.3

SaO_2, arterial oxygen saturation; HR, heart rate; RR, respiration rate; MAP, mean arterial pressure; pCO_2, partial pressure of carbon dioxide; pO_2, partial pressure of oxygen. * $p < 0.01$ compared to baseline

6.3.2. Reproducibility of hypocapnia and ischemia

Analysis of variance with physiological condition (*i.e.*, baseline, hypocapnia, or ischemia) as a within-subject factor and modality (*i.e.*, CT perfusion or DCE-NIR) as between-subject factors revealed a significant condition effect on CBF measurements acquired with the two modalities ($F_{2,18} = 10.27$, $p < 0.01$) but no significant condition by modality interaction. Post-hoc analysis was performed with Tukey's method to further elucidate this condition effect. Compared with baseline, hypocapnia induced by artificially increasing the ventilator respiration rate from an average of 29 min^{-1} to an average of 46 min^{-1} resulted in a significant reduction in CBF measured with CT perfusion (43.0 ± 4.2 ml min^{-1} $100g^{-1}$ during hypocapnia vs. 61.7 ± 3.1 ml min^{-1} $100g^{-1}$ at baseline; $p < 0.05$) and with DCE-NIR (42.6 ± 3.7 ml min^{-1} $100g^{-1}$ during hypocapnia vs. 62.2 ± 4.7 ml min^{-1} $100g^{-1}$ at baseline; $p < 0.05$). A further reduction in blood flow was observed following intracortical injection of endothelin-1, which resulted in an average CBF value of 39.9 ± 3.1 and 32.7 ± 3.6 ml min^{-1} $100g^{-1}$, measured by CT perfusion and DCE-NIR, respectively.

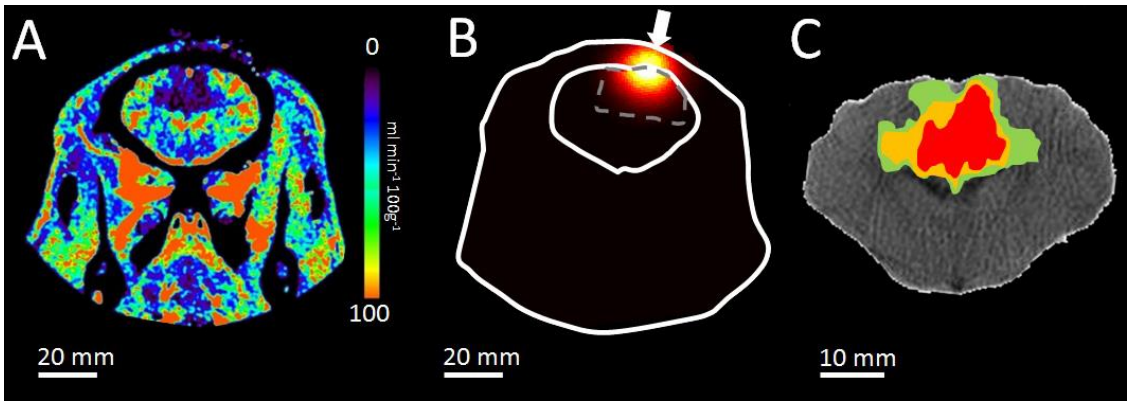

Figure 6.3: Sensitivity of optical measurements to endothelin-1 lesion.

(A) CT perfusion blood flow map with visible large lesion caused by endothelin-1 injection. (B) Map showing spatial sensitivity of optical signal measured at 40 mm source-detector distance (arrow represents source; arbitrary units). (C) Segmentation map showing regions identified as infarct (red), penumbra (orange), benign oligemia (green) based on thresholding of panel A.

A closer examination of the CT perfusion data acquired during ischemia identified the presence of four tissue states with clinical importance: infarct (< 10 ml min^{-1} $100g^{-1}$), penumbra (10-20 ml min^{-1} $100g^{-1}$), benign oligemia (20-40 ml min^{-1} $100g^{-1}$) in addition to normal tissue (> 40 ml min^{-1} $100g^{-1}$). The reproducibility of endothelin-1 induced ischemia was investigated in terms of the change in CBF compared to baseline *within the optical region of interrogation* as well as the total volume of the ischemic lesion (*i.e.*, infarct and penumbra regions). A mean percent decrease in CT perfusion-measured CBF of 36.5 ± 7.3% (S.D.) was observed during ischemia in the region interrogated by the NIR light, and the mean volume of the ischemic lesion was estimated to be 27.6 ± 10.4 ml (S.D.).

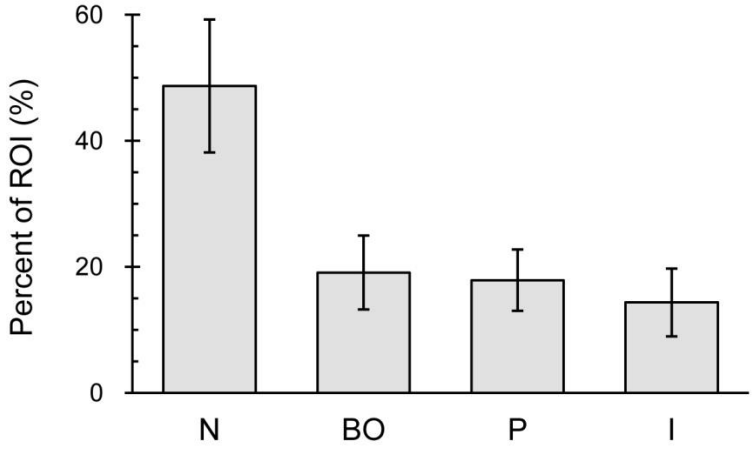

Figure 6.4: Average contribution of tissue states to the optical ROI

The average contribution of these tissue states to the optical region-of-interrogation across five animals. I, infarct (< 10 ml min^{-1} $100g^{-1}$); P, penumbra (10-20 ml min^{-1} $100g^{-1}$; BO, benign oligemia (20-35 ml min^{-1} $100g^{-1}$); N, normal.

Figure 6.3 shows a representative example of a CT perfusion map acquired during ischemia, a corresponding Monte Carlo sensitivity map, and a threshold map of the abnormal tissue states. To further investigate the robustness of the ischemic model to produce clinically relevant lesions, the percentage of the region-of-interest (ROI) representing the four tissue states was measured across all animals subjected to ischemia. On average, the three abnormal tissue states represented 48.7% of the total optical ROI. In Figure 6.4, a bar graph shows the mean percent contribution of the four tissue states within the region of interrogation.

6.3.3. DCE-NIR signal and recovered ICG concentration curves

Time-resolved data were collected before and during bolus injection enhancement at four source-detector distances. Changes in the statistical moments of time-of-flight distribution—attenuation, mean time-of-flight, and variance—were calculated for subsequent analysis by the KDOR method. Figure 6.5 shows a representative example of the change in attenuation and change in variance signals measured at two of the source-detector distances (40 and 6 mm) during DCE measurements acquired under the three

physiological conditions. The tissue concentration curves recovered from the same data for the scalp and brain regions, along with the arterial input functions measured with the dye densitometer, are also shown. In these three datasets, the CBF (determined using the KDOR method) was equal to 45 ml min^{-1} $100g^{-1}$ at baseline, 32.5 ml min^{-1} $100g^{-1}$ during hypocapnia, and 22.6 ml min^{-1} $100g^{-1}$ during ischemia.

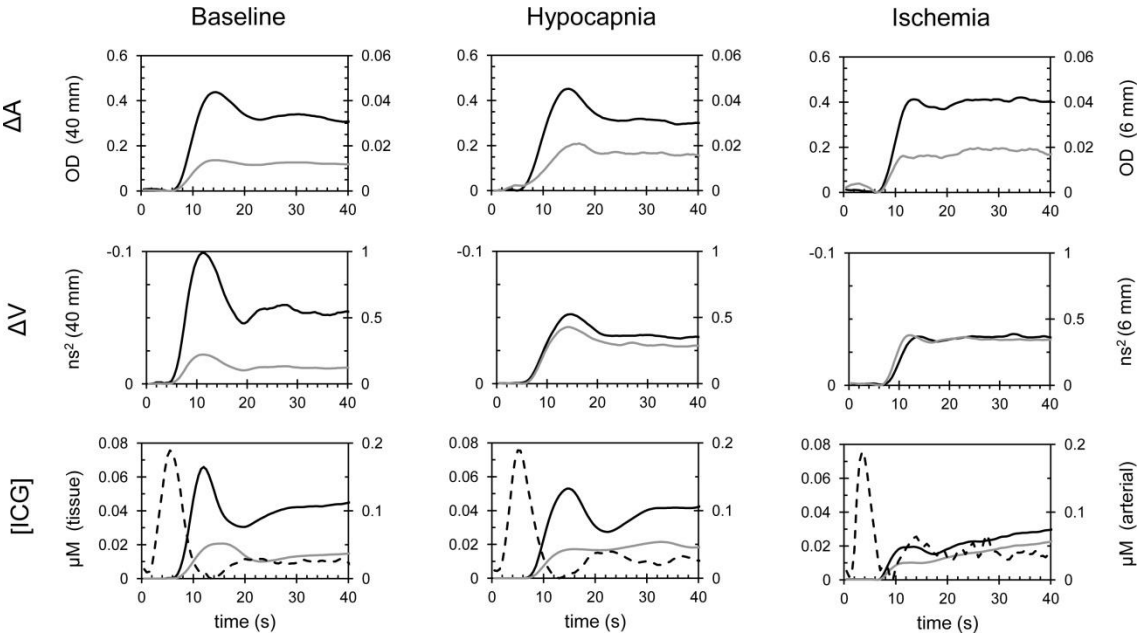

Figure 6.5: Dynamic contrast-enhanced signals during the three conditions

The attenuation (top row) and variance (middle row) signal measured at 40 mm (black line) and 6 mm (gray line) source-detector distances during baseline, hypocapnia and ischemia (left-to-right). The recovered tissue concentration curves for the brain (solid black line) and ECL (solid gray line), and the corresponding arterial input function (dashed line) for the same data are presented in the bottom row.

6.3.4. Comparison of hemodynamic parameters calculated using DCE-NIR and CT perfusion

As stated in the methods section, a simple linear regression approach could not be performed because both independent and within-subject data are represented. Therefore, regression analysis was performed on data from each animal, individually, and the average of the eight analyses was determined. This approach was used to determine the relationship between CT perfusion

and DCE-NIR measured CBF, and between CT perfusion and DCE-NIR values of BV. Figure 6.6 shows the regression plot of the CBF data; the line-of-best fit averaged across the individual regression analyses had a slope of 1.06 ± 0.08, and a y-intercept of −4.37 ± 4.33 ml min^{-1} $100g^{-1}$. The average slope was significantly different from the null ($p < 0.001$) but not significantly different from the line of identity ($p = 0.81$). The average y-intercept was not significantly different from zero ($p = 0.76$). The average r value, calculated from the individual regression analyses was 0.86 ± 0.06.

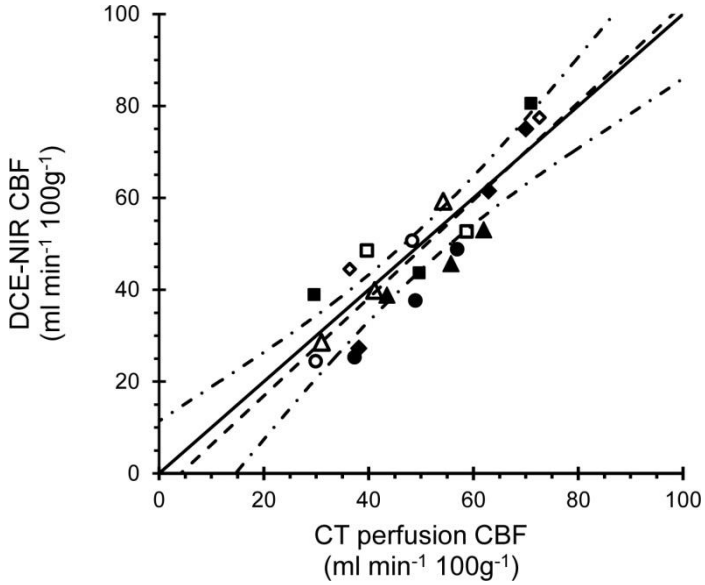

Figure 6.6: Cerebral blood flow regression plot

Regression plot comparing CBF values calculated from DCE-NIR data and concomitant CT perfusion values of CBF. Data are grouped by animal (n=8) and represented with a unique symbol. Regression analysis was performed on each group individually, and the average line-of-best fit is indicated by the dashed line (*slope* = 1.06 ± 0.08, *y-intercept* = -4.37 ± 4.33 ml min^{-1} $100g^{-1}$).

The regression analysis of BV measured with the two techniques yielded an average line-of-best fit with a slope of 2.49 ± 0.34 and a y-intercept of 0.14 ± 1.60 ml $100g^{-1}$. The average slope was significantly different from the null ($p < 0.01$) and significantly different from the line of identity ($p < 0.05$). The y-intercept was not significantly different from zero ($p = 0.90$). The average r value for the CBV regression analyses was 0.56 ± 0.13. The mean difference

between BV calculated with the two techniques was 6.53 ml $100g^{-1}$, and the data was bound by a 95% confidence interval of 3.12 – 9.95 ml $100g^{-1}$. Finally, the average difference between the two techniques was significantly different from the null ($p < 0.001$), suggesting the presence of a systemic bias that would allow one technique to be calibrated to the other.

Figure 6.7 shows the Bland-Altman plot comparing the CBF measurements from the two techniques. The mean difference between the two techniques was −1.7 ml min^{-1} $100g^{-1}$, which was bound by a 95% confidence interval of −16.3 to 12.9 ml min^{-1} $100g^{-1}$. In this case, the average difference between the two techniques was not significantly different from the null ($p = 0.31$).

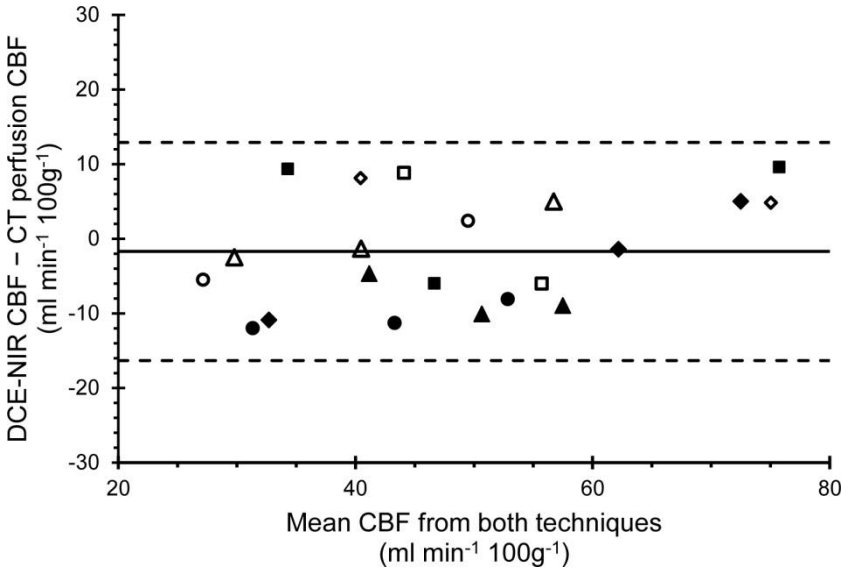

Figure 6.7: Cerebral blood flow Bland-Altman plot

Bland-Altman plot comparing the CBF measurements obtained with the DCE-NIR method and the CT perfusion method. Data are grouped by animal using the same symbols as in Figure 6.6. The mean difference between the two methods is indicated by the solid line, and the 95% confidence interval is demarcated by the dashed line. No statistically significant CBF magnitude effect was detected.

6.3.5. Error analysis

Two error analyses were conducted to investigate potential sources of model uncertainty that could occur within the context of the KDOR framework presented in Figure 6.2. Uncertainties in probe holder position, which was determined from segmented CT images corregistered to the optical imaging domain, were investigated by generating forward optical data (replicating the experimental data) for an ECL thickness of 15 mm, and then reconstructing the same optical data with light propagation models assuming ECL thickness values from 13 to 17 mm. No significant differences were observed across ECL thickness values ($p = 0.83$). The results of this error analysis are shown in Figure 6.8A.

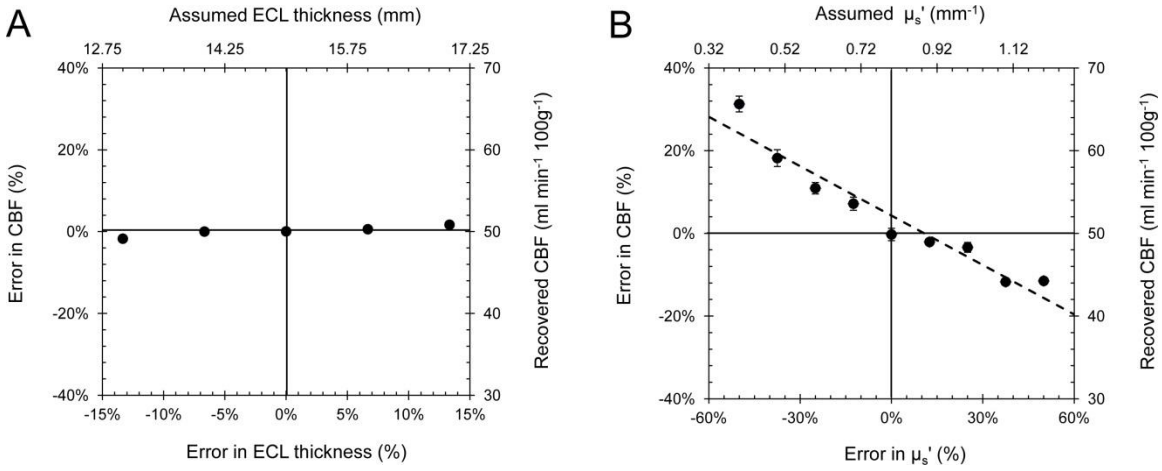

Figure 6.8: Probe position and scattering coefficient error analysis

(A) The relationship between error in assumed ECL thickness and error in the recovered CBF, simulated for a range of ECL thicknesses between 13 and 17 mm. (B) The relationship between error in the ECL reduced scattering coefficient, μ_s', and the error in recovered CBF. The regression line-of-best fit (*slope* = -0.39, *y-intercept* = 4%) is also shown (dashed line).

The value of directly measuring the ECL reduced scattering coefficient was evaluated by generating forward optical data with an ECL reduced scattering coefficient of 0.8 mm^{-1}, and then reconstructing the same data with light propagation models using ECL scattering coefficient values from 0.4 to 1.2 mm^{-1}. A significant correlation between the error in reduced scattering

coefficient and error in recovered CBF was observed (*slope* = -0.39, *y-intercept* = 4%, $r = 0.96$, $p < 0.001$). These numerical results are shown in Figure 6.8B.

6.4. Discussion

Dynamic contrast-enhanced optical measurements of CBF have been proposed for over 25 years as an attractive modality for bedside clinical monitoring, especially within the context of critical care. In particular, because DII is a leading contributor to poor outcome in patients that have sustained severe traumatic brain injury (Bouma *et al* 1991), stroke (Dirnagl *et al* 1999), and subarachnoid hemorrhage (Hijdra *et al* 1988), the ability to measure CBF at the patient's bedside would be of great value. Currently, only surrogate markers of CBF (*i.e.*, intracranial pressure and cerebral perfusion pressure) are available to assess neurological recovery, and considerable controversy surrounds the use of these indirect markers of CBF to guide patient management. Despite the significant clinical potential of bedside CBF measurements, it is only recently that optical techniques have shown promise in achieving the stated goal.

An early study by Owen-Reece and colleagues identified the problem of extracerebral signal contamination as a confounding factor in optical measurements of CBF, resulting in a large underestimation of CBF. To overcome this problem, they suggested the use of a correction factor to calibrate NIRS CBF measurements to measurements obtained with an alternate technique. This was, in part, based in the assumption that the extracerebral layer effect was primarily due to a partial volume error, and that this effect would show low intrasubject variability (Owen-Reece *et al* 1996). The notion of a direct correlation between NIRS-CBF measurements and CBF measured by an alternate method was challenged by a later study. Schytz and colleagues showed an absence of any correlation between CBF

measured concomitantly with NIRS and SPECT in healthy subjects before and after administration of acetazolamide (Schytz *et al* 2009). In particular, this study highlighted the lack of a universal correction factor for NIRS measurements of CBF, underlining the importance of subject-specific modeling using anatomical priors (Elliott *et al* 2010).

The advent of more sophisticated optical methods—including time-resolved and frequency-domain NIR techniques—resulted in an increase in sensitivity to deeper tissue structures, such as the brain. In particular, time-resolved methods allowed the discrimination of photons based on the time-of-flight (*i.e.*, the time required for a photon to travel from the source fibre to the detector), providing additional improvements in brain tissue sensitivity on the basis that late-arriving photons are statistically more likely to interrogate deeper tissue (Steinbrink *et al* 2001; Liebert *et al* 2004). Several papers have been published demonstrating qualitative curve analysis (Liebert *et al* 2006, Liebert *et al* 2012) and within subject quantification (Steinkellner *et al* 2010) of ICG bolus measurements acquired in neurocritical care patients with time-resolved methods. While this work has established the sensitivity of DCE-NIR methods to CBF changes, measurements are typically relative blood flow indices calculated using methods such as time-to-peak (TTP). In Chapter 3, it was demonstrated that TTP analysis is unreliable when perturbations in cerebral blood volume and the arterial input function occur (Elliott *et al* 2013b). An alternative method of analyzing DCE-NIR data was presented, in which nonparametric kinetic analysis (Elliott *et al* 2013b) was used to calculate a relative blood flow index that showed good agreement with CBF changes determined from CT perfusion.

It is likely that absolute CBF measurements will be more clinically useful than relative blood flow indices, since well-defined CBF thresholds for cell dysfunction and irreversible cell damage are known (Jones *et al* 1981; Astrup *et al* 1981; Schaefer *et al* 2006). Therefore, to provide absolute

measurements of CBF, time-resolved instrumentation was combined with subject-specific light propagation modeling, and subsequently incorporated into an analytical framework called kinetic deconvolution optical reconstruction (KDOR). The theoretical basis for the KDOR method was described in a recent Letter, and provides a more robust means of separating the ECL and brain contributions to the optical signal through the use of anatomical priors and physiological constraints (Elliott *et al* 2012b). The main objective of this study was to confirm these theoretical predictions by validating DCE-NIR CBF measurements against CT perfusion measurements acquired concomitantly in adult pigs.

The representative example of optical signals measured in a single animal at three different physiological conditions provided in Figure 6.5 illustrates the features of DCE-NIR data. As expected from previous studies (Liebert *et al* 2004; Steinkellner *et al* 2010; Liebert *et al* 2006), including the study presented in Chapter 3, differences between attenuation and variance signals were observed. The subtle differences at baseline suggest increased sensitivity of variance to faster cerebral tracer kinetics. As CBF decreased due to hypocapnia and ischemia, greater differences between these three conditions were observed in the variance signal than in the attenuation signal—a trend observed in the Chapter 3 study. Improvements in sensitivity provided by the variance signal facilitated the recovery of tissue concentration curves, which appear to reflect the corresponding change in CBF, both in the peak concentration and the temporal dynamics. An interesting feature of the tissue concentration curves recovered for the ischemia condition is the apparent transient increase in concentration following the recirculation of dye. This is likely an artifact of the reconstruction process, as opposed to any real kinetic effect such as extravasation, and is an atypical feature. It is important to note that constraints implemented by the KDOR inversion have the greatest effect on

the first rise, and peak concentration, of the corresponding tissue concentration curves. Therefore, any small discrepancies in the shape of the reconstructed tissue curve is not indicative of a significant error in recovered CBF.

For all eight animals, values of CBF and CBV recovered with the DCE-NIR method were compared to CT perfusion values—the most common method used to assess these parameters clinically (Koenig *et al* 1998; Mayer *et al* 2000). In general, an excellent agreement was observed between CBF measurements acquired with the two modalities with a precision comparable to previous studies published by our group for the neonatal pig model (Brown *et al* 2002), as well as the juvenile pig study presented in Chapter 2. It is likely that the improvements in instrumentation (time-resolved vs. continuous-wave) and the use of the KDOR method to mitigate optical reconstruction problems (Bonfert-Taylor *et al* 2012) contributed to the strong correlation with CT perfusion measurements, despite the use of animals with thicker ECLs and reduced scalp flow. While CBV values measured with the DCE-NIR method showed a strong correlation with CT perfusion measurements, the optical technique reported values that were on average 2.5 times larger (baseline mean values of 4.7 ml $100g^{-1}$ and 11.39 ml $100g^{-1}$ determined with CT perfusion and DCE-NIR, respectively). One explanation for this discrepancy is that the two methods utilize different kinetic modeling approaches to calculate hemodynamic parameters from DCE. The CT Perfusion 4 program utilizes a variation of the adiabatic approximation to the tissue homogeneity (AATH) model (Bisdas *et al* 2008) which is essentially a plug flow model. Plug flow models have been demonstrated to underestimate mean transit time (MTT) in many situations (Schabel 2012; St. Lawrence *et al* 2013), and since CBV is directly related to MTT by the central volume principle, it is also underestimated. On the other hand, the DCE-NIR method employs a nonparametric deconvolution method to recover an arbitrary

hemodynamic function. Since the NIR region-of-interrogation is larger, it is likely to contain a distribution of MTTs that contribute to an overall larger CBV than would be observed for a single CT voxel. In addition to the transit time distribution effect, because the DCE-NIR method does not truncate the recovered hemodynamic function, it is likely that any residual scalp contribution that remains in the brain signal would contribute disproportionately to CBV, without significantly affecting CBF values. Nevertheless, it is important to recognize that the discrepancy between CBV values attributed to these differences resulted in a consistent bias across all eight animals, suggesting that a simple calibration curve could be used to relate the two modalities if desirable.

Given the strong correlation between the DCE-NIR method and the clinical standard, a closer investigation of the analytical framework is pertinent. In particular, it is worthwhile investigating the relative importance of the priors incorporated into the workflow before the KDOR routine is executed. First, while the acquisition of anatomical imaging (*i.e.*, CT or MRI) is ubiquitous in almost all neurotrauma centers, the segmentation and incorporation of this data into a subject-specific model may not be trivial within the context of acute care. In particular, it may be difficult to provide an accurate method of coregistering the anatomical data with the location of the optical probes, which was rather straightforward in these experiments given the visibility of the polychloroprene probe holder on the CT images. While the use of feducal markers has been explored elsewhere, it is likely that a landmark system such as the 10-20 international system (Custo *et al* 2010) used for electroencephalogram placement would be more clinically compatible. To this end, the effect of small errors in optical probe corregistration was investigated by varying the ECL thickness within a range typical of small but non-negligible positional changes on an average human head. No significant difference was found in the recovered blood flow

values across the range of ECL thicknesses, suggesting that the DCE-NIR method is insensitive to small perturbations in ECL thickness. As a result, it is reasonable to assume that a less accurate positioning system, such as the SLM 10-20, would provide acceptable accuracy. The importance of measuring the optical properties of the ECL using time-resolved data collected at the 6 mm source-detector distance was also investigated. Across a range of values for the reduced scattering coefficient, a significant correlation between error in CBF and error in μ_s' was determined. More specifically, an error of about 40% in μ_s' resulted in a 20% error in CBF. Given that reported values of μ_s' for the scalp of the human head include 1.0 mm^{-1} (Boas *et al* 2002), 1.2 mm^{-1} (Choi *et al* 2004), and 1.7 mm^{-1} (Okada and Delpy 2003), using an assumed value for μ_s' would introduce a large amount of uncertainty. In part, the results of this second error analysis provide a strong justification for the use of time-resolved instrumentation to directly measure the optical properties in the ECL, despite its relative sensitivity to stray light compared to continuous-wave systems.

In this study of cerebral ischemia, intracortical injection of endothelin-1 was used to produce a large lesion containing infarct and penumbra tissue states, which persisted long enough to acquire the three measurements needed for this study. A limitation with this model is that only a portion of the lesion (14%) was reduced to ischemic levels, as defined by CBF less than 10 ml min^{-1} $100g^{-1}$, with penumbra (10 - 20 ml min^{-1} $100g^{-1}$) and benign oligemia (20 - 35 ml min^{-1} $100g^{-1}$) regions also contributing to 18 and 19%, respectively. Since the NIR region-of-interrogation encapsulated all of these components, the recovered CBF values by DCE-NIR and corresponding CT perfusion values averaged over a representative region-of-interest did not reach ischemic levels. However, given that the difference between the two techniques, as determined with the Bland-Altman method (Fig. 6.7) did not

depend on the blood flow level, it is reasonable to assume that DCE-NIR would quantify even lower levels of CBF with comparable precision.

6.5. Conclusions

The present study validated the DCE-NIR method of measuring CBF, which combines multi-distance time-resolved measurements, arterial input function characterization, and subject-specific light propagation modeling using the KDOR analytical framework. This work provides a convincing argument for using this robust optical method to measure CBF in the neurocritical care unit, where quantitative CBF measurements may provide a means of guiding patient management and intervention.

6.6. References

Arora R, Ridha M, Lee D, Elliott JT, Diop M, Rosenberg H, Lee TY and St. Lawrence K 2013 Preservation of the metabolic rate of oxygen in preterm infants during indomethacin therapy for closure of the ductus arteriosus *Pediatr Res* doi:10.1038/pr.2013.53.

Bonfert-Taylor P, Leblond F, Holt RW, Tichauer K., Pogue BW, Taylor EC 2012 Information loss and reconstruction in diffuse fluorescence tomography *JOSA A* 29(3) 321-330.

Biega TJ, Lonser RR, Butman JA 2006 Differential cortical thickness across the central sulcus: a method for identifying the central sulcus in the presence of mass effect and vasogenic edema *Amer J Neurorad* 27(7) 1450-1453.

Bisdas S, Konstantinou G, Surlan-Popovic K, Khoshneviszadeh A, Baghi M, Vogl TJ, Koh TS, Mack M G 2008 Dynamic contrast-enhanced CT of head and neck tumors: comparison of first-pass and permeability

perfusion measurements using two different commercially available tracer kinetics models *Acad Radiol* 15(12) 1580-1589.

Brown DW, Picot PA, Naeini JG, Springett R, Delpy DT, Lee T-Y 2002 Quantitative near infrared spectroscopy measurement of cerebral hemodynamics in newborn piglets *Pediatr Res* 51(5) 564-570.

Boas D, Culver J, Stott J, Dunn A 2002 Three dimensional Monte Carlo code for photon migration through complex heterogeneous media including the adult human head *Opt Exp* 10(3) 159-170.

Bouma GJ, Muizelaar JP, Choi SC, Newlon PG, Young HF 1991 Cerebral circulation and metabolism after severe traumatic brain injury: the elusive role of ischemia *J Neurosurg* 75(5) 685-693.

Choi J, Wolf, M., Toronov V, Wolf U, Polzonetti C, Hueber D, Safonova LP, Gupta R, Michalos A, Mantuilin W, Gratton E 2004 Noninvasive determination of the optical properties of adult brain: near-infrared spectroscopy approach *J Biomed Opt* 9(1) 221-229.

Corlu A, Choe R, Durduran T, Lee K, Schweiger M, Arridge SR, Yodh AG 2005 Diffuse optical tomography with spectral constraints and wavelength optimization *Appl Opt* 44(11) 2082-2093.

Custo A, Boas DA, Tsuzuki D, Dan I, Mesquita R, Fischl B, Grimson WEL, Wells W 2010 Anatomical atlas-guided diffuse optical tomography of brain activation *Neuroimage* 49(1) 561-567.

Diop M, Tichauer KM, Elliott JT, Migueis M, Lee T-Y, St. Lawrence K 2010 Time-resolved near-infrared technique for bedside monitoring of absolute cerebral blood flow *Proc SPIE* 7555 75550Z.

Dirnagl U, Iadecola C, Moskowitz MA 1999 Pathobiology of ischaemic stroke: an integrated view *Trend Neurosci* 22(9) 391-397.

Elliott JT, Diop M, Morrison LB, Lee TY, St. Lawrence K 2013a Reconstruction of cerebral hemodynamics with dynamic contrast-enhanced time-resolved near-infrared measurements before and during ischemia *Proc SPIE* 8578 857810.

Elliott JT, Milej D, Gerega A, Weigl W, Diop M, Morrison LB, Lee TY, Leibert A, St. Lawrence K 2013b Variance of time-of-flight distribution is sensitive to cerebral blood flow as demonstrated by ICG bolus-tracking measurements in adult pigs *Biomed Opt Exp* 4(2) 206-18.

Elliott JT, Wright EA, Tichauer KM, Diop M, Morrison LB, Pogue BW, Lee TY, St. Lawrence K 2012a Arterial input function of an optical tracer for dynamic contrast enhanced imaging can be determined from pulse oximetry oxygen saturation measurements *Phys Med Biol* 57(24) 8285.

Elliott JT, Diop M, Lee TY, St. Lawrence K 2012b Model-independent dynamic constraint to improve the optical reconstruction of regional kinetic parameters *Opt Lett* 37(13) 2571-73.

Fang Q, Boas DA 2009 Monte Carlo simulation of photon migration in 3D turbid media accelerated by graphics processing units. *Opt Expr* 17(22) 20178-20190.

Franceschini MA, Joseph DK, Huppert TJ, Diamond SG, Boas DA 2006 Diffuse optical imaging of the whole head *J Biomed Opt* 11(5) 054007-054007.

Friberg L, Kastrup J, Hansen M, Bulow J 1986 Cerebral effects of scalp cooling and extracerebral contribution to calculated blood flow values

using the intravenous 133Xe technique *Scand J Clin Lab Invest* 46 375-379

Gora F, Shinde S, Elwell CE, Goldstone JC, Cope M, Delpy DT, Smith M 2002 Noninvasive measurement of cerebral blood flow in adults using near-infrared spectroscopy and indocyanine green: a pilot study *J Neurosurg Anesthesiol* 14, 218-222.

Hijdra A, Van Gijn J, Nagelkerke NJ, Vermeulen M, Van Crevel H 1988 Prediction of delayed cerebral ischemia, rebleeding, and outcome after aneurysmal subarachnoid hemorrhage *Stroke* 19(10) 1250-1256.

Jelzow A, Wabnitz H, Obrig H, Macdonald R, Steinbrink J 2012 Separation of indocyanine green boluses in the human brain and scalp based on time-resolved in-vivo fluorescence measurements *J Biomed Opt* 17(5) 057003-1.

Jones TH, Morawetz RB, Crowell RM, Marcoux FW, FitzGibbon SJ, DeGirolami U, Ojemann RG 1981 Thresholds of focal cerebral ischemia in awake monkeys *J Neurosurg* 54(6) 773-782.

Kienle A, Patterson MS 1997 Improved solutions of the steady-state and the time-resolved diffusion equations for reflectance from a semi-infinite turbid medium *J Opt Soc Am A Opt Image Sci Vis* 14(1) 246-254.

Koenig M, Klotz E, Luka B, Venderink DJ, Spittler JF, Heuser L 1998 Perfusion CT of the brain: diagnostic approach for early detection of ischemic stroke *Radiol* 209(1) 85-93.

Liebert A, Milej D, Weigl W, Gerega A, Kacprzak M, Mayzner-Zawadzka E, Maniewski R 2012 Assessment of brain perfusion disorders by ICG bolus tracking with time-resolved fluorescence monitoring in

BIOMED Conference Proceedings (Optical Society of America: Miami, Fl) BTu3A.

Liebert A, Wabnitz H, Obrig H, Erdmann R, Moller M, Macdonald R, Rinneberg H, Villringer A, Steinbrink J 2006 Non-invasive detection of fluorescence from exogenous chromophores in the adult human brain *Neuroimage* 31 600-608.

Liebert A, Wabnitz H, Steinbrink J, Obrig H, Moller M, Macdonald R, Villringer A, Rinneberg H 2004 Time-resolved multidistance near-infrared spectroscopy of the adult head: intracerebral and extracerebral absorption changes from moments of distribution of times of flight of photons *Appl Opt* 43 3037-3047.

Mayer TE Hamann GF, Baranczyk J, Rosengarten B, Klotz E, Wiesmann M, Brueckmann HJ 2000 Dynamic CT perfusion imaging of acute stroke. *AJNR Am J Neuroradiol* 21(8) 1441-1449.

Meier P, Zierler KL 1954 On the theory of the indicator-dilution method for measurement of blood flow and volume *J Appl Physiol* 6 731-744.

Savitzky A, Golay MJ 1964 Smoothing and differentiation of data by simplified least squares procedures *Anal Chem* 36(8) 1627-1639.

Schabel MC 2012 A unified impulse response model for DCE-MRI *Magn Res Med* 68(5) 1632-46.

Schaefer PW, Roccatagliata L, Ledezma C, Hoh B, Schwamm LH, Koroshetz W, Gonzalez RG, Lev MH 2006 First-pass quantitative CT perfusion identifies thresholds for salvageable penumbra in acute stroke patients treated with intra-arterial therapy *AJNR Am J Neuroradiol* 27(1) 20-25.

Schytz HW, Wienecke T, Jensen LT, Selb J, Boas DA and Ashina M 2009 Changes in cerebral blood flow after acetazolamide: an experimental study comparing near-infrared spectroscopy and SPECT *Eur J Neurol* 16(4) 461-467.

Steinbrink J, Wabnitz H, Obrig H, Villringer A, Rinneberg H 2001 Determining changes in NIR absorption using a layered model of the human head *Phys Med Biol* 46(3) 879.

Steinkellner O, Gruber C, Wabnitz H, Jelzow A, Steinbrink J, Fiebach JB, Macdonald R, Obrig H 2010 Optical bedside monitoring of cerebral perfusion: technological and methodological advances applied in a study on acute ischemic stroke *J Biomed Opt* 15 061708.

St Lawrence K, Verdecchia K, Elliott J, Tichauer K, Diop M, Hoffman L, Lee T-Y 2013 Kinetic model optimization for characterizing tumour physiology by dynamic contrast-enhanced near-infrared spectroscopy *Phys Med Biol* 58(5) 1591.

United States Food and Drug Administration 2012 Approved Drug Products with Therapeutic Equivalence Evaluations (Government Printing Office: Washington, DC).

Waydhas C 1999 Intrahospital transport of critically ill patients *Crit Care* 3 R93-99.

Chapter 7

CONCLUSIONS AND FUTURE WORK

The final chapter of this thesis provides a summary of the dynamic contrast enhanced (DCE) near-infrared (NIR) method developed to measure hemodynamic parameters in neurocritical care unit (NCU) patients. As the objectives of this thesis were advanced, improvements were made to the instrumentation and the analytical approach, beginning with the depth-resolved continuous-wave (CW) near-infrared spectroscopy (NIRS) method in Chapter 2. Next, a blood flow index calculated from the variance of time-resolved (TR) NIR distribution of time-of-flight (DTOF) measurements was described as a reliable technique to measure changes in cerebral blood flow (CBF) (Chapter 3). Finally, a multi-distance TR moments-based method using the kinetic deconvolution optical reconstruction (KDOR) approach was validated in an adult pig model of ischemia (Chapter 6). Each of these developments will be summarized within the context of the objectives presented in Chapter 1. Following this, the future work for this technology will be discussed and the principle conclusions of the thesis will be stated.

7.1. Summary of stated objectives

The four objectives of this thesis focused mainly on: *(i)* the design and optimization of clinically compatible instruments, *(ii)* the development of an analytical framework, *(iii)* the development of clinically relevant animal

model for NCU applications, and finally, *(iv)* the validation of the technique against CT perfusion. These will now be addressed in turn.

7.1.1. Design and optimization of NIR instrumentation

The design and optimization of the DCE-NIR system was accomplished in three main steps. First, a two-channel continuous-wave broadband system was developed, based on the previous work of our group in using CW NIRS to measure CBF in neonatal pigs (Brown *et al* 2002; Tichauer *et al* 2006) and more recently, in the neonatal intensive care unit (Arora *et al* 2013). In the subsequent study, a time-resolved system was introduced to improve brain sensitivity through the use of statistical moments of DTOF data. Chapter 3 highlighted the results obtained using the variance signal measured at 30 mm to calculate a relative blood flow index, *dBF*, which is capable of tracking changes in CBF. It was evident from the error analysis and the strong agreement with CBF changes measured by CT perfusion that a necessary precursor in proper kinetic analysis of DCE-NIR is the acquisition of the AIF. Therefore, in Chapter 4, an alternate method of capturing the AIF was described to eliminate the need of a specialized dye densitometer. The goal in developing this pulse oximeter (PO)-based method was to facilitate clinical implementation of DCE-NIR by leveraging the ubiquity of POs in the critical care setting. Finally, in Chapter 6, a multichannel TR-NIR system was presented that enabled the three statistical moments (A, $\langle t \rangle$, and V) acquired at four source-detector distances (6, 20, 30, and 40 mm) to be measured simultaneously. This sophisticated instrumentation enabled accurate and precise characterization of CBF, even in the presence of substantial ECL contamination. In particular, an error analysis demonstrated the importance of direct determination of extracerebral layer (ECL) optical properties, which can be done effectively using TR-NIR.

7.1.2. Development of the analytical framework

In parallel to the developments in instrumentation, improvements in analytical methodology were made. In the first pig study, the inter-subject variability in sensitivity factors (*i.e.*, mean partial pathlengths (MPPs)) was identified as the likely cause of reported failure of DCE NIRS to measure or even track changes in CBF in adult subjects (Schytz *et al* 2009). Therefore, subject-specific Monte Carlo simulations were implemented and a lookup table of MPPs was generated using two-layer models with varying ECL thicknesses. For each animal, MPPs were selected from the library using an objective cost function that optimized two error norms: ECL thickness of the two-layer model compared to the value measured from the animal's CT image, and the resulting brain water concentration compared with the assumed value of 80%. Compared to the simple subtraction method, in which a group averaged MPP set was used, the subject-specific approach significantly reduced the inter-subject variability and, as a result, NIRS CBF measurements showed good agreement with CT perfusion values. Time-resolved NIR was implemented as a way to further improve depth sensitivity by measuring the DTOFs. The use of the change in statistical variance of the DTOF during ICG uptake and washout to calculate a deconvolution-based blood flow index (*dBF*) was investigated, avoiding the need for the subject-specific modeling used in the previous study. A secondary goal of this study was to highlight the pitfalls of using the TTP as a surrogate of CBF changes: a commonly used approach in DCE optics. A more robust analytical approach based on the deconvolution method was developed, and it is arguably the most significant advancement of this doctoral work. The ill-posed nature of optical reconstruction impacts almost every field of biomedical optics and any additional unique information that can be included in the reconstruction problem will likely improve the results. The KDOR method, described in Chapter 5, is a novel reconstruction approach that uses dynamic priors. The

ability of this method to recover CBF accurately was demonstrated in Chapter 6.

7.1.3. Development of the animal model

Adult pigs were used in all three DCE NIR studies since they have similar ECL thickness to humans. Furthermore, the average CBF of an adult pig is similar to the human adult. The main limitations of the pig model are small size of the brain relative to the head and the higher scalp blood flow than in the humans due to the thicker temporalis muscles that have evolved to enable strong mastication. The former issue is not a problem because the farthest source-detector distance (40 mm) was well within the length of the brain. To overcome the second limitation, three incisions were made rostral, caudal and lateral to the optodes in the second and third pig studies to reduce scalp blood flow to less than 10 ml min^{-1} $100g^{-1}$, as observed in humans. In all three animal studies, CBF was varied over a range of values by adjusting the $PaCO_2$ (*i.e.*, hypercapnia and hypocapnia). However, two limitations of this approach were identified within the context of DCE NIR validation. First, hypocapnia does not decrease CBF below the clinically important thresholds of either infarct or penumbra. Second, a vascular response to $PaCO_2$ may occur in the ECL, as well as in the brain. The latter could confound the ability to assess whether depth-resolved NIRS is truly sensitive to only flow changes occurring in the brain. For these two reasons, we introduced the ischemic model in Chapter 6, which involves inducing a large ischemic lesion by intracortical injection of endothelin-1. Computed tomography maps were used to demonstrate the reproducibility of the model in causing a large volume (27.6 ± 10.4 ml) lesion with infarct, penumbra and benign oligemia tissue states.

7.1.4. Validation of the method against CT perfusion

Finally, validation of the DCE-NIR method was accomplished at each stage of development through comparisons to CT perfusion, the current clinical standard for CBF measurements. In the first study, the DCE-NIR measurements of CBF showed strong agreement with CT perfusion values ($r = 0.84$, $p < 0.001$), and the mean difference between the two techniques was -2.83 ml $min^{-1} \cdot 100$ g^{-1} with a 95% confidence interval of -19.63 ml min^{-1} 100 g^{-1} to 14.00 ml min^{-1} 100 g^{-1}. In the second study, the specificity and sensitivity of the *dBF* index measured from the variance signal was investigated in four animals. First, extracerebral blood flow and composition was modulated to determine the effect of the ECL on the measured index: the average change in *dBF* during these manipulations was 0.2 ± 2.4%. Second, the ability of *dBF* to track changes in CBF was examined by inducing hypocapnia and performing concomitant measurements of CBF with CT perfusion. In this case, measurements of dBF acquired on the surface of the head showed a similar decrease compared with CT perfusion values of CBF. In the third pig study, DCE-NIR measurements of CBF analyzed using KDOR showed strong agreement with CT perfusion values ($r = 0.86$, $p < 0.001$) across a range of blood flow levels from about 25 to 75 ml min^{-1} $100g^{-1}$. The mean difference between the two techniques was -1.7 ml min^{-1} $100g^{-1}$, which was bound by a 95% confidence interval of −16.3 to 12.9 ml min^{-1} $100g^{-1}$. Furthermore, the validation was performed in animals with an ECL thickness similar to adults. This final validation study confirmed that accurate measurements of CBF can be obtained from DCE-NIR measurements acquired on the surface of the head, during normal, oligemic and ischemic blood flows.

7.2. Future work

7.2.1. Improvements to DCE-NIR and KDOR analysis

The analytical method described in this thesis can be advanced in two different directions, depending on the demands of the situation. In certain cases, a large amount of information might be sought from a large number of inputs—*e.g.*, for imaging applications. To properly characterize the spatial distribution of a parameter, such as CBF, it is necessary to increase the number of channels of data so that the system is not underdetermined. For example, a recent study demonstrated the use of a CW-NIRS instrument for acquiring DCE data on the surface of the head, simultaneously, in 900 channels (Habermehl *et al* 2013). Another large-scale problem arises when attempting to analyze the DTOFs directly, instead of reducing the problem to the three statistical moments A, $\langle t \rangle$, and V.

Since KDOR differs from traditional optical reconstruction methods, in that it uses the NNLS algorithm with equality and inequality constraints, its current implementation is computationally demanding, due to a need to perform a full pseudo-inverse calculation for each iteration (Chen and Plemmons 2009). This limitation can be somewhat mitigated by applying a dimension-reduction method. For example, principle component analysis (PCA) has been incorporated into FMT reconstruction schemes without significant performance cost (Cao *et al* 2012). It stands to reason that an analogous method could be applied to KDOR large-scale problems with similar results. One immediate application could be to distinguish flow in an infarct region from normal brain and ECL. There are other applications in which DCE measurements could improve the clinical utility of NIRS such as characterizing the uptake of a tracer into a tumor. In such cases, the goal would be to reconstruct dynamic parameters on an image space defined by a set of arbitrary node coordinates.

Moving in the other direction, there are certain clinical settings where it would be desirable to obtain hemodynamic measurements, but where there is no *a priori* spatial information. Considering that the accuracy of the CBF measurements obtained with the KDOR method were fairly insensitive to uncertainties in the ECL thickness in the error analysis from Chapter 6, it may be possible to use a standard landmarking system to place one or two optodes on the head and estimate CBF using a population average head geometry (Custo *et al* 2010; Okamoto *et al* 2004). Removing the dependence of the KDOR workflow on anatomical priors from another imaging modality would enable its use in remote or hostile environments. The development of "field-unit" optical systems has been investigated by government defense and humanitarian organizations as a means of directly assessing brain injury in patients for whom access to NCU is not available. In particular, the portability of biomedical optics compared to traditional imaging methods is desirable in remote villages or on the battlefield. Near-infrared spectroscopy has shown promise in assessing severity of brain injury and presence of hematoma (Kessel *et al* 2007; Gopinath *et al* 1995). Unlike these studies, which used simple CW instrumentation and did not account for ECL contributions, time-resolved NIR in combination with the methods described in this thesis would significantly improve accuracy and precision, and therefore the predictive value of the recovered parameters. While TR NIR is considerably less compact than CW NIR, scaled-down versions have been developed (Wilmink *et al* 2011; Re *et al* 2010) and are therefore quite feasible.

7.2.2. Clinical validation

Clinical trials, including validation studies and randomized controlled trials, are ambitious, yet necessary next steps before DCE-NIR can be accepted as a clinically useful tool for the management of NCU patients. Three principle objectives should be addressed.

First, CBF measurements determined using the DCE-NIR method should be compared to a clinical standard such as CT perfusion to determine their accuracy and precision in NCU patients compared with the animal model. The comparisons could be made during routine CT imaging, adding the CT perfusion scan to the protocol with only a slight increase in dose to the patient (2.0-3.4 mSv compared to 1.5-2.5 mSv for a routine head CT (Hoeffner *et al* 2004)).

Second, it is necessary to determine the predictive value of DCE-NIR measurements of CBF for identifying DII in susceptible patients. For example, along the same lines as a previous study (Pham *et al* 2007), CT perfusion and DCE-NIR measurements could be obtained in SAH patients during the first two weeks of admission to the NCU. The two modalities could be compared in their abilities to predict the development of DII, as defined by the presence of delayed infarction on CT.

Finally, should the first two objectives be met, a randomized controlled trial should be conducted comparing clinically relevant endpoints (*i.e.*, Glasgow outcome scale, survival, etc.) of two groups of patients: those in whom CBF values are calculated with DCE-NIR at regular intervals during the acute recovery stage to inform patient management, and a control group for whom management is determined using current clinical practices. This final objective will be necessary before DCE-NIR can be recommended as standard-of-care.

7.2.3. Future applications

In Appendix A, the results of a recent numerical simulation are presented to highlight the use of the KDOR method in a completely different application. In particular, we investigated the ability of KDOR to recover the rate constants and molecular binding potential of a targeted tracer using the dual-tracer method (Tichauer *et al* 2012). These numerical experiments suggest

that the KDOR method improves the quantification of other dynamic parameters, compared with the traditional two-step method employed in FMT and DOT. Since commercially available solutions already exist for small animal preclinical imaging, KDOR can likely be incorporated into existing systems to improve the accuracy of these devices in evaluating molecular expression and drug binding.

In addition to small animal experiments, KDOR could be used in conjunction with targeted tracers to detect primary or metastatic cancer *in vivo*. In one potential application, the dual tracer method could be applied to breast cancer imaging targeting the HER2 receptor, which is expressed in the majority of primary tumors and lymph node metastasis (Carlsson *et al* 2004). In another application, a passive leaky tracer could be used to assess tissue permeability, a hallmark of cancer progression, in a variety of different cancers (St. Lawrence *et al* 2013). In both cases, accurate quantification of dynamic parameters is necessary to properly direct and monitor treatment.

7.3. Principle conclusions

The salient finding of this thesis is that DCE-NIR techniques have the potential to assess cerebral hemodynamics at the bedside of NCU patients, given that:

(i) CBF measurements obtained using a depth-resolved CW NIRS method showed strong agreement with CT perfusion measurements of CBF acquired in juvenile pigs.

(ii) Relative changes in CBF derived from statistical moments of TR-NIR data were in good agreement with percent change in CBF measured by CT perfusion.

(iii) Numerical simulations demonstrated that KDOR significantly improves the accuracy of flow measurements obtained from a heterogeneous medium (*e.g.*, the adult head).

(iv) Experimental multichannel TR-NIR data analyzed with the KDOR method provided accurate quantification of CBF in an adult pig model of ischemia.

7.4. References

Arora R, Ridha M, Lee D, Elliott JT, Diop M, Rosenberg H, Lee TY and St. Lawrence K 2013 Preservation of the metabolic rate of oxygen in preterm infants during indomethacin therapy for closure of the ductus arteriosus *Pediatr Res* doi:10.1038/pr.2013.53.

Branche PC, Johnston WS, Pujary CJ, Mendelson Y 2004 Measurement reproducibility and sensor placement considerations in designing a wearable pulse oximeter for military applications in *30th Annual Northeast Bioengineering Conference Proceedings of the IEEE* 216-217.

Carlsson J, Nordgren H, Sjöström J, Wester K, Villman K, Bengtsson NO, Ostenstad B, Lundqvist H, Blomqvist C 2004 HER2 expression in breast cancer primary tumours and corresponding metastases. Original data and literature review *Brit J Canc* 90(12) 2344-2348.

Chen D, Plemmons RJ 2009 Nonnegativity constraints in numerical analysis (World Scientific Press: River Edge, NJ) 109-140.

Custo A, Boas DA, Tsuzuki D, Dan I, Mesquita R, Fischl B, Grimson WEL, Wells W 2010 Anatomical atlas-guided diffuse optical tomography of brain activation *Neuroimage* 49(1) 561-567.

Durduran T, Yu G, Burnett MG, Detre JA, Greenberg JH, Wang J, Yodh AG 2004 Diffuse optical measurement of blood flow, blood oxygenation, and metabolism in a human brain during sensorimotor cortex activation *Opt Lett* 29(15) 1766-1768.

Gopinath SP, Robertson CS, Contant CF, Narayan RK, Grossman RG, Chance B 1995 Early detection of delayed traumatic intracranial hematomas using near-infrared spectroscopy *J Neurosurg* 83(3) 438-444.

Hoeffner EG, Case I, Jain R, Gujar SK, Shah GV, Deveikis JP, Carlos RC, Thompson BG, Harrigan MR, Mukherji SK 2004 Cerebral Perfusion CT: Technique and Clinical Applications *Radiol* 231(3) 632-644.

Jolliffe, IT 2002 Principal Component Analysis (Springer-Verlag: Berlin, Germany).

Kessel B, Jeroukhimov I, Ashkenazi I, Khashan T, Oren M, Haspel J, Alfici R 2007 Early detection of life-threatening intracranial haemorrhage using a portable near-infrared spectroscopy device *Injury* 38(9) 1065-1068.

Muench E, Horn P, Bauhuf C, Roth H, Philipps M, Hermann P, Quintel M, Schmiedek P, Vajkoczy P: Effects of hypervolemia and hypertension on regional cerebral blood flow, intracranial pressure, and brain tissue oxygenation after subarachnoid hemorrhage *Crit Care Med* 2007.

Okamoto M, Dan H, Sakamoto K, Takeo K, Shimizu K, Kohno S, Oda I, Isobe S, Suzuki T, Kohyama K, Dan I 2004 Three-dimensional probabilistic anatomical cranio-cerebral correlation via the international 10-20

system oriented for transcranial functional brain mapping *Neuroimage* 21(1) 99.

Re R, Contini D, Caffini M, Cubeddu R, Spinelli L, Torricelli A 2010 A compact time-resolved system near-infrared spectroscopy based on wavelenth space multiplexing *Rev Sci Instrum* 81 113101.

Rempp KA, Brix G, Wenz F, Becker CR, Gueckel F, Lorenz WJ 1994 Quantification of regional cerebral blood flow and volume with dynamic susceptibility contrast-enhanced MR imaging *Radiol* 193(3) 637-641.

St Lawrence K, Verdecchia K, Elliott J, Tichauer K, Diop M, Hoffman L, Lee T-Y 2013 Kinetic model optimization for characterizing tumour physiology by dynamic contrast-enhanced near-infrared spectroscopy *Phys Med Biol* 58(5) 1591.

Schytz HW, Wienecke T, Jensen LT, Selb J, Boas DA, Ashina M 2009 Changes in cerebral blood flow after acetazolamide: an experimental study comparing near-infrared spectroscopy and SPECT *Eur J Neurol* 16(4) 461-467.

Tichauer KM, Brown DW, Hadway J, Lee T-Y, St. Lawrence KS 2006 Near-infrared spectroscopy measurements of cerebral blood flow and oxygen consumption following hypoxia-ischemia in newborn piglets *J App Physiol* 100(3) 850-857.

Tichauer, KM, Samkoe KS, Sexton KJ, Hextrum SK, Yang HH, Klubben WS, Gunn JR, Hasan T, Pogue BW 2012 In vivo quantification of tumor receptor binding potential with dual-reporter molecular imaging *Mol Imag Biol* 14(5) 584-592.

Vajkoczy P, Horn P, Thome C, Munch E, Schmiedek P 2003 Regional cerebral blood flow monitoring in the diagnosis of delayed ischemia following aneurysmal subarachnoid hemorrhage *J Neurosurg* 98(6) 1227-1234.

Verdecchia K, Diop M, Lee T-Y, Lawrence KS 2013 Quantifying the cerebral metabolic rate of oxygen by combining diffuse correlation spectroscopy and time-resolved near-infrared spectroscopy *J Biomed Opt* 18(2) 027007-027007.

Yalavarthy PK, Pogue BW, Dehghani H, Paulsen KD 2007 Weight-matrix structured regularization provides optimal generalized least-squares estimate in diffuse optical tomography *Medical Physics* 34(6) 2085–2098.

APPENDIX A

Applying KDOR to small animal fluorescence imaging of molecular binding

A.1. Background

The kinetic deconvolution optical reconstruction (KDOR) approach can be extended to more complex tracer kinetic models to characterize the behaviour of targeted tracers which bind to receptors of interest. Targeted tracer methods have been extensively used in more established imaging modalities such as positron emission tomography (PET), and have recently been applied to planar fluorescence imaging to quantify molecular expression of epidermal growth factor receptor (EGFR) in tumors (Tichauer *et al* 2012). Similar to computed tomography (CT) perfusion, PET molecular imaging methodology involves two-steps: spatial reconstruction of tracer concentration and subsequent kinetic analysis. Spatial reconstruction in PET is a well-posed problem: the radioisotope undergoes positive beta decay, and subsequent postitron-electron annihilation, producing two 511 keV gamma photons that are emitted at almost 180° and can be used to localize the source of the decay (*i.e.*, a radiolabeled tracer) with sub-centimeter resolution. However, using a two-step (TS) reconstruction process in optical tomography will result in loss-of-information that will decrease the accuracy of recovered kinetic parameters. An alternative approach is to use the kinetic deconvolution optical reconstruction (KDOR) algorithm to characterize the $R(t)$ function for

each region directly, and then to obtain information from these recovered functions by fitting them with a kinetic model. This approach allows the kinetic information to be extracted from the imaging data in a single inversion, mitigating the loss-of-information from the spatial reconstruction step.

In molecular imaging with targeted and untargeted probes, the uptake of a tracer by the tissue can be described by the following convolution:

$$C(t) = K_1 C_a(t) * R(t), \tag{A.1}$$

where K_1 is the rate constant governing the extraction of the tracer into the interstitial space, and $K_1 = F \times E$, where E is the extraction fraction, and F is the blood flow. Note that this notation differs slightly from applications involving vascular tracers such as ICG, since this model specifically characterizes the *uptake* of tracer into the tissue and does not attempt to model the vascular dynamics of the dye. To extract meaningful information from the impulse residue functions of targeted and untargeted tracers, mathematical models are derived through compartmental analysis (Goldberg *et al* 1980; Hine *et al* 1980; Tichauer *et al* 2012), assuming the targeted tracer can be in one of three "spaces": the arterial space, $C_a(t)$, unbound in the extracellular extravascular space (EES), $C_f(t)$, or bound to its receptor in the EES, $C_b(t)$. The untargeted tracer is assumed to only occupy the arterial space and the unbound EES. The transport of each tracer from one compartment to the other is described by first order rate constants (*e.g.* K_1 and k_2 describe transport between blood and the ESS, and k_3 and k_4 describe transport between the free and bound states), and is summarized in Figure A.1.

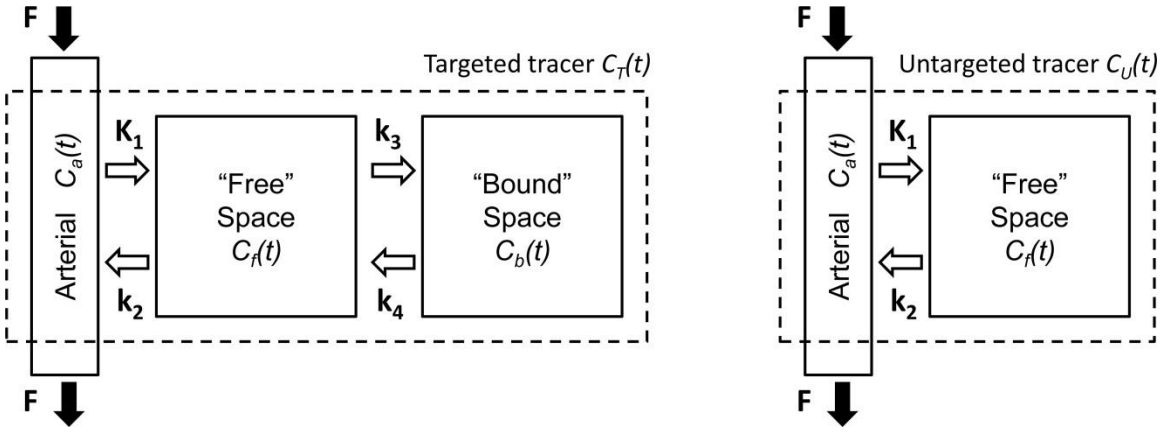

Figure A.1: The dual-tracer compartment model

The targeted tracer, $C_T(t)$, characterizes the delivery, uptake and binding of a ligand to a receptor-of-interest. The untargeted tracer, $C_U(t)$, is designed to behave identical to the targeted tracer in terms of delivery and uptake, but does not have the ability to occupy the bound space. By the simultaneous injection of targeted and untargeted tracers, parameters K_1, k_2, and k_3/k_4 can be characterized. (Adapted from Tichauer *et al* 2012).

If an untargeted tracer is selected that has the same arterial input function, $C_a(t)$, as the targeted tracer, and the binding kinetics (k_3 and k_4) are much faster than the vascular leakage kinetics (k_2), then the following set of equations describes the residue function in Eq. A.1 for the targeted, $R_T(t)$, and untargeted, $R_U(t)$, tracers:

$$R_T(t) = e^{-\frac{k_2}{1+BP}t} \qquad \text{(A.2a)}$$

$$R_U(t) = e^{-k_2 t}, \qquad \text{(A.2b)}$$

where BP is the binding potential and is equal to k_3/k_4 by definition (Tichauer *et al* 2012). Often, the measurement of $C_a(t)$ is difficult, and is avoided by combining the targeted and untargeted model-specific versions of Eq A.1 (Lammertsma and Hume 1996). However, pulse dye densitometers can quantify the $C_a(t)$ of indocyanine green and its derivatives (Iijima *et al* 1997), and $C_a(t)$ can be estimated for near-infrared and red dyes using widely available standard pulse oximeters (Elliott JT *et al* 2012b). Since both of

these approaches enable the $C_a(t)$ to be measured independent of the FMT data at high temporal resolution, $C_a(t)$ can be used as a time-reference for the FMT projection data. In this case, the KDOR method recovers the $K_1R(t)$ from each region, which is analogous to vector $\mathbf{R_F}$ from Eq. 5.3. (see Chapter 5) in the dual-tracer approach, and can be formulized as:

$$\mathbf{S_U} = \left(\mathbf{C_A} \otimes \mathbf{A}\right)\mathbf{R_U} \tag{A.3a}$$

$$\mathbf{S_T} = \left(\mathbf{C_A} \otimes \mathbf{A}\right)\mathbf{R_T} \tag{A.3b}$$

where $\mathbf{S_U}$ and $\mathbf{S_T}$ represent the signal vector measured at the wavelengths corresponding to the untargeted and targeted tracers, respectively, and $\mathbf{R_U}$ and $\mathbf{R_T}$ represent the stacked $R_T(t)$ and $R_U(t)$ functions from each region. An implicit assumption in this technique is that $\mathbf{C_A}$, the Toeplitz matrix of the AIF, is the same for both tracers; this requires consideration when designing probe pairs, but has been demonstrated to be a valid assumption in applications using IRDye 700DX and IRDye 800CW-EGF (both by LI-COR Biosciences, Lincoln, NE) (Samkoe *et al* 2012). The kinetic parameters (*i.e.*, K_1, k_2, BP) are recovered by optimizing the following expression:

$$\underset{K_1,k_2,BP}{\arg\min}\left\{\left\|K_1R_{T,rec}(t) - K_1e^{-\frac{k_2}{1+BP}t}\right\|_2^2 + \left\|K_1R_{U,rec}(t) - K_1e^{-k_2t}\right\|_2^2\right\} \tag{A.4}$$

Optimization was performed in MATLAB using the *fminsearchbnd* function (D'Errico 2005).

A.2. Numerical experiment

The numerical simulations presented in this subsection demonstrate the ability of KDOR to quantify the molecular expression of a targeted tracer in small animal imaging of cancer using FMT. Numerical simulations were performed with NIRFAST using the heterogenous optical digimouse (Dogdas

et al 2007) and the previously described fan-beam FMT configuration (Tichauer *et al* 2011). This configuration is shown in Fig. A.2. Fluorescence at the targeted (800 nm) and untargeted (700 nm) dye wavelengths was simulated in the digimouse head and signal was recorded in the five detectors simultaneously with an integration time of 12 seconds. This was repeated for 32 source detector positions, with a rotation time (deadtime) between positions of 32 seconds. A complete set of optical data (32 source-positions x 5 detectors) was acquired every 23.5 minutes for 2.5 hours.

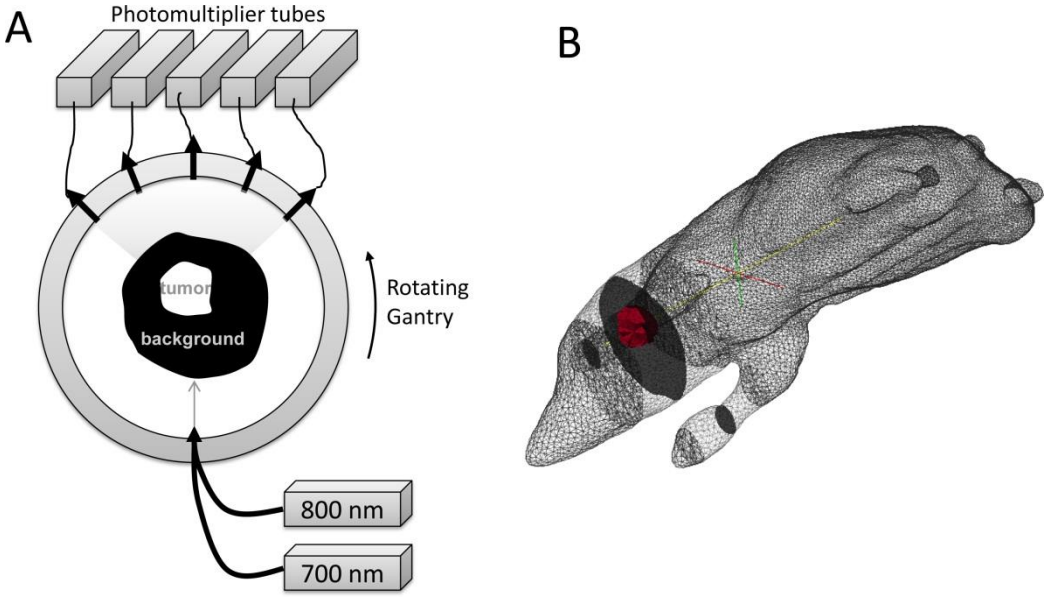

Figure A.2: Fan beam FMT and digimouse mesh used in simulations

(A) The FMT system, based on published work by the Optics in Medicine group at Dartmouth College, consists of one source position and five detector positions, which rotate around a gantry to collect tomography data. A cross section of the mouse head with a tumor region is shown in the centre of the system. (B) The digimous mesh used in the simulations, showing the tumor inclusion located in the head slice.

Targeted and untargeted tracer uptake in each tissue region was simulated using Eq. A.1. The true (input) values for the kinetic parameters are given in Table 1 and are from kinetic planar imaging data (Tichauer *et al* 2012). An arterial input function was simulated using a biexponential model of the form $ae^{-tb}+ce^{-td}$, for which parameters *a*-*d* were defined as 0.15 uM,

3.6 min^{-1}, 0.05 uM, and 44 min^{-1}. This model was previously shown to fit experimental arterial input functions in mice with good agreement (Samkoe *et al* 2012). Gaussian white-noise of 20% was added to the FMT signal and to $C_a(t)$. The targeted and untargeted uptake curves are shown in Figure A.3.

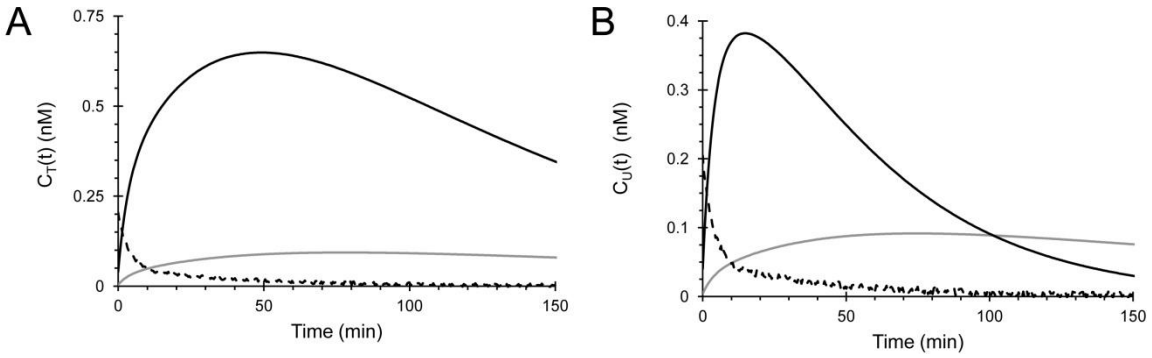

Figure A.3: Simulated uptake curves

The uptake curves used in the forward model for the background (grey solid line) and the tumor (black solid line) regions, for the targeted (A) and untargeted (B) tracers. The arterial input function is also shown (black dashed line).

Reconstruction of kinetic parameters was performed using the KDOR and TS methods. In the KDOR approach, the region-specific $K_1R(t)$ functions for the targeted and untargeted tracers were reconstructed from Eq. A.3, and kinetic parameters were extracted by minimizing Eq. A.4. In the TS approach, a time-series of targeted and untargeted concentration maps were reconstructed using a Levenberg-Marquardt approach (Dehghani *et al* 2008) with hard anatomical priors and these regions-of-interest were then used to define the tracer uptake curves. Kinetic parameters were extracted by fitting the tracer uptake curves with the convolution in Eq. A.1. In both cases, reconstruction was performed on a homogeneous mesh (μ_a = 0.01 mm^{-1}, μ_s' = 1.0 mm^{-1}) rather than the heterogeneous mesh used in the forward data, to avoid the inverse crime. To compare the precision and accuracy of the two approaches, the reconstruction procedure was repeated 100 times.

A.3. Results and discussion

For the tumor region, the KDOR-recovered $K_1R(t)$ functions and the tissue uptake curves recovered from the reconstructed fluorophore maps are shown in Fig. A.4. Both untargeted and targeted $R(t)$ functions recovered with the KDOR approach show a strong agreement with input values—the percent difference in area under the fitted and input curves was less than 0.01% in all cases and were not significantly different. Whereas the values recovered using the TS method show marked deviations from the true values.

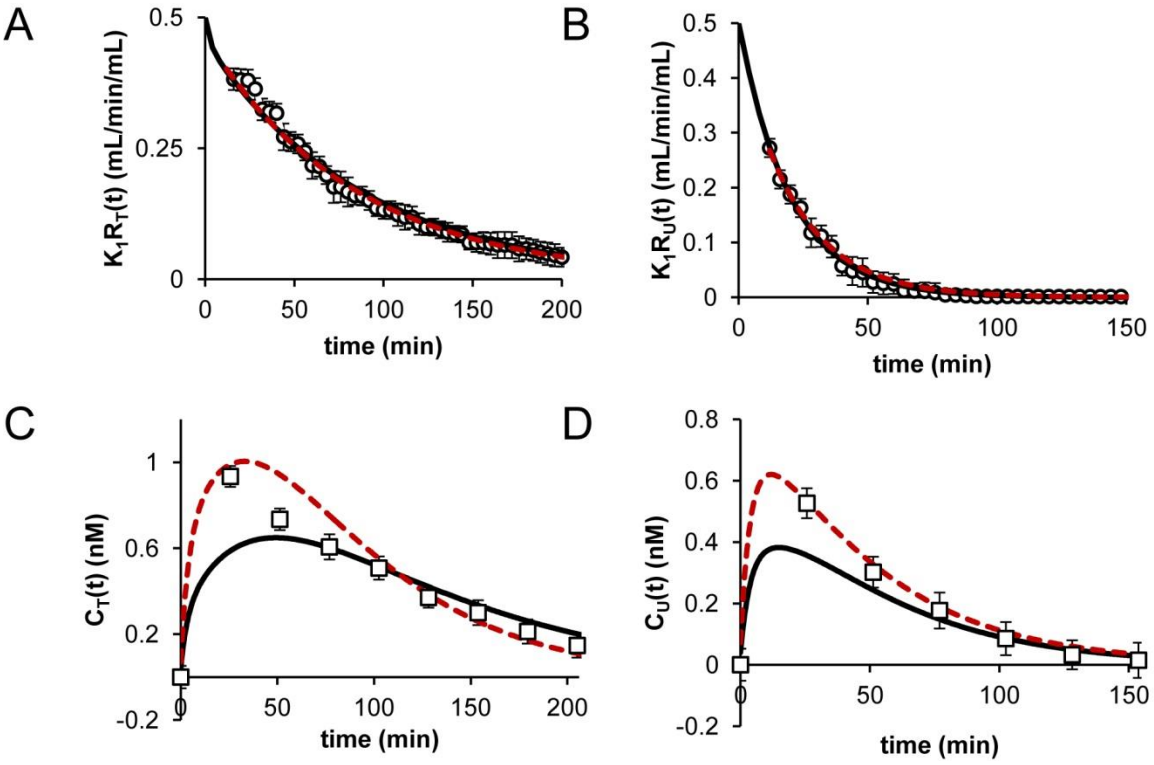

Figure A.4: Functions recovered with KDOR and TS methods

The mean KDOR-recovered $K_1R(t)$ (open circles ± SD) for the 100 repetitions, along with the true (black line) and mean model-fitted (red line) $K_1R(t)$ functions for the targeted (A) and untargeted (B) tracers. The mean $C(t)$ uptake curves recovered with the two-step approach (open squares ± SD), along with the true (black line) and mean model-fitted (red line) uptake curves for the targeted (C) and untargeted (D) tracers.

Kinetic parameters were recovered by fitting the corresponding dual-tracer model functions to these curves. Figure A.5 presents box-and-whisker

plots for the three kinetic parameters recovered for the two regions (background and tumor) with KDOR and TS methods. In general, KDOR is more accurate and precise in recovering the kinetic parameters. In fact, the TS method is only capable of accurately recovering the background K_1 parameter, and in even in this case, exhibits high variability.

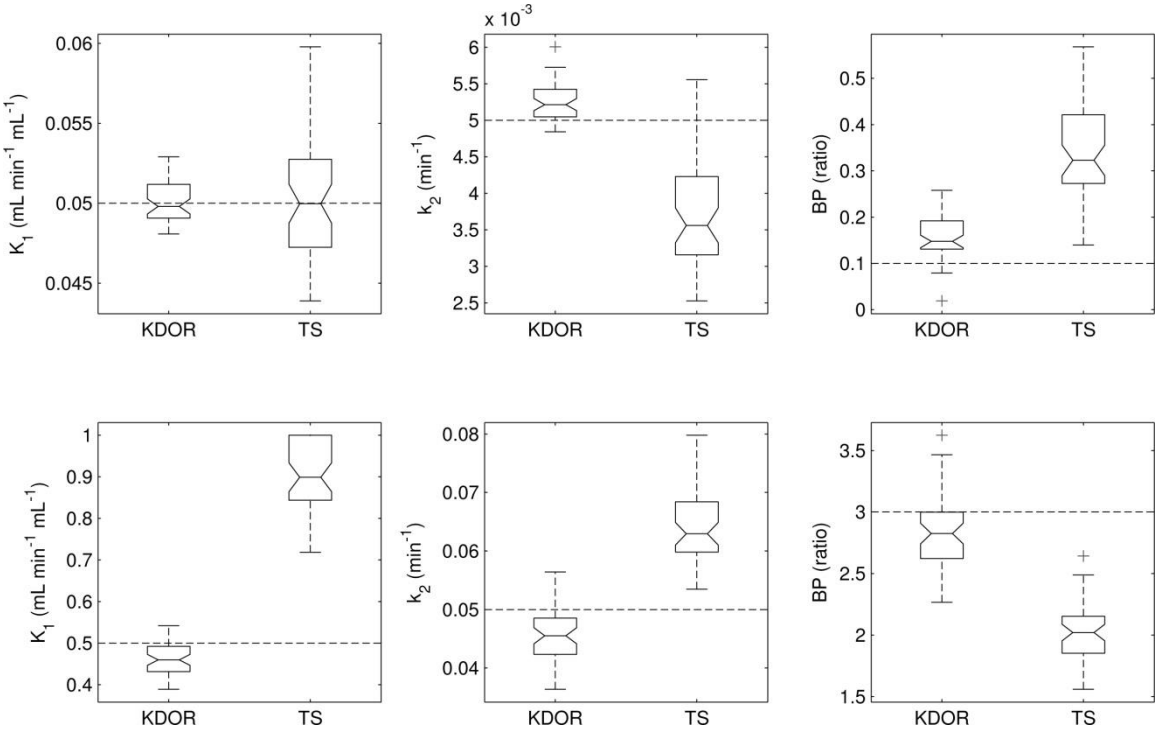

Figure A.5: Kinetic parameters recovered with the two approaches

Box-and-whisker plots of K_1, k_2 and binding potential recovered with the KDOR and TS method for the background (top row) and tumor (bottom row) regions. Boxes are bound by the 1st and 3rd quartiles, and the median is given by the centre line. Error bars are min and max, with outliers shown as crosses. Dashed lines show the true value of the parameter.

The most important parameter in preclinical cancer imaging applications is *BP*, which can be used to assess molecular expression of a particular receptor, and evaluate the affinity of a particular ligand (*e.g.*, a prospective drug) for its receptor. Both methods exhibited different levels of BP underestimation, likely owing to spatial blurring causing contamination from the low-*BP* background. However, this underestimation was five times less pronounced when KDOR was used. Also contributing to this

improvement, the temporal resolution of the functions recovered with KDOR show significant improvement over the uptake curves characterized from the reconstruction fluorophore maps. This is a direct result of using the independently-measured AIF to time-stamp each data projection. Of particular interest, the mean error and 95% confidence interval in the tumor *BP* recovered by KDOR was −5.86% (−25.0 - 13.3%), whereas the with the TS approach, the error was −32.6% (−49.0 - −16.5%). The improved accuracy in the KDOR-recovered values of K_1 and k_2 are also notable, since these parameters could indicate enhanced vascular permeability, which is a hallmark of tumor angiogenesis. Surprisingly, the errors in all KDOR-derived parameters were comparable to reported results using more robust planar imaging techniques (Tichauer *et al* 2012). This finding can be explained by the negative monotonicity temporal constraint on the *R(t)* reconstructions (see Chapter 5), which is valid irrespective of the kinetic model used since all compartment models decay exponentially. Further studies are ongoing to investigate the accuracy of this KDOR approach in animal studies.

A.4. References

Dehghani H, Eames ME, Yalavarthy PK, Davis SC, Srinivasan S, Carpenter CM, Pogue BW, Paulsen KD 2008 Near infrared optical tomography using NIRFAST: Algorithm for numerical model and image reconstruction *Commun Numer Methods* 25(6) 711-32.

D'Errico J 2005 fminsearchbnd, fminsearchcon in *MATLAB Central File Exchange http://www.mathworks.com/matlabcentral/fileexchange/8277-fminsearchbnd*

Dogdas B, Stout D, Chatziioannou A, and Leahy RM 2007 Digimouse: A 3D Whole Body Mouse Atlas from CT and Cryosection Data *Phys Med Biol* 52(3) 577-87.

Elliott JT, Diop M, Lee T-Y, St. Lawerence K 2012a Model-independent dynamic constraint to improve the optical reconstruction of regional kinetic parameters *Opt Lett* 37 2571-73.

Elliott JT, Wright EA, Tichauer KM, Diop M, Morrison LB, Pogue BW, Lee T-Y, St. Lawrence K 2012b Arterial input function of an optical tracer for dynamic contrast enhanced imaging can be determined from pulse oximetry oxygen saturation measurements *Phys Med Biol* 57(24) 8285.

Goldenberg DM, Kim EE, DeLand FH, Bennett S, Primus FJ 1980 Radioimmunodetection of cancer with radioactive antibodies to carcinoembryonic antigen *Cancer Res* 40 2984-92

Hine KR, Bradwell AR, Reeder TA, Drolc Z, Dykes PW 1980 Radioimmunodetection of gastrointestinal neoplasms with antibodies to carcinoembryonic antigen *Cancer Res* 40 2993-96.

Iijima T, Aoyagi T, Iwao Y, Masuda J, Fuse M, Kobayashi N, Sankawa H 1997 Cardiac output and circulating blood volume analysis by pulse dye-densitometry *J Clin Monit* 13 81–9.

Lammertsma AA, Hume SP 1996 Simplified reference tissue model for PET receptor studies *Neuroimage* 4 153–158.

Lee TY 2005 Method and apparatus for calculating blood flow parameters. *US Patent No. 6,898,453.*

Liebert A, Wabnitz H, Steinbrink J, Obrig H, Moller M, Macdonald R, Villringer A, Rinneberg H 2004 Time-resolved multidistance near-infrared spectroscopy of the adult head: intracerebral and extracerebral absorption changes from moments of distribution of times of flight of photons *Appl Opt* 43(15) 3037-3047.

Meier P, Zierler KL 1954 On the theory of the indicator-dilution method for measurement of blood flow and volume *J Appl Physiol* 6(12) 731-44.

Samkoe KS, Sexton K, Tichauer KM, Hextrum SK, Pardesi O, Davis SC, O'Hara JA, Hoopes PJ, Hasan T, Pogue BW 2012 High vascular delivery of EGF, but low receptor binding rate is obesrved in AsPC-1 tumors as compared to normal pancreas *Mol Imag Biol* 14(4) 472-79.

Sourbron SP, Buckley DL 2012 Tracer kinetic modelling in MRI: estimating perfusion and capillary permeability *Phys Med Biol* 57(2) R1-R33.

Thompson HK, Starmer CF, Whalen RE, McIntosh HD 1964 Indicator transit time considered as a gamma variate *Circ Res* 14 502-515.

Tichauer KM, Samkoe KS, Klubben WS, Hasan T, Pogue BW 2012 Advantages of a dual-tracer model over reference tissue models for binding potential measurement in tumors *Phys Med Biol* 57 6647-6659.

Tichauer KM, Holt RW, El-Ghussein F, Zhu Q, Dehghani H, Leblond F, Pogue BW 2011 Imaging workflow and calibration for CT-guided time-domain fluorescence tomography *Biomed Opt Expr* 2(11) 3021-36.

Zierler KL 1965 Equations for measuring blood flow by external modeling of radioisotopes *Circ Res* 16 309-21.

APPENDIX B

Copyright releases and animal ethics approval forms

B.1. List of copyright permissions and animal use protocols

No.	Description of document	Relevant sections
1	JBO permission to use copyrighted materials	Chapter 2
2	OSA permission to use copyrighted materials	Chapter 3, Chapter 5
3	IOP permission to use copyrighted materials	Chapter 4
4	AUS approval Mod #7 to AUP #2007-050-06	Chapter 1 (Fig. 1.7), Chapter 3, Chapter 6.
5	AUS approval for AUP #2007-050-06	Chapter 2
6	AUS approval for AUP #2009-087	Chapter 4

(Note: signatures, addresses, email addresses, and phone numbers have been removed from original correspondence as per School of Graduate and Postdoctoral Studies requirements.)

1.

Subject: RE: Permission to use copyrighted material in a doctoral thesis
From: ---
Date: March 4, 2013
To: ---

Dear Jonathan,

Thank you for seeking permission from SPIE to reprint material from our publications. Publisher's permission is hereby granted under the following conditions:

(1) You obtain permission of one of the authors;
(2) The material to be used has appeared in our publication without credit oracknowledgment to another source; and
(3) You credit the original SPIE publication. Include the authors' names, title of paper, volume title, SPIE volume number, and year of publication in your credit statement.

Sincerely,

Karen Thomas for
Eric Pepper, Director of Publications
SPIE

> From: ---
> Sent: Thursday, March 21, 2013 11:39 AM
> To: ---
> Subject: Permission to use copyrighted material in a doctoral thesis
>
> I would like permission to allow inclusion of the following material in my thesis:
>
> Elliott JT et al. Qunatitative measurement of cerebral blood flow in a juvenile
> porcine model by depth-resolved near-infrared spectroscopy J Biomed Opt 15
> 037014; 2010.
>
>The material will be attributed through a citation. Please confirm by email that
>these arrangements meet with your approval.
>
> Sincerely
> Jonathan Elliott

2.

Subject: RE: Request copyright agreement for purpose of PhD Thesis
From: ---
Date: Tue, January 8, 2013 4:46 pm
To: ---

Dear Mr. Elliott,

Thank you for contacting The Optical Society.

Because you are the author of the source paper from which you wish to reproduce material, OSA considers your requested use of its copyrighted materials to be permissible within the author rights granted in the Copyright Transfer Agreement submitted by the requester on acceptance for publication of his/her manuscript. It is requested that a complete citation of the original material be included in any publication. This permission assumes that the material was not reproduced from another source when published in the original publication.

Please let me know if you have any questions.

Kind Regards,

Susannah Lehman
January 8, 2013
Authorized Agent, The Optical Society

> From: ---
> Sent: Tuesday, January 08, 2013 11:58 AM
> To: ---
> Subject: Request copyright agreement for purpose of PhD Thesis
>
> I am writing to request a copyright agreement granting permission to use the
> following published papers for the purpose of my doctoral thesis:

> Elliott JT et al., Optics Letters 2012; 37 (13): 2571-2573
> Elliott JT et al., Biomed Opt Exp 2013; 4 (2): 206-218

> Thank you for your assistance in this matter, as I prepare for my upcoming
> thesis defense.

3.

Subject: Re: Permission to Use Copyrighted Material in a Doctoral Thesis
From: ---
Date: Fri, Mar 22, 2013 6:47 AM
To: ---

Dear Mr. Elliott,

Thank you for your email and for taking the time to seek this permission.

When you assigned the copyright in your article to IPEM, we granted back to you certain rights, including the right to include the article within any thesis or dissertation. Therefore, please go ahead and make what use you wish of the article in its accepted form - that is, your own version following any amendments made during peer review, rather than the final published version copy-edited and type-set by IOP.

Please let me know if you have any further questions. In the meantime, I wish you the best of luck with the completion of your dissertation.

Kind regards,

Laura Sharples
Rights & Permissions Officer
IOP Publishing Ltd

> From: ---
> Sent: Thu, Mar 21, 2013 at 2:45 PM
> To: ---
> Subject: Permission to Use Copyrighted Material in a Doctoral Thesis
>
> Dear Managing Editor
>
> I would like permission to allow inclusion of the following material in my thesis:
>
>Elliott JT et al. Phys Med Biol 57(24) 8285; 2012.
>
>The material will be attributed through a citation. Please confirm by email that
>these arrangements meet with your approval.

4.

From: ---
Sent: Tuesday, April 17, 2012 10:00 AM
To: ---
Cc: ---
Subject: eSirius Notification - New Protocol Modification Has Been APPROVED2007-050-06::5

Western

AUP Number: 2007-050-06
PI Name: St. Lawrence, Keith
AUP Title: Using Near-Infrared Spectroscopy to Measure Cerebral Blood Flow in the Neurointensive Care Unit

Official Notification of AUS Approval: A MODIFICATION to Animal Use Protocol 2007-050-06 has been approved.

The holder of this Animal Use Protocol is responsible to ensure that all associated safety components (biosafety, radiation safety, general laboratory safety) comply with institutional safety standards and have received all necessary approvals. Please consult directly with your institutional safety officers.

Submitted by: Kinchlea, Will D
on behalf of the Animal Use Subcommittee

[signature]

The University *of* Western Ontario
Animal Use Subcommittee / University Council on Animal Care
Health Sciences Centre, ● London, Ontario ● CANADA – N6A 5C1
PH: 519-661-2111 ext. 86768 ● FL 519-661-2028
Email: auspc@uwo.ca ● http://www.uwo.ca/animal/website/

5.

From: eSiriusWebServer [mailto:---]
Sent: Friday, October 07, 2011 3:14 PM
To: ---
Cc: ---
Subject: eSirius Notification - New Animal Use Protocol is APPROVED2007-050-06::5

Western

AUP Number: 2007-050-06
PI Name: St. Lawrence, Keith
AUP Title: Using Near-infrared Spectroscopy To Measure Cerebral Blood Flow In The Neurointensive Care Unit

Official Notice of Animal Use Subcommittee (AUS) Approval: Your new Animal Use Protocol (AUP) entitled "Using Near-infrared Spectroscopy To Measure Cerebral Blood Flow In The Neurointensive Care Unit" has been APPROVED by the Animal Use Subcommittee of the University Council on Animal Care. This approval, although valid for four years, and is subject to annual Protocol Renewal.2007-050-06::5

1. This AUP number must be indicated when ordering animals for this project.
2. Animals for other projects may not be ordered under this AUP number.
3. Purchases of animals other than through this system must be cleared through the ACVS office. Health certificates will be required.

The holder of this Animal Use Protocol is responsible to ensure that all associated safety components (biosafety, radiation safety, general laboratory safety) comply with institutional safety standards and have received all necessary approvals. Please consult directly with your institutional safety officers.

Submitted by: Copeman, Laura
on behalf of the Animal Use Subcommittee
University Council on Animal Care

[signature]

The University *of* Western Ontario
Animal Use Subcommittee / University Council on Animal Care
Health Sciences Centre, ● London, Ontario ● CANADA – N6A 5C1
PH: 519-661-2111 ext. 86768 ● FL 519-661-2028
Email: auspam@uwo.ca ● http://www.uwo.ca/animal/website/

6.

From: ---
Sent: Wednesday, February 01, 2012 11:38 AM
To: ---
Cc: ---
Subject: eSirius Notification - Annual Protocol Renewal APPROVED by the AUS 2009-087::2

AUP Number: 2009-087
PI Name: Lee, Ting Y
AUP Title: Maintenance of VX2 Tumor Cell Line in Rabbit Thigh Muscle

The YEARLY RENEWAL to Animal Use Protocol (AUP) 2009-087 has been approved.

1. This AUP number must be indicated when ordering animals for this project.
2. Animals for other projects may not be ordered under this AUP number.
3. Purchases of animals other than through this system must be cleared through the ACVS office.
   Health certificates will be required.

REQUIREMENTS/COMMENTS
Please ensure that individual(s) performing procedures on live animals, as described in this protocol, are familiar with the contents of this document.

The holder of this Animal Use Protocol is responsible to ensure that all associated safety components (biosafety, radiation safety, general laboratory safety) comply with institutional safety standards and have received all necessary approvals. Please consult directly with your institutional safety officers.

Submitted by: Thompson, Sharla H
on behalf of the Animal Use Subcommittee

[signature]

The University *of* Western Ontario
Animal Use Subcommittee / University Council on Animal Care
Health Sciences Centre, ● London, Ontario ● CANADA – N6A 5C1
PH: 519-661-2111 ext. 86768 ● FL 519-661-2028
Email: auspam@uwo.ca ● http://www.uwo.ca/animal/website/

CURRICULUM VITAE

Jonathan T. Elliott

Education

The University of Western Ontario
London, Ontario, Canada
2008 – 2013 Ph.D.

The University of Western Ontario
London, Ontario, Canada
2003 – 2008 B.M.Sc.

Honours and Awards

Canadian Institutes of Health Research
Postdoctoral Fellowship
2013-2015

Ontario Graduate Scholarship
2011-2012, 2012-2013

Ontario Graduate Scholarship in Science and Technology
2010-2011

SPIE Scholarship in Optical Science and Engineering
2010-2011

Western Graduate Research Scholarship
2008-2013

Alfred Jay Entrepreneurship Award
2012

OSA BIOMED Poster Competition 2nd prize
2012

Teaching Experience

Teaching Assistant
The University of Western Ontario
2008 – 2013

Guest Lecturer, Medical Biophysics
The University of Western Ontario
2011

Physics Instructor
The Princeton Review
2007 - 2009

Selected Publications

St. Lawrence K, Verdecchia K, Elliott JT, Tichauer KM, Diop M, Hoffman L, and Lee T-Y. Kinetic model optimization for characterizing tumour physiology by dynamic contrast-enhanced near-infrared spectroscopy. Physics in Medicine and Biology 2013; 58(5): 1591.

Arora R, Ridha M, Elliott JT, Diop M, Lee DS, Lee T-Y, St. Lawrence K. Preservation of the metabolic rate of oxygen in preterm infants during indomethacin therapy for closure of the ductus arteriosus. Pediatric Research. In press.

Elliott JT, Milej D, Gerega A, Weigl W, Diop M, Morrison LB, Lee T-Y, Adam Liebert and St. Lawrence K. Variance of time-of-flight distribution is sensitive to cerebral flow dynamics of indocyanine green as confirmed by comparing scalp and brain measurements in adult pigs. Biomedical Optics Express 2013; 4(2):206-218.

Elliott JT, Eric Wright, Tichauer KM, Diop M, Morrison LB, Pogue BW, Lee T-Y, St. Lawrence K. Arterial input function of an optical tracer can be determined from pulse oximetry oxygen saturation measurements. Physics in Medicine and Biology 2012; 57:8285-95.

Yeganeh HZ, Toronov V, Elliott JT, Diop M, Lee T-Y, and St. Lawrence K. Broadband continuous wave technique to measure baseline values and changes in the tissue chromophore concentrations. Biomedical Optics Express 2012; 3(11):2761-70.

Elliott JT, Diop M, Lee T-Y, and St. Lawrence K. Model-independent dynamic constraint to improve the optical reconstruction of regional kinetic parameters. Optics Letters 2012; 37(13): 2571-2573.

Cooper JA, Tichauer KM, Boulton M, Elliott JT, Diop M, Arango M, Lee T-Y, and St. Lawrence K Continuous Monitoring of Absolute Cerebral Blood Flow by Near-Infrared Spectroscopy During Global and Focal Temporary Vessel Occlusion. Journal of Applied Physiology 2011; 110: 1691-1698.

Tichauer KM, Migueis M, Frederic Leblond, Elliott JT Diop M, St. Lawrence K, and Lee T-Y. Depth resolution and multiexponential lifetime analyses of reflectance-based time-domain fluorescence data. Applied Optics 2011; 50(21): 3962-72.

Diop M, Tichauer KM, Elliott JT, Migueis M, Lee T-Y and St. Lawrence K. A comparison of time-resolved and continuous-wave near-infrared techniques measuring cerebral blood flow in piglets. Journal of Biomedical Optics 2010; 15(5), 057004.

Elliott JT, Diop M, Tichauer KM, Lee T-Y and St. Lawrence K. Quantitative measurement of cerebral blood flow in a juvenile porcine model by depth-resolved near-infrared spectroscopy. Journal of Biomedical Optics 2010; 15(3), 037014.

Tichauer KM, Elliott JT, Hadway JA, Lee DS, Lee T-Y and St. Lawrence K. Using near-infrared spectroscopy to measure the cerebral metabolic rate of oxygen under multiple levels of hypoxia in piglets. Journal of Applied Physiology 2010; 109(3):878-85.

Diop M, Elliott JT, Tichauer KM, Lee T-Y, and St. Lawrence K. A Broadband Continuous-Wave Multi-Channel NIRS System for Measuring Regional Cerebral Blood Flow in Neonates. Review of Scientific Instruments 2009; 80(5), 054302.

Tichauer KM, Elliott JT, Hadway JA, Lee T-Y, and St. Lawrence K. Cerebral metabolic rate of oxygen and amplitude-integrated electroencephalography during early reperfusion after hypoxia-ischemia in piglets. Journal of Applied Physiology 2009; 106(5):1506-12.

Conference Abstracts

Elliott JT, Diop M, Morrison LB, Lee T-Y, and St. Lawrence K. Dynamic contrast enhanced time-resolved near-infrared measurement of cerebral hemodynamics before and during ischemia. BiOS conference, SPIE, San Francisco, CA, January 2013. (Submitted July, 2012).

Elliott JT, Diop M, Lee T-Y, St. Lawrence K. Comparison of CT perfusion and bedside optical measurements of cerebral blood flow in an adult pig model of ischemia. World Stroke Congress, Brasilia, Brazil, October 2012.

Elliott JT, Tichauer KM, Holt RW, Kanick SC, St. Lawrence K, Pogue BW, Frederic Leblond. Comparison of Monte Carlo and diffusion approximation light modeling in small animal fluorescence tomography. Biomedical Optics and 3-D Imaging: OSA Optics and Photonics Congress, Miami, Florida, April 2012.

Elliott JT, Diop M, Lee T-Y, St. Lawrence K. Cerebral blood flow quantification during ischemia using a multi-distance moments-based time-resolved technique. Biomedical Optics and 3-D Imaging: OSA Optics and Photonics Congress, Miami, Florida, April 2012.

Yeganeh HZ, Toronov V, Elliott JT, Diop M, Lee T-Y, and St. Lawrence K. Quantitative measurement of Cerebral Blood Flow, using broad band, continuous wave near infrared spectroscopy. Biomedical Optics and 3-D Imaging: OSA Optics and Photonics Congress, Miami, Florida, April 2012.

Elliott JT, Chin CJ, Franklin JA. Using computational fluid dynamic modeling to predict flow disturbance and thrombosis within

arterial microvascular anastomosis. International Conference on Head and Neck Cancer, Toronto, ON, July 21-25, 2012.

Chin CJ, Elliott JT, Franklin JH. A computational fluid dynamic model of the microvascular venous anastomotic options in head and neck reconstruction. International Conference on Head and Neck Cancer, Toronto, ON, July 21-25, 2012

Elliott JT, Diop M, Lee T-Y, St. Lawrence K. Measuring hemodynamic parameters during ischemia with an optical indicator-dilution technique *(Oral presentation).* London Health Research Day, London, Ontario, March 2012.

Chin CJ, Elliott JT, Franklin JH. Using CFD modeling to predict disturbance and thrombosis within microvascular anastomosis. London Health Research Day, London, Ontario, March 2012.

Toronov V, Elliott JT, Lee T-Y, and St. Lawrence K. Depth-resolved quantitative measurement of cerebral blood flow using broad-band near infrared spectroscopy and a two-layer head model. SPIE/OSA European Conferences on Biomedical Optics, Munich, Germany, May 2011.

Elliott JT, Diop M, Morrison LB, Lee T-Y, and St. Lawrence K. Quantitative measurement of cerebral blood flow in an adult porcine model of ischemia using a time-resolved near-infrared technique. Brain 2011 (25thInternational Symposium on Cerebral Blood Flow, Metabolism, and Function) Barcelona, Spain, May 2011.

Elliott JT, Diop M, Lee T-Y, St. Lawrence K. Theoretical time-resolved near-infrared measurements of indicator-dilution in the

human head using tracer kinetic modeling and serial Monte Carlo simulations. Brain 2011 (25th International Symposium on Cerebral Blood Flow, Metabolism, and Function) Barcelona, Spain, May 2011.

Elliott JT, Diop M, Lee T-Y, St. Lawrence K. Non-invasive bedside optical measurement of cerebral blood flow *(Oral presentation)*. Lawson Research Day, London, Ontario, Mar. 2011.

Ridha M, Elliott JT, Arora R, Lee T-Y, Lee DS, St. Lawrence K. Using near-infrared spectroscopy to monitor cerebral hemodynamics and metabolism in very low birth weight neonates treated for patent ductus arteriosus. Hot Topics in Neonatology, Washington, D.C. Dec 5-7, 2010.

Elliott JT, Diop M, Tichauer KM, Lee T-Y, St. Lawrence K. Monte Carlo based modeling of indocyanine green bolus tracking in the adult human head (*Oral Presentation).* BiOS conference, SPIE, San Francisco, CA, Jan. 2011.

Elliott JT, Tichauer KM, Diop M and St. Lawrence K. Fast Monte Carlo fitting of two-layered tissue structures for short source-detector distances. BiOS conference, SPIE, San Francisco, CA, January 2011.

Elliott JT, Diop M, Tichauer KM, Lee T-Y, and St. Lawrence K. Quantification of cerebral blood flow in the adult using near-infrared spectroscopy assisted by subject-individualized Monte Carlo modeling (*Oral Presentation*).Biomedical Optics and 3-D Imaging: OSA Optics and Photonics Congress, Miami Beach, Florida, March 2010.

Elliott JT, Tichauer KM, Diop M, and St. Lawrence K. Fast Monte Carlo simulations for quantifying optical properties from short source-detector separation geometries. Biomedical Optics and 3-D Imaging: OSA Optics and Photonics Congress, Miami Beach, FL, March 2010.

Diop M, Tichauer KM, Elliott JT, Lee T-Y, and St. Lawrence K. Time-resolved near-infrared technique for bedside monitoring of absolute blood flow (*Oral Presentation*). BiOS conference, SPIE, San Francisco, California, January 2010.

Elliott JT, Diop M, Tichauer KM, Lee T-Y, St. Lawrence K. Measurement of Cerebral Blood Flow in the Adult Pig by Depth-Resolved Broadband Near-Infrared Spectroscopy. Brain '09 (24rd International Symposium on Cerebral Blood Flow, Metabolism, and Function) Chicago, Illinois, July 2009.

Tichauer KM, Elliott JT, Hadway JA, Lee T-Y, St. Lawrence K. Real-Time Tracking of Cerebral Blood Flow during Arterial Occlusion by Near-Infrared Spectroscopy. Brain '09 (24rd International Symposium on Cerebral Blood Flow, Metabolism, and Function) Chicago, Illinois, July 2009.

Tichauer KM, Elliott JT, Hadway JA, Lee T-Y, St. Lawrence K. Comparison of Independent Techniques for Measuring Cerebral Venous Oxygenation in Neonates. Oral Presentation. Brain '09 (24rd International Symposium on Cerebral Blood Flow, Metabolism, and Function) Chicago, Illinois, July 2009.

Diop M, Elliott JT, Tichauer KM, Lee T-Y, St. Lawrence K. A Broadband Multi-Channel NIRS System for Measuring Focal Ischemic Brain Injury in Newborns. Brain '09 (24rd International

Symposium on Cerebral Blood Flow, Metabolism, and Function) Chicago, Illinois, July 2009.

Diop M, Elliott JT, Tichauer KM, Keenliside L, Lee T-Y, St. Lawrence K. Development of a broadband multi-channels NIRS system for measuring regional cerebral blood flow. OSA (Optical Society of America) Biomedical Optics Topical Meetings, St. Petersburg, Florida, March 2008.

Patents and Intellectual Property

Kinetic deconvolution optical reconstruction method. PCT Application No. PCT/CA2013/000202 filed March 4, 2013.

Professional Activities

Professional Societies

President and Founder
UWO SPIE Student Chapter
2011-2013

Journal Referee

Neurological Research
Physiological Measurement
Journal of Biomedical Optics
Biomedical Optics Express
Applied Optics
Optics Letters